

Ph.D. thesis on

**Application of polarized line formation theory
to the solar spectrum**

Submitted by
H. N. Smitha

Thesis Supervisor
Prof. K. N. Nagendra
Indian Institute of Astrophysics
Bangalore



**Registered for Ph.D. degree in the
Department of Physics, Pondicherry University
Puducherry**

Declaration

I hereby declare that the material presented in this thesis, submitted to the Department of Physics, Pondicherry University, for the award of Ph.D. degree, is the result of investigations carried out by me, at Indian Institute of Astrophysics, Bangalore under the supervision of Prof. K. N. Nagendra. The results reported in this thesis are new, and original, to the best of my knowledge, and have not been submitted in whole or part for a degree in any University. Whenever the work described is based on the findings of other investigators, due acknowledgment has been given. Any unintentional omission is duly regretted.

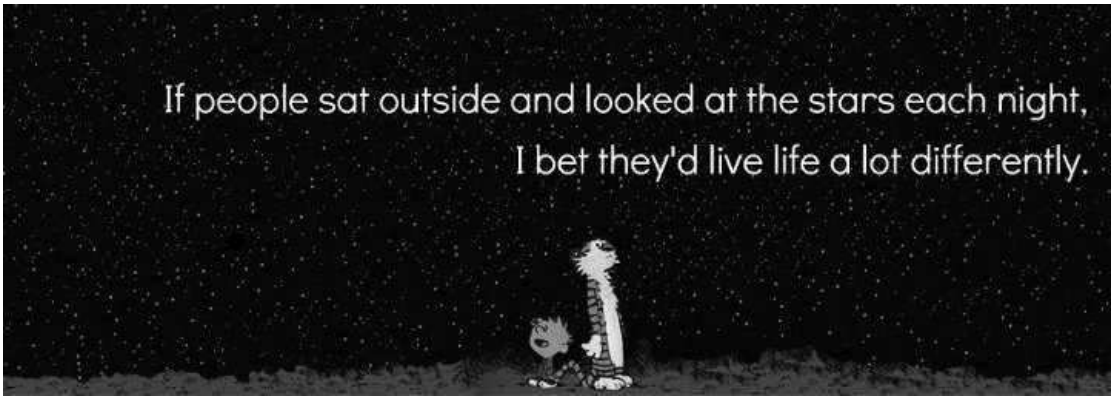
H. N. Smitha
(Ph.D candidate)
Indian Institute of Astrophysics
Bangalore - 560 034
June 2014

Certificate

This is to certify that the work embodied in this thesis entitled “Application of polarized line formation theory to the solar spectrum”, has been carried out by Ms. H. N. Smitha, under my supervision and the same has not been submitted in whole or part for Degree, Diploma, Associateship Fellowship or other similar title to any University.

Prof. K. N. Nagendra
(Thesis supervisor)
Indian Institute of Astrophysics
Bangalore - 560 034
June 2014

If people sat outside and looked at the stars each night,
I bet they'd live life a lot differently.



– Bill Watterson, *Calvin and Hobbes*

To
My parents,
Santosh, Sindhu, Aditi,
and
Pradeep

Acknowledgements

I would like to express my sincere and deepest gratitude to my thesis supervisor Prof. K. N. Nagendra for his valuable guidance, consistent support and encouragement which made it possible to carry out this research work. He has been a great mentor since the time I did my summer research project under him in 2008. I also thank him for bringing me in contact with Prof. J. O. Stenflo, Dr. M. Bianda, and providing me an opportunity to visit the solar observatory (IRSOL) in Locarno, Switzerland.

I am thankful to the Director, IIA, for providing me the opportunity and excellent research facilities to work at IIA. I would like to thank the Dean and the BGS for their help and guidance in various official matters during my Ph.D.

I thank Dr. Sampoorna and Dr. Anusha for their help and guidance at various stages of my Ph.D.

My sincere thanks to Prof. J. O. Stenflo, for his valuable inputs on the work carried out in this thesis. I have enjoyed every discussion, both scientific and others, with him during my stay at IRSOL. I would also like to thank him and his wife Joyce for their kind hospitality during my visit to their house in 2012.

Meeting Dr. Michele Bianda, his wife Anna and their daughter Aline has been one of the nicest experiences during my Ph.D. I cherish every moment spent with them. From Dr. Bianda, I have had the opportunity to learn about the instrument at IRSOL and its working. He has supported me greatly during my stay there. His wife Anna has been a great friend to me. I would like to express my deepest gratitude to their family. I also like to thank Dr. Renzo Ramelli for his help in the observations and the interesting discussions on several issues during my stay at IRSOL. It is a pleasure to thank Mrs. Annaliese who took very good care of me, and Ms. Katya for her help in official matters during my visit to IRSOL. It was a pleasure to meet Prof. E. Wiehr, at IRSOL, and discuss various aspects of instrumentation, solar prominences and flares. I thank him for taking me around the city of Locarno.

I thank the members of my Doctoral committee Prof. K. E. Rangarajan, Prof. Arun Mangalam and Prof. N. Satyanarayana for their encouragement, valuable inputs, and for monitoring the progress of my research work. I also thank the H.O.D of the physics department at the Pondicherry University, Prof. G. Chandrasekharan, for the help and

guidance in administrative procedures.

A very special thanks to Dr. B. S. Shylaja, Mr. H. R. Madhusudhan, and the staff at the Jawaharlal Nehru Planetarium, Bangalore, who laid the foundation for my research interests in physics. I have greatly benefited from the Research Education Advancement Program (REAP) conducted at the Planetarium as a part of which, I had the opportunity to learn some important topics like Quantum mechanics, Electrodynamics, Astronomy etc, from Prof. B. R. Iyer, Prof. K. Lokanathan, and Dr. Shylaja. I had the opportunity to learn various aspects of experimental physics from Mr. Madhusudhan, who gave me the freedom to conduct any experiment of my choice during the first two years of REAP. Every discussion I have had with him on the experimental results, their interpretation, has been very insightful. My special thanks to Dr. Shylaja for her personal care during the three years of REAP.

I take this opportunity to thank all my teachers from whom I developed my interests in physics and mathematics. I would also like to express my gratitude towards the professors at the Bangalore University, Prof. A. R. Ushadevi, Prof. B. N. Meera, Prof. Sarbari Bhattacharya, and Prof. Sharath Ananthamurthy for their support and encouragement during my M.Sc. A very special thanks to late Prof. K. S. Ramprasad for nurturing my interests in mathematics.

I thank the administrative staff at IIA, Mr. S. B. Ramesh, Mr. Narasimha Raju, Mr. Shankaranarayanan, Mr. Rajendran, Mr. K. T. Rajan, Mrs. Malini Rajan, Mrs. Pramila, Mr. Monnappa, and others for their kind and timely help with various administrative matters during my Ph.D. I also thank the library staff for their kind help in matters related to books and publications. My sincere thanks to Dr. Baba Varghese for installing all the necessary software in my computer, and the staff at the computer center, especially Mr. Ashok, for the help towards all computer related problems. I also thank Dr. Rekhesh Mohan and Mr. Anish for their help and guidance in using the high performance computing facilities at IIA.

I thank the staff of the Bhaskara guest house for making my stay very comfortable. During this stay, I have been lucky to have made some great friends without whom this journey would not have been as smooth. A very dear and special thanks to Sangeetha, Shubham, Sowmya, and Supriya for being there for me whenever I needed them. Every celebration, every laugh, every adventure, every moment we have spent together will be treasured forever. These five years of my Ph.D has been made very memorable by all the students at IIA and also by several others whom I met during this journey: Athray, Filis, John, Priya, Preethi, Rakhee, Radhika, and Stanislav. A very special thanks to Anantha for being a wonderful roommate. I also thank Indu, Drisya, Sindhuja, Susmitha, Manpreet and Pradeep for creating a comfortable working environment at our office.

It is a pleasure to thank my dearest friends Anjali, Ashwini, Deepa, and Priyanka

Acknowledgements

for their limitless support and encouragement at every stage of my life. Time spent with Shruthi, Vinay, Sidharth, Kamalam, Nagaranjini, Sujatha, Avinash, Jinesh, Swathi, Vatsala, Sanjay, Bhargavi, Zahara, Rakesh, and Sonam will always be memorable. I thank my relatives, and all my cousins for their constant support and encouragement which has always given me the strength to achieve my goals.

I am greatly indebted to my parents, my family, Pradeep, my “twin sister” Chaitra, and Varsha for their support, encouragement, patience, and trust. It is not possible to thank them enough in words.

Finally, I would like to thank everyone who has directly or indirectly supported me in the past years and my apologies to those, whom I may have left out unintentionally.

List of publications

In International refereed journals

1. *The Quantum Interference Effects in the Sc II 4247 Å Line of the Second Solar Spectrum*
Smitha, H. N., Nagendra, K. N., Stenflo, J. O., Bianda, M., & Ramelli, R. 2014, under review
2. *Polarized Line Formation with J and F-state Interferences in the Collisionless Non-magnetic Regime*
Smitha, H. N., Nagendra, K. N., & Stenflo, J. O. 2014, under review
3. *Modeling the Quantum Interference Signatures of the Ba II D₂ 4554 Å Line in the Second Solar Spectrum*
Smitha, H. N., Nagendra, K. N., Stenflo, J. O., & Sampoorna, M. 2013, **ApJ**, 768, 163.
4. *Polarized Line Formation with J-state Interference in the presence of Magnetic Fields: A Heuristic Treatment of Collisional Frequency Redistribution*
Smitha, H. N., Nagendra, K. N., Sampoorna, M., & Stenflo, J. O. 2013, **JQSRT**, 115, 46
5. *Polarized Line Transfer with F-state Interference in a Non-magnetic Medium: Partial Frequency Redistribution Effects in the Collisionless Regime*
Smitha, H. N., Sowmya, K., Nagendra, K. N., Sampoorna, M., & Stenflo, J. O. 2012, **ApJ**, 758, 112
6. *J-state Interference Signatures in the Second Solar Spectrum: Modeling the Cr I Triplet at 5204-5208 Å*
Smitha H. N., Nagendra, K. N., Stenflo, J. O., Bianda, M., Sampoorna, M., Ramelli, R., & Anusha, L. S. 2012, **A&A**, 541, 24
7. *Radiative Transfer with J-state Interference in a Two-term atom: Partial Frequency Redistribution in the Non-magnetic Case*

- Smitha, H. N.**, Nagendra, K. N., Sampoorna, M., & Stenflo, J. O. 2011, **A&A**, 535, 35
8. *Polarized Line Formation with J-state Interference in the Presence of Magnetic Fields I: Partial Frequency Redistribution in the Collisionless Regime*
Smitha, H. N., Sampoorna, M., Nagendra, K. N., & Stenflo J. O. 2011, **ApJ**, 633, 4
9. *Quantum Interference with Angle-dependent Partial Frequency Redistribution: Solution of the Polarized Line Transfer in the Non-magnetic Case*
Supriya, H. D., **Smitha, H. N.**, Nagendra, K. N., Ravindra, B., & Sampoorna, M. 2013, **MNRAS**, 429, 275
10. *Center to Limb Observations and Modeling of the Ca I 4227 Å Line*
Supriya, H. D., **Smitha, H. N.**, Nagendra, K. N., Stenflo, J. O., Bianda, M., Ramelli, R., Ravindra, B., & Anusha, L. S. 2014, under review
11. *Analysis of the Forward-scattering Hanle Effect in the Ca I 4227 Å Line*
Anusha, L. S., Nagendra, K. N., Bianda, M., Stenflo, J. O., Holzreuter, R., Sampoorna, M., Frisch, H., Ramelli, R., & **Smitha, H. N.** 2011, **ApJ**, 737, 95
12. *Observations of the Forward Scattering Hanle Effect in the Ca I 4227 Å Line*
Bianda, M., Ramelli, R., Anusha, L. S., Stenflo, J. O., Nagendra, K. N., Holzreuter, R., Sampoorna, M., Frisch, H., & **Smitha, H. N.** 2011, **A&A**, 530L, 13

In refereed conference proceedings

1. *The Role of Quantum Interference and Partial Redistribution in the Solar Ba II D₂ 4554 Å Line*
Smitha, H. N., Nagendra, K. N., Stenflo, J. O., & Sampoorna, M. 2014, in Solar Polarization Workshop 7, in press
2. *Forward-scattering Hanle Effect in the Solar Ca I 4227 Å Line*
Frisch, H., Anusha, L. S., Bianda, M., Holzreuter, R., Nagendra, K. N., Ramelli, R., Sampoorna, M., **Smitha, H. N.**, Stenflo, J. O. 2012, **EAS**, 55, 59

Abstract

One of the primary causes for the occurrence of observed features on the Sun is its magnetic field. The traditional way of measuring the solar magnetic fields is through the Zeeman effect. Over the decades, as the precision of the observing instruments has improved, our understanding of the solar magnetic fields has deepened. We now know that there exist fields on the Sun which remain invisible to the Zeeman effect. This apparent invisibility of the fields can be due to their lower strength, orientation, or their tangled nature. However, these fields can still be detected with the help of the Hanle effect.

In the absence of magnetic fields, the Sun's radiation is linearly polarized due to the coherent scattering processes, and the resulting spectrum is known as the "Second Solar Spectrum". It contains a wealth of richly structured atomic and molecular lines arising from a variety of atomic systems and atmospheric conditions. In the presence of weak magnetic fields, this linearly polarized spectrum gets modified by the Hanle effect. This modification is in the form of a decrease or an increase in the linear polarization (Q/I) depending on the scattering geometry. In addition to this, the Hanle effect also rotates the plane of polarization generating a U/I signal. Understanding the physics of light scattering on atoms and the measurement of weak magnetic fields requires a detailed forward modeling of the spectral line profiles. For this, adequate theoretical tools which can handle the physical processes involving complex atomic systems are needed. Of particular interest are the quantum interferences occurring between the atomic states. There are several lines in the Second Solar Spectrum which are governed by this phenomenon and their analysis demands a proper theoretical treatment of the quantum interferences. This thesis is devoted to exploring the quantum interferences between the fine structure states (J) and hyperfine structure states (F), followed by application of the theoretical derivations to the actual solar observations.

The thesis is divided into three parts. In the first part, we derive the redistribution matrix taking account of the J -state interference effects which occurs in atoms with non-zero electron spin S (Chapter 2). For the first time, we derive this matrix semi-classically starting from the Kramers-Heisenberg formula by taking full account of the effects of partial frequency redistribution (PRD) in the presence of magnetic fields,

and present the expressions both in the atomic and laboratory frames. The J -state interference acts in the wings between the lines arising from the transitions involving fine structure states. The redistribution matrix relates the Stokes vector of the incident ray and that of the scattered ray. It contains the physics of line scattering. The matrix, derived in Chapter 2, holds good only in the linear Zeeman regime of magnetic fields. In this regime, the magnetic substates (m) belonging to different J -states do not overlap. For the range field strengths found in the solar atmosphere, this theory holds good in most of the cases.

The redistribution matrix is then included in the polarized radiative transfer equation and solved for one-dimensional isothermal constant property atmospheric slabs in order to understand the nature of the redistribution phenomenon in the non-magnetic (Chapter 3) and magnetic cases (Chapter 4). We present a heuristic approach of including different types of collisions into the J -state interference theory (Chapter 4). We then apply this theory to the modeling of Stokes ($I, Q/I$) profiles of the Cr I triplet around 5206 Å observed near the solar limb (Chapter 5). The theoretical ($I, Q/I$) profiles computed from our theory match closely with the observed profiles, especially at the cross over points in Q/I which are due to the J -state interference effects. We demonstrate the importance of the PRD effects. Clearly, the profiles computed under the assumption of complete frequency redistribution (CRD) fail to reproduce the observed profiles. To obtain a good match at the far wings, we find it necessary to slightly modify the temperature structure of one of the standard one-dimensional (1-D) model atmospheres. With such a small modification, we are able to reproduce the Q/I profile not only at the line core but also in the continuum.

In the second part of the thesis, we extend the above formalism to the case of F -state interference which occurs in atoms with non-zero nuclear spin I_s . Unlike the J -state interference, the F -state interference acts only in the line core. It causes a decrease in the line core polarization. Like in the previous case, we include the redistribution matrix into the polarized transfer equation and study the nature of the emergent Stokes profiles (Chapter 6), confining our attention to the non-magnetic case. By taking example of the Ba II D₂ line profile, we test our theory by reproducing the observed ($I, Q/I$) profiles (Chapter 7). Barium is a complex atomic system with seven isotopes. Only two out of these seven are odd and exhibit F -state interference. The rest are even isotopes whose atomic levels do not undergo hyperfine structure splitting. The observed ($I, Q/I$) profiles have contributions from both the odd and the even isotopes in ratio 18:82 (as established from solar abundance studies). The two odd isotopes are treated using the F -state interference theory and the five even isotopes are treated using the simple two-level atom theory. These are then combined in their respective ratios in the scattering integral while solving the transfer equation. However to obtain a good match with the observed profiles at the line core, we find it necessary to slightly modify the temperature

structure of a standard 1-D model atmosphere. We also show that it is not possible to model this line using CRD alone.

We consider another example, namely the Sc II 4247 Å line which also is governed by the F -state interference (Chapter 8). The core of this line is composed of thirteen hyperfine transitions which are to be accounted for while modeling it. These thirteen transitions are due to the five upper and five lower F -states resulting from hyperfine structure splitting of the upper and lower $J = 2$ states. From our efforts so far, we find it difficult to reproduce the triple peak structure seen in the observed Q/I profiles, and also the rest intensity. We get a good match at the wing PRD peaks and at the near wing continuum but the central peak seems to be completely suppressed due to enhanced depolarization by the F -state interference. We suspect that the lower level Hanle effect, which is not accounted for in our treatment, might be playing a role since it can increase the line core polarization when the fields are weak. We are yet to develop the theory of lower level Hanle effect including PRD. This derivation is extremely complex, although in principle it is achievable. Therefore we feel that the Q/I spectra of the Sc II 4247 Å line has remained enigmatic to us. It would be very interesting to investigate it in the near future.

In the last part of the thesis, we combine the theories of J -state and F -state interference effects and derive a unified redistribution matrix which can handle both these effects simultaneously. In atoms with non-zero S and I_s , the atomic states undergo fine structure and hyperfine structure splitting, and exhibit both kinds of interferences. We confine our attention to the collisionless non-magnetic regime, and study the Stokes profiles formed in a 90° single scattering event (Chapter 9). Finally, the work presented in this thesis is summarized and the possibilities of extending it to measure the solar magnetic fields is discussed in the last chapter (Chapter 10).

Contents

Acknowledgements	i
List of publications	v
Abstract	ix
1 Introduction	1
1.1 The Solar magnetic fields	1
1.2 The Second Solar Spectrum and the Hanle effect	2
1.3 Measurement of Stokes parameters	4
1.3.1 Difficulties in polarimetry	5
1.3.2 The ZIMPOL camera	6
1.4 Modeling the Second Solar Spectrum	8
1.4.1 The Ca I 4227 Å line	9
1.5 Quantum mechanical interferences	10
1.5.1 Fine structure splitting and J -state interference	10
1.5.2 Hyperfine structure splitting and F -state interference	13
1.6 Modeling the quantum interference signatures	13
1.6.1 Redistribution matrices	14
1.6.2 Polarized radiative transfer equation	15
1.6.3 Numerical methods	16
1.6.4 Model atmospheres and model atoms	17
1.7 Thesis outline	18
1.7.1 Part-I	18
1.7.2 Part-II	19
1.7.3 Part-III	20

I	<i>Polarized line formation with J-state interference</i>	21
2	Collisionless redistribution in the presence of magnetic fields	23
2.1	Introduction	23
2.2	The Muller scattering matrix	26
2.3	The type-II redistribution matrix	27
2.4	The redistribution matrix in terms of irreducible spherical tensors	30
2.5	Analytical Expressions for the $L = 0 \rightarrow 1 \rightarrow 0$ transition	32
2.5.1	Normalisation	33
2.6	Results and Discussions	34
2.7	Conclusions	42
3	Radiative transfer in a two-term atom in the absence of magnetic fields	45
3.1	Introduction	46
3.2	The polarized radiative transfer equation	47
3.2.1	Stokes vectors decomposition	51
3.3	Solving the transfer equation	52
3.3.1	The iteration scheme	52
3.3.2	Source vector corrections	53
3.4	Results and discussions	54
3.4.1	Optically thin slab case	54
3.4.2	Stokes profiles with and without J -state interference	56
3.4.3	Effects of optical thickness T	57
3.4.4	Effects of the thermalization parameter ϵ	59
3.4.5	Effect of the unpolarized background continuum	60
3.4.6	Effect of separation between fine structure components	60
3.4.7	Redistribution matrix approach vs the $W_2(\lambda)$ theory of Stenflo	61
3.5	Conclusions	63
4	Collisional redistribution in the presence of magnetic fields: <i>A heuristic treatment</i>	65
4.1	Introduction	66
4.2	An approximate treatment of collisions	69
4.2.1	Polarized PRD matrix from a semi-classical approach	69
4.2.2	Coherency matrix in the atomic rest frame	71
4.2.3	Coherency matrix in the laboratory frame for type-III redistribution	72
4.3	The redistribution matrix expressed in terms of irreducible tensors	72

4.3.1	Identification and physical significance of the multipolar index K in the collisional branching ratios	74
4.3.2	Redistribution matrix \mathbf{R}^{III} in laboratory frame	78
4.4	The polarized radiative transfer equation	79
4.4.1	The redistribution matrix for the non-magnetic case	81
4.4.2	The redistribution matrix for the magnetic case	81
4.5	Results and discussion	84
4.5.1	The single 90° scattering case	84
4.5.2	Polarized line profiles formed due to multiple scattering in an atmospheric slab	87
4.6	Conclusions	89
5	Modeling the Cr I triplet at 5204-5208 Å in the Second Solar Spectrum	93
5.1	Introduction	94
5.2	Polarized line transfer equation for a two-term atom	95
5.3	Observational details	98
5.4	Modeling of Cr I triplet	99
5.4.1	Model atom and model atmosphere	99
5.5	Results and discussion	102
5.5.1	Comparison between PRD and CRD	102
5.5.2	Comparison with observations	103
5.6	Conclusions	107
II	<i>Polarized line formation with F-state interference</i>	109
6	Collisionless partial frequency redistribution in the non-magnetic regime	111
6.1	Introduction	112
6.2	Basic equations	113
6.2.1	The redistribution matrix	113
6.2.2	The polarized line transfer equation	114
6.2.3	Decomposition of the Stokes vectors into the reduced basis . . .	116
6.3	Numerical methods	116
6.3.1	Operator perturbation method	116
6.3.2	Scattering expansion method	117
6.4	Results and discussion	119
6.4.1	F -state interference effects in the case of single scattering . . .	120

6.4.2	Effects of F -state interference in multiply scattered Stokes profiles	122
6.4.3	Comparison with wavelength dependent polarizability theory of Stenflo	124
6.5	Conclusions	125
7	Modeling the Ba II D₂ 4554 Å line in the Second Solar Spectrum	127
7.1	Introduction	128
7.2	Polarized line transfer equation with F -state interference	129
7.3	Observational details	132
7.4	Modeling procedure	133
7.4.1	Model atom	134
7.4.2	Model atmosphere	134
7.5	Results	135
7.5.1	Modeling the Ba II D ₂ line profile	136
7.5.2	The importance of PRD	140
7.5.3	Modeling the CLV observations	141
7.6	Conclusions	142
8	Quantum interference effects in the Sc II 4247 Å line of the Second Solar Spectrum	145
8.1	Introduction	146
8.2	Computing the theoretical profiles	147
8.3	Observations	148
8.3.1	Determining the absolute zero level of polarization	150
8.3.2	Stray light correction	151
8.4	Comparing the theoretical and the observed Stokes profiles	151
8.4.1	The $(I, Q/I)$ profiles from different model atmospheres	152
8.4.2	Studying the sensitivity of the $(I, Q/I)$ profiles	154
8.5	Conclusions	158
 III Polarized line formation with J and F-state combined interferences		 161
9	Collisionless partial frequency redistribution in the absence of magnetic fields	163
9.1	Introduction	164
9.2	Redistribution matrix for J and F -state interferences	165

9.2.1	Redistribution matrix in terms of irreducible spherical tensors	168
9.3	Stokes profiles from a 90° single scattering event	170
9.4	Conclusions	172
10	Summary and future work	175
10.1	Summary	175
10.2	Future prospects	177
	Appendices	179
A	Rayleigh scattering phase matrix including fine-structure splitting	181
B	Expression for the type II redistribution matrix	187
C	Magnetic redistribution functions for type-III redistribution	193
	Bibliography	195

1

Introduction

1.1 The Solar magnetic fields

The story of the Sun's magnetic field began in 1908, with George Ellery Hale predicting the presence of magnetic fields in Sunspots. Quoting from [Hale \(1908a\)](#),
“Soon after the discovery of the vortices associated with sun-spots, it occurred to me that if a preponderance of positive or negative ions or corpuscles could be supposed to exist in the rapidly revolving gases, a magnetic field, analogous to that observed by Rowland in the laboratory, should be the result. An equal number of positive and negative ions, when whirled in a vortex, would produce no resultant field, since the effect of the positive charges would exactly offset that of the negative charges. But Thomson's statement regarding the possible copious emission of corpuscles by the photosphere, and the tendency of negative ions to separate themselves, by their greater velocity, from positive ions, led to the belief that the conditions necessary for the production of a magnetic field might be realized in the solar vortices.”

With this opened up a new area of research dedicated to the understanding of solar magnetic fields. Although the mechanism for the production of magnetic fields in sunspots is more clearly understood now, the intuitive picture given by [Hale \(1908a\)](#) represents the first attempt to think about magnetic fields on the Sun.

The Sun is the only star whose disk can be observed in great detail and the features appearing on it be well resolved. Some of these features include the sunspots, flares, granules, supergranules, bright points, plages, etc. One of the principal elements influ-

encing the dynamics of these features is the magnetic field. Few of the longstanding problems like the coronal heating, solar wind acceleration are also probably related to the magnetic fields. Hence it is of profound importance to study and understand their nature. The most commonly used method to measure the solar magnetic fields is by studying the Zeeman pattern of the spectral lines. [Hale \(1908b\)](#) was the first to observe these patterns in the spectra of sunspots. Since then several ground based and space based instruments like the HINODE, SOHO, SDO, etc., are dedicated to the solar magnetic field studies.

The magnetic fields on the Sun vary over a wide range of field strengths from a few tens of gauss up to a few kilogauss. Some of the larger magnetic structures known to us extend up to a few hundred megameters in size while the smaller magnetic structures are still being discovered. With the help of Zeeman effect it is possible to measure both strength and orientation of the magnetic fields. The longitudinal Zeeman effect produces circular polarization which responds to the line-of-sight component of the magnetic fields. The transverse Zeeman effect produces linear polarization and responds to the component perpendicular to the line-of-sight. Thus from the linear and circular polarization measurements, it is possible to measure the vector magnetic fields. However it is not possible to detect all the different kinds (see below) of fields by the Zeeman effect alone. [Howard & Stenflo \(1972\)](#) showed that more than 90% of the magnetic flux in the photosphere exists in the form of strong fields but occupy only a tiny fraction on the solar surface, and the average observed fields are the order of a few gauss (see also [Stenflo, 1973, 1976](#)). With this emerged a topological picture that nearly 99.8% of the solar photosphere is filled with turbulent, mixed polarity, small-scale magnetic fields whereas the rest is filled with networks of strong magnetic fields (see [Stenflo, 1982](#)). Detection of the turbulent magnetic fields is limited by the spatial resolution of the observing instrument. Fields smaller than this limit remain invisible to the Zeeman effect. A valuable alternative which can be used for the detection of turbulent fields is the Hanle effect.

1.2 The Second Solar Spectrum and the Hanle effect

Radiation gets polarized when the spatial symmetry is broken in the physical process generating it. In the Sun, such a symmetry breaking can be caused by the magnetic fields or by scattering. The scattering polarization is maximum at the limb and zero at the disk center (due to symmetry reasons). The solar spectrum including the lines and the continuum is polarized by coherent scattering processes in the solar atmosphere (for details on the continuum polarization see [Section 1.4](#)). When an atom is illuminated anisotropically, and if there exists a phase relation between the absorption and emission process, then the scattered light is polarized. This is known as coherent scattering. It

becomes incoherent when the scattering atom suffers a collision and the phase relation is wiped out. In this case, no polarization is generated. Understanding the processes by which the line polarization is generated allows us to diagnose the physical conditions in the magnetic elements on the Sun.

The linearly polarized spectrum of the Sun produced due to coherent scattering processes appears completely different from the ordinary intensity spectrum and carries a wealth of information about the physics of line scattering (Stenflo & Keller, 1996, 1997). This spectrum was named as the ‘‘Second Solar Spectrum’’ by Ivanov (1991).

In the presence of a weak magnetic field, the degree of linear polarization is reduced and the plane of polarization is rotated. This is due to the Hanle effect. It is named after Wilhelm Hanle who provided a correct explanation to this effect in 1924. This effect was first observed in the laboratory by R. W. Wood in 1912 and later by Lord Rayleigh in 1919 who measured different polarizations in the 253.7 nm line of mercury from different experiments. Wood & Ellett (1923a,b) realized that the degree of polarization depends on the orientation of the experimental setup with respect to the earth’s magnetic field. Hanle (1924) gave the first explanation to these observations using both the classical, and quantum theory. Classically, this effect can be explained in terms of the rosette motion of an electron in the presence of a magnetic field (for details see Moruzzi & Strumia, 1991). Quantum mechanically, this effect can be understood using a simple atomic picture shown in Figure 1.1. The magnetic field removes the degeneracy be-

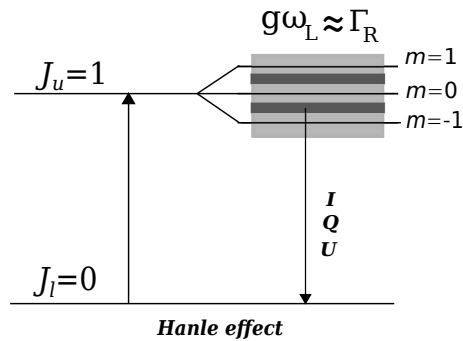


Figure 1.1: Atomic level diagram illustrating the partial removal of degeneracy of the magnetic substates by a weak magnetic field, giving rise to the Hanle effect. In the figure, g , ω_L , and Γ_R are the Landé g -factor, Larmor frequency and radiative width respectively. J and m are the total angular momentum quantum number and magnetic quantum number respectively.

tween the magnetic substates of a given atomic state. The corresponding polarization of the radiation scattered off from such an atom depends on the extent of departure from degeneracy. In other words, the Hanle depolarization depends on the ratio between the Zeeman splitting and the damping width of the atomic states. If these two quantities are comparable to each other, in magnitude, then the splitting sensitivity is maximum and we are in the Hanle regime. The range of field strengths at which this occurs depends on

the atomic system under consideration. When the Zeeman splitting is much larger than the damping width, then we are in the Hanle saturated regime (Stenflo, 1994; Trujillo Bueno, 2001; Samporna et al., 2007a).

The Hanle effect complements the Zeeman effect by serving as a diagnostic tool to detect magnetic fields invisible to the Zeeman effect. When the fields are tangled with random orientation of field vectors, the net depolarization due to Hanle effect is still seen, whereas the polarization due to the Zeeman effect cancels out. However, the Hanle effect is sensitive only when the magnetic field has a horizontal component. This limitation can be overcome with the Zeeman effect which can measure vertical fields. The diagnostic potential of the Hanle effect to measure weak magnetic fields in the Sun has been explored in several works such as Leroy (1985); Moruzzi & Strumia (1991); Faurobert-Scholl et al. (1995); Faurobert-Scholl (1996); Trujillo Bueno (1999); Faurobert (2000); Trujillo Bueno (2001); Stenflo (2002); Faurobert (2003, 2012).

To exploit the magnetic field diagnostic potential of the Hanle effect, we need highly sensitive spectropolarimeters which can measure them. The scattering polarization is dependent on the angular anisotropy, which is due to the Sun's limb darkening. This anisotropy is quite small at visible wavelengths (Stenflo, 2005). Hence the scattering polarization is also small. In the presence of a magnetic field, it is further reduced by the Hanle effect. The spectropolarimeters thus needed should have the sensitivity to measure these small polarization signals. The ZIMPOL is one such instrument, working of which will be discussed briefly in the section below.

1.3 Measurement of Stokes parameters

The polarization properties of light are measured in terms four Stokes parameters

$$\mathbf{S} = \begin{pmatrix} I \\ Q \\ U \\ V \end{pmatrix}, \quad (1.1)$$

which were first introduced by Sir. George Stokes in 1852 and later brought to extensive usage by Chandrasekhar (1950). Here, I, Q, U and V are a measure of the intensity, linear polarization, inclination of the plane of polarization and circular polarization respectively. They can be graphically represented as shown in Figure 1.2. The main advantage of this description is its ability to define partially polarized light. To know the polarization information about a photon, we need to measure its four Stokes parameters. However there are several difficulties involved in measuring them.

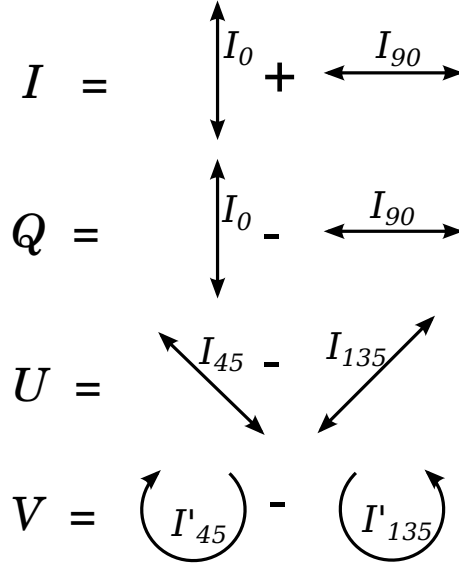


Figure 1.2: Pictorial representation of the Stokes parameters. I_0 , I_{90} , I_{45} and I_{135} are the intensity components measured at 0° , 90° , 45° , and 135° respectively with respect to the observer facing the radiation source. I'_{45} and I'_{135} are the components measured at 45° and 135° with a retarder (quarter-wave plate) in between the observer and source.

1.3.1 Difficulties in polarimetry

In polarimetry the desired task is to image the full Stokes vector, i.e., to record four simultaneous images of the four Stokes parameters, I , Q , U and V . This is a challenging task, because we need to image a four component vector from a scalar (the intensity). In addition to this, most of the interesting polarization signatures have very small amplitudes which are difficult to measure. The main challenge is to eliminate as far as possible the various sources of noise that generate spurious polarization, while working with large detector arrays.

A polarization image, e.g. Stokes Q/I , is formed from the difference between two images that represent orthogonal polarization states as shown in Figure 1.2. If I_0 and I_{90} are the two orthogonal components then the degree of linear polarization is

$$Q/I = \frac{I_0 - I_{90}}{I_0 + I_{90}}. \quad (1.2)$$

The incident intensity beam can be split into two orthogonal components using a beam splitter. If these two images are recorded simultaneously, then the seeing noise, arising due to the air turbulence, will in principle subtract out. However the noise due to the different pixel sensitivities which is known as the gain-table noise will remain. To eliminate gain-table noise one needs to use the same detector area for the orthogonally polarized images. This can be done by modulating the polarization state. By modulation, the images are temporally (instead of spatially) separated and they will contain different seeing noise. To eliminate the seeing noise, the temporal separation between

the two images must be less than the intensity fluctuation arising due to seeing, i.e. less than a few milliseconds. Therefore the modulation has to be in the kHz range. The problem with this is that large CCD arrays have a slow read out, far slower than what would be needed to beat the seeing frequency. This problem is solved in the ZIMPOL.

1.3.2 The ZIMPOL camera

The Zurich Imaging Polarimeter (ZIMPOL) is a highly sensitive imaging polarimeter with a sensitivity of 10^{-5} , developed by the Institute of Astronomy at ETH, Zurich. Over the past two decades, the instrument has been developed from its first version ZIMPOL-I to the current version ZIMPOL-III to achieve higher accuracies. A detailed description of the working of this instrument can be found in [Povel \(1995\)](#), see also [Stenflo 1984, 1985](#); [Stenflo & Povel 1985](#); [Povel et al. 1990](#)).

The problem of fast modulation and slow readout has been solved in the ZIMPOL camera where masked CCD is used as a synchronous demodulator. This technique was first realised in ZIMPOL-I ([Povel et al., 1990](#)). Here, every second row of the CCD was covered with an opaque mask (see first panel of [Figure 1.3](#)). The masked area served as temporary storage rows which allowed to separate the photons generated in two different phases of the modulation. The charges were shifted back and forth along the column, in sync with the modulation. The complete CCD was read out after integration over several modulation cycles. The demodulation was done by calculating the difference between the two corresponding rows. Thus synchronous demodulation of the fast intensity modulations was made possible with the CCDs. However this allows measurement of one Stokes parameter at a time ([Stenflo, 2007](#)). With ZIMPOL-II all the four Stokes parameters can be measured simultaneously ([Povel, 1995, 2001](#)). For this, four image planes are created within the CCD with one exposed and three masked rows (second panel of [Figure 1.3](#)). The photo charges are cycled between the four image planes at a rate of kHz which helps in synchronous demodulation of the modulated beam. This is repeated for many thousand modulation cycles till CCD has been filled and then it is read out. The readout then contains the four simultaneous images that represent different polarization states. Through simple linear combinations of these four images, the images of the four Stokes parameters are obtained. The gain table noise entirely divides out while obtaining the fractional polarizations $Q/I, U/I$ and V/I ([Stenflo, 2007](#)).

However, with the above method of masking three out of four pixel rows, 75% of the light falling on the CCD is wasted. To overcome this, in ZIMPOL-III, the CCD surface is covered with cylindrical microlenses which focuses the light falling on the 3 masked pixel rows onto the unmasked pixel row. In this way, the efficiency increases by a factor of 4 ([Ramelli et al., 2010](#)).

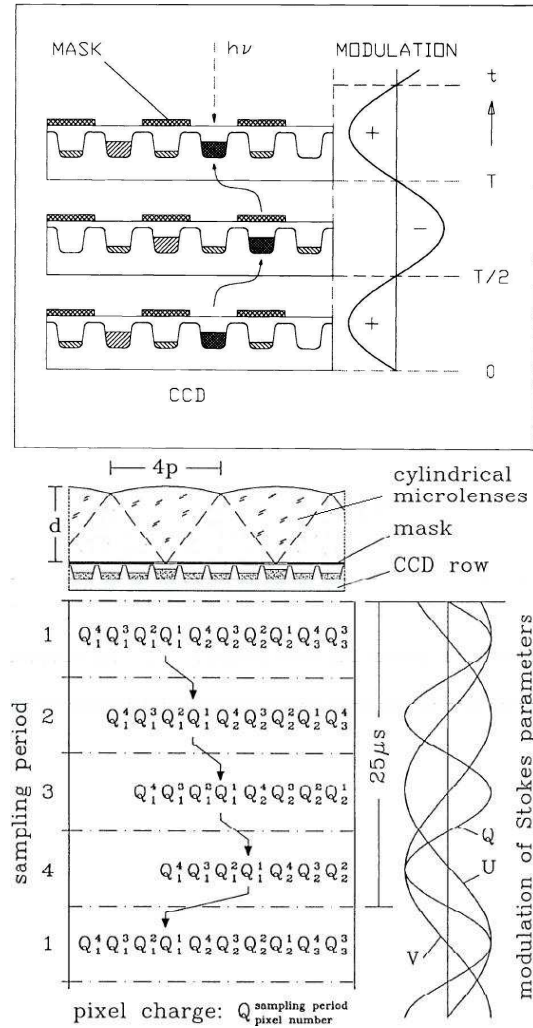


Figure 1.3: Principle of CCD demodulator. *First panel:* The cross-section of CCD with every alternate pixel rows being masked. This is used in ZIMPOL-I (taken from Povel, 1995). *Second panel:* The cross-section of CCD with three out of four rows masked which is used in ZIMPOL-II. In ZIMPOL-III, the CCD surface is covered with microlenses (taken from Stenflo, 2007).

Thus, using such an advanced and a highly sensitive spectropolarimeter, it is possible to measure even the smallest polarization signals and record their spectrum (linear and circular). An example of the observations of the CN molecular lines taken with the ZIMPOL at NSO/Kitt Peak in March 2005 is shown in Figure 1.4. The image on the left is observed in a quiet region and hence does not show much variation in Q/I along the slit, and no U/I signal. The image on the right is observed near a sunspot. The Q/I shows variations along the slit. Prominent Zeeman signatures are seen in $Q/I, U/I$ and V/I between $30'' - 50''$. In order to use such a spectrum to understand the physics of line scattering; the nature of solar magnetic fields; the solar atmosphere; etc., we need to develop powerful tools to analyze it. The two well known methods are the inversion technique and the forward modeling. In this thesis, we develop some tools which are

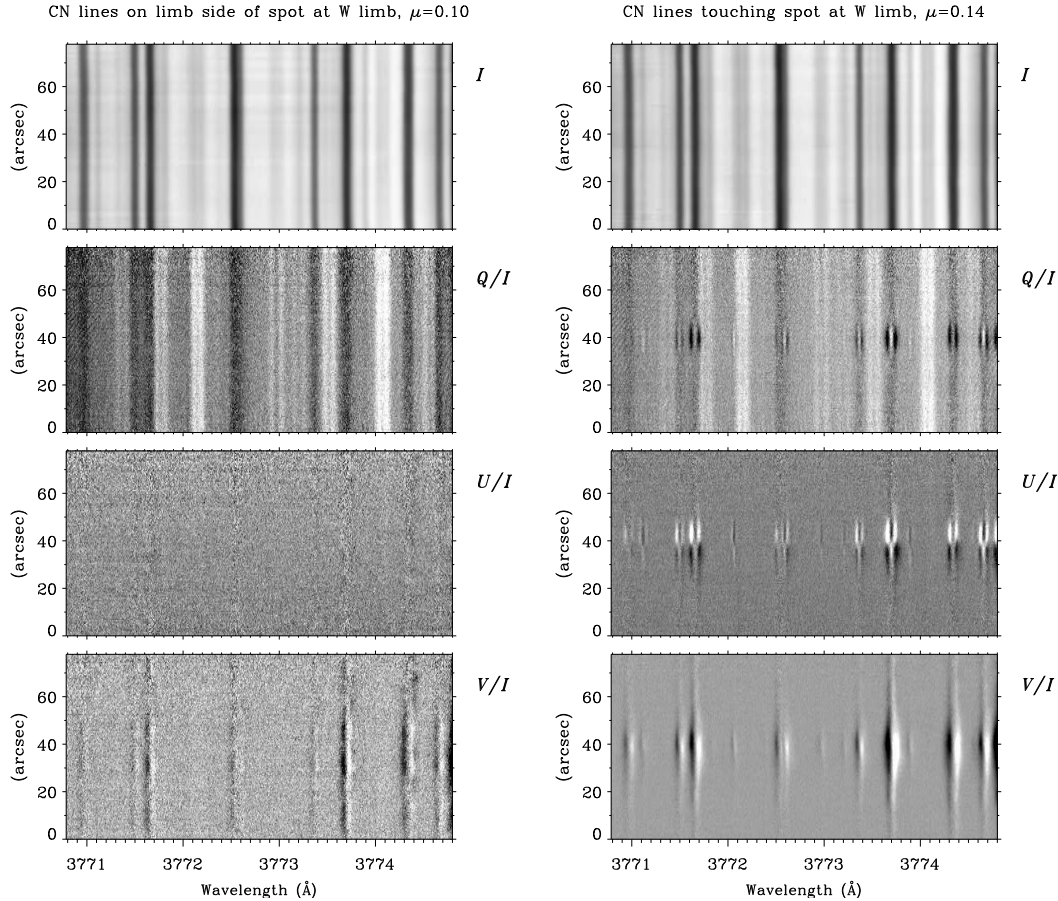


Figure 1.4: CCD image of the Stokes spectra around 3773 Å region which is mostly dominated by the CN molecular lines. The observation on the left is taken in a quiet region and that on the right near a sunspot (taken from [Stenflo 2009b](#)).

used in forward modeling of the observed Stokes profiles in the Second Solar Spectrum.

1.4 Modeling the Second Solar Spectrum

The Second Solar Spectrum contains several molecular and atomic lines, linearly polarized by coherent scattering processes. An atlas of this spectrum observed at $\mu = 0.1$ in a quiet region covering a range of wavelengths from the UV to the visible has been developed by [Gandorfer \(2000, 2002, 2005\)](#). Some of the lines like the Ca I 4227 Å, Sr I 4607 Å, Na I D₁ (5896 Å) & D₂ (5890 Å), Ba II D₁ (4934 Å) & D₂ (4554 Å), Ca II H (3965 Å) & K (3933 Å), etc., have been well known for their prominent polarization signals and form good candidates for modeling. Forward modeling of these line profiles involves the computation of the theoretical profiles accounting for the necessary atomic physics and atmospheric effects, and comparing them with the observations. A mismatch between the two indicates possible deficiencies in the atomic physics and/or the atmospheric models used. These deficiencies are identified and corrected for till we

get a close match with the observed profiles. With each such iteration, we get closer to an actual representation of the physical processes giving rise to the observed solar spectra.

Modeling the observed spectrum involves reproducing both the line as well as the continuum profiles. In the Second Solar Spectrum, the continuum is also polarized due to coherent scattering processes. The dominant contribution to this comes from scattering in the far wings of the Lyman series of hydrogen. Though the Lyman lines fall in the UV region of the spectrum, their far wings extend to the visible wavelengths. Due to the high abundance of hydrogen in the Sun, the scattering probability is sufficiently large even in the far wings, making it the primary source of continuum polarization. The other source of continuum polarization is the Thomson scattering on free electrons. Both polarizing and non-polarizing spectral lines are superposed on this polarized continuum background. The polarizing lines appear as emission lines and the non-polarizing lines appear as absorption lines. More details on this can be found in [Stenflo \(2005, 2009a\)](#).

Each spectral line observed in the Second Solar Spectrum is unique in its own ways. They arise from atoms with varying complexities; they are formed at different heights in the atmosphere; they have varying sensitivity to magnetic fields, collisions, temperature variations, etc. Here we broadly classify these lines into two categories. In the first category are the lines which can be modeled using a simple two level atom picture like the Ca I 4227 Å, Sr I 4607 Å, etc. In the second category are the lines which arise from fine structure splitting and hyperfine structure splitting like the Na I D₁ & D₂, Ba II D₁ & D₂, Ca II H & K, etc., that are relatively difficult to model.

The present thesis is dedicated to the development of the theory, and modeling of lines in the second category. Before discussing the details of these complex systems, in the section below we briefly describe some of the works dedicated to the modeling of spectral lines in the first category, by taking the example of the Ca I 4227 Å line.

1.4.1 The Ca I 4227 Å line

Among the atomic lines in the visible wavelengths, the Ca I 4227 Å line has the largest degree of linear polarization which makes it one of the most observed and studied lines. It arises due to the $J = 0 \rightarrow 1 \rightarrow 0$ scattering transition, where J is the total angular momentum quantum number (see Figure 1.5). This atomic system known as the normal Zeeman triplet is the only system which can be fully described in terms of time-dependent classical oscillator theory. One of the earliest observations of this line was by [Brückner \(1963\)](#), later followed by [Stenflo \(1974\)](#); [Wiehr \(1975\)](#). One of the earliest attempts to understand the resonance polarization of this line was by [Dumont et al. \(1973\)](#). Since then this line has attracted the attention of several, who have extensively used it to observe and study, for example, the physics of line scattering on a two-level

atom; to determine the depth dependence of turbulent magnetic fields; to measure vector magnetic fields on the solar surface; to constrain realistic 1D model atmospheres by modeling its center-to-limb variation (CLV), etc. To name a few: [Stenflo \(1974\)](#); [Auer et al. \(1980\)](#); [Stenflo \(1982\)](#); [Faurobert-Scholl \(1992, 1994\)](#); [Bianda et al. \(1998, 2003\)](#); [Holzreuter et al. \(2005\)](#); [Sampoorna et al. \(2009\)](#); [Anusha et al. \(2010\)](#); [Bianda et al. \(2011\)](#); [Anusha et al. \(2011b\)](#); [Supriya et al. \(2014\)](#).

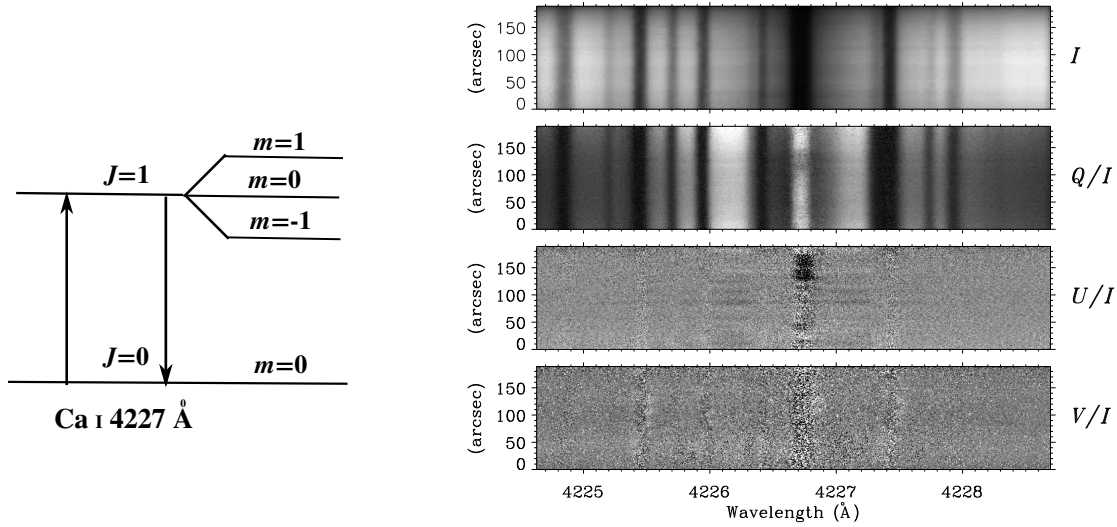


Figure 1.5: *Left Side*: Level diagram representing the atomic system of the Ca I 4227 Å line. In the presence of a magnetic field, the J -states are split into magnetic substates (m). *Right Side*: CCD image of Ca I 4227 Å line observed at IRSOL using ZIMPOL-II by [Anusha et al. \(2010\)](#).

In the next section, we describe the properties of the lines belonging to the second category, namely those governed by the quantum interference phenomenon - which are studied in detail in this thesis.

1.5 Quantum mechanical interferences

There are several lines in the Second Solar Spectrum which cannot be understood in terms of the simple two level atom model described above. This is because, they arise from atoms with more complex atomic structures. The fine structure splitting and hyperfine structure splitting are two such complexities. Radiation scattered on such atoms carry imprints of the fine structure and/or hyperfine structure splitting in their spectrum.

1.5.1 Fine structure splitting and J -state interference

When an atom has a non-zero electron spin S , the atomic states with orbital angular momentum quantum number L undergoes coupling with S and splits into J -states. Such an atom is known as a “two-term atom” where transitions involve an upper and a

lower term¹ (see left panel in Figure 1.6). Such an atomic system gives rise to a set of spectral lines known as multiplets, rather than a single line. These spectral lines show up in the spectrum, and was first observed by [Michelson & Morley \(1887\)](#) in the H α line. However an explanation to this splitting was given much later by [Sommerfeld \(1915, 1916a,b\)](#)

Some of the well known examples in the solar spectrum which arise due to fine structure splitting are the Na I D₁ & D₂, Ca II H & K, Ba II D₁ & D₂, Mg II h & k, Cr I triplet around 5206 Å, Ly α lines of H I and He II, O I triplet around 7773 Å, Mg I b-lines, etc. When the Ca II H & K lines were first observed with a high resolution spectropolarimeter by [Stenflo et al. \(1980, see also Stenflo 1980\)](#), the authors noticed a very interesting polarization feature in Q/I in the form of a “double S” extending over more than 100 Å around the H & K lines. These observations are shown in Figure 1.6 (right panel). It was demonstrated by [Stenflo \(1980\)](#) that this feature can be explained only in terms of the quantum mechanical interferences between the upper J -states. The H & K lines are separated by 35 Å and yet they cannot be treated as two independent lines but need to be treated as one single unit. The interference between the J -states is known as the “ J -state interference”. In optics, interference is a well known phenomenon and

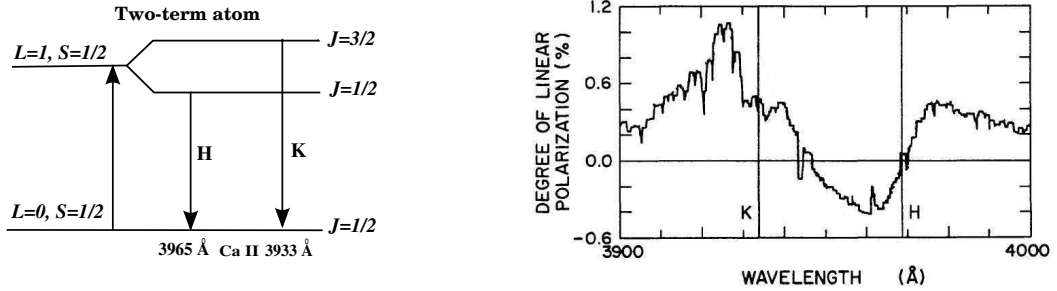


Figure 1.6: *Left Side*: Level diagram representing the atomic system of the Ca II H & K line system. *Right Side*: Linear polarization profiles of Ca II H & K observed by [Stenflo \(1980\)](#).

optical fields obey the principle of superposition. The amplitude of field A at any given point is the sum of the amplitudes A_i from other sources at that point. Assuming that the fields are coherent, the resulting amplitude of the field is

$$W = A^2 = \left| \sum_i A_i \right|^2 = \sum_i |A_i|^2 + \sum_{i \neq k} A_i A_k^* \neq \sum_i |A_i|^2, \quad (1.3)$$

where $\sum_{i \neq k} A_i A_k^*$ represents the interference term. The principle of superposition is also valid in quantum mechanics which results in interference of atomic states and has been studied since the 1950's and 1960's ([Podgoretskii & Khrustalev, 1964](#); [Penny, 1969](#)). We now know that the Hanle effect, which was known since the 1920's ([Hanle,](#)

¹A term is a group of J -states with same L and S quantum numbers

1924), is also an interference effect. It arises due to the quantum mechanical interferences between the magnetic substates m and is known as the m -state interference.

These interferences can also be understood as being analogous to the photons passing through the double-slit. For the creation of the interference pattern, it is important that the photons pass through both the slits at the same time. Similarly, the observed “double S ” in the Q/I profiles of the Ca II H & K lines is due to the photons getting scattered from both the upper $J = 1/2$ and $J = 3/2$ states at the same time. The resulting scattering amplitude is a linear superposition of the scattering amplitudes of the H & K transitions. When the scattering amplitude is squared to compute the scattering probability, we get cross terms between the H and K scattering amplitudes. These cross terms represent the interferences, and can take negative values. This gives rise to the crossover seen in between the H & K lines in Figure 1.6. The crossover in the Q/I spectrum between the two fine structure components is the most prominent signature of J -state interference. Figure 1.7 shows the $(I, Q/I)$ profiles of the Na I D₁ & D₂ where the cross over is clearly visible in the Q/I spectrum whereas the intensity spectrum shows only the fine structure components D₁ & D₂ and no interference signatures. An interesting explanation to the quantum interferences in terms of the Schrödinger cat states is given in Stenflo (2009b).

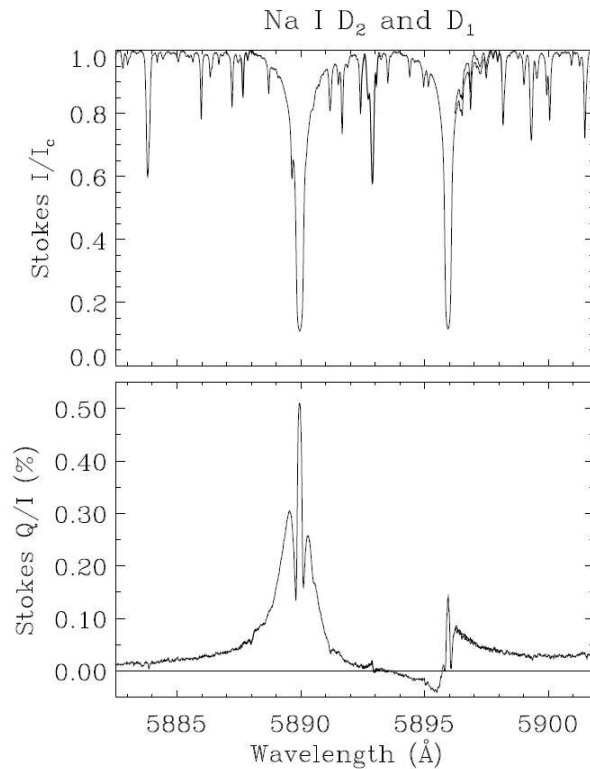


Figure 1.7: Stokes $(I, Q/I)$ profiles of the Na I D₁ & D₂ observed by Stenflo & Keller (1997).

1.5.2 Hyperfine structure splitting and F -state interference

The F -state interference arises between the hyperfine structure states which are due to the coupling between the J -states and the nuclear spin (I_s) of the atom. The hyperfine structure splitting was first observed by Michelson in 1881 in Sodium which was later published in [Michelson \(1891\)](#). He could not explain the observed splitting of the Na line into large number of components and noted the radiation to be ‘defective’. Later, this splitting was first explained by [Pauli \(1924\)](#) in terms of the small magnetic moment associated with the spinning nucleus. The Na I D₂, Ba II D₂, Sc II 4247 Å are some of the well known lines governed by this phenomenon. The F -state interference acts only in the core of the line unlike the J -state interference which acts in the wings of the lines. It causes a depolarization, i.e., reduces the polarization, in the line core. In the intensity it leads to a broadening of the line profile.

Modeling lines governed by interferences provides a check on our current understanding of the atomic physics and quantum mechanical scattering theory in such atomic systems. In the section below, we describe the various stages involved in modeling the ($I, Q/I$) profiles observed in the Second Solar Spectrum.

1.6 Modeling the quantum interference signatures

Studying the quantum interference signatures in the spectral line profiles observed in the Second Solar Spectrum has been taken up in several earlier works using different formalisms.

In [Stenflo \(1980, 1994\)](#); [Stenflo & Keller \(1997\)](#); [Stenflo \(1997\)](#), the authors compute the atomic polarizability factor $W_2(\lambda)$ which contains the physics of quantum interference, and computes the Stokes profiles using a parametrized atmospheric model, bypassing the detailed radiative transfer. The computed profiles are then compared with the observed profiles.

Using the density matrix formalism developed in [Landi Degl’Innocenti & Landolfi \(2004\)](#), analysis of the spectral lines governed by quantum interferences has been carried out recently by [Belluzzi et al. \(2007, 2009\)](#); [Belluzzi \(2009\)](#); [Belluzzi & Trujillo Bueno \(2011, 2012\)](#).

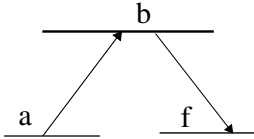
In most of the papers mentioned above, the effects of radiative transfer and partial frequency redistribution (PRD) are neglected. In this thesis, we study the spectral lines by accounting for quantum interferences with PRD and radiative transfer. The steps involved in such a study includes the computation of the scattering matrix, incorporating it into the polarized radiative transfer equation, and solving the transfer equation using appropriate numerical methods. While doing so, a suitable model atmosphere representative of the solar atmosphere and a model atom representing the atomic system are

given as inputs.

1.6.1 Redistribution matrices

The redistribution matrix, also known as the scattering matrix, contains the physics of line scattering and transforms the incident Stokes vector to the scattered Stokes vector. There are different ways of deriving this matrix. One is the classical approach and the other is the QED approach. A simple system like the normal Zeeman triplet with $J = 0 \rightarrow 1 \rightarrow 0$ scattering transition can be described completely in terms of the classical theory. For other complex systems we need the QED approach. A historical account on the development of the theory of light scattering on atoms is presented in [Sampoorna \(2008\)](#), see also Section 2.1).

For the atomic systems considered in this thesis, we use the semi-classical approach of [Stenflo \(1994, 1998\)](#). In this approach we start from the Kramers-Heisenberg dispersion formula to compute the scattering amplitude



$$[w_{\alpha\beta}]_b \sim \sum_b \frac{\langle f | \mathbf{r} \cdot \mathbf{e}_\alpha | b \rangle \langle b | \mathbf{r} \cdot \mathbf{e}_\beta | a \rangle}{\omega_{bf} - \omega - i\gamma/2}, \quad (1.4)$$

where the scattering is from $a \rightarrow b \rightarrow f$. This formula was developed by [Kramers & Heisenberg \(1925\)](#) based on the correspondence principle. The quantum mechanical derivation of this was later given by [Dirac \(1927a,b\)](#).

The $w_{\alpha\beta}$ in Equation (1.4) forms elements of the w matrix called the Jones scattering matrix ([Stenflo, 1994](#)). To compute the scattering probability which is the square of scattering amplitude, we determine the bilinear product $w_{\alpha\beta} w_{\alpha\beta}^*$ which gives us the \mathbf{W} matrix. This can be converted to the Mueller matrix \mathbf{M} by applying suitable transformations (see Equation (7) of [Stenflo, 1998](#)). The Mueller matrix is analogous to the redistribution matrix.

The redistribution matrix so derived is then written in terms of the irreducible spherical tensors for polarimetry $\mathcal{T}_Q^K(i, \mathbf{n})$ introduced by [Landi Degl'Innocenti \(1984\)](#). The index i takes values 0,1,2 and 3 representing four Stokes parameters I, Q, U and V respectively. \mathbf{n} represents the direction of the scattered radiation. The index K takes values $K = 0, 1$ and 2 with $-K \leq Q \leq +K$. Expressing the redistribution matrix in terms of $\mathcal{T}_Q^K(i, \mathbf{n})$ helps in factorizing the terms dependent on the incoming and outgoing ray directions, \mathbf{n}' and \mathbf{n} respectively. A detailed procedure to carry out this factorization is given in [Sampoorna et al. \(2007b\)](#). The significance of the irreducible spherical tensors $\mathcal{T}_Q^K(i, \mathbf{n})$ and the advantages of introducing them in the scattering matrix is given in Section 4.3.1.

In the derivation of the redistribution matrix, we take account of the effects of PRD. This accounts for a proper description of the correlations between the incident and

scattered radiation. The redistribution matrix is a 4×4 matrix $\mathbf{R}(\lambda', \mathbf{n}', \lambda, \mathbf{n})$, and carries a dependency over \mathbf{B} if there is a magnetic field. It relates the wavelength and direction (λ', \mathbf{n}') of the incident radiation to that of the scattered radiation (λ, \mathbf{n}) . Other than PRD, the redistribution matrix can also be derived under the assumption of complete frequency redistribution or frequency coherent scattering. In the former, the correlation between the incident and scattered radiation is assumed to be completely destroyed by collisions. In the latter, the incident and scattered radiation are assumed to have the same frequency and differ only in the direction. Both these assumptions are far from reality, except in certain special conditions. It is the PRD theory that represents an actual scattering event, the closest. The importance of accounting for PRD effects in realistic modeling of the spectral lines has been highlighted in several works (see for e.g., Rees & Saliba, 1982; Faurobert-Scholl, 1992, 1994; Samporna et al., 2009; Faurobert et al., 2009; Anusha et al., 2010; Smitha et al., 2012a, 2013b).

The redistribution matrix contains the necessary atomic physics. However the observed line profiles are significantly modified by the atmospheric effects which are broadly referred to as the radiative transfer effects. To account for this, we have to incorporate the redistribution matrix into the polarized radiative transfer equation and solve it using suitable numerical methods.

1.6.2 Polarized radiative transfer equation

The radiative transfer equation is a mathematical expression for the conservation of radiant energy along a ray. This is written for the polarized case as

$$\mu \frac{\partial \mathbf{I}(\lambda, \mathbf{n}, z)}{\partial z} = -k_{\text{tot}}(\lambda, z) [\mathbf{I}(\lambda, \mathbf{n}, z) - \mathbf{S}(\lambda, \mathbf{n}, z)], \quad (1.5)$$

where $\mathbf{I} = (I, Q, U, V)$ is the Stokes vector, k_{tot} is the total opacity and \mathbf{S} is the total source vector. $\mu = \cos \theta$ with θ being the heliocentric angle with respect to the line of sight and \mathbf{n} defines the ray direction and z is the geometric height in the atmosphere. The total source vector is given by

$$\mathbf{S}(\lambda, \mathbf{n}, z) = \frac{k_l(z)\phi(\lambda, z)\mathbf{S}_l(\lambda, \mathbf{n}, z) + \sigma_c(\lambda, z)\mathbf{S}_c(\lambda, \mathbf{n}, z) + k_c(\lambda, z)\mathbf{S}_{\text{th}}(\lambda, z)}{k_{\text{tot}}(\lambda, z)}. \quad (1.6)$$

Here \mathbf{S}_{th} is the thermal source vector which is same as the Planck function, \mathbf{S}_c is the continuum source vector, and \mathbf{S}_l is the line source vector. k_l, k_c are the line and continuum opacities respectively. σ_c is the continuum scattering coefficient. The line source vector can be written as

$$\mathbf{S}_l(\lambda, \mathbf{n}, z) = \epsilon \mathbf{S}_{\text{th}}(\lambda, z) + \int_0^{+\infty} \oint \frac{\mathbf{R}(\lambda, \mathbf{n}, \lambda', \mathbf{n}', z, \mathbf{B})}{\phi(\lambda, z)} \mathbf{I}(\lambda', \mathbf{n}', z) \frac{d\mathbf{n}' d\lambda'}{4\pi}, \quad (1.7)$$

where $\mathbf{R}(\lambda, \mathbf{n}, \lambda', \mathbf{n}', z, \mathbf{B})$ is the redistribution matrix described in Section 1.6.1.

The source vector \mathbf{S} and the Stokes vector \mathbf{I} depend on $\mathbf{n} = (\theta, \phi)$, with θ, ϕ being the colatitude and azimuth of the scattered radiation respectively. Frisch (2007) showed that it is possible to decompose \mathbf{I} and \mathbf{S} into six cylindrically symmetric components \mathcal{I}_Q^K and \mathcal{S}_Q^K using the irreducible spherical tensors \mathcal{T}_Q^K . The resulting Stokes vector \mathcal{I} is independent of ϕ and the source vector \mathcal{S} is independent of \mathbf{n} , and these vectors are said to be in the reduced basis. Computationally it is advantageous to work in such a reduced basis. Transformation of the Stokes vectors to such a reduced basis is referred to as the decomposition of the Stokes vectors.

1.6.3 Numerical methods

Fast and efficient numerical methods for solving the radiative transfer equation have been developed over the past few decades. One of the most commonly used methods is the Approximate Lambda iteration (ALI) method which is based on the concept of operator perturbation. This was first developed by Olson et al. (1986). The ALI method can be used to solve only the scalar radiative transfer equation. In order to solve the polarized transfer equation discussed in Section 1.6.2, the ALI method was extended to the polarized case. This is known as the polarized ALI or the PALI method. The PALI method was first developed for the CRD case in the absence of a magnetic field by Faurobert-Scholl et al. (1997). This was extended to the case of PRD by Paletou & Faurobert-Scholl (1997). The PALI method to handle the Hanle effect but for the case of CRD was developed by Nagendra et al. (1998) and later extended for PRD by Nagendra et al. (1999); Fluri et al. (2003b). For a detailed review on the PALI methods see Nagendra (2003a); Nagendra et al. (2003); Trujillo Bueno (2003); Nagendra & Sampoorana (2009); Nagendra et al. (2009). The PALI method to solve the polarized radiative transfer equation which has been decomposed using the irreducible spherical tensors for polarimetry (as described in Frisch, 2007) is developed in Sampoorana et al. (2008a).

An important simplification done while solving the transfer equation is replacing the angle dependent redistribution matrix with its angle averaged version. Though such a simplification is consistent while solving only for the intensity, it is rather not completely justified when computing the Stokes vector, particularly in the presence of a moving media. The differences in the emergent Stokes profiles for the angle averaged and angle dependent cases for different physical problems are studied in Faurobert (1987, 1988) and Nagendra et al. (2002). In a series of papers Frisch (2010); Sampoorana et al. (2011); Sampoorana (2011b); Nagendra & Sampoorana (2011); Supriya et al. (2013a), the authors have devised numerical methods which can take account of the angle dependence in the PRD matrix for physical processes of increasing complex-

ity and overcome the approximation of angle averaged PRD . However in [Supriya et al. \(2013b\)](#), the authors demonstrated that the angle averaged versions are accurate enough for all practical purposes.

In most of the papers mentioned above, the radiative transfer equation is solved for the case of an isothermal constant property atmospheric slabs. However, while modeling the actual spectral line profiles observed in the Sun, it is important to consider realistic atmospheric models which can mimic the solar atmosphere as closely as possible. In addition to this, an atom model which represents the atomic system under study also needs to be given as an input. In the section below we briefly describe the model atom and the model atmospheres.

1.6.4 Model atmospheres and model atoms

A model atmosphere is a realistic empirical model which represents the solar atmosphere. One dimensional (1-D) model basically contains information on the depth dependence of various atmospheric quantities like the temperature, mass column, turbulent velocity, electron and hydrogen densities, etc. A three dimensional (3-D) model contains the variations of these quantities along three dimensions. In all the results presented in this thesis we use 1-D models. To use two-dimensional (2-D) or 3-D models we need the theory of polarized radiative transfer in multi-dimensional geometries and suitable numerical methods to solve them. Such works have been carried out, for example, by [Auer et al. \(1994\)](#); [Fabiani Bendicho et al. \(1997\)](#); [Manso Sainz & Trujillo-Bueno \(1999\)](#); [Shchukina & Trujillo Bueno \(2009\)](#); [Trujillo Bueno & Shchukina \(2009\)](#). Recently more powerful and elegant methods have been developed by [Anusha & Nagendra \(2011a\)](#); [Anusha et al. \(2011a\)](#); [Anusha & Nagendra \(2011b,c, 2012\)](#), see also [Štěpán & Trujillo Bueno 2013](#)).

There are several 1D models which have been built over the last few decades, to name a few – [Kurucz \(1969, 1973\)](#); [Vernazza et al. \(1973, 1976\)](#); [Kurucz \(1979\)](#); [Vernazza et al. \(1981\)](#); [Machado et al. \(1980\)](#); [Avrett et al. \(1984\)](#); [Maltby et al. \(1986\)](#); [Fontenla et al. \(1990, 1991, 1993\)](#); [Avrett \(1995\)](#); [Gu et al. \(1997\)](#); [Fontenla et al. \(2002, 2006, 2007\)](#); [Avrett & Loeser \(2008\)](#); [Fontenla et al. \(2009\)](#). The 1-D realistic models used in this thesis are taken from [Fontenla et al. \(1993\)](#) and [Avrett \(1995\)](#).

A fine comparison between the various 1-D and 3-D model atmospheres and a detailed study on how closely they represent the real solar atmosphere has been presented in [Pereira et al. \(2013\)](#). They find the 3-D models to be best suited. Thus, in general, it is difficult to model the observed Stokes profiles using 1-D model atmospheres. In Chapters 5 and 7, we find it necessary to slightly modify the existing 1-D standard model atmosphere to obtain Stokes profiles that match closely with the observed ones. Recently [Supriya et al. \(2014\)](#) have also tried to model the CLV observations of the

Ca I 4227 Å line profiles and find that it is not possible to simultaneously reproduce the intensity and polarization profiles at all limb distances, using 1-D model atmospheres. Though the authors construct combined model by placing one atmosphere above the other, they find it difficult to model the CLV. Thus going beyond the 1-D models has now becoming inevitable if we need a better understanding of the processes occurring in the Sun.

In addition to the model atmosphere, a model atom is also needed for the computation of the Stokes profiles. This model atom contains the information on the atomic levels of our interest and the ones coupled to them radiatively and/or collisionally. The model includes realistic inputs on bound-bound and bound-free transitions arising from these atomic levels and the photo-ionization cross sections. An interesting paper on the various atmospheric and atomic data required to study the solar spectrum and the available resources is by [Kurucz \(1990\)](#).

1.7 Thesis outline

In this thesis we have derived the redistribution matrices for complex atomic systems with fine and hyperfine structure splitting by taking account of the quantum interferences occurring between the split levels. Our treatment includes the effects of PRD and a heuristic inclusion of collisions. We have extended the polarized radiative transfer equation for a two-level atom to the case of a two-term atom and also suitably modified the existing numerical methods to solve this equation. Finally, we have tested our theory by modeling the Stokes profiles of some of the atomic lines observed in the Sun.

The thesis is divided into three parts. First part is devoted to the study of J -state interference. In the second part we treat the case of F -state interference. In the third part, we combine the two parts and derive the redistribution matrix for a system governed by both J and F -state interferences.

1.7.1 Part-I

Part-I of this thesis is dedicated to the understanding and development of the theory of J -state interference. In Chapter 2, we derive the redistribution matrix accounting for the quantum interference between J -state, the effects of PRD and magnetic fields. However we confine our attention to the collisionless regime. The derived redistribution matrix holds good in the linear Zeeman regime of field strengths where the magnetic substates (m) of different J states do not overlap. For the field strengths found in the solar atmosphere, this is valid in most cases. Using this redistribution matrix, we compute the Stokes profiles resulting from a 90° single scattering event. This is because at 90° , the degree of polarization is maximum. We assume the scattering to be occurring on

a hypothetical atomic system with $L_{\text{upper}} = 1$, $L_{\text{lower}=0}$ and $S = 1/2$. The transitions from the fine structure states are assumed to be centered at 5000 \AA and 5001 \AA . The Stokes profiles are computed for different magnetic field strengths and also for different separations between the fine structure states.

In Chapter 3, we incorporate the above derived redistribution matrix into the polarized radiative transfer equation but consider only the non-magnetic case. We extend the commonly used two-level atom transfer equation to the case of a two-term atom. The transfer equation is then solved using the PALI method after decomposing the Stokes vector into the reduced basis. The method of short characteristics is used to compute the formal solver and the frequency by frequency (FBF) method is used to compute the source vector corrections. The model atmosphere is assumed to be an isothermal constant property plane-parallel slab. We study the nature of the emergent Stokes profiles by varying different properties of the atmosphere such as its optical thickness, thermalization parameter, continuum opacity, etc. Finally, we compare our redistribution matrix approach with the $W_2(\lambda)$ approach of Stenflo and find that they provide identical results.

Chapter 4 is an extension of Chapters 2 and 3 to include the collisional redistribution. In this chapter we present a heuristic approach of including the effects of collisions into the J -state interference theory by making a few assumptions which are listed in the chapter. We then compute the 90° single scattered profiles like in Chapter 2. We also propose a method to handle the polarized radiative transfer equation with the J -state interference redistribution matrix in the presence of weak magnetic fields. We then solve this transfer equation and study the nature of the emergent Stokes profiles.

In Chapter 5, we apply the theory and the numerical techniques developed in the previous three chapters to model the Cr I triplet around 5206 \AA observed at a quiet region near the solar limb. These observations were taken by us using the ZIMPOL-III polarimeter at IRSOL, Switzerland. We find that in order to get a good match with the observations, we need to modify the temperature structure of a standard model atmosphere in the deeper layers. We get a good fit to both the intensity and the linear polarization profiles with the modified model.

1.7.2 Part-II

In Part-II of the thesis, we extend the above developed theory of J -state interference to the case of F -state interference. In Chapter 6, we present the redistribution matrix and use it in the polarized radiative transfer equation. We compare the PALI method and the Scattering expansion method (SEM). We compute the emergent Stokes profiles for an isothermal constant property atmospheric model and study their nature.

In Chapter 7, we take the example of the Ba II D_2 line and use the F -state in-

terference theory to model its Stokes profiles. We take account of the contributions from different isotopes and their isotopic shifts. Once again, to obtain a good fit to the observed profiles, we find it necessary to reduce the temperature of a standard model atmosphere at the heights where the line center is formed. Though, the modified model provides a good fit to the limb observations ($\mu = 0.1$), it fails at other limb distances $\mu > 0.1$.

In Chapter 8, we consider another example, the Sc II 4247 Å line which is governed by F -state interference effects and apply our theory to model its observed profiles. None of the model atmospheres tried by us provides a match. We suspect the role of lower level Hanle effect in shaping the observed profiles, which is not accounted for in our treatment.

1.7.3 Part-III

In Part-III of the thesis, we derive the redistribution matrix taking account of both J -state and F -state interferences in the collisionless, non-magnetic regime. We compute the 90° single scattered profiles by assuming a hypothetical atomic system and study their behaviour.

The overall summary of the thesis is presented in Chapter 10 followed by future outlook in this area. A few appendices are added at the end of the thesis giving some specialized aspects of the derivations presented in the thesis.

Part I

Polarized line formation with J -state interference

Chapters 2-5

Based on:

Smitha, H. N., Sampoorna, M., Nagendra, K. N., & Stenflo J. O. 2011, *ApJ*, 633, 4

2

Collisionless redistribution in the presence of magnetic fields

An Overview

Quantum interference phenomena play a fundamental role in astrophysical spectra that are formed by coherent scattering processes. In this chapter (Smitha et al., 2011b), we derive a partial frequency redistribution (PRD) matrix that includes J -state interference in the presence of magnetic fields of arbitrary strength. Here, we focus on the collisionless regime, which in the traditional PRD terminology is referred to as Hummer's type II scattering. By limiting the treatment to the linear Zeeman regime, for which the Zeeman splitting is much smaller than the fine structure splitting, we formulate analytical expressions for the PRD matrices. In the special case of non-magnetic scattering we recover the redistribution matrix derived from an independent QED formulation based on the metalevel theory.

2.1 Introduction

The interpretation of Second Solar Spectrum requires the use of advanced theories of scattering in the presence of magnetic fields. The Rayleigh (non-magnetic) scattering phase matrix for a $J = 0 \rightarrow 1 \rightarrow 0$ scattering transition was derived by Chandrasekhar (1950) using classical electrodynamics. The phase matrix for arbitrary (namely, a

$J_a \rightarrow J_b \rightarrow J_a$) scattering transition was derived by [Hamilton \(1947\)](#) using quantum mechanics. A classical electrodynamic expression of the Hanle phase matrix for polarized light scattering on atoms in the presence of weak magnetic fields was given by [Stenflo \(1978\)](#). The QED theory of polarized scattering on atoms in the presence of arbitrary strength magnetic fields was formulated in [Bommier & Sahal-Brechot \(1978\)](#) and [Landi Degl’Innocenti \(1983, 1984, 1985\)](#), under the assumption of complete frequency redistribution (CRD).

The interpretation of observed linear polarization in resonance lines often requires the use of PRD in scattering. The problem of frequency redistribution in resonance lines for non-magnetic and weak magnetic field cases was formulated by [Omont et al. \(1972, 1973\)](#) using a quantum approach. Based on this work [Domke & Hubeny \(1988\)](#) derived an explicit form of the polarized PRD matrix for resonance scattering. Using a master equation theory, [Bommier \(1997a,b\)](#) derived the polarized PRD matrices for scattering in non-magnetic and arbitrary strength magnetic fields. Her theory can handle an arbitrary scattering transition $J_a \rightarrow J_b \rightarrow J_a$, with J_a and J_b being the angular momentum quantum numbers of the lower and the upper states, respectively. The lower level in this theory is assumed to be unpolarized.

A classical PRD theory for the scattering of polarized radiation in the presence of arbitrary strength magnetic fields was developed by [Bommier & Stenflo \(1999\)](#). They solved the time-dependent oscillator equation, in combination with a classical model for collisions (see [Stenflo, 1994](#), Chapter 10). However, [Bommier & Stenflo \(1999\)](#) present the polarized PRD matrices in the atomic rest frame. The corresponding laboratory frame redistribution matrices were derived in [Sampoorna et al. \(2007a\)](#). For the particular case of a $J = 0 \rightarrow 1 \rightarrow 0$ scattering transition, [Sampoorna et al. \(2007b\)](#) showed that the QED theory of [Bommier \(1997b\)](#) and the classical oscillator theory give identical results. Following the suggestion given in Section 5 of [Sampoorna et al. \(2007a\)](#), [Sampoorna \(2011a\)](#) has extended the classical theory to treat atomic transitions with arbitrary J -quantum numbers. This extension proceeds in a phenomenological way, drawing on the analogy between the Kramers-Heisenberg scattering amplitude for line scattering in quantum mechanics and the Jones matrix for classical polarized scattering. The PRD matrices derived from such a semi-classical approach are in agreement with those derived by [Bommier \(1997b\)](#). The complex problem of polarized line formation in multilevel atoms taking account of the PRD effects has recently been addressed by [Sampoorna et al. \(2013\)](#).

[Stenflo \(1980, 1994, 1997\)](#) formulated the quantum theory of J -state interference for frequency coherent scattering. A QED theory for the multi-term atom (that includes also the J -state interference) under the assumption of CRD is given in [Landi Degl’Innocenti & Landolfi \(2004\)](#). A metalevel theory (also including J -state interference) has been formulated by [Landi Degl’Innocenti et al. \(1997\)](#) to deal with PRD

problems in the presence of magnetic fields of arbitrary strength in the absence of collisions.

In the present chapter, based on the Kramers-Heisenberg scattering formula, we derive polarized PRD matrices including the J -state interference. Here we restrict our attention to scattering in the absence of collisions (the so-called type-II scattering of [Hummer, 1962](#)). Our formulation however has the advantage that it allows elastic collisions to be taken into account by following an approach similar to that described in [Sampoorna et al. \(2007a\)](#), in the context of m -state interference phenomenon. We consider an $L_a \rightarrow L_b \rightarrow L_f$ scattering transition, where L_a , L_b and L_f denote the orbital angular momentum quantum numbers of the initial, intermediate, and final levels, respectively, but limit ourselves here to the case of resonance scattering with common initial and final states, $L_a = L_f$, which is known as a two-term atom (see [Figure 2.1](#))

Due to L - S coupling, a given (L, S) state splits into several J -states, with $|L-S| \leq J \leq |L+S|$. Here we account for interference between the J_b -states belonging to a given excited L_b -state. This includes the interference between the magnetic substates of different J_b -states. However, the present treatment is limited to the regime where the Zeeman splitting is much smaller than the fine-structure splitting. Therefore, the Paschen-Back regime is not covered and the level crossings are not dealt with. Thus, in the linear Zeeman regime of relatively weak fields, the interference between magnetic substates belonging to different J -states takes place mainly in the line wings, outside the Doppler cores. The Paschen-Back theory that covers the regime of relatively strong fields but under the assumption of CRD is given in [Landi Degl'Innocenti & Landolfi \(2004\)](#). The PRD theory of J -state interference in the Paschen-Back regime is now developed in [Sowmya et al. \(2014a\)](#).

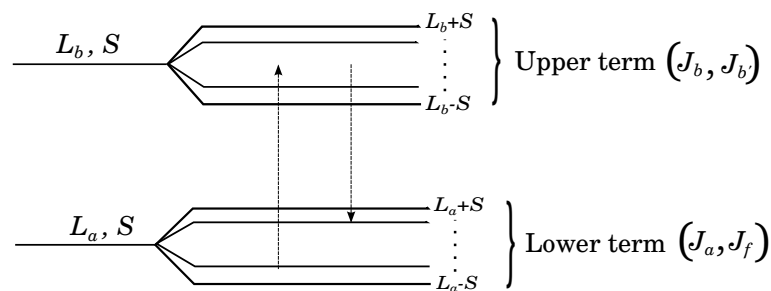


Figure 2.1: Schematic Level diagram of a two-term atom. The lower term is assumed to be infinitely sharp whereas the upper term is radiatively broadened.

In [Section 2.2](#) we recall the expressions of the Kramers-Heisenberg formula and the Mueller scattering matrix. In [Section 2.3](#) we derive the elements of the redistribution matrix in both the atomic and the laboratory frames. In [Section 2.4](#) we rewrite the redistribution matrix derived in [Section 2.3](#) in terms of the irreducible spherical tensors. In [Section 2.5](#), we derive the analytical expressions for the $L = 0 \rightarrow 1 \rightarrow 0$ transition.

The Stokes profiles obtained from single scattering are discussed in detail in Section 2.6. The concluding remarks are given in Section 2.7.

2.2 The Muller scattering matrix

The complex probability amplitude for scattering from a given initial magnetic substate a to a final substate f via all possible intermediate substates b is given by the Kramers–Heisenberg formula (see [Stenflo, 1998](#))

$$w_{\alpha\beta} \sim \sum_b \frac{\langle f | \mathbf{r} \cdot \mathbf{e}_\alpha | b \rangle \langle b | \mathbf{r} \cdot \mathbf{e}_\beta | a \rangle}{\omega_{bf} - \omega - i\gamma/2}, \quad (2.1)$$

where $\omega = 2\pi\xi$ is the angular frequency of the scattered radiation in the atomic rest frame, $\hbar\omega_{bf}$ is the energy difference between the excited and final states, and γ is the damping constant that accounts for the broadening of the excited state, while the initial and final states are assumed to be infinitely sharp. The damping parameter is assumed to be same for all the magnetic substates of the excited state. The matrix elements appearing in Equation (2.1) can be expanded using the Wigner–Eckart theorem (see [Stenflo, 1994](#), pp. 145 and 199). This gives us

$$\begin{aligned} w_{\alpha\beta}(J_f\mu_f J_a\mu_a) &\sim \sum_{J_b\mu_b} (-1)^{q-q'} \sqrt{(2J_a+1)(2J_f+1)(2J_b+1)(2L_a+1)} \\ &\times \begin{Bmatrix} L_a & L_b & 1 \\ J_b & J_f & S \end{Bmatrix} \begin{Bmatrix} L_a & L_b & 1 \\ J_b & J_a & S \end{Bmatrix} \begin{pmatrix} J_b & J_a & 1 \\ -\mu_b & \mu_a & -q' \end{pmatrix} \begin{pmatrix} J_b & J_f & 1 \\ -\mu_b & \mu_f & -q \end{pmatrix} \\ &\times \Phi_\gamma(\nu_{J_b\mu_b J_f\mu_f} - \xi) \varepsilon_q^{\alpha*} \varepsilon_{q'}^\beta, \end{aligned} \quad (2.2)$$

where μ_b represents the magnetic substates of the upper level b with total angular momentum quantum number J_b , orbital angular momentum quantum number L_b , and spin S . The total angular momentum quantum numbers of the initial and final states are J_a and J_f with orbital angular momentum quantum number L_a , spin S , and magnetic substates μ_a and μ_f , respectively. The quantities ε are the geometrical factors (see Equations (2) and (27) of [Stenflo, 1998](#)) with α and β denoting the outgoing and incoming rays, respectively. In Equation (2.2), q and q' satisfy

$$q = \mu_f - \mu_b; \quad q' = \mu_a - \mu_b. \quad (2.3)$$

The frequency-normalized profile function is given by

$$\Phi_\gamma(\nu_{J_b\mu_b J_f\mu_f} - \xi) = \frac{1/(\pi i)}{\nu_{J_b\mu_b J_f\mu_f} - \xi - i\gamma/(4\pi)}, \quad (2.4)$$

where

$$\nu_{J_b\mu_b J_f\mu_f} = \nu_{J_b J_f} + (g_b\mu_b - g_f\mu_f)\nu_L. \quad (2.5)$$

Here $h\nu_{J_b J_f}$ is the energy difference between the upper state J_b and lower state J_f in the absence of magnetic fields, $g_{b,f}$ are the Landé factors of the J_b and J_f states, and ν_L is the Larmor frequency. Equation (2.2) refers to the frequency-coherent scattering case. The Mueller matrix \mathbf{M} that describes the transformation from the incident to the scattered Stokes vector is of the form (see Equation (7) of [Stenflo, 1998](#))

$$\mathbf{M} = \mathbf{T}\mathbf{W}\mathbf{T}^{-1}, \quad (2.6)$$

where

$$\mathbf{W} = \sum_{J_a\mu_a} \rho_{\mu_a\mu_a} \sum_{J_f\mu_f} \mathbf{w}(J_f\mu_f J_a\mu_a) \otimes \mathbf{w}^*(J_f\mu_f J_a\mu_a). \quad (2.7)$$

The symbol \otimes stands for the tensor product. $\rho_{\mu_a\mu_a}$ represents the relative populations of the initial magnetic substates μ_a (diagonal elements of the density matrix for the initial state, normalized such that the sum over $\rho_{\mu_a\mu_a}$ is unity). Without initial-state polarization, all the $\rho_{\mu_a\mu_a}$ are equal and can therefore be absorbed in the normalization constant for the Mueller matrix \mathbf{M} . In Equation (2.6), \mathbf{T} and \mathbf{T}^{-1} are purely mathematical transformation matrices, and their explicit forms are given in Equation (9) of [Stenflo \(1998\)](#).

2.3 The type-II redistribution matrix

The matrix form of the tensor product $\mathbf{w}(J_f\mu_f J_a\mu_a) \otimes \mathbf{w}^*(J_f\mu_f J_a\mu_a)$ in Equation (2.7), which is needed for the computation of the redistribution matrix, is given by Equation (10) of [Stenflo \(1998\)](#). Bilinear products $w_{\alpha\beta}(J_f\mu_f J_a\mu_a)w_{\alpha'\beta'}^*(J_f\mu_f J_a\mu_a)$ make up this matrix. The profile function $\Phi_\gamma(\nu_{J_b\mu_b J_f\mu_f} - \xi)$ appearing in Equation (2.2) for outgoing frequency (ξ) may be replaced by $\Phi'_\gamma(\nu_{J_b\mu_b J_a\mu_a} - \xi')$ for incoming frequency (ξ'), through an application of energy conservation (see Equation (9.10) of [Stenflo, 1994](#)). The profile function $\Phi'_\gamma(\nu_{J_b\mu_b J_a\mu_a} - \xi')$ is given by Equation (2.4) with ξ replaced by ξ' , while $\nu_{J_b\mu_b J_f\mu_f}$ is replaced by $\nu_{J_b\mu_b J_a\mu_a}$ which is defined similar to Equation (2.5). Thus the bilinear product $w_{\alpha\beta}(J_f\mu_f J_a\mu_a)w_{\alpha'\beta'}^*(J_f\mu_f J_a\mu_a)$ can be written in the atomic frame as

$$\begin{aligned} w_{\alpha\beta}(J_f\mu_f J_a\mu_a)w_{\alpha'\beta'}^*(J_f\mu_f J_a\mu_a) &\sim \sum_{J_b\mu_b J_{b'}\mu_{b'}} (-1)^{q-q'} (-1)^{q''-q'''} \varepsilon_q^{\alpha*} \varepsilon_{q''}^{\alpha'} \varepsilon_{q'}^\beta \varepsilon_{q'''}^{\beta'*} \\ &\times \cos \beta_{J_{b'}\mu_{b'} J_b\mu_b} e^{i\beta_{J_{b'}\mu_{b'} J_b\mu_b}} \Phi_{J_b\mu_b J_{b'}\mu_{b'} J_a\mu_a}^\gamma(\xi') \delta(\xi - \xi' - \nu_{J_a\mu_a J_f\mu_f}) (2J_a + 1) \\ &\times (2J_f + 1)(2J_b + 1)(2J_{b'} + 1)(2L_a + 1)^2 \begin{Bmatrix} L_a & L_b & 1 \\ J_b & J_f & S \end{Bmatrix} \begin{Bmatrix} L_a & L_b & 1 \\ J_b & J_a & S \end{Bmatrix} \end{aligned}$$

$$\begin{aligned}
 & \times \begin{Bmatrix} L_a & L_b & 1 \\ J_{b'} & J_f & S \end{Bmatrix} \begin{Bmatrix} L_a & L_b & 1 \\ J_{b'} & J_a & S \end{Bmatrix} \begin{pmatrix} J_b & J_a & 1 \\ -\mu_b & \mu_a & -q' \end{pmatrix} \begin{pmatrix} J_{b'} & J_a & 1 \\ -\mu_{b'} & \mu_a & -q''' \end{pmatrix} \\
 & \times \begin{pmatrix} J_b & J_f & 1 \\ -\mu_b & \mu_f & -q \end{pmatrix} \begin{pmatrix} J_{b'} & J_f & 1 \\ -\mu_{b'} & \mu_f & -q'' \end{pmatrix}. \tag{2.8}
 \end{aligned}$$

In the above equation we have introduced the delta-function term $\delta(\xi - \xi' - \nu_{J_a\mu_a J_f\mu_f})$, which is simply the statement of energy conservation (see Equations (9.7) and (9.10) of [Stenflo, 1994](#)). This term is essential as we are dealing with type-II scattering which represents coherent scattering in the atom's rest frame. The $\nu_{J_a\mu_a J_f\mu_f}$ appearing in the delta function is given by

$$\nu_{J_a\mu_a J_f\mu_f} = \nu_{J_a J_f} + (g_a\mu_a - g_f\mu_f)\nu_L, \tag{2.9}$$

where $h\nu_{J_a J_f}$ is the energy difference between the states J_a and J_f in the absence of a magnetic field.

The angle $\beta_{J_{b'}\mu_{b'} J_b\mu_b}$ (arising due to the combined effects of the J -state and m -state interferences) is defined by

$$\tan \beta_{J_{b'}\mu_{b'} J_b\mu_b} = \frac{\omega_{J_{b'} J_b} + (g_{b'}\mu_{b'} - g_b\mu_b)\omega_L}{\gamma}, \tag{2.10}$$

where $h\omega_{J_{b'} J_b}$ represents the energy difference between the $J_{b'}$ and J_b states in the absence of a magnetic field. When $J_b = J_{b'}$, the angle $\beta_{J_{b'}\mu_{b'} J_b\mu_b}$ describes the m -state interference (see [Stenflo, 1994](#), pp. 87) and when $J_b \neq J_{b'}$, it characterizes the J -state interference. In the present chapter (see also [Smitha et al., 2011b](#)) we limit the treatment to the linear Zeeman regime, in which the Zeeman splitting is much smaller than the fine structure splitting. When $J_b \neq J_{b'}$, the contribution from the second term with ω_L in Equation (2.10) to the angle $\beta_{J_{b'}\mu_{b'} J_b\mu_b}$ can therefore be ignored, because it is insignificant in comparison with the first term.

The ‘‘generalized profile function’’ is defined as

$$\Phi_{J_b\mu_b J_{b'}\mu_{b'} J_f\mu_f}^\gamma(\xi) = \frac{1}{2} [\Phi_\gamma(\nu_{J_b\mu_b J_f\mu_f} - \xi) + \Phi_\gamma^*(\nu_{J_{b'}\mu_{b'} J_f\mu_f} - \xi)]. \tag{2.11}$$

When deriving Equation (2.8), we have made use of the following relation

$$\Phi_\gamma(\nu_{J_b\mu_b J_f\mu_f} - \xi)\Phi_\gamma^*(\nu_{J_{b'}\mu_{b'} J_f\mu_f} - \xi) = \frac{4 \Phi_{J_b\mu_b J_{b'}\mu_{b'} J_f\mu_f}^\gamma(\xi)}{\gamma - i(\omega_{J_{b'}\mu_{b'} J_f\mu_f} - \omega_{J_b\mu_b J_f\mu_f})}. \tag{2.12}$$

Equation (2.8) can be transformed to the laboratory frame following exactly the same steps as described in Section 2.2 of [Sampoorna et al. \(2007a\)](#) (see also Section 3.3 of [Bommier, 1997b](#)). Thus in the laboratory frame, the bilinear product is given by

Equation (2.8), but with the following replacement:

$$\Phi_{J_b\mu_b, J_{b'}\mu_{b'}, J_a\mu_a}^\gamma(\xi')\delta(\xi - \xi' - \nu_{J_a\mu_a J_f\mu_f}) \longrightarrow \left[(h_{J_b\mu_b, J_{b'}\mu_{b'}}^{\text{II}})_{J_a\mu_a J_f\mu_f} + i(f_{J_b\mu_b, J_{b'}\mu_{b'}}^{\text{II}})_{J_a\mu_a J_f\mu_f} \right], \quad (2.13)$$

where

$$(h_{J_b\mu_b, J_{b'}\mu_{b'}}^{\text{II}})_{J_a\mu_a J_f\mu_f} = \frac{1}{2} \left[R_{J_b\mu_b, J_a\mu_a J_f\mu_f}^{\text{II, H}} + R_{J_{b'}\mu_{b'}, J_a\mu_a J_f\mu_f}^{\text{II, H}} \right], \quad (2.14)$$

$$(f_{J_b\mu_b, J_{b'}\mu_{b'}}^{\text{II}})_{J_a\mu_a J_f\mu_f} = \frac{1}{2} \left[R_{J_{b'}\mu_{b'}, J_a\mu_a J_f\mu_f}^{\text{II, F}} - R_{J_b\mu_b, J_a\mu_a J_f\mu_f}^{\text{II, F}} \right], \quad (2.15)$$

and the magnetic redistribution functions of type II are given by

$$R_{J_b\mu_b, J_a\mu_a J_f\mu_f}^{\text{II, H}}(x_{ba}, x'_{ba}, \Theta) = \frac{1}{\pi \sin \Theta} \exp \left\{ - \left[\frac{x_{ba} - x'_{ba} + x_{J_a\mu_a J_f\mu_f}}{2 \sin(\Theta/2)} \right]^2 \right\} \times H \left(\frac{a}{\cos(\Theta/2)}, \frac{\nu_{J_b\mu_b, J_a\mu_a} + \nu'_{J_{b'}\mu_{b'}, J_a\mu_a} + x_{J_a\mu_a J_f\mu_f}}{2 \cos(\Theta/2)} \right), \quad (2.16)$$

and

$$R_{J_b\mu_b, J_a\mu_a J_f\mu_f}^{\text{II, F}}(x_{ba}, x'_{ba}, \Theta) = \frac{1}{\pi \sin \Theta} \exp \left\{ - \left[\frac{x_{ba} - x'_{ba} + x_{J_a\mu_a J_f\mu_f}}{2 \sin(\Theta/2)} \right]^2 \right\} \times 2F \left(\frac{a}{\cos(\Theta/2)}, \frac{\nu_{J_b\mu_b, J_a\mu_a} + \nu'_{J_{b'}\mu_{b'}, J_a\mu_a} + x_{J_a\mu_a J_f\mu_f}}{2 \cos(\Theta/2)} \right). \quad (2.17)$$

In the above equations, $H(a, x)$ and $F(a, x)$ are the Voigt and Faraday-Voigt functions defined by

$$H(a, x) = \frac{a}{\pi} \int_{-\infty}^{+\infty} \frac{e^{-y^2} dy}{(x-y)^2 + a^2}; \quad F(a, x) = \frac{1}{2\pi} \int_{-\infty}^{+\infty} \frac{e^{-y^2} (x-y) dy}{(x-y)^2 + a^2}. \quad (2.18)$$

The scattering angle between the incident and scattered rays is denoted by Θ (see Figure 2.2). The dimensionless quantities appearing in Equations (2.16) and (2.17) are given by

$$x_{ba} = \frac{\nu_{0ba} - \nu}{\Delta\nu_D}; \quad \nu_{\mu_b\mu_f} = x + (g_b\mu_b - g_a\mu_f) \frac{\nu_L}{\Delta\nu_D}; \quad a = \frac{\gamma}{4\pi\Delta\nu_D}, \\ x_{J_a\mu_a J_f\mu_f} = \frac{\nu_{J_a\mu_a J_f\mu_f}}{\Delta\nu_D}; \quad \nu_{J_b\mu_b, J_a\mu_a} = x_{ba} + (g_b\mu_b - g_a\mu_a) \frac{\nu_L}{\Delta\nu_D}, \quad (2.19)$$

where x_{ba} , a and $\Delta\nu_D$ are the emission frequency, damping parameter, and Doppler width, respectively. We note that $(f_{J_b\mu_b, J_{b'}\mu_{b'}}^{\text{II}})_{J_a\mu_a J_f\mu_f}$ is zero when both $J_b = J_{b'}$ and $\mu_b = \mu_{b'}$.

Substituting Equation (2.8) in Equations (2.6) and (2.7), we obtain the Hanle - Zee-

man redistribution matrix with the J -state interference included appropriately.

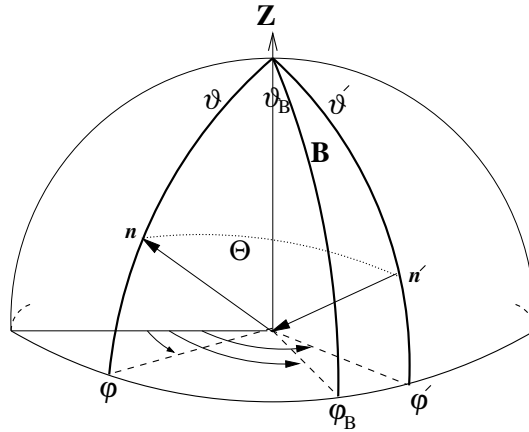


Figure 2.2: Illustration of the scattering geometry in a coordinate system where the magnetic field makes an angle ϑ_B with the polar z -axis and has an azimuth φ_B . (ϑ', φ') refer to the incident ray and (ϑ, φ) to the scattered ray defined with respect to the z -axis. Θ is the scattering angle.

2.4 The redistribution matrix in terms of irreducible spherical tensors

The irreducible tensors $\mathcal{T}_Q^K(i, \mathbf{n})$ have been introduced by [Landi Degl'Innocenti \(1984\)](#) to deal with problems in polarized radiative transfer. Here index i refers to the Stokes parameters ($i = 0, 1, 2, 3$), while $K = 0, 1, 2$ with $-K \leq Q \leq +K$. In the following we will express the redistribution matrix in terms of \mathcal{T}_Q^K , which allows it to be written as a sum of its multipolar (K) components. The details are presented in [Appendix A](#). We will need this form in particular for the collisional redistribution matrix (type III). Furthermore, in the weak field limit the expansion in terms of \mathcal{T}_Q^K allows us to express the Stokes intensity and source vectors in terms of the respective ‘cylindrically symmetric’ irreducible components I_Q^K and S_Q^K (see [Frisch, 2007](#)).

We start by expressing the equations given in [Sections 2.2 and 2.3](#) in terms of the irreducible spherical tensors for polarimetry, following [Appendix C](#) of [Sampoorna et al. \(2007b\)](#) (see also [Landi Degl'Innocenti & Landolfi, 2004](#)). In [Appendix A](#), we show that for the non-magnetic case we recover the fine-structure scattering phase matrix derived in [Landi Degl'Innocenti & Landolfi \(2004, see their Equation \(10.132\)\)](#). Following the same procedure as described in this appendix, we can express the magnetic PRD matrix of [Section 2.3](#) in terms of \mathcal{T}_Q^K . After some algebra, we can write the mag-

netic redistribution matrix in the Stokes vector formalism as (see Appendix A)

$$\begin{aligned}
 \mathbf{R}_{ij}^{\text{II}}(\xi, \mathbf{n}; \xi', \mathbf{n}', \mathbf{B}) &= \frac{2}{3} \sum_{K'K''QJ_a\mu_aJ_f\mu_fJ_b\mu_bJ_{b'}\mu_{b'}} \sqrt{(2K'+1)(2K''+1)} \\
 &\times (2J_a+1)(2J_f+1)(2J_b+1)(2J_{b'}+1)(2L_a+1)^2 (-1)^{q''+q'+Q} \cos\beta_{J_{b'}\mu_{b'}J_b\mu_b} \\
 &\times e^{i\beta_{J_{b'}\mu_{b'}J_b\mu_b}} \Phi_{J_b\mu_bJ_{b'}\mu_{b'}J_a\mu_a}^{\gamma}(\xi') \delta(\xi - \xi' - \nu_{J_a\mu_aJ_f\mu_f}) \begin{pmatrix} J_b & J_a & 1 \\ -\mu_b & \mu_a & -q' \end{pmatrix} \\
 &\times \begin{pmatrix} J_b & J_f & 1 \\ -\mu_b & \mu_f & -q \end{pmatrix} \begin{pmatrix} J_{b'} & J_a & 1 \\ -\mu_{b'} & \mu_a & -q''' \end{pmatrix} \begin{pmatrix} J_{b'} & J_f & 1 \\ -\mu_{b'} & \mu_f & -q'' \end{pmatrix} \begin{pmatrix} 1 & 1 & K'' \\ q & -q'' & -Q \end{pmatrix} \\
 &\times \begin{pmatrix} 1 & 1 & K' \\ q''' & -q' & Q \end{pmatrix} \begin{Bmatrix} L_a & L_b & 1 \\ J_b & J_f & S \end{Bmatrix} \begin{Bmatrix} L_a & L_b & 1 \\ J_b & J_a & S \end{Bmatrix} \begin{Bmatrix} L_a & L_b & 1 \\ J_{b'} & J_f & S \end{Bmatrix} \begin{Bmatrix} L_a & L_b & 1 \\ J_{b'} & J_a & S \end{Bmatrix} \\
 &\times (-1)^Q \mathcal{T}_{-Q}^{K''}(i, \mathbf{n}) \mathcal{T}_Q^{K'}(j, \mathbf{n}'). \tag{2.20}
 \end{aligned}$$

Using Equation (C2) of [Sampoorna et al. \(2007b\)](#) and Equation (2.13) we can write the normalized type-II redistribution matrix in the laboratory frame as

$$\begin{aligned}
 \mathbf{R}_{ij}^{\text{II}}(x, \mathbf{n}; x', \mathbf{n}', \mathbf{B}) &= \frac{3(2L_b+1)}{2S+1} \sum_{K'K''QJ_a\mu_aJ_f\mu_fJ_b\mu_bJ_{b'}\mu_{b'}} \sqrt{(2K'+1)(2K''+1)} \\
 &\times (2J_a+1)(2J_f+1)(2J_b+1)(2J_{b'}+1) (-1)^{q''+q'+Q} \cos\beta_{J_{b'}\mu_{b'}J_b\mu_b} e^{i\beta_{J_{b'}\mu_{b'}J_b\mu_b}} \\
 &\times \left[(h_{J_b\mu_b, J_{b'}\mu_{b'}}^{\text{II}})_{J_a\mu_aJ_f\mu_f} + i(f_{J_b\mu_b, J_{b'}\mu_{b'}}^{\text{II}})_{J_a\mu_aJ_f\mu_f} \right] \begin{pmatrix} J_b & J_a & 1 \\ -\mu_b & \mu_a & -q' \end{pmatrix} \\
 &\times \begin{pmatrix} J_b & J_f & 1 \\ -\mu_b & \mu_f & -q \end{pmatrix} \begin{pmatrix} J_{b'} & J_a & 1 \\ -\mu_{b'} & \mu_a & -q''' \end{pmatrix} \begin{pmatrix} J_{b'} & J_f & 1 \\ -\mu_{b'} & \mu_f & -q'' \end{pmatrix} \begin{pmatrix} 1 & 1 & K'' \\ q & -q'' & -Q \end{pmatrix} \\
 &\times \begin{pmatrix} 1 & 1 & K' \\ q''' & -q' & Q \end{pmatrix} \begin{Bmatrix} L_a & L_b & 1 \\ J_b & J_f & S \end{Bmatrix} \begin{Bmatrix} L_a & L_b & 1 \\ J_b & J_a & S \end{Bmatrix} \begin{Bmatrix} L_a & L_b & 1 \\ J_{b'} & J_f & S \end{Bmatrix} \begin{Bmatrix} L_a & L_b & 1 \\ J_{b'} & J_a & S \end{Bmatrix} \\
 &\times (-1)^Q \mathcal{T}_{-Q}^{K''}(i, \mathbf{n}) \mathcal{T}_Q^{K'}(j, \mathbf{n}'). \tag{2.21}
 \end{aligned}$$

In Section 2.6 we present the results computed using Equation (2.21). When the magnetic field is set to zero in Equation (2.21), it takes a particularly simple form given by

$$\begin{aligned}
 \mathbf{R}_{ij}^{\text{II}}(x, \mathbf{n}; x', \mathbf{n}') &= \frac{3(2L_b+1)}{2S+1} \sum_{KQJ_aJ_fJ_bJ_{b'}} (-1)^{J_f-J_a} \cos\beta_{J_{b'}J_b} e^{i\beta_{J_{b'}J_b}} (2J_a+1) \\
 &\times (2J_f+1) \left[(h_{J_b, J_{b'}}^{\text{II}})_{J_aJ_f} + i(f_{J_b, J_{b'}}^{\text{II}})_{J_aJ_f} \right] (2J_b+1)(2J_{b'}+1) \\
 &\times \begin{Bmatrix} L_a & L_b & 1 \\ J_b & J_f & S \end{Bmatrix} \begin{Bmatrix} L_a & L_b & 1 \\ J_b & J_a & S \end{Bmatrix} \begin{Bmatrix} L_a & L_b & 1 \\ J_{b'} & J_f & S \end{Bmatrix} \begin{Bmatrix} L_a & L_b & 1 \\ J_{b'} & J_a & S \end{Bmatrix} \\
 &\times \begin{Bmatrix} 1 & 1 & K \\ J_{b'} & J_b & J_a \end{Bmatrix} \begin{Bmatrix} 1 & 1 & K \\ J_{b'} & J_b & J_f \end{Bmatrix} (-1)^Q \mathcal{T}_Q^K(i, \mathbf{n}) \mathcal{T}_{-Q}^K(j, \mathbf{n}'). \tag{2.22}
 \end{aligned}$$

The quantities appearing in Equation (2.22) are given by Equations (2.10) and (2.14)-(2.17), but with $\nu_L = 0$. We have verified that Equation (2.22), when written in the atomic rest frame, is identical to the redistribution matrix given in [Landi Degl'Innocenti et al. \(1997\)](#) based on the metalevel approach (see their Equation (15)).

2.5 Analytical Expressions for the $L = 0 \rightarrow 1 \rightarrow 0$ transition

To gain a physical insight, we have derived the analytical form of the Hanle-Zeeman redistribution matrix for the case when $L_a = L_f = 0$ and $L_b = 1$, and for a co-ordinate system in which the polar axis is along the magnetic field. The incident ray is defined by polar and azimuth angles θ' and ϕ' , the outgoing ray by θ and ϕ (see Figure 2.2). The redistribution matrix for arbitrary orientations of vector magnetic fields can be obtained by using the Mueller rotation matrices (see Appendix D in [Sampoorna et al., 2007b](#)). Following [Stenflo \(1998\)](#), we simplify the expressions by introducing the following auxiliary quantities:

$$\begin{aligned} (c_{J_b\mu_b J_{b'}\mu_{b'}}^{\text{II}})_{J_a\mu_a J_f\mu_f} &= \cos\beta_{J_{b'}\mu_{b'} J_b\mu_b} \left[\cos[(\mu_{b'} - \mu_b)(\phi - \phi')] \right. \\ &\times \left\{ \cos\beta_{J_{b'}\mu_{b'} J_b\mu_b} (h_{J_b\mu_b J_{b'}\mu_{b'}}^{\text{II}})_{J_a\mu_a J_f\mu_f} - \sin\beta_{J_{b'}\mu_{b'} J_b\mu_b} (f_{J_b\mu_b J_{b'}\mu_{b'}}^{\text{II}})_{J_a\mu_a J_f\mu_f} \right\} \\ &+ \sin[(\mu_{b'} - \mu_b)(\phi - \phi')] \left\{ \sin\beta_{J_{b'}\mu_{b'} J_b\mu_b} (h_{J_b\mu_b J_{b'}\mu_{b'}}^{\text{II}})_{J_a\mu_a J_f\mu_f} \right. \\ &\left. \left. + \cos\beta_{J_{b'}\mu_{b'} J_b\mu_b} (f_{J_b\mu_b J_{b'}\mu_{b'}}^{\text{II}})_{J_a\mu_a J_f\mu_f} \right\} \right], \quad (2.23) \end{aligned}$$

and

$$\begin{aligned} (s_{J_b\mu_b J_{b'}\mu_{b'}}^{\text{II}})_{J_a\mu_a J_f\mu_f} &= \cos\beta_{J_{b'}\mu_{b'} J_b\mu_b} \left[\sin[(\mu_{b'} - \mu_b)(\phi - \phi')] \right. \\ &\times \left\{ \cos\beta_{J_{b'}\mu_{b'} J_b\mu_b} (h_{J_b\mu_b J_{b'}\mu_{b'}}^{\text{II}})_{J_a\mu_a J_f\mu_f} - \sin\beta_{J_{b'}\mu_{b'} J_b\mu_b} (f_{J_b\mu_b J_{b'}\mu_{b'}}^{\text{II}})_{J_a\mu_a J_f\mu_f} \right\} \\ &- \cos[(\mu_{b'} - \mu_b)(\phi - \phi')] \left\{ \sin\beta_{J_{b'}\mu_{b'} J_b\mu_b} (h_{J_b\mu_b J_{b'}\mu_{b'}}^{\text{II}})_{J_a\mu_a J_f\mu_f} \right. \\ &\left. \left. + \cos\beta_{J_{b'}\mu_{b'} J_b\mu_b} (f_{J_b\mu_b J_{b'}\mu_{b'}}^{\text{II}})_{J_a\mu_a J_f\mu_f} \right\} \right]. \quad (2.24) \end{aligned}$$

When $J_b \neq J_{b'}$ and $\mu_b = \mu_{b'}$,

$$\begin{aligned} (c_{J_b\mu_b J_{b'}\mu_{b'}}^{\text{II}})_{J_a\mu_a J_f\mu_f} &= 2 \cos\beta_{J_{b'}\mu_{b'} J_b\mu_b} \left[\cos\beta_{J_{b'}\mu_{b'} J_b\mu_b} (h_{J_b\mu_b J_{b'}\mu_{b'}}^{\text{II}})_{J_a\mu_a J_f\mu_f} \right. \\ &\left. - \sin\beta_{J_{b'}\mu_{b'} J_b\mu_b} (f_{J_b\mu_b J_{b'}\mu_{b'}}^{\text{II}})_{J_a\mu_a J_f\mu_f} \right]. \quad (2.25) \end{aligned}$$

Since for the case of $L = 0 \rightarrow 1 \rightarrow 0$ transition with $S = 1/2$, $J_a = J_f = 1/2$, we make the following replacement to simplify the notations

$$(c_{J_b\mu_b J_{b'}\mu_{b'}}^{\text{II}})_{J_a\mu_a J_f\mu_f} = (c_{J_b\mu_b J_{b'}\mu_{b'}}^{\text{II}})_{\mu_a\mu_f}; (s_{J_b\mu_b J_{b'}\mu_{b'}}^{\text{II}})_{J_a\mu_a J_f\mu_f} = (s_{J_b\mu_b J_{b'}\mu_{b'}}^{\text{II}})_{\mu_a\mu_f}. \quad (2.26)$$

Notice that the above auxiliary quantities obey the symmetries

$$(c_{J_b\mu_b J_{b'}\mu_{b'}}^{\text{II}})_{\mu_a\mu_f} = (c_{J_{b'}\mu_{b'} J_b\mu_b}^{\text{II}})_{\mu_a\mu_f}; (s_{J_b\mu_b J_{b'}\mu_{b'}}^{\text{II}})_{\mu_a\mu_f} = -(s_{J_{b'}\mu_{b'} J_b\mu_b}^{\text{II}})_{\mu_a\mu_f}. \quad (2.27)$$

For the particular case of $J_a = J_f = 1/2$ and $J_b = 1/2$, μ_a , μ_f and μ_b take values $+1/2$ and $-1/2$, while for $J_b = 3/2$, μ_b takes the values $+3/2$, $+1/2$, $-1/2$ and $-3/2$. To simplify the appearance of quantities like $(c_{J_b\mu_b J_{b'}\mu_{b'}}^{\text{II}})_{\mu_a\mu_f}$ and $(s_{J_b\mu_b J_{b'}\mu_{b'}}^{\text{II}})_{\mu_a\mu_f}$, we replace the subscripts J_b , μ_b , $J_{b'}$, $\mu_{b'}$, μ_a and μ_f by twice their actual values. Note that such a replacement is made only for notational simplicity. In the computations the actual values of both the total angular momentum and magnetic quantum numbers must of course be used.

2.5.1 Normalisation

The general Hanle-Zeeman redistribution matrix for an $L = 0 \rightarrow 1 \rightarrow 0$ transition can be written as,

$$\mathbf{R}^{\text{II}}(x, \mathbf{n}; x', \mathbf{n}', \mathbf{B}) = \text{N.C} \times \mathbf{M}, \quad (2.28)$$

where \mathbf{M} is the Mueller matrix (see Equation (2.6)) and N.C is the normalization constant.

$$\mathbf{M} = \mathbf{M}_{\lambda_1\lambda_1} + \mathbf{M}_{\lambda_2\lambda_2} + \mathbf{M}_{\lambda_1\lambda_2}, \quad (2.29)$$

where $\mathbf{M}_{\lambda_1\lambda_1}$, $\mathbf{M}_{\lambda_2\lambda_2}$ are the Mueller matrices for the $J = 1/2 \rightarrow 1/2 \rightarrow 1/2$ and $J = 1/2 \rightarrow 3/2 \rightarrow 1/2$ transitions, and $\mathbf{M}_{\lambda_1\lambda_2}$ represents the interference term between the two upper J -states. We determine the normalization constant by going to the non-magnetic case. When the magnetic field is zero, the Hanle angles $\beta_{J_{b'}\mu_{b'} J_b\mu_b} = 0$ when $J_{b'} = J_b$. In the absence of a magnetic field the frequency redistribution part remains the same for all the elements of the redistribution matrix. Therefore the angular phase matrix \mathbf{P} of the redistribution matrix can be normalized independently of the frequency redistribution. This implies a ‘‘flat normalization’’, which means that the phase matrix elements are normalized to the same value for all the frequency points covering the bandwidth of the multiplet. Using Equation (8.38) of [Stenflo \(1994\)](#), we get

$$\begin{aligned} \frac{\text{N.C}}{4\pi} \int_{-1}^{+1} (\mathbf{P})_{11} d\mu' d\phi' &= \frac{\text{N.C}}{4\pi} \int_{-1}^{+1} d\mu' d\phi' [(\mathbf{P}_{\lambda_1\lambda_1})_{11} + (\mathbf{P}_{\lambda_2\lambda_2})_{11} + (\mathbf{P}_{\lambda_1\lambda_2})_{11}] \\ &= 1. \end{aligned} \quad (2.30)$$

The terms containing $\cos[(\mu_{b'} - \mu_b)(\phi - \phi')]$ and $\sin[(\mu_{b'} - \mu_b)(\phi - \phi')]$ become zero when integrated for $\mu_{b'} \neq \mu_b$. We therefore obtain

$$\text{N.C} \times \left\{ \frac{4}{9} f_{\frac{1}{2}\frac{1}{2}}^2 + \frac{2}{9} f_{\frac{1}{2}\frac{3}{2}}^2 + 0 \right\} = 1, \quad (2.31)$$

$$\text{N.C} = \frac{9}{2} \times \frac{1}{2f_{\frac{1}{2}\frac{1}{2}}^2 + f_{\frac{1}{2}\frac{3}{2}}^2}, \quad (2.32)$$

where $f_{\frac{1}{2}\frac{1}{2}}$ and $f_{\frac{1}{2}\frac{3}{2}}$ are the oscillator strengths for the absorption transitions $J = 1/2 \rightarrow 1/2$ and $J = 1/2 \rightarrow 3/2$, respectively. They are defined in Equation (8.51) of [Stenflo \(1994\)](#). We note that the $6 - j$ symbols appearing in Equation (2.2) can be written in terms of oscillator strengths (see Equations (9.48) and (9.74) of [Stenflo, 1994](#)). Using Equation (2.32), we can rewrite Equation (2.28) as

$$\mathbf{R}^{\text{II}}(x, \mathbf{n}; x', \mathbf{n}', \mathbf{B}) = \frac{9}{2} \times \frac{1}{2f_{\frac{1}{2}\frac{1}{2}}^2 + f_{\frac{1}{2}\frac{3}{2}}^2} \mathbf{M}. \quad (2.33)$$

The explicit form of \mathbf{R}^{II} is given in Appendix B.

2.6 Results and Discussions

To illustrate the general behavior of the redistribution matrix we present the Stokes profiles resulting from a single 90° scattering event for an $L = 0 \rightarrow 1 \rightarrow 0$ scattering transition with $S = 1/2$. The J quantum numbers of the lower and upper levels are $J_a = J_f = 1/2$ and $J_b = 1/2, 3/2$, which give rise to a doublet. Well-known examples of such doublets are the Na I D₁ and D₂, Ca II H and K, and Mg II h and k lines. The Na I D₁ and D₂ lines, in particular, are in addition affected by the presence of hyperfine structure, which would have to be taken into account for modeling purposes, but which is not dealt with here. Instead, a pair of hypothetical lines is used for the theoretical studies in the present chapter. We study the influence of the field strength, the wavelength separation between the doublets, and the effect of a background continuum on the Stokes profiles. The magnetic field orientation is defined by angles ϑ_B and φ_B with respect to the polar z -axis (see Figure 2.2). For all the figures presented here, $\vartheta_B = 90^\circ$ and $\varphi_B = 45^\circ$. The incident radiation is assumed to be unpolarized ($[I_{\text{in}} = 1, 0, 0, 0]^T$) and spectrally flat (frequency independent). It is assumed to be incident in the vertical direction (parallel to the polar z -axis). Note that the PRD effects are contained in the redistribution matrix and manifest themselves irrespective of the spectral shape of the incident spectrum. The use of a flat spectrum is only a convenient choice. The singly scattered Stokes vectors are then determined exclusively by the first column of the redistribution matrix. As the elements of the redistribution matrix depend explicitly on λ

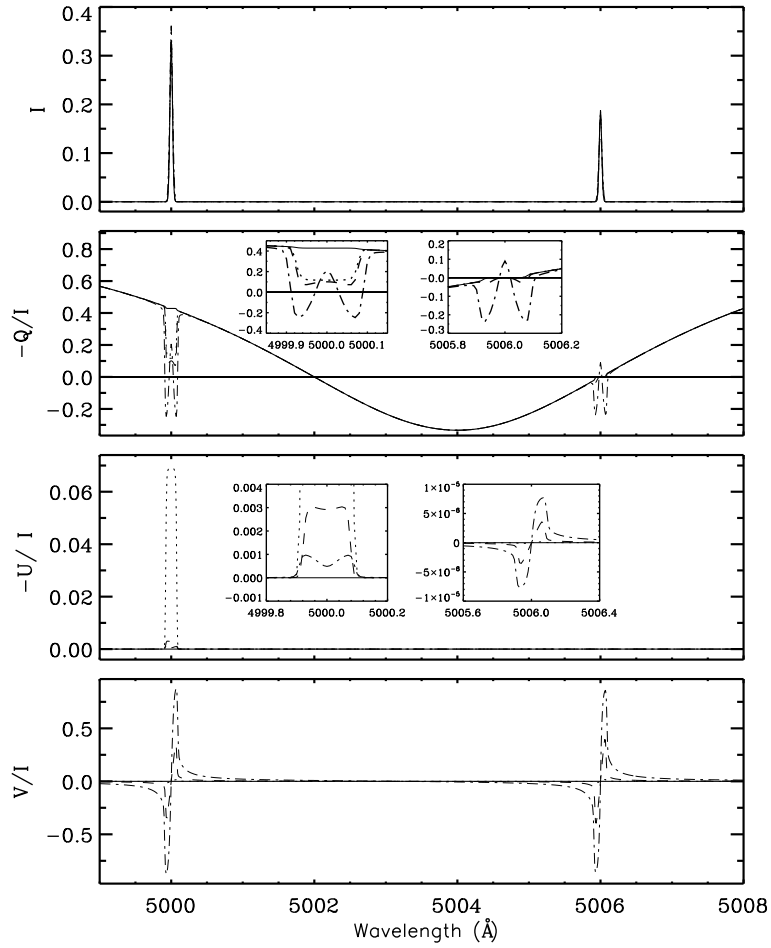


Figure 2.3: Profiles of the intensity I and the fractional polarizations Q/I , U/I , and V/I plotted for a hypothetical doublet at 5000 \AA and 5006 \AA with field strength parameter $v_H = 0$ for the solid line, $v_H = 0.004$ for the dotted line, $v_H = 0.1$ for the dashed line, and $v_H = 0.5$ for the dash-dotted line. The fine structure splitting is 6 \AA . Single 90° scattering is assumed at the extreme limb ($\mu = 0$). The model parameters are $a = 0.00143$, $\vartheta_B = 90^\circ$, and $\varphi_B = 45^\circ$. The Doppler width $\Delta\lambda_D = 0.025 \text{ \AA}$. These profiles characterize scattering exclusively in the line pair without any background continuum.

and λ' , an integration over λ' is necessary to obtain the scattered Stokes profiles at λ . The magnetic field strength is parametrized by the splitting parameter v_H given by

$$v_H = \frac{\lambda_0^2 e_0 B}{4\pi m c^2} \times \frac{1}{\Delta\lambda_D}, \quad (2.34)$$

where B is the field strength, e_0 is the charge of the electron and m is its mass. $\Delta\lambda_D$ is the Doppler width. The radiative widths of both the lines are represented by a single damping parameter a , which is assumed to be 0.00143 . The Doppler widths of both lines are 0.025 \AA . Figures 2.3, 2.4 and 2.5 show I , Q/I , U/I and V/I profiles for a range of field strengths and for three values of wavelength separations between the

doublets. The direction of the positive Stokes Q for the incident and scattered beams lie on the respective meridian planes shown in Figure 2.2. If λ_1 and λ_2 denote the line center wavelengths of the two lines, then $\delta\lambda = |\lambda_1 - \lambda_2|$ denotes the separation between them. We have chosen $\delta\lambda = 6 \text{ \AA}$, 1 \AA and 0.1 \AA , respectively, for Figures 2.3, 2.4 and 2.5. Different line types correspond to different values of v_H . Note the characteristic signature of J -state interference in Q/I , namely, a polarization profile with two sign reversals, one between the two lines, the other at the center of the $J = 1/2 \rightarrow 1/2 \rightarrow 1/2$ transition line. In the absence of a background continuum, Q/I in the far wings approaches unity on both sides of the lines (see the solid line in the top left panel of Figure 9.2 in Stenflo, 1994).

The wavelength dependence of J -state interference signature in the non-magnetic Q/I profile (based on the assumption of frequency coherent scattering in a doublet transition) is discussed in detail in Stenflo (1994). A wavelength-dependent depolarizability factor $W_2(\lambda)$ was introduced in that approach to conveniently describe the profile shape. In contrast, the present approach includes PRD in the doublet transition. The wavelength-dependent depolarizability of the line pair is implicitly built into the redistribution matrix. For the single scattering case presented in Figure 2.3, the Q/I profile computed with our PRD theory (solid line) gives results similar to the Q/I profile (solid line) in the top left panel in Figure 9.2 of Stenflo (1994).

In the weak field regime ($v_H = 0.004$), the shapes of the $(Q/I, U/I)$ profiles are governed by the Hanle effect (depolarization in Q/I with respect to the non-magnetic case, and creation of a non-zero U/I signature). When the fields are sufficiently strong (for example for $v_H = 0.1$), signatures of the transverse Zeeman effect show up in the cores of the two lines. In the core of the $J = 1/2 \rightarrow 1/2 \rightarrow 1/2$ transition line, the contribution from scattering polarization is zero (because $W_2 = 0$). As the field strength increases, one can clearly notice the characteristic Q/I profiles typical of the transverse Zeeman effect (see the dash-dotted lines in Figures 2.3, 2.4, and 2.5). The J -state interference (scattering) effects dominate the Q/I profiles outside the line cores.

As $\delta\lambda$ decreases, interesting signatures begin to show up in U/I more strongly (see the inset panels in Figures 2.3, 2.4, and 2.5). For the sake of discussion, let us consider the $\delta\lambda = 1 \text{ \AA}$ case. The signatures seen at the centers of both the lines at 5000 \AA and 5001 \AA for $v_H = 0.1$ and 0.5 appear to be entirely due to the J -state interference effects (because the contribution from the Zeeman effect to U is zero for the chosen geometry). However, the shapes of the U/I profiles are different from each other near the centers of the two lines. They can be understood in terms of the explicit expressions derived for the case of $L = 0 \rightarrow 1 \rightarrow 0$ scattering transition. For the particular geometry used for Figure 2.4, these expressions take the following simple form:

$$U(\lambda, \lambda') = \frac{3}{16\sqrt{2}}(f_{\frac{1}{2}\frac{3}{2}})^2 U_{\lambda_2} + \frac{3}{4\sqrt{2}}(f_{\frac{1}{2}\frac{1}{2}} f_{\frac{1}{2}\frac{3}{2}}) U_{\lambda_1 \lambda_2}, \quad (2.35)$$

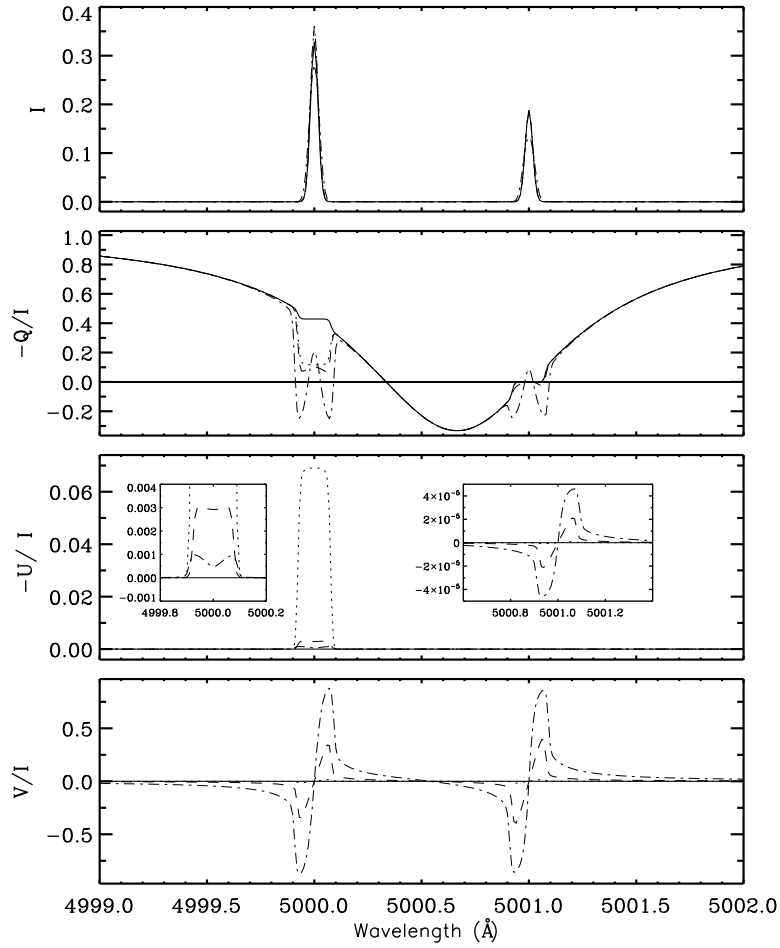


Figure 2.4: Same as Figure 2.3 except for the fine structure splitting, which is 1 \AA here. Note the shape of the U/I profiles (due to the increased magnitude of the J -state interference).

where $f_{\frac{1}{2}\frac{1}{2}}$ and $f_{\frac{1}{2}\frac{3}{2}}$ are the oscillator strengths for the absorption transitions $J = 1/2 \rightarrow 1/2$ and $J = 1/2 \rightarrow 3/2$, respectively. They are defined in Equation (8.51) of Stenflo (1994). We note that the $6 - j$ symbols appearing in Equation (2.2) can be written in terms of oscillator strengths (see Equations (9.48) and (9.74) of Stenflo, 1994). U_{λ_2} and $U_{\lambda_1\lambda_2}$ appearing in Equation (2.35) are given by

$$\begin{aligned}
 U_{\lambda_2} &= \left[\left\{ \cos^2 \beta_{\frac{3}{2}\frac{3}{2}\frac{3}{2}\frac{-1}{2}} \left(f_{\frac{3}{2}\frac{-1}{2}, \frac{3}{2}\frac{3}{2}}^{\text{II}} \right)_{\frac{1}{2}\frac{1}{2}} \right\} + \left\{ \cos \beta_{\frac{3}{2}\frac{3}{2}\frac{3}{2}\frac{-1}{2}} \sin \beta_{\frac{3}{2}\frac{3}{2}\frac{3}{2}\frac{-1}{2}} \left(h_{\frac{3}{2}\frac{-1}{2}, \frac{3}{2}\frac{3}{2}}^{\text{II}} \right)_{\frac{1}{2}\frac{1}{2}} \right\} \right] \\
 &+ \left[\left\{ \cos \beta_{\frac{3}{2}\frac{1}{2}\frac{3}{2}\frac{-3}{2}} \left(f_{\frac{3}{2}\frac{-3}{2}, \frac{3}{2}\frac{1}{2}}^{\text{II}} \right)_{\frac{-1}{2}\frac{-1}{2}} \right\} + \left\{ \cos \beta_{\frac{3}{2}\frac{1}{2}\frac{3}{2}\frac{-3}{2}} \sin \beta_{\frac{3}{2}\frac{1}{2}\frac{3}{2}\frac{-3}{2}} \left(h_{\frac{3}{2}\frac{-3}{2}, \frac{3}{2}\frac{1}{2}}^{\text{II}} \right)_{\frac{-1}{2}\frac{-1}{2}} \right\} \right], \quad (2.36) \\
 U_{\lambda_1\lambda_2} &= \cos \beta_{\frac{3}{2}\frac{1}{2}} \sin \beta_{\frac{3}{2}\frac{1}{2}} \left[\left(h_{\frac{1}{2}\frac{-1}{2}, \frac{3}{2}\frac{3}{2}}^{\text{II}} \right)_{\frac{1}{2}\frac{1}{2}} - \left(h_{\frac{1}{2}\frac{-3}{2}, \frac{1}{2}\frac{1}{2}}^{\text{II}} \right)_{\frac{-1}{2}\frac{-1}{2}} \right] \\
 &- \cos^2 \beta_{\frac{3}{2}\frac{1}{2}} \left[\left(f_{\frac{1}{2}\frac{-1}{2}, \frac{3}{2}\frac{3}{2}}^{\text{II}} \right)_{\frac{1}{2}\frac{1}{2}} + \left(f_{\frac{3}{2}\frac{-3}{2}, \frac{1}{2}\frac{1}{2}}^{\text{II}} \right)_{\frac{-1}{2}\frac{-1}{2}} \right]. \quad (2.37)
 \end{aligned}$$

Since $J_a = J_f = 1/2$ for the $L = 0 \rightarrow 1 \rightarrow 0$ scattering transition, we have omitted the

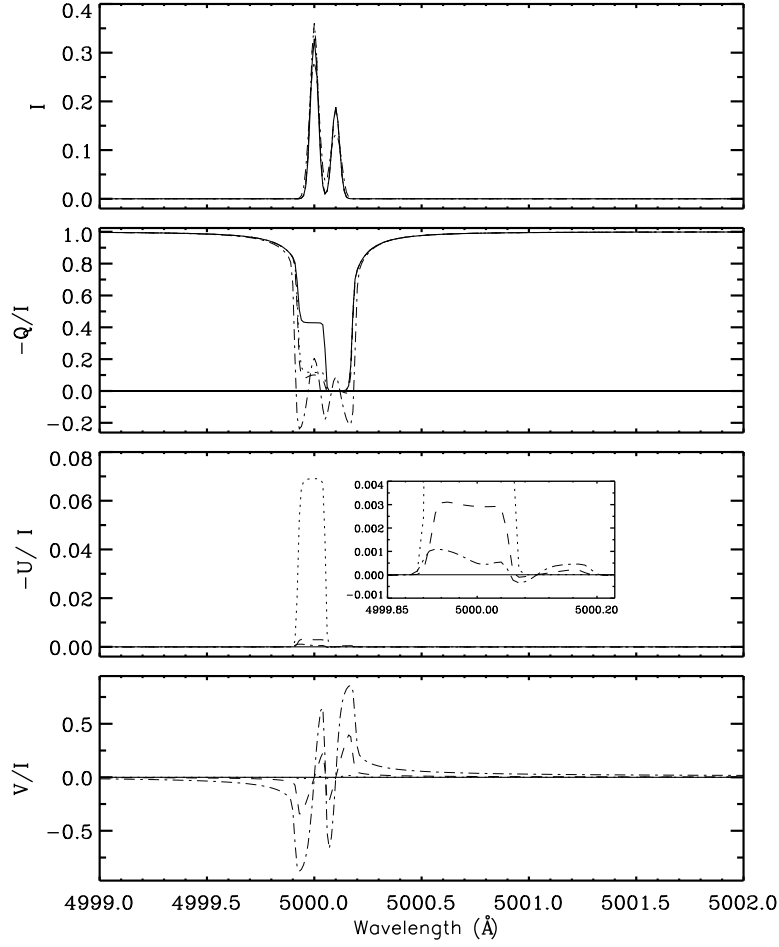


Figure 2.5: Same as Figure 2.3 except for the fine structure splitting, which is now 0.1 Å. The polarization profiles overlap substantially, greatly enhancing the impact of the J -state interference.

subscripts J_a and J_f on the h^{II} and f^{II} type functions appearing in the above equations. Stokes $U(\lambda)$ is obtained by integrating Equation (2.35) over λ' . In Equation (2.37) the dependence of β on μ_b and $\mu_{b'}$ is dropped, because it is insignificant when $J_b \neq J_{b'}$ (see the discussion below Equation (2.10)). Let us consider the behavior of U/I near $\lambda_1 = 5001$ Å line. Here the dominant contribution to $U(\lambda, \lambda')$ comes from $U_{\lambda_1 \lambda_2}$, the J -state interference term. For $\delta\lambda = 1$ Å, the angle $\beta_{\frac{3}{2} \frac{1}{2}}$ is 89.993° , so that $\sin\beta_{\frac{3}{2} \frac{1}{2}} \simeq 1$ and $\cos\beta_{\frac{3}{2} \frac{1}{2}}$ is of order 10^{-4} . Away from the line center the Faraday-Voigt functions decline more slowly than the Voigt functions. A few Doppler widths away from λ_1 the h^{II} functions are of order 10^{-5} , while the f^{II} functions are of order 10^{-1} . Hence the terms containing $\cos\beta_{\frac{3}{2} \frac{1}{2}} \sin\beta_{\frac{3}{2} \frac{1}{2}}$ and $\cos^2\beta_{\frac{3}{2} \frac{1}{2}}$ both contribute significantly to U . At the line center ($\lambda_1 = 5001$ Å) these two terms cancel each other to give $U(\lambda, \lambda') = 0$. The S shape of the U/I profile at λ_1 can be understood from the wavelength dependence of $U_{\lambda_1 \lambda_2}$.

Next let us consider the behavior of U/I near $\lambda_2 = 5000$ Å. In this case both U_{λ_2}

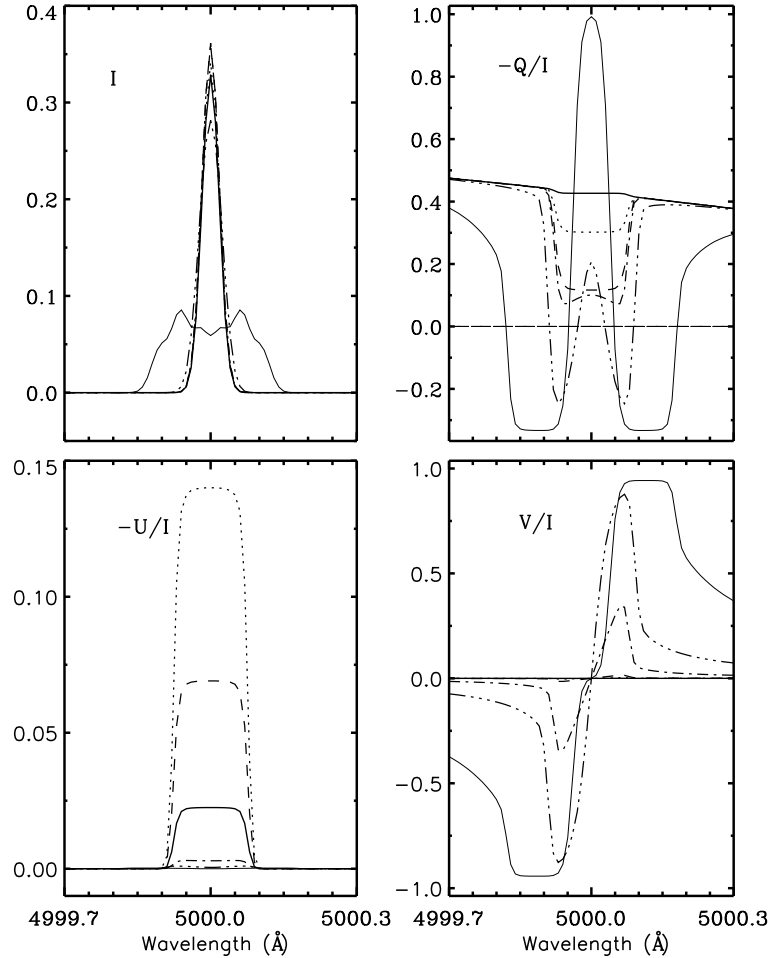


Figure 2.6: Profiles of the intensity I and the fractional polarizations Q/I , U/I , and V/I , plotted for a hypothetical line at 5000 \AA (of a line pair with the other line at 5006 \AA) with field strength parameter $v_H = 0.00008$ for the solid line, $v_H = 0.0008$ for the dotted line, $v_H = 0.004$ for the dashed line, $v_H = 0.1$ for the dash-dotted line, $v_H = 0.5$ for the dash-triple-dotted line, and $v_H = 2.5$ for the thin solid line. Single 90° scattering is assumed at the extreme limb. The other model parameters are the same as in Figure 2.3. As before these profiles characterize scattering exclusively in the line without any background continuum.

and $U_{\lambda_1\lambda_2}$ contribute significantly to $U(\lambda, \lambda')$. U_{λ_2} at $v_H = 0.5$ has a box-like shape similar to that for $v_H = 0.004$ (see the dotted line in Figure 2.4) but with a much smaller amplitude (due to Hanle saturation, see Figure 3 of Stenflo, 1998). As $U_{\lambda_1\lambda_2}$ is significant and contributes to an S-shaped U/I profile, the original box-shaped profile at $\lambda_2 = 5000 \text{ \AA}$ gets modified into a double peaked U/I profile, due to the superposition of both U_{λ_2} and $U_{\lambda_1\lambda_2}$ in Equation (2.35).

Note that for the line separation 0.1 \AA (see Figure 2.5), the near-wings of the two lines overlap. This results in Q/I and U/I profiles with more complex shapes. However, it is possible to understand the shapes of these profiles again from Equation (2.35). Note also that the J -state interference effects change the shape of the V/I profiles (asymmetric S-shaped profiles) for a closely spaced doublet (see Figure 2.5).

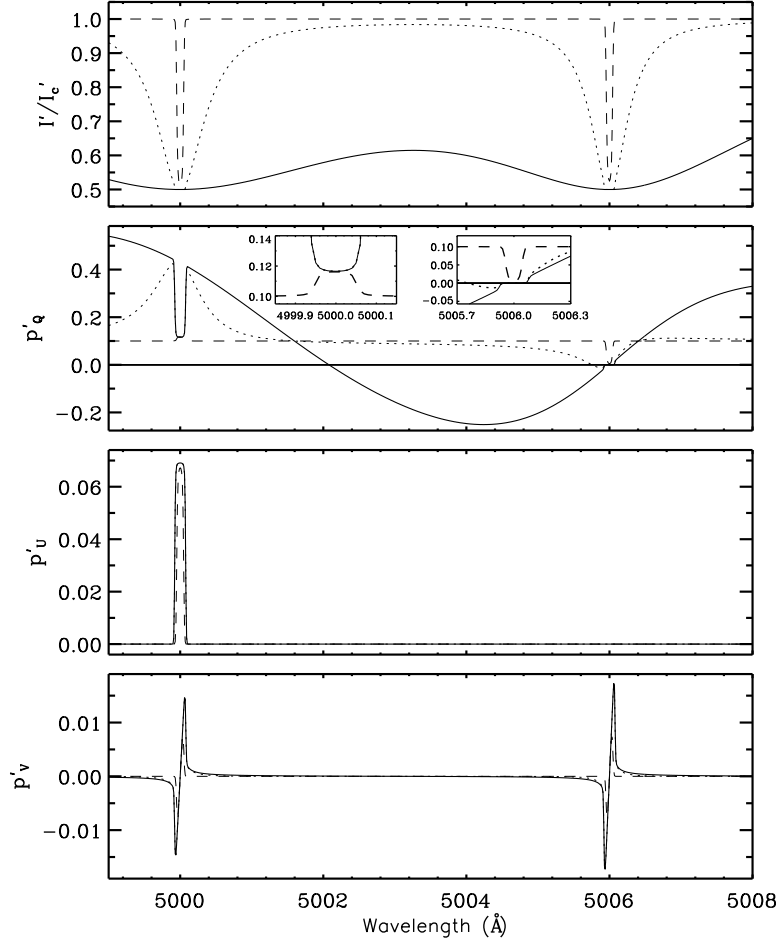


Figure 2.7: Profiles of the intensity I'/I'_c (see Equation (2.39)) and the fractional polarizations p'_Q, p'_U , and p'_V (see Equation (2.38)) plotted for the doublet at 5000 Å and 5006 Å in the presence of a background continuum. The field strength parameter used is $v_H = 0.004$. Different strengths of the background continuum are represented by $c = 1 \times 10^{-8}$ for the solid line, 1×10^{-6} for the dotted line, and 1×10^{-2} for the dashed line. The limb-darkening parameter $\beta = 0.5$, and $b = 0.1$ for Q , while $b = 0$ for U and V . The other model parameters are the same as in Figure 2.3.

Extensive theoretical work and modelling of the J -state interference in the well known D_1 and D_2 lines of Na I (including also the hyperfine structure and lower level polarization, but without PRD) have been carried out by [Trujillo Bueno et al. \(2002\)](#), and [Casini & Manso Sainz \(2005\)](#). Our emphasis in the present chapter is to study the J -state interference effects in a hypothetical doublet when PRD effects are accounted for. In Figure 2.6 we show the effect of the magnetic field on the Stokes profiles in the core of the 5000 Å line of the doublet for a wide range of field strengths. Here the doublet separation is chosen to be 6 Å. Therefore the J -state interference effect is extremely weak at the core of the line and shows up only in the wings (see the thick solid line in the Q/I panel). As the field strength increases from $v_H = 0.00008$ ($B \sim 0.1$ G) to $v_H = 2.5$ ($B \sim 4$ kG), the weak field Hanle scattering signatures make way for

the strong field Zeeman signatures. The values of the Hanle $\Gamma (= \omega_L/\gamma)$ parameter that correspond to the chosen set of v_H values are respectively 0.03, 0.28, 1.4, 7, 35, and 175. For $\Gamma \leq 7$ the shapes of the polarization profiles are typical of the Hanle effect. For $\Gamma > 7$ we have entered the Zeeman regime, and the shapes of the polarization profiles become typical of the Zeeman effect. A comparison of Figure 2.6 for the $J = 1/2 \rightarrow 3/2 \rightarrow 1/2$ transition with Figure 3 of Stenflo (1998) for the $J = 0 \rightarrow 1 \rightarrow 0$ transition shows that the field-strength dependence is similar. Note that the $(a, \Delta\lambda_D) = (0.00143, 0.025 \text{ \AA})$ chosen by us is different from the corresponding values $(a, \Delta\lambda_D) = (0.004, 0.03 \text{ \AA})$ chosen in Stenflo (1998). Due to our choice of relatively smaller $(a, \Delta\lambda_D)$ values we enter the Zeeman regime already for $v_H = 0.1$. In the real solar spectrum

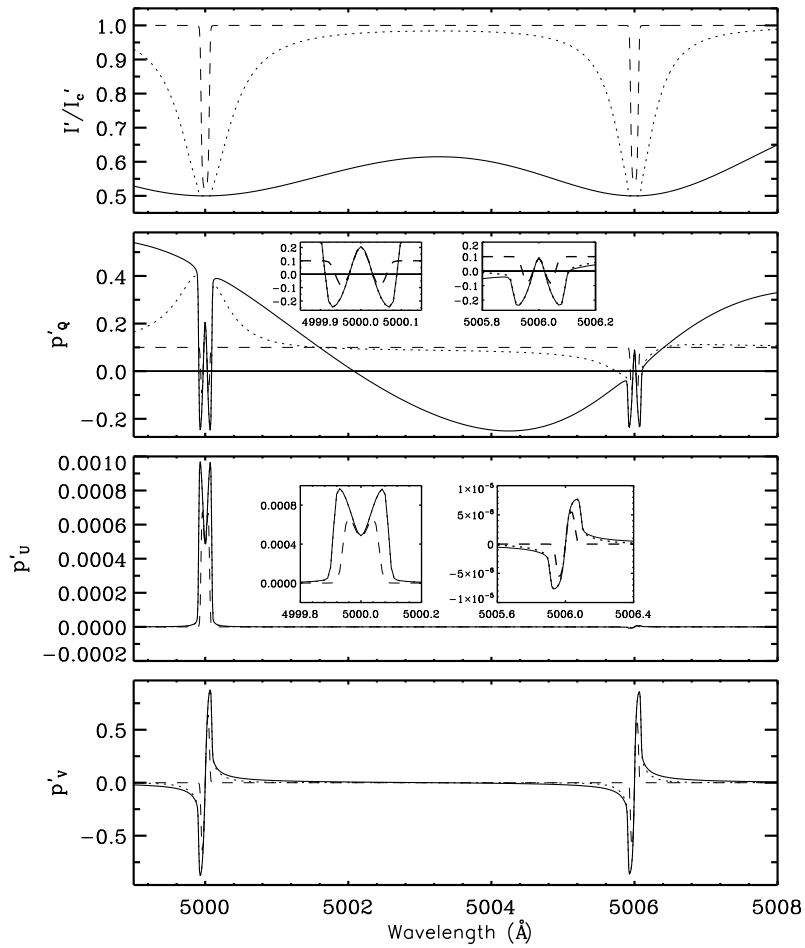


Figure 2.8: Same as Figure 2.7, but with $v_H = 0.5$, which represents a strong field regime ($B \sim 900 \text{ G}$). The Zeeman effect dominates in the line cores. J -state interference effects are responsible for the shapes of $(Q/I, U/I)$ in the line wings.

the line emission is superposed on a background continuum that is weakly polarized. The relative importance of the line emission scales as $I/(I + c)$, where I is the line scattering probability and c is a constant representing the background continuum (see Stenflo, 1998). The observed fractional polarization p' in the presence of a continuum

is given by

$$p' = \frac{I}{(I+c)} p + \frac{c}{(I+c)} b, \quad (2.38)$$

where p is the fractional polarization given by $-Q/I$, $-U/I$, and V/I . The continuum polarization is represented by b (see Equation (58) in [Stenflo, 1998](#)). In the presence of continuum, the Stokes I can be modeled by assuming LTE and using a Milne–Eddington model (see [Stenflo, 1998](#), for more details). With this assumption, one can show that (see Equation (61) of [Stenflo, 1998](#))

$$\frac{I'}{I'_c} = 1 - \beta + \frac{c}{(I+c)} \beta, \quad (2.39)$$

where β is the limb-darkening parameter (see Equation (61) of [Stenflo, 1998](#)), I' is the total intensity of scattered radiation, and I'_c is the intensity of the background continuum. Figures [2.7](#) and [2.8](#) show the Stokes profiles in the presence of a continuum for various values of c and for two values of v_H . Similar to [Stenflo \(1998\)](#) we choose the limb darkening parameter $\beta = 0.5$ and continuum polarization $b = 0.1$ for Q and $b = 0$ for U and V . As the contributions from the background continuum increase, Stokes I takes the shape of a deep absorption line. The linear polarization Q/I approaches the continuum polarization level in the far wings. As the continuum parameter c increases from 10^{-8} to 10^{-2} , the J -state interference effects nearly vanish in the line wings. While the wings are dominated by the continuum polarization, the line core polarization is dominated by the Hanle or Zeeman effects depending on the field strength, irrespective of the strength of the background continuum. This can be seen from the inset figure in the Q/I panels of Figures [2.7](#) and [2.8](#).

2.7 Conclusions

In this chapter, we have derived a PRD matrix that includes J -state interference in a two-term atomic framework. The present treatment is limited to the collisionless regime, and assumes that the Zeeman splitting is much smaller than the fine-structure splitting. With these restrictions we have derived laboratory frame expressions in the presence of magnetic fields of arbitrary strength and orientation (Hanle-Zeeman regime). A heuristic approach to derive the collisional redistribution matrix will be discussed in Chapter [4](#).

In the non-magnetic case we recover the collisionless PRD matrix derived by [Landi Degl'Innocenti et al. \(1997\)](#), who used a metalevel approach that can also treat J -state interference in the presence of a magnetic field. We also reproduce the results computed with the frequency coherent J -state interference theory of [Stenflo \(1994, 1997\)](#).

Examples of the Stokes profiles computed for the single scattering case are illustrated, with and without a background continuum. Due to the frequency coherent na-

ture of the R^{II} function in the wings, the $(Q/I, U/I)$ profiles are quite similar to the corresponding profiles computed with the pure coherent scattering theory of [Stenflo \(1994\)](#). However, when the PRD matrices are used in radiative transfer computations, we expect to find significant differences with respect to the pure coherent scattering case, especially for optically thick lines.

As the fine-structure splitting decreases, the J -state interference effects show up in the line wings as well as the line cores. The shapes of the Stokes profiles depend strongly on the separation of the doublet. Interesting signatures appear in the U/I profiles, particularly for strong fields.

Based on:

Smitha, H. N., Nagendra, K. N., Sampoorna, M., & Stenflo, J. O. 2011, A&A, 535, 35

3

Radiative transfer in a two-term atom in the absence of magnetic fields

An Overview

In the previous chapter, we demonstrated the fundamental role played by the J -state interference phenomenon in shaping the linearly polarized profiles resulting from scattering on a two-term atom. In this chapter (see also [Smitha et al., 2011a](#)), we solve the polarized radiative transfer equation for a two-term atom with an unpolarized lower term, including the effect of the interference between the upper J -states and partial frequency redistribution (PRD). We consider only the case of non-magnetic scattering. The magnetic scattering will be discussed in Chapter 4. The PRD matrix for the J -state interference derived in previous chapter is incorporated into the polarized transfer equation. The standard form of the two-level atom transfer equation is extended to a two-term atom. The transfer problem is then solved using a traditional polarized approximate lambda iteration method. We show how the PRD and the J -state interference together affect the shapes of the $(I, Q/I)$ profiles. We present the benchmark solutions for isothermal, constant-property slabs of a given optical thickness. We consider a hypothetical ${}^2S - {}^2P$ doublet produced by an $L = 0 \rightarrow 1 \rightarrow 0$ scattering transition with spin $S = 1/2$. We present the emergent $(I, Q/I)$ profiles for different values of (i) the line separation, (ii) optical thickness, (iii) thermalization parameter, and (iv) the continuum opacity.

3.1 Introduction

To analyze the shapes of the spectral lines in the Second Solar Spectrum the solution of the polarized line transfer equation is necessary. A quantum theory of upper J -state interference for frequency coherent scattering in the laboratory frame was formulated by [Stenflo \(1980, 1994, 1997\)](#). He introduced a wavelength-dependent polarizability factor $W_2(\lambda)$ to describe the phenomenon of quantum interference. [Stenflo \(1980\)](#) used this approach to model the observed scattering polarization signals in solar Ca II H and K lines. He applied the concept of the last scattering approximation for this purpose. The quantum interference theory of [Stenflo \(1980\)](#) was later included in the radiative transfer computations along with PRD in [Fluri et al. \(2003a\)](#), see also [Holzreuter et al. 2006](#)). A PRD matrix for the J -state interference in a two-term atom with unpolarized lower term and in the collisionless regime was derived in the atomic frame by [Landi Degl’Innocenti et al. \(1997\)](#) using a meta-level approach. [Smitha et al. \(2011b\)](#) have derived the same PRD matrix starting from the Kramers-Heisenberg scattering formula and these results are presented in Chapter 2. In that chapter the expression for the laboratory frame PRD matrix is given. In the present chapter (see also [Smitha et al., 2011a](#)) we incorporate the PRD matrix derived in Chapter 2 into the polarized line transfer equation. For this purpose we generalize the vector version of the standard two-level atom NLTE line transfer equation ([Mihalas, 1978](#); [Stenflo, 1994](#)) to the case of a two-term atom. We restrict our attention to the non-magnetic case. The solution of the polarized radiative transfer equation for a two-term atom, in the presence of a magnetic field will be discussed in Chapter 4.

It is necessary to distinguish between linear and non-linear NLTE radiative transfer problems for polarized radiation (e.g., [Trujillo Bueno, 2003](#)). An example of a linear radiative transfer problem is the standard problem of scattering polarization and the Hanle effect in a gas of two-level atoms assuming that the lower level is unpolarized (e.g., [Faurobert-Scholl, 1991](#); [Nagendra et al., 2002](#); [Sampoorna, 2011a](#), and the references cited therein). Examples of non-linear problems are the problems of scattering polarization and the Hanle effect in two-level or multilevel systems with atomic polarization in all levels ([Trujillo Bueno & Landi Degl’Innocenti, 1997](#); [Manso Sainz & Trujillo Bueno, 2003, 2010](#)). It is important to note that the two-term atom problem with an unpolarized lower term considered in this chapter is essentially similar to the two-level atom problem without lower-level polarization. In other words, it is a linear problem that does not involve the simultaneous solution of the statistical equilibrium and the Stokes-vector transfer equations. All couplings between different components of the multiplet enter the transfer problem only through the PRD matrix.

Novel iterative schemes have been developed by Trujillo Bueno and coworkers (see [Trujillo Bueno, 2003](#), and references therein to their previous works) to solve the com-

plete frequency redistribution (CRD) polarized NLTE transfer equation in multilevel atoms with the polarization of all levels taken into account. A recent review by [Trujillo Bueno \(2011\)](#) describes the modeling of scattering polarization and the Hanle effect in some spectral lines. Reviews by [Nagendra \(2003a,b\)](#); [Nagendra & Sampurna \(2009\)](#), and [Nagendra et al. \(2009\)](#) list several exact and approximate numerical methods of solving the polarized transfer equation for a two-level atom without lower level polarization. The polarized approximate lambda iteration (PALI) methods based on the Jacobi iterative scheme of [Olson et al. \(1986\)](#) have been developed to solve the two-level atom polarized transfer equation (see e.g. [Nagendra, 2003a](#)). In the present chapter we use one of the methods described in [Nagendra & Sampurna \(2009\)](#) generalized appropriately to the case of a two-term atom to solve the J -state interference problem.

In Section 3.2 we discuss the transfer equation for a two-term atom model. In Section 3.2.1 we describe the decomposition of the Stokes vector I and source vector S into the two cylindrically symmetric components to cast the Stokes vector transfer equation in a reduced form. The numerical method of the solution is presented in Section 3.3. The computed results are discussed in Section 3.4. In Section 3.5 we present the conclusions.

3.2 The polarized radiative transfer equation

The radiation field in a non-magnetic plane parallel atmosphere with axisymmetric boundary conditions is axisymmetric. This axially symmetric polarized radiation field can be described by the two Stokes parameters I and Q (see [Chandrasekhar, 1950](#)). The relevant line transfer equation for the problem of resonance scattering polarization may be written as

$$\frac{\partial}{\partial s} \begin{pmatrix} I \\ Q \end{pmatrix} = \begin{pmatrix} \epsilon_I \\ \epsilon_Q \end{pmatrix} \begin{pmatrix} \eta_I & \eta_Q \\ \eta_Q & \eta_I \end{pmatrix} \begin{pmatrix} I \\ Q \end{pmatrix}. \quad (3.1)$$

Equation (3.1) is a special case of the general polarized transfer equation given by Equation (8.2) of [Landi Degl'Innocenti & Landolfi \(2004\)](#), when the axial symmetry of the polarized radiation field is imposed. In Equation (3.1) ∂s denotes the incremental distance along the ray; $\epsilon_{I,Q}$ are the emission coefficients in the Stokes vector $(I, Q)^T$ basis; and $\eta_{I,Q}$ are the corresponding absorption coefficients. Under the assumption that the lower level of the transition is unpolarized, $\eta_Q = 0$. In this case the (2×2) absorption matrix becomes diagonal. For a line formed in the presence of a continuum

$$\eta_I = \eta_0 + k_c, \quad (3.2)$$

where η_0 is the line absorption coefficient, and k_c the continuum absorption coefficient. In the case of a standard two-level atom model, $\eta_0 = k_L \phi(x)$ where k_L is the frequency integrated line absorption coefficient, and $\phi(x)$ is the Voigt profile function for the reduced frequency x . The expression for η_0 in the particular case of a two-term atom can be derived starting from the general expressions for multi-term atom, given in [Landi Degl'Innocenti & Landolfi \(2004, see Equation \(7.47a\)\)](#). Alternatively, η_0 can also be derived by generalizing to the case of a two-term atom, the standard expression for intensity absorption coefficient of a two-level atom given in [Mihalas \(1978\)](#). Neglecting the induced emission term, it can be written as

$$\eta_0(J_a, J_b) = \frac{h\nu_{J_b J_a}}{4\pi} B(J_a \rightarrow J_b) N(J_a) \phi(\nu_{J_b J_a} - \nu), \quad (3.3)$$

where J_a and J_b are the total angular momentum quantum numbers of the lower and upper level respectively. $B(J_a \rightarrow J_b)$ is the Einstein's coefficient. $N(J_a)$ is the number density of atoms in the lower (J_a) level. $\nu_{J_b J_a}$ is the line center frequency for the transition $J_b \rightarrow J_a$. $\phi(\nu_{J_b J_a} - \nu)$ is the normalized Voigt profile function with line center frequency at $\nu_{J_b J_a}$. Equation (3.3) can be generalized to the case of two-term atom by summing over various components of the multiplet, namely

$$\eta_M = \sum_{J_a J_b} \eta_0(J_a, J_b). \quad (3.4)$$

A two-term atom is characterized by the orbital angular momentum L_a and L_b of the lower and upper terms respectively with spin S . Owing to $L - S$ coupling, a given (L, S) state splits into several J -states, with $|L - S| \leq J \leq |L + S|$. The coefficient $B(J_a \rightarrow J_b)$ is then related to $B(L_a \rightarrow L_b)$ through the expression

$$B(J_a \rightarrow J_b) = B(L_a \rightarrow L_b) (2L_a + 1)(2J_b + 1) \left\{ \begin{matrix} L_b & L_a & 1 \\ J_a & J_b & S \end{matrix} \right\}^2, \quad (3.5)$$

(see Equations (8.43) and (9.74) of [Stenflo, 1994](#)). The populations of the lower J -levels are related to the populations of the lower L -term through the relation

$$N(J_a) = (2J_a + 1) \frac{N(L_a)}{(2S + 1)(2L_a + 1)}, \quad (3.6)$$

where the assumption of unpolarized lower term is made. Using Equations (3.3), (3.5), and (3.6) in Equation (3.4), we obtain

$$\eta_M(\nu) = \frac{k_M}{(2S + 1)} \sum_{J_a J_b} (2J_a + 1)(2J_b + 1) \left\{ \begin{matrix} L_b & L_a & 1 \\ J_a & J_b & S \end{matrix} \right\}^2 \phi(\nu_{J_b J_a} - \nu), \quad (3.7)$$

where

$$k_M = \frac{h\nu_{J_a J_b}}{4\pi} N(L_a) B(L_a \rightarrow L_b), \quad (3.8)$$

is the frequency-integrated absorption co-efficient of the entire multiplet. In the case of an $L = 0 \rightarrow 1 \rightarrow 0$ scattering transition with $S = 1/2$

$$\eta_M(\nu) = k_M \left[\frac{2}{3} \phi(\nu_{\frac{3}{2}\frac{1}{2}} - \nu) + \frac{1}{3} \phi(\nu_{\frac{1}{2}\frac{1}{2}} - \nu) \right]. \quad (3.9)$$

An expression analogous to that of the two-level atom can be recovered by introducing a combined profile function that for ${}^2S \rightarrow {}^2P \rightarrow {}^2S$ doublet is given by

$$\phi(x) = \left[\frac{2}{3} \phi(\nu_{\frac{3}{2}\frac{1}{2}} - \nu) + \frac{1}{3} \phi(\nu_{\frac{1}{2}\frac{1}{2}} - \nu) \right]. \quad (3.10)$$

Notice that the combined profile function $\phi(x)$ is a weighted sum of Voigt profiles of the two lines of the doublet. For the more general case of a $L_a \rightarrow L_b \rightarrow L_a$ scattering transition with spin S , Equation (3.7) has to be used to obtain explicit expressions for the corresponding combined profile function. The combined profile function $\phi(x)$ can also be derived using the theoretical framework of [Stenflo \(1997, see his Section 3.1\)](#). It is also implicitly contained in the general definition for the intensity absorption coefficient for a multi-term atom given in [Landi Degl'Innocenti & Landolfi \(2004\)](#).

Defining the optical depth scale as $d\tau = -k_M dz$, we can rewrite Equation (3.1) as

$$\mu \frac{\partial \mathbf{I}(\tau, x, \mu)}{\partial \tau} = (\phi(x) + r) [\mathbf{I}(\tau, x, \mu) - \mathbf{S}(\tau, x, \mu)], \quad (3.11)$$

where $\mu = \cos \theta$ with θ being the colatitude with respect to the atmospheric normal. $\mathbf{I} = (I, Q)^T$ is the Stokes vector. $\mathbf{S} = (S_I, S_Q)^T$ is the total source vector given by

$$S_{I,Q} = \frac{\epsilon_{I,Q}}{\eta_I}. \quad (3.12)$$

x is the scattered frequency in Doppler width units. r is the ratio of continuum to the frequency-integrated line absorption co-efficient. The positive Stokes Q represents electric vector vibrations perpendicular to the solar limb. The total source vector \mathbf{S} is given by

$$\mathbf{S}(\tau, x, \mu) = \frac{\phi(x) \mathbf{S}_l(\tau, x, \mu) + r \mathbf{S}_c}{\phi(x) + r}, \quad (3.13)$$

where the unpolarized continuum source vector $\mathbf{S}_c = BU$, with B being the Planck function and $\mathbf{U} = (1, 0)^T$. The line source vector for a two-term atom has the form

$$S_l(\tau, x, \mu) = \epsilon BU + \frac{1}{\phi(x)} \int_{-\infty}^{+\infty} dx' \int_{-1}^1 \frac{d\mu'}{2} \mathbf{R}(x, \mu, x', \mu') \mathbf{I}(\tau, x', \mu'), \quad (3.14)$$

where x' is the incoming frequency in Doppler width units and $\epsilon = \Gamma_I/(\Gamma_I + \Gamma_R)$ is the photon destruction probability per scattering with Γ_I and Γ_R being the inelastic and radiative de-excitation rates of the upper term L_b . We assume that Γ_I and Γ_R are the same for all fine structure levels of the upper term. The non-magnetic two-term atom redistribution matrix is given by Equation (2.22).

Note that the redistribution matrix derived in Chapter 2 depends on incoming and outgoing ray directions $\mathbf{n}'(\theta', \varphi')$ and $\mathbf{n}(\theta, \varphi)$ which are defined with respect to the atmospheric normal. The angular dependence appears not only in the phase matrix part of the redistribution matrix, but also in the redistribution functions. To simplify the problem, following Rees & Saliba (1982), we here replace the angle-dependent redistribution functions by their angle-averaged analogues. The angle-averaged functions can be computed from the angle-dependent functions by integrating over the scattering angle between the incident and scattered ray (cf. Bomnier, 1997b).

Owing to the azimuthal symmetry of the problem, one can then integrate the phase matrix part of the redistribution matrix over the azimuths φ' of the incoming radiation to obtain $\mathbf{R}(x, \mu, x', \mu')$, which is given by

$$\mathbf{R}_{ij}(x, \mu; x', \mu') = \sum_K \mathcal{R}^K(x, x') \tilde{\mathcal{T}}_0^K(i, \mu) \tilde{\mathcal{T}}_0^K(j, \mu'), \quad (3.15)$$

where $i, j = 0, 1$ and $\tilde{\mathcal{T}}_0^K(i, \mu)$ are given by Equation (28) of Frisch (2007) with $K = 0, 2$. $\tilde{\mathcal{T}}_Q^K(i, \mu)$ are related to the irreducible spherical tensors for polarimetry $\mathcal{T}_Q^K(i, \mathbf{n})$ introduced by Landi Degl'Innocenti (1984), through

$$\mathcal{T}_Q^K(i, \mathbf{n}) = \tilde{\mathcal{T}}_Q^K(i, \mu) e^{iQ\varphi}, \quad (3.16)$$

with Q taking values $-K \leq Q \leq +K$.

The redistribution function components $\mathcal{R}^K(x, x')$ are given by

$$\begin{aligned} \mathcal{R}^K(x, x') &= \frac{3(2L_b + 1)}{2S + 1} \sum_{J_a J_f J_b J_{b'}} (-1)^{J_f - J_a} (2J_a + 1)(2J_f + 1)(2J_b + 1) \\ &\times (2J_{b'} + 1) \cos \beta_{J_{b'}, J_b} [\cos \beta_{J_{b'}, J_b} (h_{J_b, J_{b'}}^{\text{II}})_{J_a J_f} - \sin \beta_{J_{b'}, J_b} (f_{J_b, J_{b'}}^{\text{II}})_{J_a J_f}] \\ &\times \begin{Bmatrix} L_a & L_b & 1 \\ J_b & J_f & S \end{Bmatrix} \begin{Bmatrix} L_a & L_b & 1 \\ J_b & J_a & S \end{Bmatrix} \begin{Bmatrix} L_a & L_b & 1 \\ J_{b'} & J_f & S \end{Bmatrix} \begin{Bmatrix} L_a & L_b & 1 \\ J_{b'} & J_a & S \end{Bmatrix} \\ &\times \begin{Bmatrix} 1 & 1 & K \\ J_{b'} & J_b & J_a \end{Bmatrix} \begin{Bmatrix} 1 & 1 & K \\ J_{b'} & J_b & J_f \end{Bmatrix}, \end{aligned} \quad (3.17)$$

where $L_{a,b}$ are the orbital angular momentum quantum numbers of the lower and upper terms respectively and S is the spin. $J_{a,f}$ are the total angular momentum quantum numbers of the fine structure levels of the lower term and $J_{b,b'}$ are the total angular mo-

mentum quantum numbers of the fine structure levels of the upper term. The auxiliary functions $(h_{J_b, J_{b'}}^{\text{II}})_{J_a J_f}$ and $(f_{J_b, J_{b'}}^{\text{II}})_{J_a J_f}$ are defined in Equations (2.14) and (2.15) but are used here for the non-magnetic case and with angle-averaged redistribution functions of type-II. The angle $\beta_{J_{b'}, J_b}$ is defined in Equation (2.10).

3.2.1 Stokes vectors decomposition

In general the source vector \mathcal{S} and the Stokes vector \mathcal{I} depend on the colatitude θ of the radiation field. Computationally it is advantageous to work in a reduced basis, where the source vector components do not depend on θ (see for e.g. Faurobert-Scholl et al., 1997). Transformation of the Stokes vectors to such a reduced basis is referred to as the “decomposition” of the Stokes vectors. Using $\mathcal{T}_Q^K(i, \mathbf{n})$, Frisch (2007) has presented an elegant decomposition technique for the case of the Hanle effect. It is straightforward to apply this decomposition technique to the problem at hand. Here we briefly present a few important equations of this decomposition.

Let us denote $I_i = (I, Q)$ with $i = 0, 1$ as the components of the Stokes vector. For the cylindrically symmetric case, the components I_i of the Stokes vector can be decomposed in terms of two irreducible components \mathcal{I}_Q^K as follows

$$I_i(\tau, x, \mu) = \sum_{K=0,2} \tilde{\mathcal{T}}_0^K(i, \mu) \mathcal{I}_0^K(\tau, x, \mu). \quad (3.18)$$

Similarly, the source vector \mathcal{S} can be decomposed in terms of two cylindrically symmetric components \mathcal{S}_0^K , which become independent of even μ . $\tilde{\mathcal{T}}_0^K(i, \mu)$ are real for $K = 0, 2$ and $i = 0, 1$, and thus \mathcal{I}_0^K and \mathcal{S}_0^K are also real. The spherical irreducible tensors satisfy the conjugation relation

$$[\mathcal{T}_Q^K(i, \mathbf{n})]^* = (-1)^Q \mathcal{T}_{-Q}^K(i, \mathbf{n}). \quad (3.19)$$

Since \mathcal{I} is real, \mathcal{I}_Q^K also satisfies the above conjugation relation.

For the non-magnetic case, we define the two-component vectors $\mathcal{I} = \{\mathcal{I}_0^0, \mathcal{I}_0^2\}^T$ and $\mathcal{S} = \{\mathcal{S}_0^0, \mathcal{S}_0^2\}^T$. From Equation (3.19), both \mathcal{T}_Q^K and \mathcal{I}_Q^K are real for $Q = 0$. After such a decomposition \mathcal{S} becomes independent of the ray direction and \mathcal{I} becomes independent of the azimuthal angle φ . The transfer equation for \mathcal{I} can now be written as

$$\mu \frac{\partial \mathcal{I}(\tau, x, \mu)}{\partial \tau} = (\phi(x) + r) [\mathcal{I}(\tau, x, \mu) - \mathcal{S}(\tau, x)]. \quad (3.20)$$

The irreducible total source vector takes the form

$$\mathcal{S}(\tau, x) = \frac{\phi(x) \mathcal{S}_l(\tau, x) + r \mathcal{G}(\tau)}{\phi(x) + r}, \quad (3.21)$$

where $\mathcal{G}(\tau) = \{B, 0\}^T$ is the primary source vector. The irreducible line source vector is given by

$$\mathcal{S}_l(\tau, x) = \epsilon \mathcal{G}(\tau) + \int_{-\infty}^{+\infty} \frac{\tilde{\mathcal{R}}(x, x')}{\phi(x)} \mathcal{J}(\tau, x') dx'. \quad (3.22)$$

Here $\tilde{\mathcal{R}}(x, x')$ is a (2×2) diagonal matrix with elements $\tilde{\mathcal{R}} = \text{diag}(\mathcal{R}^0, \mathcal{R}^2)$, where \mathcal{R}^K are defined in Equation (3.17).

The mean intensity $\mathcal{J}(\tau, x)$ for the non-magnetic case is a two-component vector defined by

$$\mathcal{J}(\tau, x) = \frac{1}{2} \int_{-1}^{+1} \Psi(\mu') \mathcal{I}(\tau, x, \mu') d\mu'. \quad (3.23)$$

The elements of the (2×2) matrix $\Psi(\mu)$ are given in [Landi Degl'Innocenti & Landolfi \(2004\)](#) (see also Appendix A of [Frisch, 2007](#)). In the following sections, for notational brevity we specify the functional dependence of physical quantities as subscripts.

3.3 Solving the transfer equation

We solve the polarized line radiative transfer equation for non-magnetic (Rayleigh) scattering on a two-term atom including the effects of J -state interference given in Equation (3.20). We use the PALI method developed in [Nagendra & Sampurna \(2009\)](#) appropriately extended to handle the present problem. In the following subsections we briefly describe this iterative technique.

3.3.1 The iteration scheme

The formal solution of the transfer equation may be stated in terms of the full lambda operator as

$$\mathcal{J}_x = \Lambda_x[\mathcal{S}_x], \quad (3.24)$$

where Λ_x operates on the quantity within []. By defining a local monochromatic approximate Lambda operator Λ_x^* as

$$\Lambda_x = \Lambda_x^* + \delta\Lambda_x = \Lambda_x^* + (\Lambda_x - \Lambda_x^*), \quad (3.25)$$

we can set up an iterative scheme to compute the source vectors, namely

$$\mathcal{S}_x^{(n+1)} = \mathcal{S}_x^{(n)} + \delta\mathcal{S}_x^{(n)}, \quad (3.26)$$

$$\mathcal{S}_{l,x}^{(n+1)} = \mathcal{S}_{l,x}^{(n)} + \delta\mathcal{S}_{l,x}^{(n)}, \quad (3.27)$$

where the superscript (n) refers to the n^{th} iteration step. From Equations (3.25) and (3.26) it follows, by keeping only terms up to the first order, that

$$\mathcal{J}_x^{(n+1)} \approx \mathcal{J}_x^{(n)} + \Lambda_x^*[\delta\mathcal{S}_x^{(n)}]. \quad (3.28)$$

Inserting Equations (3.22) and (3.28) into Equation (3.27), we obtain a set of linear equations for the corrections to the line source vector $\delta\mathcal{S}_{l,x}^{(n)}$:

$$\delta\mathcal{S}_{l,x}^{(n)} - \int_{-\infty}^{+\infty} \frac{\tilde{\mathcal{R}}_{x,x'}}{\phi_x} p_{x'} \Lambda_{x'}^*[\delta\mathcal{S}_{l,x'}^{(n)}] dx' = \mathbf{r}_x^{(n)}. \quad (3.29)$$

In deriving the above equation we have used the relation

$$\Lambda_x^*[\delta\mathcal{S}_x^{(n)}] = p_x \Lambda_x^*[\delta\mathcal{S}_{l,x}^{(n)}], \quad (3.30)$$

where $p_x = \phi_x/(\phi_x + r)$ is a scalar quantity defining the fractional line absorption and Λ_x^* is a linear operator. The frequency dependent residual vector is given by

$$\mathbf{r}_x^{(n)} = \mathcal{S}_{\text{FS},l,x}^{(n)} - \mathcal{S}_{l,x}^{(n)}. \quad (3.31)$$

The formal line source vector is obtained from

$$\mathcal{S}_{\text{FS},l,x}^{(n)} = \epsilon\mathcal{G}(\tau) + \int_{-\infty}^{+\infty} \frac{\tilde{\mathcal{R}}_{x,x'}}{\phi(x)} \mathcal{J}_{x'}^{(n)} dx', \quad (3.32)$$

where the mean intensity $\mathcal{J}_x^{(n)} = \Lambda_x[\mathcal{S}_x^{(n)}]$ is computed using a short characteristic formal solver.

3.3.2 Source vector corrections

The important step of the iterative method is the calculation of the source vector corrections $\delta\mathcal{S}_{l,x}^{(n)}$. Here we use the frequency by frequency (FBF) method of [Paletou & Auer \(1995\)](#) to compute these corrections, suitably generalized to the vector case (see also [Sampoorna et al., 2008a](#)). The system of linear equations (Equation (3.29)) can be organized in the matrix form as

$$\mathbf{A}\delta\mathcal{S}_l = \mathbf{r}, \quad (3.33)$$

where the vector \mathbf{r} is the right-hand side of Equation (3.29). At each depth point, for the non-magnetic case, \mathbf{A} is a $2N_x \times 2N_x$ matrix with N_x the number of frequency points, and \mathbf{r} has a length $2N_x$. Each element of \mathbf{A} corresponding to a given value of x and x'

is a 2×2 block denoted by \mathbf{A}^2 , which is given by

$$\mathbf{A}_{ij}^2 = \delta_{i,j} \mathbf{E} - \frac{\tilde{\mathcal{R}}_{i,j}}{\phi_i} p_j \Lambda_j^*; \quad i, j = 1, 2, 3, \dots, N_x. \quad (3.34)$$

Here \mathbf{E} is the 2×2 identity matrix. $\delta_{i,j}$ is the Kronecker's delta. The indices (i, j) refer to discretized values of (x, x') , respectively. The matrix \mathbf{A} is computed only once because it does not change during the iteration.

We note that the polarized radiative transfer equation and its method of solution presented in Sections 3.2 and 3.3 are valid for any scattering transition of the type $L_a \rightarrow L_b \rightarrow L_a$ in a two-term atom. In Section 3.4 we present the results only for an $L = 0 \rightarrow 1 \rightarrow 0$ scattering transition with $S = 1/2$, which corresponds to a doublet. The absorption profile function $\phi(x)$ for this doublet is given in Equation (3.10).

3.4 Results and discussions

In this section we present the emergent Stokes profiles obtained by solving the polarized line radiative transfer equation for a hypothetical doublet at 5000 \AA and 5001 \AA . They arise from an $L = 0 \rightarrow 1 \rightarrow 0$ scattering transition with spin $S = 1/2$ and include the effects of J -state interference. We consider isothermal constant property slabs with a given optical thickness T to perform the tests. T is varied from optically thin ($T \ll 1$) to optically thick ($T \gg 1$) slabs. The slabs are assumed to be self-emitting unless stated otherwise. The slabs are illuminated at the lower boundary when they are assumed as pure scattering media ($\epsilon = 0$). The atmospheric model parameters used for the computations are represented by (T, a, ϵ, r) , where a is the damping parameter. The Planck function B is taken as unity. The Doppler width for both lines are assumed to be the same and equal to 0.025 \AA . The grid resolution in the physical variables is given by the values of (N_d, N_x, N_μ) . The quantity N_d represents the number of depth points per decade in a logarithmically spaced τ -grid. Unless stated otherwise, the first depth point $\tau_{min} = 10^{-2}$ and $N_d = 5$. The frequency grid points are very closely and equally spaced near the cores of the two lines as well as in between the two lines, and sparsely but equally spaced in the wings of the two lines. The total number of frequency points $N_x = 308$. We use a Gauss-Legendre quadrature for colatitude θ (μ) with $N_\mu=5$ points.

3.4.1 Optically thin slab case

To mimic a single scattering event from a radiative line transfer problem with PRD, we consider an optically thin slab illuminated at the lower boundary by an unidirectional unpolarized beam of radiation, namely, $\mathcal{I}(\tau = T, x', \mu' = 0.995) = \mathbf{U}$. The other parameters used are $(T = 2 \times 10^{-2}, a = 10^{-3}, \epsilon = 0, r = 0)$. The first depth point

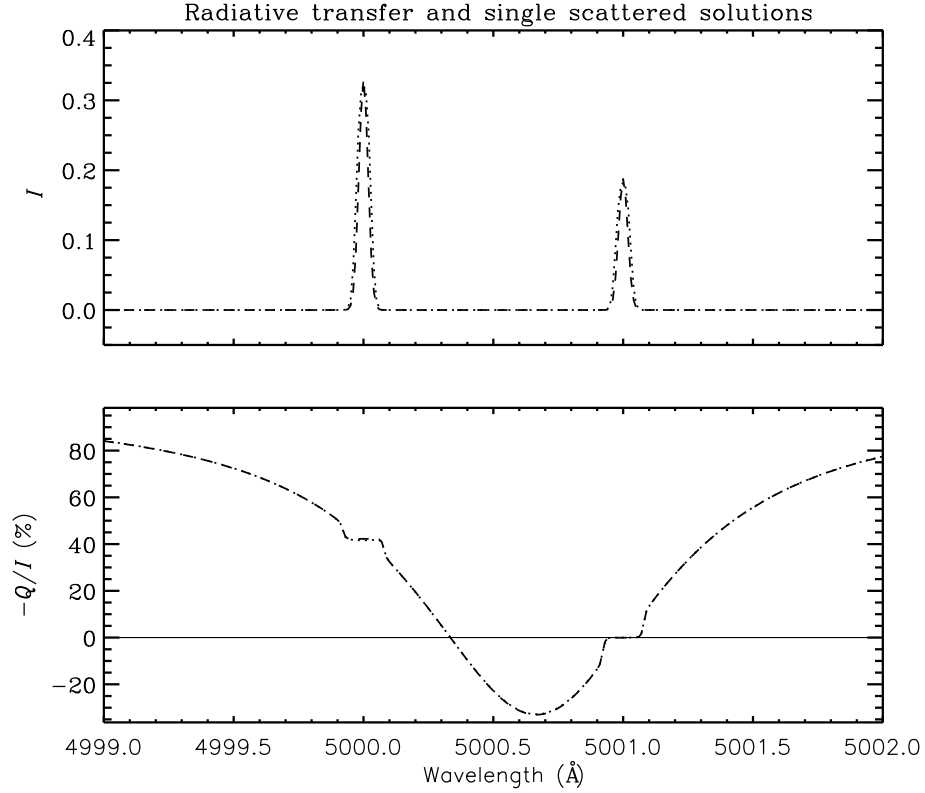


Figure 3.1: Emergent Stokes profiles formed in an optically thin medium shown as a function of wavelength for nearly tangential emergence $\mu = 0.47 \times 10^{-2}$ (dotted line). The model parameters are $T = 2 \times 10^{-2}$, $a = 10^{-3}$, $\epsilon = 0$, and $r = 0$. A nearly vertical beam of radiation incident at $\mu' = 0.995$ is used as the lower boundary condition. In this case, the intensity is scaled up by a factor of 102 for comparison with the single scattered solution. The dashed line shows the emergent Stokes profiles computed for the single scattering case with the same value of scattering angle.

is $\tau_{min} = 10^{-4}$ and $N_\mu = 17$. The optical thickness is chosen to be very small so that the emergent diffuse radiation field is dominated by single scattered photons. The choice of parameters $\epsilon = 0$ and $r = 0$ represents a purely scattering medium without any continuum absorption. In Figure 3.1 we compare emergent profiles computed from the line transfer problem that mimics a nearly 84° single scattering event (dotted line) with the profiles computed for the exact 84° single scattering case (dashed line). The intensity computed from the transfer code has been scaled up by a factor of 102 (dotted line), to match with intensity obtained from the single scattering case. The scaling factor depends on the optical thickness of the slab. For a slab of thickness $T = 2 \times 10^{-4}$ the scaling factor would be 10^4 . This is because, in the transfer problem we have taken 17 colatitudes (N_μ), and the intensity gets distributed among these 17 angles. The profiles are however plotted for one single value of μ . In order to compare the results computed from the transfer code with those from the actual single scattering case, such a scaling of the emergent intensity is necessary.

From Figure 3.1 we see that the shape of the profiles computed with the transfer

code are very similar to the profiles for the single scattering case. They are similar to the single scattered Q/I profiles of [Stenflo \(1980, see also Figure 10.17 of Landi Degl’Innocenti & Landolfi 2004\)](#). This verifies that the \mathbf{R} matrix has been correctly incorporated into the line transfer code. We plot $-Q/I$ only in [Figure 3.1](#) to facilitate a quick comparison with the corresponding single scattered profiles presented in [Stenflo \(1980, see also Chapter 2\)](#)

3.4.2 Stokes profiles with and without J -state interference

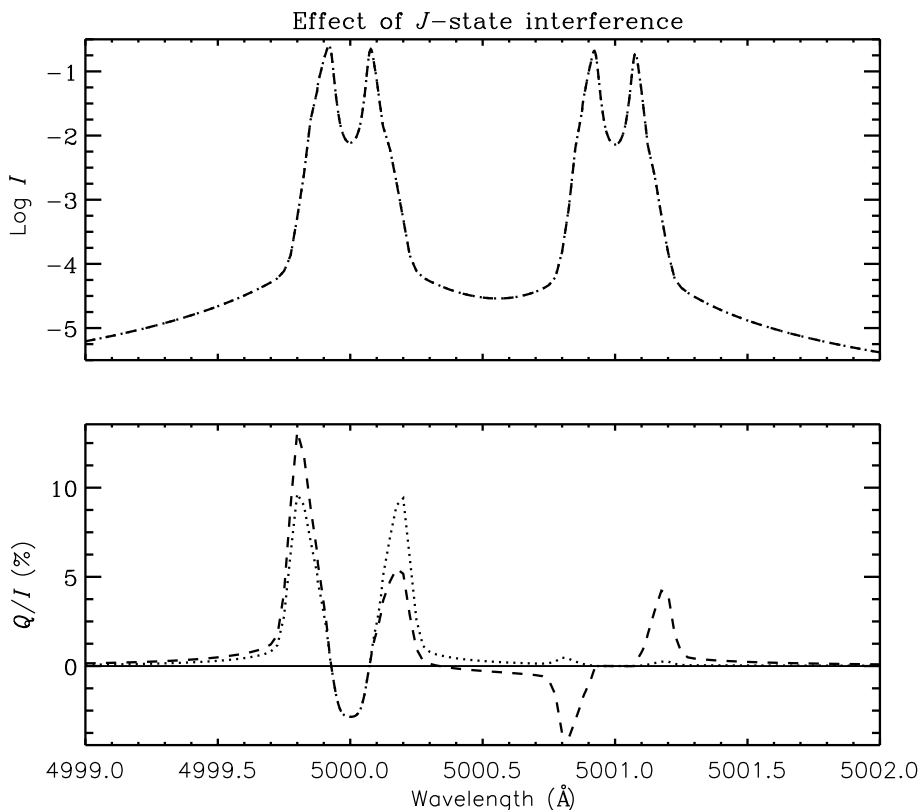


Figure 3.2: Emergent Stokes profiles computed without J -state interference (dotted line) and with J -state interference (dashed line) at $\mu = 0.047$ for an optical thickness $T = 2 \times 10^4$. The other model parameters are $(a, \epsilon, r) = (10^{-3}, 10^{-4}, 0)$.

Figure 3.2 shows a comparison between the Stokes profiles computed with and without the effects of J -state interference. The effects of J -state interference in a doublet (or even a multiplet) system can be neglected by simply setting $J_b = J_{b'}$ in the RHS of Equation (3.17), so that there is only one summation over J_b . These profiles are plotted for an atmosphere with $T = 2 \times 10^4$, $a = 10^{-3}$, $\epsilon = 10^{-4}$, and $r = 0$. It is well known from the single line two-level atom transfer computations that owing to the effects of PRD, two symmetric wing peaks appear in the Q/I profiles on either side of the line center. These peaks are referred to as the PRD peaks. For a doublet without the effect of J -state interference, or in other words, two non-interacting lines, these sym-

metric PRD peaks are visible around the lines at 5000 Å and 5001 Å (see dotted line in Figure 3.2). Q/I at the 5001 Å line (arising from the $1/2 \rightarrow 1/2 \rightarrow 1/2$ scattering transition) is zero because the polarizability factor W_2 is zero for this line. If one includes J -state interference effects between the two lines, the near wing PRD peaks around the 5000 Å line become asymmetric (see the dashed line). The amplitude of the PRD peak at 4999.8 Å is increased, whereas the amplitude of the PRD peak at 5000.2 Å is decreased. Moreover, the symmetric PRD peaks around 5001 Å are converted into anti-symmetric peaks by the J -state interference effects. The amplitudes of these peaks are also enhanced. Comparing the dotted line with the dashed line, it is evident that these effects are caused by J -state interference.

The prominent signature of the J -state interference is the sign reversal in Q/I in the region of interference between the two lines. This is clearly visible in the dashed line, which includes this effect, but not in the dotted line which represents the case of the non-interacting lines.

Though there are striking differences between the Q/I for the two cases - with and without J -state interference, the intensity I is unaffected by this phenomenon.

3.4.3 Effects of optical thickness T

In Figure 3.3 we present the Stokes profiles for slabs with different values of optical thickness T . For all examples, $T \geq 2 \times 10^2$ with the thermalization parameter $\epsilon = 10^{-4}$. The chosen values of T represent a wide variety of the scattering media ranging from those that are effectively thin ($\epsilon T = 2 \times 10^{-2}$, for $T = 2 \times 10^2$) to those that are effectively thick ($\epsilon T = 2 \times 10^4$, for $T = 2 \times 10^8$). The other model parameters are ($a = 10^{-3}$, $r = 0$).

The variation of I and Q/I with T in the case of a doublet is similar to that of a single-line case. This can be seen from the inset panels in I and Q/I in Figure 3.3 and in turn comparing them with the left panel in Figure 10 (dashed lines) of Sampoorna (2011a). In the inset panels I and Q/I are plotted as a function of the non-dimensional frequency (x), which is measured from the center of the line at 5000 Å. As the optical thickness increases, the magnitudes of Q/I at the PRD peaks initially increase and then decrease. This decrease is caused by the influence of multiple scattering. The thicker the atmosphere, the more isotropic is the radiation field because of multiple scattering. Accordingly, the polarization is reduced (see Rees, 1978).

Furthermore, as T increases, the PRD peaks shift away from the line centers of the two lines. For $T = 2 \times 10^6$ and $T = 2 \times 10^8$, the PRD peaks occur far away from the centers of the two lines. For instance, at the wing frequencies between the two lines, the interference effects dominate over PRD-effects, resulting in suppression of the PRD peaks. Hence, there are no PRD peaks visible in between the two lines for these two

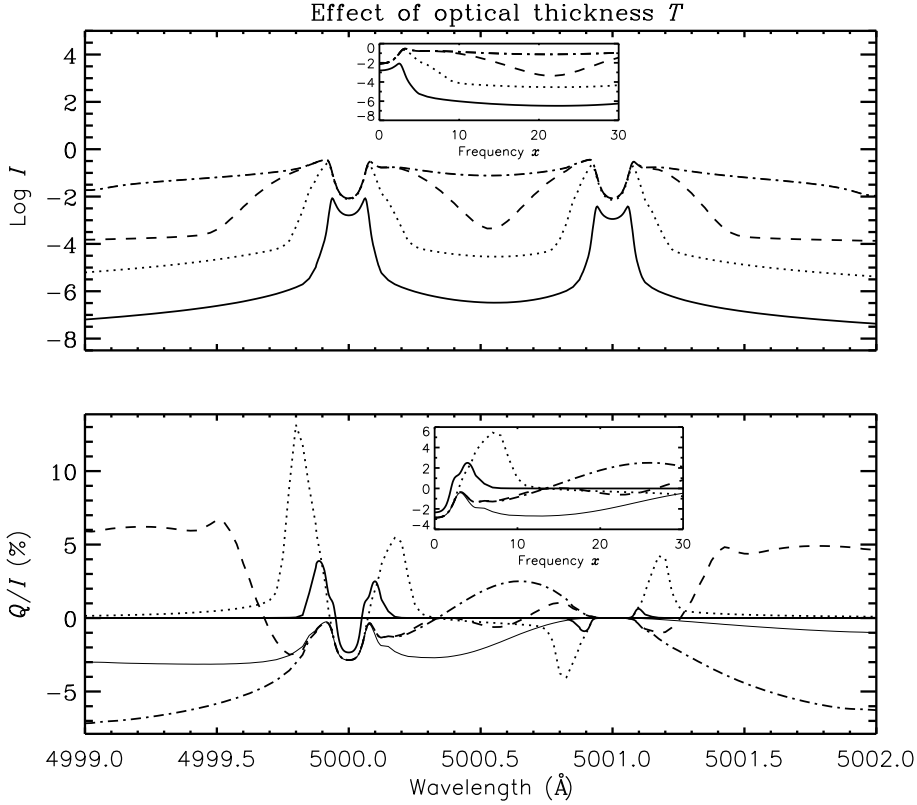


Figure 3.3: Emergent Stokes profiles at $\mu = 0.047$ computed for optical thickness $T = 2 \times 10^2$ (thick solid line), $T = 2 \times 10^4$ (dotted line), $T = 2 \times 10^6$ (dashed line) and $T = 2 \times 10^8$ (dot-dashed line). The thin solid line represents a profile without J -state interference for $T = 2 \times 10^8$. The other model parameters are the same as in Figure 3.2. The insets are plotted as functions of the non-dimensional frequency (x), measured from the line at 5000 \AA to compare with the single line results (see Figure 10 of Sampoorna, 2011a).

values of T . However, their counterpart PRD peaks are visible on the outer sides of the two lines that are away from the region of interference between the two lines. For $T = 2 \times 10^8$ the PRD peaks occur so far out in the wings that they cannot be shown in the scale adopted for Figure 3.3.

For $T = 2 \times 10^8$, an interesting feature is visible in the region of interference between the two lines. The Q/I profile displays a bump in the interference region between them (see the dot-dashed line). This behavior can be understood by comparing it with the thin solid curve that represents the result for the same model atmosphere, but without the effects of J -state interference, namely for the case of two non-interacting lines (shown only in the Q/I panel). The bump arises because of the sign reversal in Q/I that is in turn caused by the J -state interference effects. For two non-interacting lines, as seen from the thin solid curve, the Q/I between the two lines is negative. The J -state interference effects flip the sign of Q/I in this region which causes this bump, as seen in the dot-dashed curve. A smaller bump visible at 5000.8 \AA for $T = 2 \times 10^6$ can also be understood in a similar way (the corresponding curve for two non-interacting

lines is not shown in the figure).

3.4.4 Effects of the thermalization parameter ϵ

In Figure 3.4 we present the Stokes profiles for different values of the thermalization parameter ϵ . The optical thickness of the medium is fixed at $T = 2 \times 10^4$. The value of ϵ is varied from 10^{-2} to 0, which covers effectively thick to effectively thin slabs. The other model parameters are $a = 10^{-3}$ and $r = 0$.

For $\epsilon = 0$, there are no internal sources of photons. This is an example of a pure scattering medium. We give $I_0^0(\tau = T, x, \mu) = 1$ as the boundary condition at the lower boundary. In this case, the emergent intensity is an absorption profile. The variation of

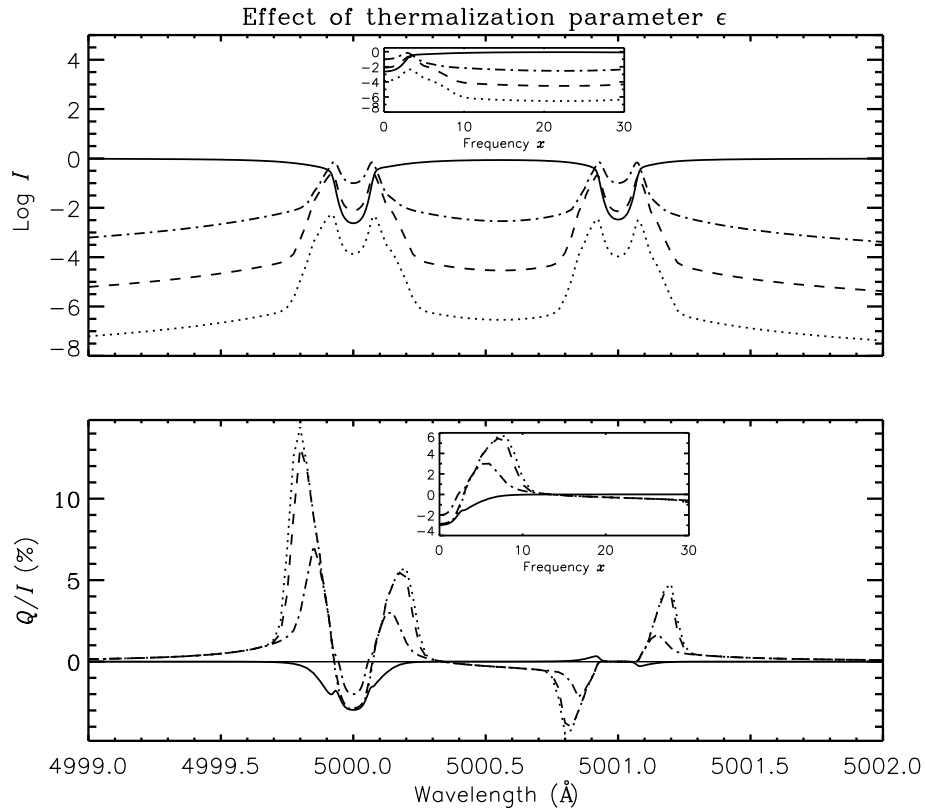


Figure 3.4: Same as Figure 3.3 but for various values of the thermalization parameter $\epsilon = 0$ (solid line), $\epsilon = 10^{-6}$ (dotted line), $\epsilon = 10^{-4}$ (dashed line) and $\epsilon = 10^{-2}$ (dot-dashed line). The remaining parameters are $(T, a, r) = (2 \times 10^4, 10^{-3}, 0)$.

I and Q/I with ϵ in the case of a doublet is similar to that of the single line case. This can be seen from the inset panels in I and Q/I in Figure 3.4. As ϵ increases from 10^{-6} to 10^{-2} , the intensity increases and the degree of linear polarization Q/I decreases in the line core and near wings of both the lines. For $\epsilon \neq 0$, the emergent intensity profiles become self-reversed emission lines. This behavior is similar to that of the single line case as can be seen from the right panel in Figure 10 (dashed lines) of [Sampoorna \(2011a\)](#).

It is worth noting that the wavelength region between 5000.3 Å to 5000.7 Å is insensitive to the variation in ϵ , except when $\epsilon = 0$ (in which case Q/I approaches zero). The J -state interference effects show up most prominently in this wavelength region in between the two lines. For $\epsilon = 0$, the emergent radiation in the wings approach the incident radiation which is unpolarized (see [Sampoorna et al., 2008a](#)). The curve for two non-interacting lines (not shown in the figure) for this case nearly coincides with the curve including the effects of J -state interference (solid line) except for the two small PRD peaks on either side of the line at 5001 Å, which are slightly enhanced because of this effect, as discussed above.

3.4.5 Effect of the unpolarized background continuum

The results shown in the previous sections were obtained without a background continuum ($r = 0$). In Figure 3.5 we show the Stokes profiles for different values of the continuum strength r . The other model parameters are ($T = 2 \times 10^4$, $a = 10^{-3}$, $\epsilon = 10^{-4}$). r is varied from 10^{-10} to 10^{-4} in steps of 10^{-2} . When r increases, we observe a significant decrease in the amplitude of the near wing PRD peaks in Q/I . Also the J -state interference effects vanish for $r = 10^{-4}$ away from the line cores (see the dot-dashed line in Figure 3.5). The insets in Figure 3.5 show a behavior similar to the single line case seen in Figure 11 (dashed lines) of [Sampoorna \(2011a\)](#). As r increases, the intensity profile evolves from a ‘self-reversed emission line’ to an absorption line.

3.4.6 Effect of separation between fine structure components

In Figure 3.6 we present the scattered Stokes profiles for three different values of the separation between the lines. The model parameters are ($T = 2 \times 10^4$, $a = 10^{-3}$, $\epsilon = 10^{-4}$, $r = 0$). The line separations used are 1 Å, 3 Å and 6 Å (measured from the 5000 Å line). Evidently, the Q/I amplitudes of the near wing PRD peaks about the lines at 5001 Å, 5003 Å and 5006 Å decrease with the increase in line separation. This behavior is expected, because the polarizability factor $W_2 = 0$ for the $1/2 \rightarrow 1/2 \rightarrow 1/2$ transition, producing no polarization at the line center. J -state interference together with PRD in scattering is responsible for polarization signals near the resonance frequency of this line component. As the separation of the $1/2 \rightarrow 1/2 \rightarrow 1/2$ component increases, the J -state interference effects naturally decrease, resulting in successively weaker signals. It is useful to note that although characteristic signals are generated near the $1/2 \rightarrow 1/2 \rightarrow 1/2$ resonance frequency, $Q/I = 0$ at the actual line center. As the figure shows, PRD along with the effects of J -state interference can indeed generate Q/I signals near the centers of multiplet components with $W_2 = 0$, but these signatures have an anti-symmetric shape with a zero crossing at the exact line center. These antisymmetric polarization signals can also be produced at the $1/2 \rightarrow 1/2 \rightarrow 1/2$ transition using

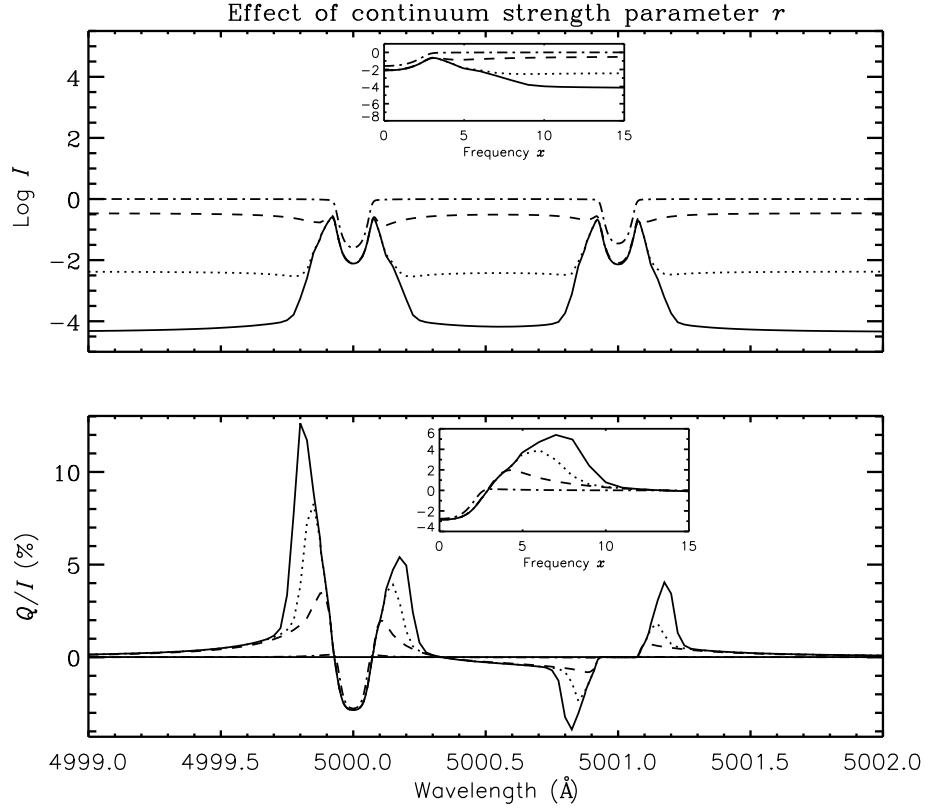


Figure 3.5: Same as Figure 3.3 but for different values of the continuum parameter $r = 10^{-10}$ (solid line), $r = 10^{-8}$ (dotted line), $r = 10^{-6}$ (dashed line) and $r = 10^{-4}$ (dot-dashed line). The other model parameters are $(T, a, \epsilon) = (2 \times 10^4, 10^{-3}, 10^{-4})$. The insets are plotted as functions of the non-dimensional frequency (x), measured from the line at 5000 Å to compare with the single line results (see Figure 11 of [Sampoorna, 2011a](#)).

CRD (see [Trujillo Bueno et al., 2002](#); [Casini & Manso Sainz, 2005](#), where also the role of hyperfine structure and lower term polarization are investigated).

3.4.7 Redistribution matrix approach vs the $W_2(\lambda)$ theory of Stenflo

In this section we compare our redistribution matrix approach and the quantum interference theory of [Stenflo \(1980, see also Stenflo 1997\)](#). The comparison is shown in Figure 3.7. The solid line shows the profile computed with the exact J -state interference theory presented in Section 3.2. We refer to this as the redistribution matrix approach. The dotted line shows the profiles computed from an independent line transfer code. In this code, in place of $\mathcal{R}^K(x, x')$ we use

$$W_K(\nu)[R^{\text{II-A}}(3/2 \rightarrow 1/2) + R^{\text{II-A}}(1/2 \rightarrow 1/2)],$$

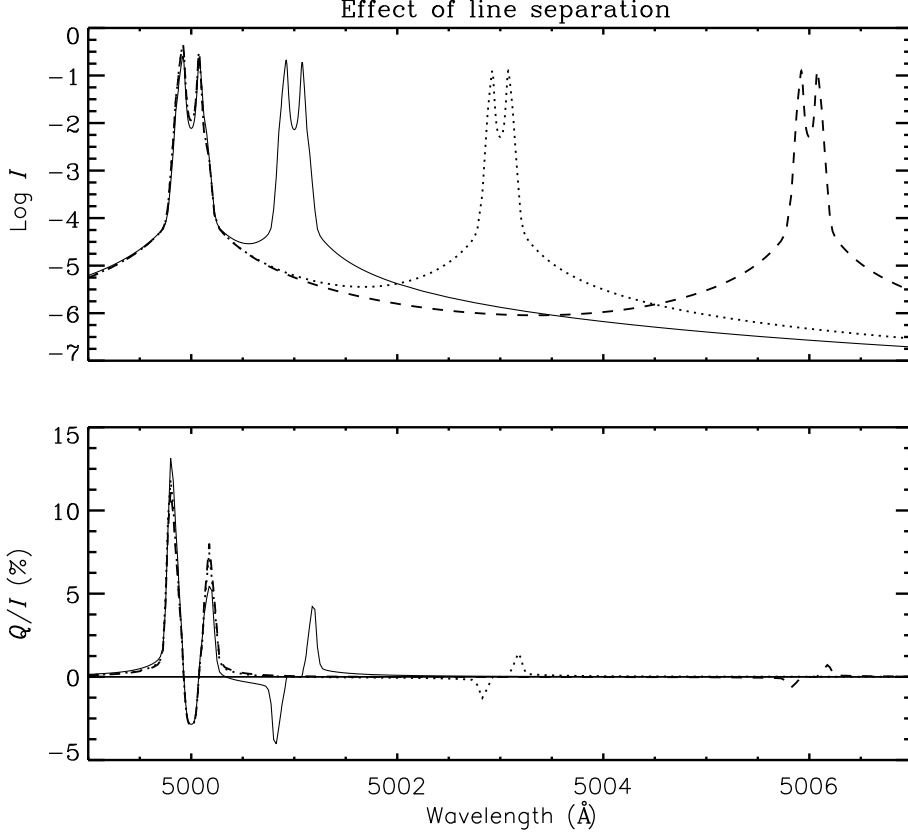


Figure 3.6: Effect of line separation between the doublets. Three different line separations are chosen, namely 1 Å (solid line), 3 Å (dotted line), and 6 Å (dashed line). The model parameters are ($T = 2 \times 10^4$, $a = 10^{-3}$, $\epsilon = 10^{-4}$, $r = 0$).

where $R^{\text{II-A}}(J_b \rightarrow J_a)$ are the angle-averaged frequency redistribution functions of [Hummer \(1962\)](#) for the line with center frequency at $\nu_{J_b J_a}$ corresponding to the $J_b \rightarrow J_a$ transition. The polarizability factor $W_0(\nu) = 1$, and $W_2(\nu)$ is the frequency-dependent W_2 factor derived by [Stenflo \(1980\)](#).

The frequency-dependent $W_2(\nu)$ contains the quantum interference effects and is given by the formula (see Equation (19) of [Stenflo, 1997](#))

$$W_2(\nu) = \frac{(\nu_2 - \nu)^{-2} + 2(\nu_1 - \nu)^{-1}(\nu_2 - \nu)^{-1}}{(\nu_1 - \nu)^{-2} + 2(\nu_2 - \nu)^{-2}}. \quad (3.35)$$

Thus we use $W_2(\nu)$ instead of a constant W_2 . Also $\phi(x)$ is taken as the sum of the absorption profiles of the individual lines. From Equation (3.35) one can see a double resonance at ν_1 and ν_2 and an interference in between these two resonances, which shows up in the emergent Q/I profiles shown in Figure 3.7. Clearly, both these independent approaches give nearly the same results. The J -state interference effects along with PRD effects have been included in realistic modeling of the observed Q/I profiles of the Na I D₁ and D₂ lines by [Fluri et al. \(2003a\)](#) based on the quantum interference theory of [Stenflo \(1980, 1997\)](#). Our results computed using the isothermal slab atmo-

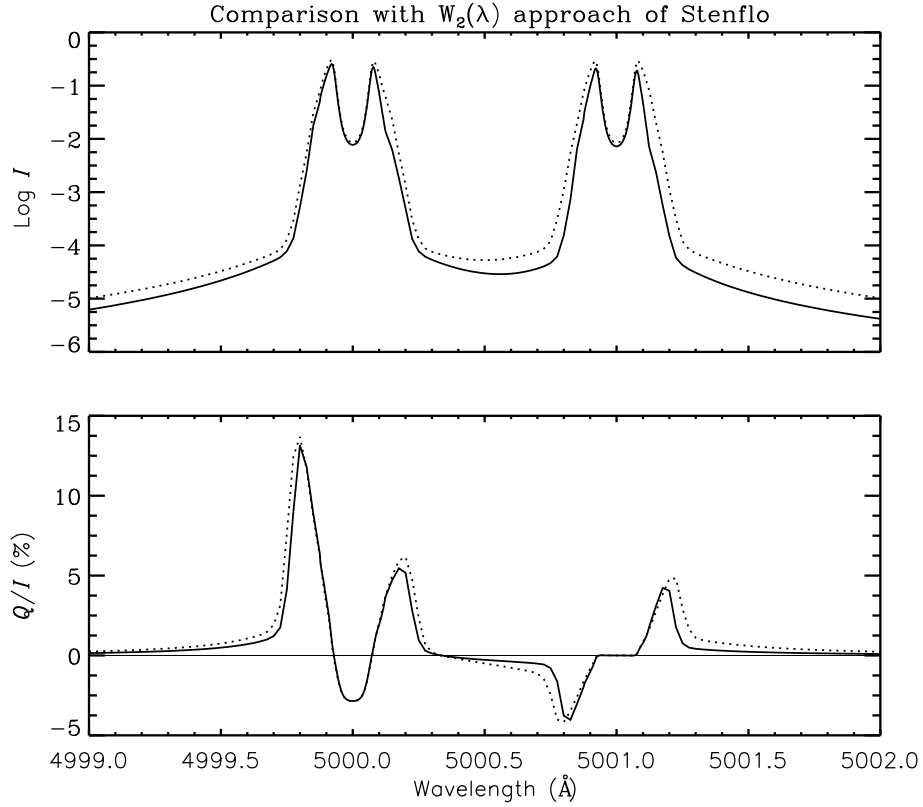


Figure 3.7: Same as Figure 3.3 but with the solid line computed using the redistribution matrix approach and the dotted line computed with the quantum interference theory that uses a wavelength-dependent $W_2(\lambda)$ factor. The model parameters are ($T = 2 \times 10^4$, $a = 10^{-3}$, $\epsilon = 10^{-4}$, $r = 0$).

spheres show a similar behavior.

3.5 Conclusions

In this chapter, we have presented the non-magnetic line transfer equation for a two-term atom including the effects of J -state interference for an arbitrary $L_a \rightarrow L_b \rightarrow L_a$ scattering transition. We have showed that the decomposition technique of Frisch (2007) that was devised for a two-level atom case can be applied to the more difficult case of a two-term atom. This technique allows us to write a polarized approximate lambda iteration method to solve the concerned transfer problem. Numerical results are presented for a doublet taking the example of an $L = 0 \rightarrow 1 \rightarrow 0$ scattering transition with $S = 1/2$.

We find that the J -state interference produces asymmetric near wing PRD peaks around the center of the $1/2 \rightarrow 3/2 \rightarrow 1/2$ scattering transition. Also, anti-symmetric peaks are produced near the center of the $1/2 \rightarrow 1/2 \rightarrow 1/2$ transition. We have showed that the J -state interference effects sensitively depend on the optical thickness of the medium. At the line core and near wings the variation of $(I, Q/I)$ with respect

to various atmospheric parameters is similar to the behavior of a single line. The wavelength region in between the two lines is somewhat insensitive to the variation in ϵ for $T = 2 \times 10^4$. In the presence of a strong background continuum the PRD as well as J -state interference effects become suppressed. Finally, as the line separation (fine structure splitting) increases, the J -state interference effects decrease strongly as one moves away from the $1/2 \rightarrow 3/2 \rightarrow 1/2$ transition at 5000 \AA .

The present extension of polarized radiative transfer theory to include two-term atoms with J -state interference is a significant step to develop the theoretical tools that are needed to interpret the wealth of polarized structures that are observed in the second solar spectrum, so that they can be used to diagnose the magnetized solar atmosphere in ways not accessible by other means. These supplementary theoretical tools required for such a diagnostic purpose will be developed in the forthcoming chapters.

Based on:

Smitha, H. N., Nagendra, K. N., Sampoorna, M., & Stenflo, J. O. 2013, *JQSRT*, 115, 46

4

Collisional redistribution in the presence of magnetic fields: *A heuristic treatment*

An Overview

After having derived the redistribution matrix for type-II in Chapter 2 and incorporating it in to the polarized radiative transfer equation in Chapter 3, we now derive an expression for the collisional redistribution matrix in the presence of magnetic fields (see also [Smitha et al., 2013a](#)). In our treatment, the influence of collisions (both elastic and inelastic), and an external magnetic field on the scattering process are taken into account. The lower term is assumed to be unpolarized and infinitely sharp. The linear Zeeman regime in which the Zeeman splitting is much smaller than the fine structure splitting is considered. The inelastic collision rates between the different levels are included in our treatment. We account for the depolarization caused by the collisions coupling the fine structure states of the upper term, but neglect the polarization transfer between the fine structure states. When the fine structure splitting goes to zero, we recover the redistribution matrix that represents the scattering on a two-level atom (which exhibits only m -state interference — namely the Hanle effect). The way in which the multipolar index of the scattering atom enters into the expression for the redistribution matrix through the collisional branching ratios is discussed. The properties of the redistribution matrix are explored for a single scattering process for an $L = 0 \rightarrow 1 \rightarrow 0$ scattering transition with $S = 1/2$ (a hypothetical doublet centered at 5000 Å and 5001 Å). Further, a method for solving the Hanle radiative transfer equation for a two-term atom in

the presence of collisions, partial frequency redistribution, and J -state interference is developed. The Stokes profiles emerging from an isothermal constant property medium are computed.

4.1 Introduction

In order to interpret the wealth of information imprinted in the Second Solar Spectrum, it is necessary to develop adequate theoretical tools that can later be used for the polarized line formation calculations. One such tool is the collisional redistribution matrix which is derived by accounting for different kinds of collisions that affect the Second Solar Spectrum.

In Chapter 2, (see [Smitha et al., 2011b](#)) we derived the polarized partial frequency redistribution (PRD) matrices for a two-term atom with an arbitrary $L_a \rightarrow L_b \rightarrow L_a$ scattering transition, taking into account the effects of J -state interference between the fine structure components of the split upper term L_b (see [Figure 2.1](#)). However, these expressions were limited to the collisionless regime. In the present chapter, where the results from [Smitha et al. \(2013a\)](#) are discussed, we generalize the semi-classical theory of [Sampoorna \(2011a\)](#) to include J -state interference for a two-term atom in the presence of collisions. In [Smitha et al. \(2012a\)](#), a simpler version of this theory has been applied to model the non-magnetic linear polarization observations of J -state interference phenomena in the CrI triplet. These results will be discussed in Chapter 5.

Collisions play a vital role in determining the polarization properties of the scattered radiation. For the case of a two-level atom with unpolarized lower level, [Omont et al. \(1972\)](#) developed the quantum theory of polarized scattering in a non-magnetic medium, including PRD effects. They describe in detail the role played by elastic and inelastic collisions. The effects of magnetic fields were considered in [Omont et al. \(1973\)](#). An explicit form of the polarized PRD matrix for resonance scattering on a two-level atom was derived by [Domke & Hubeny \(1988\)](#), based on the work of [Omont et al. \(1972\)](#), assuming that the lower level is unpolarized. Under the same assumption, a more elegant form of the PRD matrix for both the non-magnetic and magnetic cases was derived in pioneering papers by [Bommier \(1997a,b, 2003\)](#) using the master equation theory. The equivalence between the QED theory of [Bommier \(1997b\)](#) and the semi-classical theory was demonstrated in [Sampoorna et al. \(2007b\)](#) for a $J = 0 \rightarrow 1 \rightarrow 0$ scattering transition, and in [Sampoorna \(2011a\)](#) for an arbitrary $J_a \rightarrow J_b \rightarrow J_a$ scattering transition. An alternative PRD theory based on the concept of metalevels has been developed by [Landi Degl'Innocenti et al. \(1997\)](#) for the collisionless case. This formulation can also deal with J -state interference in the presence of magnetic fields.

In this chapter, starting from the Kramers-Heisenberg formula, we derive the expressions for the collisional PRD matrices including the effects of J -state interference

for a two-term atom. The following assumptions are made:

1. Infinitely sharp lower term.
2. Unpolarized lower term.
3. Weak radiation field limit (i.e., stimulated emission is neglected in comparison with the spontaneous emission).
4. Hyperfine structure is neglected.
5. The effects of inelastic collisions that couple the fine structure states are treated approximately (see below).
6. The depolarizing elastic collisions that couple m -states belonging to a given fine structure state J_b are taken into account, but are assumed to be independent of the J -quantum number for the sake of mathematical simplicity.
7. We restrict our attention to the linear Zeeman regime of magnetic field strengths.

The assumption of an unpolarized lower term is made for the sake of mathematical simplicity, but can often be justified when the lower term represents the ground state of the atom. In the stellar atmospheric conditions the ground state is generally two orders of magnitude more long lived than the excited state, which makes it correspondingly much harder for any ground state polarization to survive collisional and magnetic depolarization, as compared with the excited states (see Kerkeni & Bommier (2002)). We also ignore the induced emission, because in scattering problems it acts as a negative absorption and only affects the radiation in the exact forward direction (scattering angle exactly zero). The induced emission probability is nearly three orders of magnitude smaller than the spontaneous emission probability (see Kerkeni & Bommier (2002)).

The inelastic collisions between the upper and lower terms are treated exactly while the inelastic collisions between the upper fine structure states are treated approximately. The inelastic collisions between the upper fine structure states (denoted by $\Gamma_{IJ_bJ_{b'}}$) manifest themselves in two different ways, (i) through a depolarization of state J_b and (ii) through a transfer of alignment and orientation between J_b and $J_{b'}$.

Since the colliding particles are isotropically distributed around the radiating atom, they destroy the alignment and thereby depolarize the levels. Therefore the inelastic collisions that take the atom away from the state J_b always depolarize J_b . They also contribute to the inverse lifetime of J_b under consideration. In this chapter we take into account such inelastic collisions between the fine structure states J_b and $J_{b'}$ by adding these inelastic collision rates ($\Gamma_{IJ_bJ_{b'}}$) to the inelastic collision rate $\Gamma_{IJ_bJ_f}$ (where f is the final state). The depolarizing effects of these inelastic collisions are similar to the depolarizing effects of elastic collisions. Thus we merge these two effects and define a

common damping rate γ_b for the J_b state.

The inelastic collisions between polarized fine structure states can lead to a transfer of alignment and orientation between them (hereafter referred to as the transfer of polarization). This is similar to optical pumping by radiative transitions. The only difference is that the radiative transitions between the fine structure states J_b and $J_{b'}$ are not allowed. Taking account of such transfer rates caused by inelastic collisions actually involves formulating the statistical equilibrium equations for the concerned states including the atomic polarization of the various states. This is outside the scope of our present thesis. A formulation of statistical equilibrium equation including these collisions but neglecting the redistribution effects in scattering has been presented in [Kerkeni \(2002\)](#) and [Kerkeni & Bommier \(2002\)](#). They derive the expressions to calculate these rates taking examples of few atomic systems of relevance to the analysis of the second solar spectrum. Our present treatment of inelastic collisions is basically heuristic and only takes into account the depolarizing effects of $\Gamma_{IJ_bJ_{b'}}$.

The frequency redistribution function that describes the effect of collisions in unpolarized radiative transfer is the well known type-III (or R^{III}) function of [Hummer \(1962\)](#). Here we describe the matrix generalizations of this standard collisional redistribution function, brought about by the magnetic fields and the J -state interference. Using the method described in Appendix C of [Sampoorna et al. \(2007b\)](#), we rewrite the PRD matrices in terms of the irreducible spherical tensors for polarimetry. We discuss in detail the procedure to identify the multipolar index K , which needs to be assigned to the branching ratios that govern the effect of the depolarizing collisions. We illustrate the effects of collisions on the Stokes ($I, Q/I, U/I, V/I$) profiles of the scattered radiation for the 90° single scattering case. Then we present the technique of incorporating this Hanle redistribution matrix for the two-term atom into the polarized radiative transfer equation, and solve it for an isothermal constant property atmospheric slab. In the collisionless case, the relevant redistribution matrix derived in Chapter 2 was incorporated into the transfer equation in Chapter 3 and solved for a constant property isothermal media in the absence of a magnetic field. The same method of solution presented in Chapter 3 is also used here, but including the collisional redistribution in the presence of a magnetic field.

In Section 4.2 we derive the elements of the ensemble averaged coherency matrix both in the atomic and laboratory frames for a $L_a \rightarrow L_b \rightarrow L_a$ scattering transition taking into account the elastic collisions. In Section 4.3 we express the type-III redistribution matrix in terms of the irreducible spherical tensors both for the non-magnetic and magnetic cases. The important question of identifying the multipolar index K that describes the transfer of angular momentum in a scattering event affected by the depolarizing collisions is discussed in detail. The laboratory frame expression for the collisional redistribution matrix is also derived in this section. The procedure to incor-

porate this redistribution matrix into the polarized radiative transfer equation for both the magnetic and non-magnetic cases is discussed in Section 4.4. The Stokes profiles resulting from a single 90° scattering event and from multiple scattering in an isothermal atmospheric slab are presented in Section 4.5. Concluding remarks are given in Section 4.6. Finally, in Appendix C we give the expressions for the magnetic redistribution functions of type-III.

4.2 An approximate treatment of collisions

4.2.1 Polarized PRD matrix from a semi-classical approach

The Mueller matrix \mathbf{M} that describes the transformation from the incident to the scattered Stokes vector is given by

$$\mathbf{M} = \mathbf{T}\mathbf{W}\mathbf{T}^{-1}, \quad (4.1)$$

where \mathbf{T} and \mathbf{T}^{-1} are purely mathematical transformation matrices. Their explicit forms are given in Equation (9) of Stenflo (1998). The \mathbf{W} -matrix is defined in Equation (2.7). The elements of this matrix contain the bilinear products of the complex probability amplitude $w_{\alpha\beta}(J_f\mu_f J_a\mu_a)$. These amplitudes for transition from an initial state a to final state f via all intermediate states b are given by the Kramers-Heisenberg formula as

$$w_{\alpha\beta} \sim \sum_b \frac{\langle f | \mathbf{r} \cdot \mathbf{e}_\alpha | b \rangle \langle b | \mathbf{r} \cdot \mathbf{e}_\beta | a \rangle}{\omega_{bf} - \omega - i\gamma_b/2}, \quad (4.2)$$

where $\omega = 2\pi\xi$ is the angular frequency of the scattered radiation in the atomic rest frame, $\hbar\omega_{bf}$ is the energy difference between the excited and final states, and γ_b is the damping constant that accounts for the broadening of the excited state b , while the initial and the final states are assumed to be infinitely sharp. The damping parameter is assumed to be the same for all the magnetic substates of the excited state. The matrix elements appearing in Equation (4.2) can be expanded using the Wigner-Eckart theorem as

$$\begin{aligned} w_{\alpha\beta}(J_f\mu_f J_a\mu_a) &\sim \sum_{J_b\mu_b} (-1)^{q-q'} \sqrt{(2J_a+1)(2J_f+1)(2J_b+1)(2L_a+1)} \\ &\times \begin{Bmatrix} L_a & L_b & 1 \\ J_b & J_f & S \end{Bmatrix} \begin{Bmatrix} L_a & L_b & 1 \\ J_b & J_a & S \end{Bmatrix} \begin{pmatrix} J_b & J_a & 1 \\ -\mu_b & \mu_a & -q' \end{pmatrix} \begin{pmatrix} J_b & J_f & 1 \\ -\mu_b & \mu_f & -q \end{pmatrix} \\ &\times \Phi_{\gamma_b}(\nu_{J_b\mu_b J_f\mu_f} - \xi) \varepsilon_q^{\alpha*} \varepsilon_{q'}^\beta, \end{aligned} \quad (4.3)$$

where μ_b represents the magnetic substates of the upper state b with total angular momentum quantum number J_b , orbital angular momentum quantum number L_b , and spin

S . The quantities J_a and J_f are respectively the total angular momentum quantum numbers of the initial and final states a and f with orbital angular momentum quantum number L_a , and magnetic substates μ_a and μ_f . The quantities ε are the geometrical factors (see Equations (2) and (27) of [Stenflo, 1998](#)), with α and β denoting the outgoing and incoming radiation, respectively. In Equation (4.3), $q = \mu_f - \mu_b$ and $q' = \mu_a - \mu_b$. In the rest of the chapter we denote the indices as follows for the sake of convenience

$$\begin{aligned} J_b = b, J_a = a, J_f = f; \quad J_b\mu_b = b_m, J_a\mu_a = a_m, J_f\mu_f = f_m, \\ J_{b'}\mu_{b'} = b'_m, J_b\mu_{b''} = b''_m, J_{b'}\mu_{b'''} = b'''_m. \end{aligned} \quad (4.4)$$

The frequency-normalized profile function is given by

$$\Phi_{\gamma_b}(\nu_{b_m f_m} - \xi) = \frac{1/(\pi i)}{\nu_{b_m f_m} - \xi - i\gamma_b/(4\pi)} \quad \text{with} \quad \nu_{b_m f_m} = \nu_{bf} + (g_b\mu_b - g_f\mu_f)\nu_L. \quad (4.5)$$

Here $h\nu_{bf}$ is the energy difference between the upper (J_b) and lower (J_f) states in the absence of magnetic fields, g_b, g_f are the Landé factors of these states, and ν_L is the Larmor frequency. Equation (4.3) refers to the case of frequency-coherent scattering in the atomic rest frame.

The phenomenological extension of Equation (4.3) to the case of PRD is achieved by treating each radiative emission transition between magnetic substates μ_b and μ_f in terms of a damped oscillator that is truncated by collisions (see [Sampoorna et al., 2007a](#)). In other words, in Equation (4.3) we make the following replacement for the profile function :

$$\Phi_{\gamma_b}(\nu_{b_m f_m} - \xi) \longrightarrow (\tilde{r}_{b_m})_{a_m f_m}, \quad (4.6)$$

where the Fourier-transformed solution of the time-dependent oscillator equation is given by (see [Bommier & Stenflo, 1999](#))

$$(\tilde{r}_{b_m})_{a_m f_m} = (\tilde{r}_{b_m}^{\text{stat}})_{a_m f_m} + C (\tilde{r}_{b_m}^{\text{trans}})_{a_m f_m}. \quad (4.7)$$

Here we have omitted the unimportant phase factor, as it vanishes in the bilinear product $(\tilde{r}_{b_m})_{a_m f_m} (\tilde{r}_{b'_m}^*)_{a_m f_m}$. The constant C in Equation (4.7) defines the relative amplitudes of the stationary and the transitory parts of the solution, which are given by

$$(\tilde{r}_{b_m}^{\text{stat}})_{a_m f_m} = \Phi_{\gamma_b}(\nu_{b_m a_m} - \xi') \delta(\xi - \xi' - \nu_{a_m f_m}), \quad (4.8)$$

$$(\tilde{r}_{b_m}^{\text{trans}})_{a_m f_m} = \Phi_{\gamma_b}(\nu_{b_m a_m} - \xi') \Phi_{\gamma_b}(\nu_{b_m f_m} - \xi) [1 - e^{-i(\omega_{b_m f_m} - i\gamma_b/2 - \omega)t_c}]. \quad (4.9)$$

Here ξ' denotes the frequency of the incoming photon in the atomic rest frame, t_c is the time between two successive collisions, $\omega_{b_m f_m} = 2\pi\nu_{b_m f_m}$. The profile function $\Phi_{\gamma_b}(\nu_{b_m a_m} - \xi')$ is given by Equation (4.5) with ξ replaced by ξ' , while $\nu_{b_m f_m}$ is replaced

by $\nu_{b_m a_m}$ that is defined similar to Equation (4.5). In Equation (4.8), $\nu_{a_m f_m}$ appearing in the delta function is demanded by energy conservation (see Equation (9) of Stenflo, 1994), and is given by

$$\nu_{a_m f_m} = \nu_{af} + (g_a \mu_a - g_f \mu_f) \nu_L, \quad (4.10)$$

where $h\nu_{af}$ is the energy difference between the states J_a and J_f in the absence of a magnetic field.

4.2.2 Coherency matrix in the atomic rest frame

The elements of the ensemble averaged coherency matrix $\langle \tilde{r}_{b_m} \tilde{r}_{b'_m}^* \rangle_{a_m f_m}$ can be derived starting from Equations (4.8) and (4.9), applying the same steps that are described in detail in Bomnier & Stenflo (1999). These elements are contained in the bilinear product $w_{\alpha\beta}(f_m a_m) w_{\alpha'\beta'}^*(f_m a_m)$. In the atomic rest frame ensemble averaged coherency matrix elements are given by

$$\begin{aligned} \langle \tilde{r}_{b_m} \tilde{r}_{b'_m}^* \rangle_{a_m f_m} &= A_{bb'} \cos \beta_{b'_m b_m} e^{i\beta_{b'_m b_m}} \Phi_{b_m b'_m a_m}^{\gamma_{bb'} + \gamma_c}(\xi') \delta(\xi - \xi' - \nu_{a_m f_m}) \\ &+ B_{bb'} \cos \beta_{b'_m b_m} \cos \alpha_{b'_m b_m} e^{i(\beta_{b'_m b_m} + \alpha_{b'_m b_m})} \Phi_{b_m b'_m a_m}^{\gamma_{bb'} + \gamma_c}(\xi') \Phi_{b_m b'_m f_m}^{\gamma_{bb'} + \gamma_c}(\xi), \end{aligned} \quad (4.11)$$

where the angles $\beta_{b'_m b_m}$ and $\alpha_{b'_m b_m}$ (arising due to the combined effects of the J -state and m -state interferences) are defined respectively by

$$\begin{aligned} \tan \beta_{b'_m b_m} &= \frac{\omega_{b'b} + (g_{b'} \mu_{b'} - g_b \mu_b) \omega_L}{\gamma_{b'b} + \gamma_c}; \\ \tan \alpha_{b'_m b_m} &= \frac{\omega_{b'b} + (g_{b'} \mu_{b'} - g_b \mu_b) \omega_L}{\gamma_{b'b} + \gamma_c/2}, \end{aligned} \quad (4.12)$$

with $\gamma_{bb'}$ given by

$$\gamma_{bb'} = \frac{\gamma_b + \gamma_{b'}}{2} = \gamma_{b'b}. \quad (4.13)$$

Here γ_c is the collisional damping constant, while $h\omega_{b'b}$ is the energy difference between the $J_{b'}$ and J_b states in the absence of a magnetic field. The elastic collisional rates are in general different for each fine structure component (J_b) of the upper term. However, for simplicity we assume them to be independent of the J -quantum numbers.

$A_{bb'}$ and $B_{bb'}$ are the branching ratios for a two-term atom. The explicit expressions for them will be defined later in Section 4.3.1.

Like in Chapter 2, we limit the treatment to the linear Zeeman regime, in which the Zeeman splitting is much smaller than the fine structure splitting. When $J_b \neq J_{b'}$ the contributions from the second terms with ω_L in Equation (4.12) to the angles $\beta_{b'_m b_m}$ and $\alpha_{b'_m b_m}$ can therefore be ignored, because they are insignificant in comparison with the

first terms. The classical generalized profile function is defined as

$$\Phi_{b_m b'_m f_m}^{\gamma_{bb'}}(\xi) = \frac{1}{2} \left[\Phi_{\gamma_b}(\nu_{b_m f_m} - \xi) + \Phi_{\gamma_{b'}}^*(\nu_{b'_m f_m} - \xi) \right], \quad (4.14)$$

in the same way as in [Bommier & Stenflo \(1999\)](#).

4.2.3 Coherency matrix in the laboratory frame for type-III redistribution

We transform the ensemble averaged coherency matrix defined in Equation (4.11) to the laboratory frame using the same steps as described in Section 2.2 of [Sampoorna et al. \(2007b\)](#) and it is given by

$$\begin{aligned} \langle \tilde{r}_{b_m} \tilde{r}_{b'_m}^* \rangle_{a_m f_m} &= A_{bb'} \cos \beta_{b'_m b_m} e^{i\beta_{b'_m b_m}} \left[(h_{b_m, b'_m}^{\text{II}})_{a_m f_m} + i(f_{b_m, b'_m}^{\text{II}})_{a_m f_m} \right] \\ &+ B_{bb'} \cos \beta_{b'_m b_m} \cos \alpha_{b'_m b_m} e^{i(\beta_{b'_m b_m} + \alpha_{b'_m b_m})} \left[h_{b_m a_m, b'_m f_m}^{\text{III}} + i f_{b_m a_m, b'_m f_m}^{\text{III}} \right]. \end{aligned} \quad (4.15)$$

The various auxiliary quantities for type-II redistribution are defined in Section 2.3. Hence we do not repeat them here. Hereafter we confine our attention to the collisional redistribution (type-III). The corresponding derivation for pure radiative (collisionless) redistribution (type-II) is given in Chapter 2. The auxiliary quantities for type-III redistribution that appear in Equation (4.15) are defined by

$$\begin{aligned} h_{b_m a_m, b'_m f_m}^{\text{III}} &= \frac{1}{4} \left[R_{b'_m a_m, b'_m f_m}^{\text{III, HH}} + R_{b'_m a_m, b_m f_m}^{\text{III, HH}} + R_{b_m a_m, b'_m f_m}^{\text{III, HH}} + R_{b_m a_m, b_m f_m}^{\text{III, HH}} \right] \\ &+ \frac{i}{4} \left[R_{b'_m a_m, b'_m f_m}^{\text{III, FH}} + R_{b'_m a_m, b_m f_m}^{\text{III, FH}} - R_{b_m a_m, b'_m f_m}^{\text{III, FH}} - R_{b_m a_m, b_m f_m}^{\text{III, FH}} \right], \end{aligned} \quad (4.16)$$

$$\begin{aligned} f_{b_m a_m, b'_m f_m}^{\text{III}} &= \frac{1}{4} \left[R_{b'_m a_m, b'_m f_m}^{\text{III, HF}} - R_{b'_m a_m, b_m f_m}^{\text{III, HF}} + R_{b_m a_m, b'_m f_m}^{\text{III, HF}} - R_{b_m a_m, b_m f_m}^{\text{III, HF}} \right] \\ &+ \frac{i}{4} \left[R_{b'_m a_m, b'_m f_m}^{\text{III, FF}} - R_{b'_m a_m, b_m f_m}^{\text{III, FF}} - R_{b_m a_m, b'_m f_m}^{\text{III, FF}} + R_{b_m a_m, b_m f_m}^{\text{III, FF}} \right]. \end{aligned} \quad (4.17)$$

The magnetic redistribution functions of type-III appearing in the above equations are defined in Appendix C.

4.3 The redistribution matrix expressed in terms of irreducible tensors

The importance of expressing the PRD matrices in terms of the irreducible spherical tensors introduced by [Landi Degl'Innocenti \(1984\)](#) has been discussed in Chapter 2.

The definition and properties of irreducible spherical tensors are described in detail in Landi Degl'Innocenti & Landolfi (2004). The way to incorporate these tensors in the analytic form of the PRD matrix derived from a semi-classical approach has been described in Samporna et al. (2007b) (see also Section 2.4). Applying the same method we have obtained an expression for the type-III redistribution matrix in terms of irreducible spherical tensors. The case of the type-II redistribution matrix has been discussed in Section 2.4.

As in Chapter 2, we now express the type-III PRD matrix derived in Section 4.2 in terms of $\mathcal{T}_Q^K(i, \mathbf{n})$, where $i = 0, 1, 2, 3$, and $K = 0, 1, 2$ with $-K \leq Q \leq +K$. Following the same procedure as discussed in Section 2.4, the matrix $T_{\mu\nu, \rho\sigma}^S$ of Equation (A.3), which describes the transformation of the elements of the coherency matrix, can be written in the atomic rest frame as

$$\begin{aligned} T_{\mu\nu, \rho\sigma}^S(\xi, \mathbf{n}; \xi', \mathbf{n}', \mathbf{B}) &= (2L_a + 1)^2 \sum_{a_m f_m b_m b'_m} G Z_6 Z_3 (-1)^{q-q'+q''-q'''} \\ &\times \mathcal{E}_{qq''}^S(\mu, \nu, \mathbf{n}) \mathcal{E}_{q''q'}^S(\sigma, \rho, \mathbf{n}') \cos \beta_{b'_m b_m} e^{i\beta_{b'_m b_m}} \Phi_{b_m b'_m a_m}^{\gamma_{bb'} + \gamma_c}(\xi') \\ &\times \left\{ A_{bb'} \delta(\xi - \xi' - \nu_{a_m f_m}) + B_{bb'} \cos \alpha_{b'_m b_m} e^{i\alpha_{b'_m b_m}} \Phi_{b_m b'_m f_m}^{\gamma_{bb'} + \gamma_c}(\xi) \right\}, \end{aligned} \quad (4.18)$$

where

$$\begin{aligned} G &= (2J_a + 1)(2J_f + 1)(2J_b + 1)(2J_{b'} + 1), \\ Z_6 &= \begin{Bmatrix} L_a & L_b & 1 \\ J_b & J_f & S \end{Bmatrix} \begin{Bmatrix} L_a & L_b & 1 \\ J_b & J_a & S \end{Bmatrix} \begin{Bmatrix} L_a & L_b & 1 \\ J_{b'} & J_f & S \end{Bmatrix} \begin{Bmatrix} L_a & L_b & 1 \\ J_{b'} & J_a & S \end{Bmatrix}, \\ Z_3 &= \begin{pmatrix} J_b & J_a & 1 \\ -\mu_b & \mu_a & -q' \end{pmatrix} \begin{pmatrix} J_b & J_f & 1 \\ -\mu_b & \mu_f & -q \end{pmatrix} \begin{pmatrix} J_{b'} & J_a & 1 \\ -\mu_{b'} & \mu_a & -q''' \end{pmatrix} \begin{pmatrix} J_{b'} & J_f & 1 \\ -\mu_{b'} & \mu_f & -q'' \end{pmatrix}. \end{aligned} \quad (4.19)$$

In Equation (4.18), $\mathcal{E}_{qq''}^S(\mu, \nu, \mathbf{n})$ is a reducible spherical tensor. After transforming to the Stokes formalism (see Section 2.4), the redistribution matrix for J -state interference can be written in symbolic form as

$$\mathbf{R}_{ij}(\xi, \mathbf{n}; \xi', \mathbf{n}', \mathbf{B}) = \mathbf{R}_{ij}^{\text{II}}(\xi, \mathbf{n}; \xi', \mathbf{n}', \mathbf{B}) + \mathbf{R}_{ij}^{\text{III}}(\xi, \mathbf{n}; \xi', \mathbf{n}', \mathbf{B}), \quad (4.20)$$

where the pure radiative part of the redistribution matrix is given by branching ratio $A_{bb'}$ times Equation (2.22), and the collisional frequency redistribution is taken into account through

$$\mathbf{R}_{ij}^{\text{III}}(\xi, \mathbf{n}; \xi', \mathbf{n}', \mathbf{B}) = \frac{2}{3} (2L_a + 1)^2 \sum_{K' K'' Q_a f b b'} G Z_6 B_{bb'} \sqrt{(2K' + 1)(2K'' + 1)}$$

$$\begin{aligned}
 & \times \left\{ \sum_{\mu_a \mu_f \mu_b \mu_{b'}} Z_3 (-1)^{q''+q'+Q} \begin{pmatrix} 1 & 1 & K'' \\ q & -q'' & Q \end{pmatrix} \begin{pmatrix} 1 & 1 & K' \\ q''' & -q' & -Q \end{pmatrix} \right. \\
 & \times \frac{1}{4} \left[\Phi_{\gamma_b+\gamma_c}(\nu_{b_m a_m} - \xi') + \Phi_{\gamma_{b'}+\gamma_c}^*(\nu_{b'_m a_m} - \xi') \right] \\
 & \times \left[\Phi_{\gamma_b+\gamma_c}(\nu_{b_m f_m} - \xi) + \Phi_{\gamma_{b'}+\gamma_c}^*(\nu_{b'_m f_m} - \xi) \right] \\
 & \left. \times \cos \beta_{b'_m b_m} \cos \alpha_{b'_m b_m} e^{i(\beta_{b'_m b_m} + \alpha_{b'_m b_m})} \right\} (-1)^Q \mathcal{T}_Q^{K''}(i, \mathbf{n}) \mathcal{T}_{-Q}^{K'}(j, \mathbf{n}'). \quad (4.21)
 \end{aligned}$$

Note that in the formal expression for \mathbf{R} the branching ratios are built into the \mathbf{R}^{II} and \mathbf{R}^{III} components. As the collisional branching ratio $B_{bb'}$ depends on index K , our next task is to determine the explicit form of this dependence.

4.3.1 Identification and physical significance of the multipolar index K in the collisional branching ratios

It is well known that the spherical unit vectors form a natural basis to decouple the classical oscillator equation. [Fano \(1957\)](#) suggested that a convenient basis to be used when dealing with scattering problems in quantum mechanics, is the irreducible tensorial basis instead of the standard $|JM\rangle$ basis of Hilbert space. This is due to the fact that irreducible tensors transform under co-ordinate rotations like the spherical harmonics (Y_{lm}) and are thus suited for a study of rotationally invariant processes. With irreducible tensorial operators one can express the scattering matrix such that it formally looks the same in the magnetic (with the polar z -axis along \mathbf{B}) and the atmospheric (with the polar z -axis along the atmospheric normal) reference frames. This is the advantage of going to the irreducible tensorial basis (hereafter called the KQ basis). A more detailed historical background for the irreducible tensorial operators is given in [Sahal-Brechot et al. \(1977\)](#).

Thus the geometrical factors associated with the scattering problem, and also the density matrix for the atomic levels in question, should be transformed to the KQ basis. The transformation of the geometrical factors to the KQ basis is described in Chapter 5 of [Landi Degl'Innocenti & Landolfi \(2004\)](#) and is used in [Sampoorna et al. \(2007b\)](#). The density matrix is first written in the standard $|JM\rangle$ basis and then transformed to the KQ basis (see Equation (3.97) of [Landi Degl'Innocenti & Landolfi 2004](#)), which is then called 'multipole moments' of the density matrix, or 'irreducible statistical tensors'. In the case of the radiation field, the multipole index K has the following interpretation: $K = 0$ means isotropic scattering, $K = 1$ is related to the circular polarization, while $K = 2$ is related to the linear polarization. In the case of the atomic levels, $K = 0$ represents the population of the level under consideration, $K = 1$ is related to the orientation of the atom, while $K = 2$ is related to the alignment of the atom (this physical

interpretation can be found in pp. 128 and 129 of [Landi Degl'Innocenti & Landolfi \(2004\)](#), Section 10.4 of [Stenflo \(1994\)](#), and in [Trujillo Bueno \(2001\)](#)).

In the case of radiation field an irreducible tensor $\mathcal{T}_Q^K(i, \mathbf{n})$ is constructed by forming a suitable linear combination of the direct product of two geometrical factors. Since geometrical factors basically contain unit polarization vectors of rank one, their direct product represents a second rank tensor, with K taking values 0, 1, and 2. Note that these values of K can also be obtained through angular momentum addition of two tensors of rank 1. In the case of the density matrix of the atom, the value of K is determined by the addition of angular momenta J and J' . For example for a two-level atom with unpolarized ground level the value of K relating to the statistical tensor of the upper level is given by angular momentum addition of J_b and $J_{b'}$. Further, Q takes values $-K$ to $+K$ in steps of one, and is related to the magnetic quantum numbers of the upper level.

We can denote K' as the multipole component of the incident radiation field, K as the multipole moment of the upper level of the atom, and K'' as the multipole component of the scattered radiation. The scattering process can be understood as a transfer of the K' multipole component of the incident radiation to the K multipole moment of the atom's upper level through an absorption process, followed by a transfer of the K multipole moment of the atom's upper level to the K'' multipole component of the scattered radiation through spontaneous emission. The depolarizing collisions that govern the branching ratios and the magnetic field that governs the Hanle angles affect the upper level of the atom directly and modify the K multipole moment of the atom, but they influence the scattered radiation only indirectly, through spontaneous emission from the level that has been directly affected. Thus it is the K index of the upper level of the atom that needs to be assigned to the branching ratios and the Hanle angles, and not the multipole component of the incident or the scattered radiation. In the absence of magnetic fields or in the presence of weak magnetic fields (Hanle effect), $K' = K = K''$. In the presence of a magnetic field of arbitrary strength (Hanle-Zeeman regime) all the three K 's are distinct. This is due to the distinction preserved through the profile functions, which become different for the different Zeeman components. However, in weakly magnetic cases (when the Zeeman splitting is much smaller than the effective line width) the distinction is so small that it can be ignored.

From the above discussion it is clear that for a correct identification of K for the branching ratio we need to know the density matrix of the upper level in the KQ basis. Since the density matrix does not appear directly in the Kramers-Heisenberg approach that we use, we need to indirectly identify K either by drawing analogy with the density matrix theory, or by using a suitably defined quantum generalized profile function. Such a function was defined by [Landi Degl'Innocenti et al. \(1991\)](#) for the special case of a two-level atom (without J -state interference). The multipole moment K of the

upper level is built into this function through the third $3 - j$ symbol appearing in the following definition :

$$\begin{aligned} \Phi_Q^{K,K'}(J_a, J_b; \xi') &= \sqrt{3(2J_b + 1)(2K + 1)(2K' + 1)} \sum_{\mu_b \mu_{b'} \mu_a p p'} (-1)^{J_b - \mu_a - 1 + Q} \\ &\times \begin{pmatrix} J_b & J_a & 1 \\ -\mu_b & \mu_a & p \end{pmatrix} \begin{pmatrix} J_b & J_a & 1 \\ -\mu_{b'} & \mu_a & p' \end{pmatrix} \begin{pmatrix} J_b & K & J_b \\ -\mu_b & Q & \mu_{b'} \end{pmatrix} \begin{pmatrix} 1 & 1 & K' \\ -p & p' & Q \end{pmatrix} \\ &\times \frac{1}{2} \left[\Phi_{\gamma_b + \gamma_c}(\nu_{J_b \mu_b J_a \mu_a} - \xi') + \Phi_{\gamma_b + \gamma_c}^*(\nu_{J_b \mu_{b'} J_a \mu_a} - \xi') \right]. \end{aligned} \quad (4.22)$$

The $\Phi_Q^{K,K'}$ defined above can be seen as a frequency-dependent coupling coefficient that connects the (K', Q) multipole component of the incident radiation field with the (K, Q) multipole moment of the atomic density matrix (see [Landi Degl'Innocenti & Landolfi, 2004](#), p. 525). In the non-magnetic and weak field limits, the ν_L dependence of the profile function $\Phi_{\gamma_b + \gamma_c}$ can be neglected, which gives us

$$\lim_{\nu_L \rightarrow 0} \Phi_Q^{K,K'}(a, b; \xi') = \delta_{KK'} w_{ba}^{(K)} \phi(\nu_0 - \xi'), \quad (4.23)$$

where $w_{ba}^{(K)}$ is defined in Equation (10.11) of [Landi Degl'Innocenti & Landolfi \(2004\)](#), and ϕ denotes the usual non-magnetic profile function. In this limit we have $K' = K$.

In the case of J -state interference a suitable quantum generalized profile function has not been defined yet, but we can define it here in analogy with the two-level atom case. It has the following form for the incoming radiation:

$$\begin{aligned} \Phi_Q^{K,K'}(a, b', b; \xi') &= (2J_a + 1) \sqrt{3(2J_{b'} + 1)(2J_b + 1)(2K + 1)(2K' + 1)} \\ &\times \sum_{\mu_b \mu_{b'} \mu_a q' q''} (-1)^{1 + J_b - \mu_{b'} + q'} \begin{pmatrix} J_b & J_a & 1 \\ -\mu_b & \mu_a & -q' \end{pmatrix} \begin{pmatrix} J_{b'} & J_a & 1 \\ -\mu_{b'} & \mu_a & -q'' \end{pmatrix} \\ &\times \begin{pmatrix} J_b & J_{b'} & K \\ \mu_b & -\mu_{b'} & -Q \end{pmatrix} \begin{pmatrix} 1 & 1 & K' \\ q''' & -q' & -Q \end{pmatrix} \cos \beta_{b' m b_m} e^{i\beta_{b' m b_m}} \\ &\times \frac{1}{2} \left[\Phi_{\gamma_b + \gamma_c}(\nu_{b_m a_m} - \xi') + \Phi_{\gamma_{b'} + \gamma_c}^*(\nu_{b' m a_m} - \xi') \right], \end{aligned} \quad (4.24)$$

with a similar expression for the outgoing radiation when J_a and μ_a are replaced respectively by J_f and μ_f , and angle $\beta_{b' m b_m}$ is replaced by $\alpha_{b' m b_m}$. Notice that unlike the two-level atom case we now have included the angles $\beta_{b' m b_m}$ and $\alpha_{b' m b_m}$ in the definition of the quantum generalized profile function, as they cannot be taken outside the summation over the magnetic substates. Using the orthogonality relation of the $3 - j$ symbols, it is easy to verify that

$$\sum_K \Phi_Q^{K,K'}(a, b', b; \xi') \Phi_Q^{K,K''}(f, b', b; \xi) = 3G \sqrt{(2K' + 1)(2K'' + 1)}$$

$$\begin{aligned}
 & \times \sum_{\mu_b \mu_{b'} \mu_a \mu_f q q' q'' q'''} Z_3 (-1)^{q'+q''+Q} \begin{pmatrix} 1 & 1 & K'' \\ q & -q'' & Q \end{pmatrix} \begin{pmatrix} 1 & 1 & K' \\ q''' & -q' & -Q \end{pmatrix} \\
 & \times \frac{1}{2} \left[\Phi_{\gamma_b + \gamma_c}(\nu_{b_m a_m} - \xi') + \Phi_{\gamma_{b'} + \gamma_c}^*(\nu_{b'_m a_m} - \xi') \right] \\
 & \times \frac{1}{2} \left[\Phi_{\gamma_b + \gamma_c}(\nu_{b_m f_m} - \xi) + \Phi_{\gamma_{b'} + \gamma_c}^*(\nu_{b'_m f_m} - \xi) \right] \\
 & \times \cos \beta_{b'_m b_m} \cos \alpha_{b'_m b_m} e^{i(\beta_{b'_m b_m} + \alpha_{b'_m b_m})}, \tag{4.25}
 \end{aligned}$$

which is a useful relation that helps in the identification of the multipolar index K . An equivalent relation, but for the case of m -state interference, is Equation (22) of [Bommier \(1997b\)](#).

Comparing the terms in the flower brackets of Equation (4.21) with the RHS of Equation (4.25), we can see that they are the same (except for some factors). Therefore after substituting the terms in the flower brackets of Equation (4.21) with the LHS of Equation (4.25), we assume $\gamma_c/2 = D^{(K)}$ as a reasonable approximation (see [Stenflo, 1994](#)), where $D^{(K)}$ is the $2K$ multipole collisional destruction rate. Further, following [Bommier & Stenflo \(1999\)](#), we identify $\gamma_b = \Gamma_{Rb} + \Gamma_{Ib}$ and $\gamma_c = \Gamma_E$, where Γ_{Rb} is the radiative width of the fine structure state J_b . Γ_{Ib} is the total inelastic collision rate defined for the state J_b . It is given by

$$\Gamma_{Ib} = \sum_f \Gamma_{Ibf} + \sum_{b' \neq b} \Gamma_{Ibb'}. \tag{4.26}$$

Here Γ_{Ibf} couple the upper state J_b to the lower state J_f and $\Gamma_{Ibb'}$ couples the two fine structure states J_b and $J_{b'}$. Indeed such a definition of total inelastic collision rates can be found in [Omont et al. \(1972\)](#) and also in Equations (2.15)-(2.20) of [Heinzl & Hubený \(1982\)](#). Γ_E is the elastic collision rate and $D^{(K)}$ represent the depolarizing elastic collisions that couple the Zeeman substates (m -states) of a given J_b -state. In general $D^{(K)}$ may be different for each of the fine structure components with quantum number J_b . However, as an approximation we assume them to be independent of the J -quantum number. Thus Equation (4.21) can be rewritten as

$$\begin{aligned}
 \mathbf{R}_{ij}^{\text{III}}(\xi, \mathbf{n}; \xi', \mathbf{n}', \mathbf{B}) &= \frac{2}{9} (2L_a + 1)^2 \sum_{KK'K''Qafb b'} B_{bb'}^{(K)} Z_6 \\
 & \times (-1)^Q \mathcal{T}_Q^{K''}(i, \mathbf{n}) \mathcal{T}_{-Q}^{K'}(j, \mathbf{n}') \Phi_Q^{K, K'}(a, b', b; \xi') \Phi_Q^{K, K''}(f, b', b; \xi), \tag{4.27}
 \end{aligned}$$

where $B_{bb'}^{(K)}$ is the collisional branching ratio defined as

$$B_{bb'}^{(K)} = \frac{\bar{\Gamma}_R^{bb'}}{\bar{\Gamma}_R^{bb'} + \bar{\Gamma}_I^{bb'} + D^{(K)}} \frac{\Gamma_E - D^{(K)}}{\bar{\Gamma}_R^{bb'} + \bar{\Gamma}_I^{bb'} + \Gamma_E}. \tag{4.28}$$

Also, the branching ratio $A_{bb'}$ can be written as

$$A_{bb'} = \frac{\bar{\Gamma}_R^{bb'}}{\bar{\Gamma}_R^{bb'} + \bar{\Gamma}_I^{bb'} + \Gamma_E}, \quad (4.29)$$

where

$$\bar{\Gamma}_R^{bb'} = \frac{\Gamma_{Rb} + \Gamma_{Rb'}}{2}; \quad \bar{\Gamma}_I^{bb'} = \frac{\Gamma_{Ib} + \Gamma_{Ib'}}{2}, \quad (4.30)$$

with Γ_{Ib} defined in Equation (4.26). The total damping rates that appear in the branching ratios are the same as those that appear in the denominator of the Hanle angles (see Equations (4.12) and (4.34)). Therefore the $J_b J_{b'}$ dependence of the branching ratios defined now for a two-term atom is self-consistent. We have verified that when we set $J_b = J_{b'}$ and $J_a = J_f$ (the case of a two-level atom with only m -state interference) in Equation (4.27), we recover Equation (49) of [Bommier \(1997b\)](#).

4.3.2 Redistribution matrix \mathbf{R}^{III} in laboratory frame

We convert Equation (4.27) into the laboratory frame using the same procedure as described in Section 2.2 of [Sampoorna et al. \(2007b\)](#). The resulting expression for the normalized type-III redistribution matrix in the laboratory frame can be written as

$$\begin{aligned} \mathbf{R}_{ij}^{\text{III}}(x, \mathbf{n}; x', \mathbf{n}', \mathbf{B}) &= \frac{2L_b + 1}{2S + 1} \sum_{KK'K''Qafbb'} Z_6 B_{bb'}^{(K)} \\ &\times (-1)^Q \mathcal{T}_Q^{K''}(i, \mathbf{n}) \mathcal{T}_{-Q}^{K'}(j, \mathbf{n}') \mathcal{R}_{Q,\text{III}}^{K'',K,K'}(x, x', \Theta, \mathbf{B}), \end{aligned} \quad (4.31)$$

where $\mathcal{R}_{Q,\text{III}}^{K'',K,K'}(x, x', \Theta, \mathbf{B})$ is the laboratory frame redistribution function obtained after transformation of the atomic frame functions $\Phi_Q^{K,K'}(a, b', b; \xi') \Phi_Q^{K,K''}(f, b', b; \xi)$. The factors $(2L_b + 1)/(2S + 1)$ result from the renormalization of Equation (4.27). The function $\mathcal{R}_{Q,\text{III}}^{K'',K,K'}$ has the following form :

$$\begin{aligned} \mathcal{R}_{Q,\text{III}}^{K'',K,K'}(x, x', \Theta, \mathbf{B}) &= \sum_{\mu_a \mu_f \mu_b \mu_{b'} \mu_{b''} \mu_{b'''} q q' q''} \frac{3}{4} G(2K + 1) \sqrt{(2K' + 1)(2K'' + 1)} \\ &\times (-1)^{1+J_b - \mu_{b'} + q'} (-1)^{1+J_b - \mu_{b''} + q} \cos \beta_{b' m b_m} \cos \alpha_{b'' m b'' m}^{(K)} e^{i(\beta_{b' m b_m} + \alpha_{b'' m b'' m}^{(K)})} \\ &\times \begin{pmatrix} J_b & J_a & 1 \\ -\mu_b & \mu_a & -q' \end{pmatrix} \begin{pmatrix} J_{b'} & J_a & 1 \\ -\mu_{b'} & \mu_a & -q''' \end{pmatrix} \begin{pmatrix} J_b & J_{b'} & K \\ \mu_b & -\mu_{b'} & -Q \end{pmatrix} \begin{pmatrix} 1 & 1 & K' \\ q''' & -q' & -Q \end{pmatrix} \\ &\times \begin{pmatrix} J_b & J_f & 1 \\ -\mu_{b''} & \mu_f & -q \end{pmatrix} \begin{pmatrix} J_{b'} & J_f & 1 \\ -\mu_{b'''} & \mu_f & -q'' \end{pmatrix} \begin{pmatrix} J_b & J_{b'} & K \\ \mu_{b''} & -\mu_{b'''} & -Q \end{pmatrix} \begin{pmatrix} 1 & 1 & K'' \\ q'' & -q & -Q \end{pmatrix} \\ &\times \left\{ \left[R_{b' m a_m, b'' m f_m}^{\text{III, HH}} + R_{b' m a_m, b'' m f_m}^{\text{III, HH}} + R_{b m a_m, b'' m f_m}^{\text{III, HH}} + R_{b m a_m, b'' m f_m}^{\text{III, HH}} \right] \right. \\ &\left. + i \left[R_{b' m a_m, b'' m f_m}^{\text{III, FH}} + R_{b' m a_m, b'' m f_m}^{\text{III, FH}} - R_{b m a_m, b'' m f_m}^{\text{III, FH}} - R_{b m a_m, b'' m f_m}^{\text{III, FH}} \right] \right\} \end{aligned}$$

$$\begin{aligned}
 & +i \left[R_{b'ma_m, b''_m f_m}^{\text{III, HF}} - R_{b'_m a_m, b''_m f_m}^{\text{III, HF}} + R_{b_m a_m, b''_m f_m}^{\text{III, HF}} - R_{b_m a_m, b''_m f_m}^{\text{III, HF}} \right] \\
 & - \left[R_{b'ma_m, b''_m f_m}^{\text{III, FF}} - R_{b'_m a_m, b''_m f_m}^{\text{III, FF}} - R_{b_m a_m, b''_m f_m}^{\text{III, FF}} + R_{b_m a_m, b''_m f_m}^{\text{III, FF}} \right] \Big\}. \quad (4.32)
 \end{aligned}$$

The results presented in Section 4.5 are computed using Equation (4.31) for the type-III and Equation (2.22) for the type-II redistribution matrix. The total redistribution matrix in the laboratory frame is the same as Equation (4.20). In the non-magnetic case

$$\begin{aligned}
 \mathbf{R}_{ij}^{\text{III}}(x, \mathbf{n}; x', \mathbf{n}') &= \frac{3(2L_b + 1)}{2S + 1} \sum_{KQafbb'} G Z_6 (-1)^{J_f - J_a} B_{bb'}^{(K)} \cos \beta_{b'b} \cos \alpha_{b'b}^{(K)} \\
 &\times e^{i(\beta_{b'b} + \alpha_{b'b}^{(K)})} \left[h_{ba, b'f}^{\text{III}} + i f_{ba, b'f}^{\text{III}} \right] \begin{Bmatrix} 1 & 1 & K \\ J_{b'} & J_b & J_a \end{Bmatrix} \begin{Bmatrix} 1 & 1 & K \\ J_{b'} & J_b & J_f \end{Bmatrix} \\
 &\times (-1)^Q \mathcal{T}_Q^K(i, \mathbf{n}) \mathcal{T}_{-Q}^K(j, \mathbf{n}'). \quad (4.33)
 \end{aligned}$$

The angle $\beta_{b'b}$ and the auxiliary functions $h_{ba, b'f}^{\text{III}}$ and $f_{ba, b'f}^{\text{III}}$ are defined respectively in Equations (4.12), (4.16) and (4.17), but with $\nu_L = 0$. The angles $\alpha_{b'b}^{(K)}$ and $\beta_{b'b}$ (arising exclusively from J -state interference) are defined as

$$\tan \alpha_{b'b}^{(K)} = \frac{\omega_{b'b}}{\bar{\Gamma}_R^{b'b} + \bar{\Gamma}_I^{b'b} + D^{(K)}}; \quad \tan \beta_{b'b} = \frac{\omega_{b'b}}{\bar{\Gamma}_R^{b'b} + \bar{\Gamma}_I^{b'b} + \Gamma_E}, \quad (4.34)$$

with $\bar{\Gamma}_R^{b'b} = \bar{\Gamma}_R^{bb'}$ and $\bar{\Gamma}_I^{b'b} = \bar{\Gamma}_I^{bb'}$ (see Equation (4.30)). These branching ratios can be recovered from the more general two-term atom expressions given in Equations (4.28) and (4.29) by neglecting $\Gamma_{Ibb'}$. This is equivalent to setting $J_b = J_{b'}$ in Equations (4.28) and (4.29). The angle-averaged redistribution matrices corresponding to the angle-dependent redistribution matrices presented in Equations (4.31)-(4.33) can be recovered by replacing the angle-dependent redistribution functions (Equations (C.1)-(C.4)) by their angle-averaged analogues. These angle-averaged functions are obtained by numerical integration of the angle-dependent functions over the scattering angle Θ (see Equation (C.6)).

4.4 The polarized radiative transfer equation

The polarized radiative transfer equation for the Stokes vector \mathbf{I} in a one-dimensional planar medium for the Hanle scattering problem can be written as

$$\mu \frac{\partial \mathbf{I}(\tau, x, \mathbf{n})}{\partial \tau} = (\phi(x) + r) [\mathbf{I}(\tau, x, \mathbf{n}) - \mathbf{S}(\tau, x, \mathbf{n})], \quad (4.35)$$

where the notations are the same as those used in Chapter 3, with the positive Stokes Q representing electric vector vibrations perpendicular to the solar limb. This definition is

opposite to the way in which the positive Stokes Q is defined in the observed spectra. This can easily be accounted for (through a sign change), when comparing the observed spectra with the theoretical results. $\mathbf{n} = (\vartheta, \varphi)$ defines the ray direction where ϑ and φ are the inclination and azimuth of the scattered ray with $\mu = \cos \vartheta$ (see Figure 2.2). In the weak magnetic field limit, the Stokes vector $\mathbf{I} = (I, Q, U)^T$ and the Stokes source vector $\mathbf{S} = (S_I, S_Q, S_U)^T$. In this limit, the transfer equation for Stokes V decouples from that of the Stokes vector $(I, Q, U)^T$. This is known as the weak field approximation. In Equation (4.35), the Stokes vector \mathbf{I} and the Stokes source vector \mathbf{S} depend on \mathbf{n} . In the case of angle-averaged redistribution, it was shown by Frisch (2007) that one can decompose \mathbf{S} and \mathbf{I} into six cylindrically symmetric components \mathcal{I}_Q^K and \mathcal{S}_Q^K with the help of the irreducible spherical tensors for polarimetry (See Landi Degl'Innocenti (1984)). Here, $K = 0, 2$ and $-K \leq Q \leq +K$. Such a decomposition results in a reduced Stokes vector \mathcal{I} which is independent of φ and a reduced source vector \mathcal{S} which is independent of both ϑ and φ . We denote the quantities in the reduced basis by calligraphic letters and in Stokes basis by Roman. In such a reduced basis the transfer equation can be written as

$$\mu \frac{\partial \mathcal{I}(\tau, x, \mu)}{\partial \tau} = (\phi(x) + r)[\mathcal{I}(\tau, x, \mu) - \mathcal{S}(\tau, x)]. \quad (4.36)$$

The reduced source vector is defined as

$$\mathcal{S}(\tau, x) = \frac{\phi(x)\mathcal{S}_I(\tau, x) + r\mathcal{G}(\tau)}{\phi(x) + r}, \quad (4.37)$$

where $\mathcal{G}(\tau) = \{B, 0, 0, 0, 0, 0\}^T$ is the primary source vector. The reduced line source vector is given by

$$\mathcal{S}_I(\tau, x) = \sum_{bb'} \left[\epsilon_{bb'} \mathcal{G}(\tau) + \int_{-\infty}^{+\infty} \frac{\mathcal{R}_{bb'}(x, x', \mathbf{B})}{\phi(x)} \mathcal{J}(\tau, x') dx' \right], \quad (4.38)$$

where $\mathcal{R}_{bb'}(x, x', \mathbf{B})$ is the redistribution matrix for a two-term atom, with the summation over J_b and $J_{b'}$ not yet performed. The thermalization parameter is given by

$$\epsilon_{bb'} = \frac{\overline{\Gamma}_I^{bb'}}{\overline{\Gamma}_R^{bb'} + \overline{\Gamma}_I^{bb'}}. \quad (4.39)$$

The computation of the above defined reduced line source vector is very expensive because of the summations over J_b and $J_{b'}$ which need to be performed at each iteration. However for all practical applications, we can assume ϵ to be the same for all the $J_b J_{b'}$ states, which is a good approximation. Such an approximate ϵ is constructed by taking an average value of Γ_{Ib} for all transitions involving $J_b, J_{b'}$ and J_f , and an average value

of Γ_R for all the upper fine structure states. Under such an approximation,

$$\mathbf{S}_I(\tau, x) = \epsilon \mathbf{G}(\tau) + \int_{-\infty}^{+\infty} \frac{\mathcal{R}(x, x', \mathbf{B})}{\phi(x)} \mathcal{J}(\tau, x') dx'. \quad (4.40)$$

The mean intensity $\mathcal{J}(\tau, x)$ is defined by

$$\mathcal{J}(\tau, x) = \frac{1}{2} \int_{-1}^{+1} \Psi(\mu') \mathcal{I}(\tau, x, \mu') d\mu'. \quad (4.41)$$

The elements of the $\Psi(\mu)$ matrix are given in Landi Degl'Innocenti & Landolfi (2004) (see also Appendix A of Frisch (2007)). $\mathcal{R}(x, x', \mathbf{B})$ appearing in Equation (4.38) is a (6×6) diagonal matrix. The explicit form of this redistribution matrix with and without the presence of magnetic fields is defined in the following sections. In the absence of a magnetic field, only the \mathcal{I}_0^0 and \mathcal{I}_0^2 components contribute to the Stokes vector. Hence the (6×6) problem reduces to a (2×2) problem. The transfer equation defined in Equation (4.36) is solved using the traditional polarized accelerated lambda iteration technique presented in Chapter 3.

4.4.1 The redistribution matrix for the non-magnetic case

In the absence of a magnetic field the redistribution matrix in Equation (4.38) becomes independent of \mathbf{B} and reduces to a (2×2) diagonal matrix with elements $\mathcal{R}(x, x') = \text{diag}(\mathcal{R}^0, \mathcal{R}^2)$. The elements \mathcal{R}^K are defined as

$$\begin{aligned} \mathcal{R}^K(x, x') &= \frac{3(2L_b + 1)}{2S + 1} \sum_{bb'af} GZ_6(-1)^{J_f - J_a} \begin{Bmatrix} 1 & 1 & K \\ J_{b'} & J_b & J_a \end{Bmatrix} \begin{Bmatrix} 1 & 1 & K \\ J_{b'} & J_b & J_f \end{Bmatrix} \\ &\times \left\{ A_{bb'} \cos \beta_{b'b} e^{i\beta_{b'b}} \left[(h_{b,b'}^{\text{II}})_{af} + i(f_{b,b'}^{\text{II}})_{af} \right] \right. \\ &\left. + B_{bb'}^{(K)} \cos \beta_{b'b} \cos \alpha_{b'b}^{(K)} e^{i(\beta_{b'b} + \alpha_{b'b}^{(K)})} \left[h_{ba,b'f}^{\text{III}} + i f_{ba,b'f}^{\text{III}} \right] \right\}. \end{aligned} \quad (4.42)$$

The $(h_{b,b'}^{\text{II}})_{af}$ and $(f_{b,b'}^{\text{II}})_{af}$ are auxiliary functions for type-II defined in Equations (2.14) and (2.15) and the auxiliary functions for type-III are defined in Equations (4.16) and (4.17). They are used here for the non-magnetic case and with the angle-averaged redistribution functions of type-II and type-III. In the limit of a two-level atom model ($J_b = J'_b$ and $J_a = J_f$), the $(h_{b,b'}^{\text{II}})_{af}$ and $h_{ba,b'f}^{\text{III}}$ go respectively to R^{II} and R^{III} functions of Hummer, whereas the $(f_{b,b'}^{\text{II}})_{af}$ and $f_{ba,b'f}^{\text{III}}$ and the angles $\beta_{b'b}$ and $\alpha_{b'b}^{(K)}$ go to zero.

4.4.2 The redistribution matrix for the magnetic case

The redistribution matrix for a two-term atom defined in Equation (4.20) involves summations over the total angular momentum quantum numbers and the corresponding

magnetic quantum numbers. This does not allow direct decomposition to go from the Stokes vector basis to the reduced basis (see Section 4.4 for details on these two basis). Such a decomposition is possible in the non-magnetic case. This is because in the absence of a magnetic field, the summations over the magnetic quantum numbers can be analytically performed using Racah algebra as shown in Chapter 2 for type-II redistribution and Equation (4.33) for type-III redistribution. However in the magnetic case, all the summations remain intact and have to be performed numerically. This is very expensive. Because of these difficulties, we need to resort to the weak field approximation which allows us to apply the decomposition technique. In this regard, the summations over the J -quantum numbers can be split into three different terms namely

$$\begin{aligned} \mathcal{R}(x, x', \mathbf{B}) = & \sum_{b=b', a=f} \mathcal{R}_{b,a}^A(x, x', \mathbf{B}) + \sum_{b \neq b', a, f} \mathcal{R}_{b,b',a,f}^B(x, x', \mathbf{B}) \\ & + \sum_{b=b', a \neq f} \mathcal{R}_{b,a,f}^C(x, x', \mathbf{B}). \end{aligned} \quad (4.43)$$

The first term represents the case of ‘Resonance’ scattering in a two-level atom model with a summation over all the lines of the multiplet (see Figure 4.1a). This contributes mainly to the cores and near wings of the lines within the multiplet. Its weak field analogue has already been derived in [Bommier \(1997b\)](#) and can be expressed as

$$\mathcal{R}^A(x, x', \mathbf{B}) = \sum_{ab} \mathcal{R}_{b,a}^A(x, x', \mathbf{B}) = \sum_{ab} \mathcal{W}_{b,a} \mathcal{R}_{b,a}^H(x, x', \mathbf{B}). \quad (4.44)$$

Here $\mathcal{R}_{b,a}^H(x, x', \mathbf{B})$ is the Hanle redistribution matrix for a two-level atom with $J_a \rightarrow J_b \rightarrow J_a$ scattering transition as presented in [Bommier \(1997b\)](#). This is also the same redistribution matrix defined in Appendix A of [Anusha et al. \(2011b\)](#), but for a $J_a \rightarrow J_b \rightarrow J_a$ scattering transition. The details of the domain based decomposition of this matrix are also given in the above paper. In the reduced basis, $\mathcal{R}^A(x, x', \mathbf{B})$ is a (6×6) matrix. $\mathcal{W}_{b,a}$ are the weights for each line component of the multiplet (derived from Equation (4.42) with $J_b = J_{b'}$ and $J_a = J_f$) and are given by

$$\mathcal{W}_{b,a} = \frac{(2L_b + 1)}{2S + 1} (2J_a + 1)^2 (2J_b + 1)^2 \left\{ \begin{matrix} L_a & L_b & 1 \\ J_b & J_a & S \end{matrix} \right\}^4. \quad (4.45)$$

The second term represents only the J -state interference between different lines of the multiplet (see Figure 4.1b). It includes both the ‘Resonance’ and the ‘Raman’ scattering parts and is effective mainly in the wings between the lines. This term is quite insensitive to the strength of the magnetic field. This can be seen from Figures 2.3 and 2.4 where the magnetic field effects are confined mainly to the line cores. Hence in this component we can set the magnetic field equal to zero as a good approximation.

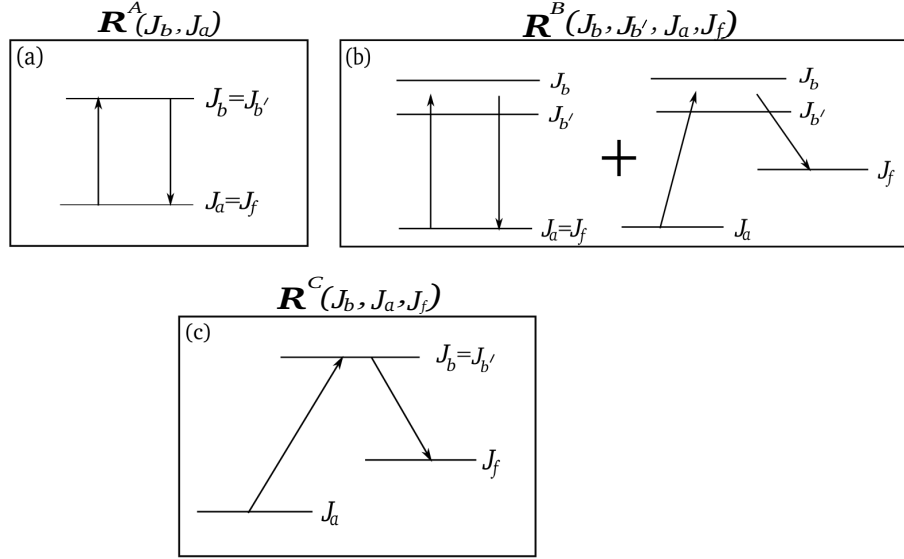


Figure 4.1: The schematic level diagrams representing the three components of the J -state redistribution matrix. Panels (a), (b), and (c) represent respectively the two-level atom resonance scattering, J -state interference, and Raman scattering (resonance fluorescence).

This makes the evaluation of both the Resonance and the Raman scattering parts similar to that performed in Chapter 3. In the reduced basis this term is simply given by a (6×6) matrix $\mathcal{R}^B(x, x')$ which is equal to $\text{diag}(\mathcal{R}^0, \mathcal{R}^2, 0, 0, 0, 0)$. Here \mathcal{R}^K are the redistribution functions which include the effects of collisions and the J -state interference between different line components in a multiplet defined in Equation (4.42). Only $J_b \neq J_b'$ terms are retained in the summations appearing in this equation. The $J_b = J_b'$ contributions are contained in the first term. However in some of the well known examples in the second solar spectrum like the Mg II h and k, Ca II H and K and the Cr I triplet, the initial and the final states are the same. Also for the case of the hypothetical doublet considered in this chapter, arising due to an $L = 0 \rightarrow 1 \rightarrow 0$ scattering transition with spin $S = 1/2$, the initial and the final states are the same. Hence the Raman scattering part does not play a role.

The third term represents the case of only Raman scattering without the J -state interference, where the initial and the final states are different (see Figure 4.1c). A derivation of the weak field analogue of this component (in a way similar to that of [Bommier \(1997b\)](#)) is yet to be performed. Recently [Sampoorna et al. \(2013\)](#) have proposed an approximate method to solve the polarized radiative transfer equation in case of Raman scattering. Again for some of the well known examples mentioned above, this component does not contribute. Thus the final expression for the redistribution matrix that is used in Equation (4.38) is

$$\mathcal{R}(x, x', \mathbf{B}) \approx \mathcal{R}^A(x, x', \mathbf{B}) + \mathcal{R}^B(x, x'). \quad (4.46)$$

4.5 Results and discussion

In this section, we study the effects of collisional redistribution matrix on the emergent Stokes profiles for the case of single scattering and also multiple scattering in an isothermal atmospheric slab. All the profiles presented in this chapter are computed for a hypothetical doublet line system with the line center wavelengths at 5000 Å and 5001 Å arising due to an $L = 0 \rightarrow 1 \rightarrow 0$ scattering transition with spin $S = 1/2$. The J quantum numbers of the lower and upper states are $J_a = J_f = 1/2$ and $J_b = 1/2, 3/2$. In Section 4.5.1 we present the scattered Stokes profiles resulting in a single 90° scattering case. In Section 4.5.2 we present the multiply scattered Stokes profiles emerging from an isothermal constant property atmospheric slab with and without the presence of a magnetic field.

4.5.1 The single 90° scattering case

To explore the general behavior of the redistribution matrix in the presence of collisions we illustrate the Stokes profiles that result from single 90° scattering event. We examine the influence of the elastic collisions on the Stokes profiles in the presence of a magnetic field. The magnetic field orientation is given by $\vartheta_B = 90^\circ$ and $\varphi_B = 45^\circ$ where the colatitude ϑ_B and azimuth φ_B characterize the magnetic field orientation with respect to the polar z -axis (see Figure 2.2). We consider an unpolarized ($\mathbf{I}_{in} = [1, 0, 0, 0]^T$) and spectrally flat (frequency independent) radiation field that is incident in the vertical direction (parallel to the polar z -axis). The singly scattered Stokes vectors are then exclusively determined by the first column of the angle-dependent redistribution matrix by integrating over the incident wavelengths. However in the multiple scattered solutions discussed in Section 4.5.2, we restrict our attention only to the angle-averaged redistribution matrix. The magnetic field strength is parametrized by the splitting parameter v_H given by

$$v_H = \frac{\lambda_0^2 e_0 B}{4\pi m c^2} \times \frac{1}{\Delta\lambda_D}, \quad (4.47)$$

where B is the magnetic field strength, e_0 is the charge of the electron and m its mass. $\Delta\lambda_D$ is the Doppler width and is assumed to be 0.025 Å for both the lines. The radiative width of the upper state is parametrized as $a_{Rb} = \Gamma_{Rb}/(4\pi\Delta\nu_D)$. It is assumed to be the same for both the lines and is chosen to be 0.001. The radiative width a_{Rb} is related to the total damping parameter through

$$a_b = a_{Rb} \left[1 + \left(\frac{\Gamma_{Ib} + \Gamma_E}{\Gamma_{Rb}} \right) \right]. \quad (4.48)$$

We assume the inelastic collision rate Γ_{Ib} to be zero.

The depolarizing collisional rates $D^{(2)} = 0.5\Gamma_E$, and $D^{(0)} = 0$. For simplicity we

set $D^{(1)} = D^{(2)}$. However in general they can differ (for example, $D^{(1)} = 0.43\Gamma_E$ and $D^{(2)} = 0.38\Gamma_E$ according to [Berman & Lamb \(1969\)](#)). We have verified that the Stokes V/I is insensitive to the values of $D^{(1)}$. The collisional effects are built into the \mathbf{R}

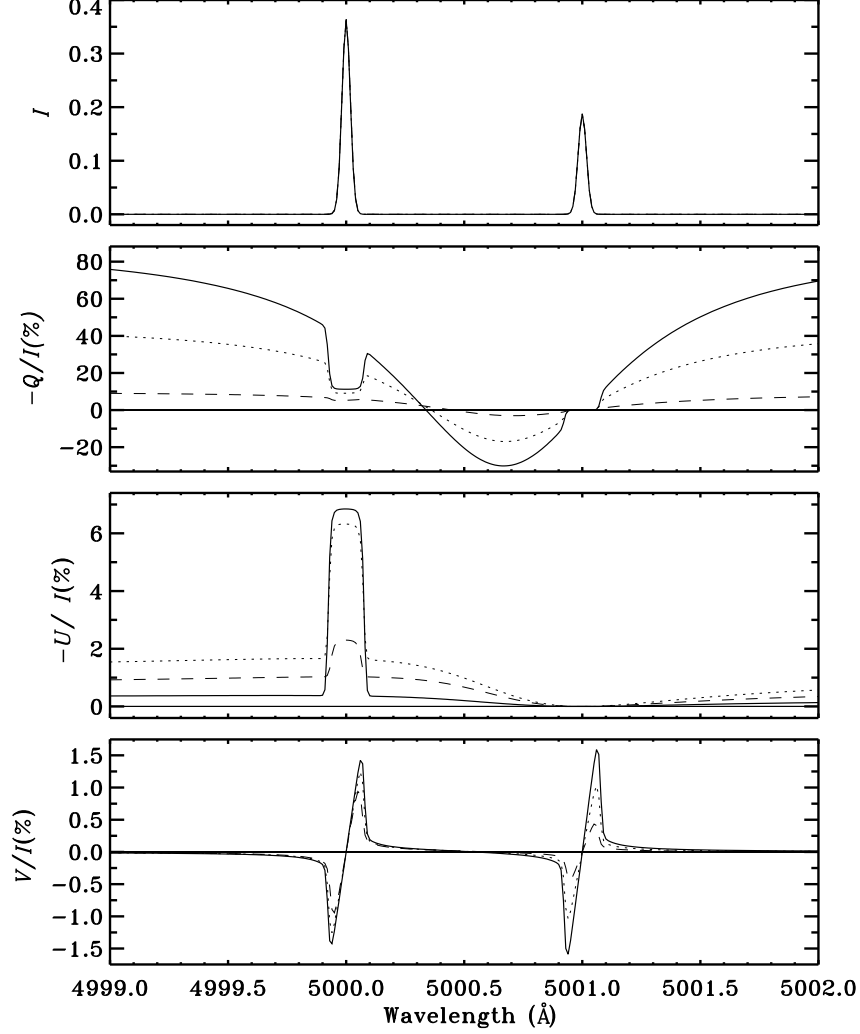


Figure 4.2: Effect of collisions: The profiles of the intensity I and the fractional polarizations $-Q/I$, $-U/I$ and V/I are plotted for a hypothetical doublet at 5000 \AA and 5001 \AA with field strength parameter $v_H = 0.004$. The coherence fractions used are $\gamma_{coh} = 0.9$ (thick solid line), $\gamma_{coh} = 0.5$ (dotted line), and $\gamma_{coh} = 0.1$ (dashed line). The fine structure splitting is 1 \AA . Single 90° scattering is assumed. The model parameters are $a_R = 0.001$, $\vartheta_B = 90^\circ$ and $\varphi_B = 45^\circ$. The Doppler width $\Delta\lambda_D = 0.025 \text{ \AA}$.

matrix derived in Section 4.3 through the branching ratios defined in Equations (4.28) and (4.29). The elastic collision rate is parametrized through the coherence fraction γ_{coh} as $\gamma_{coh} = 1/[1 + (\Gamma_E/\bar{\Gamma}_R^{bb'})]$. In the present chapter we take Γ_R to be the same for both the upper fine structure states and γ_{coh} to be the same for all $J_b J_{b'}$ combinations. When $\gamma_{coh} = 1$ the redistribution is entirely radiative (only \mathbf{R}^{II}), whereas $\gamma_{coh} = 0$ represents purely collisional redistribution (only \mathbf{R}^{III}). We consider a range of values $\gamma_{coh} \in [1, 0]$ to represent an arbitrary mix of \mathbf{R}^{II} and \mathbf{R}^{III} type redistribution.

Figure 4.2 shows the Stokes ($I, Q/I, U/I, V/I$) spectra for a doublet. The polarization of the line at 5001 Å is zero because its polarizability factor $W_2 = 0$. The collisions affect the wavelength domain outside the line core region of this line. But for the line at 5000 Å, the collisional effects are seen both in the line wings and the line core. In the line core the collisional effects compete with the Hanle effect and in the wings it is an interplay between the J -state interference and collisional redistribution effects.

The value $\gamma_{coh} = 0.9$ corresponds to a mix with 90% of \mathbf{R}^{II} and 10% of \mathbf{R}^{III} (see the thick solid line in Figure 4.2). The profiles look similar to those for pure \mathbf{R}^{II} (see Figure 2.4). However, in Q/I there is a small depolarization, mainly in the wings, due to the presence of collisions. The core of the line at 5000 Å seems to be less affected than its wings. The Q/I at the 5001 Å line remains zero. In the presence of elastic collisions, a small U/I signal is generated in the wings of the 5000 Å line. This non-zero U/I wing polarization and the depolarization in the wings of Q/I are induced by the elastic collisions in combination with the magnetic field and can together be referred to as the ‘wing Hanle effect’. This effect arises because the elastic collisions can transfer the Hanle rotation (of the plane of polarization) from the line core to the line wings before spontaneous de-excitation intervenes. In other words, in the presence of a small but significant elastic collision rate the Hanle effect does not vanish in the line wings. If the elastic collision rate is large then the collisions completely depolarize the scattered radiation throughout the line profile. This effect has been discussed in detail in [Sampoorna et al. \(2007b\)](#) for the case of a $J = 0 \rightarrow 1 \rightarrow 0$ single scattering transition. However, these effects do not survive when the radiative transfer effects with angle-averaged PRD are explicitly taken into account. The collisional redistribution process is more effective in the case of angle-dependent PRD than in the case of angle-averaged PRD. Using the domain-based PRD theory of [Bommier \(1997b\)](#) this effect was noticed even in the radiative transfer computations of [Nagendra et al. \(2002\)](#) (see also [Nagendra et al. \(2003\)](#)). It remains as effective in a pair of interfering doublet lines as in the case of a single line. However, in [Sampoorna et al. \(2009\)](#) it was shown that the wing Hanle effect alone is insufficient to explain the observed wing signatures in the Q/I and U/I profiles of the Ca I 4227 Å line.

As γ_{coh} decreases to 0.5, which represents an equal mix of \mathbf{R}^{II} and \mathbf{R}^{III} , the values of Q/I in the wings of both the lines are significantly reduced (see dotted line in Figure 4.2). The collisional effects are now seen even in the core of the 5000 Å line. This results in a decrease of the Q/I and U/I signals at the center of this line. The J -state interference signatures in Q/I are also modified. When γ_{coh} is further reduced to 0.1, the effects of \mathbf{R}^{III} start to dominate over those of \mathbf{R}^{II} and also over the J -state interference effects (see dashed line in Figure 4.2). As a result the signatures of the J -state interference begin to fade away. The Q/I and U/I start to approach zero throughout the line profiles. As γ_{coh} is further decreased to 0.0001 (not shown in the figure), the colli-

sional effects (through \mathbf{R}^{III}) completely dominate the scattering process. This situation corresponds to a regime of extremely large line broadening. As a result the amplitude of I becomes much smaller compared to the other cases. Also, the Q/I , U/I , and V/I approach zero level throughout the line profiles.

4.5.2 Polarized line profiles formed due to multiple scattering in an atmospheric slab

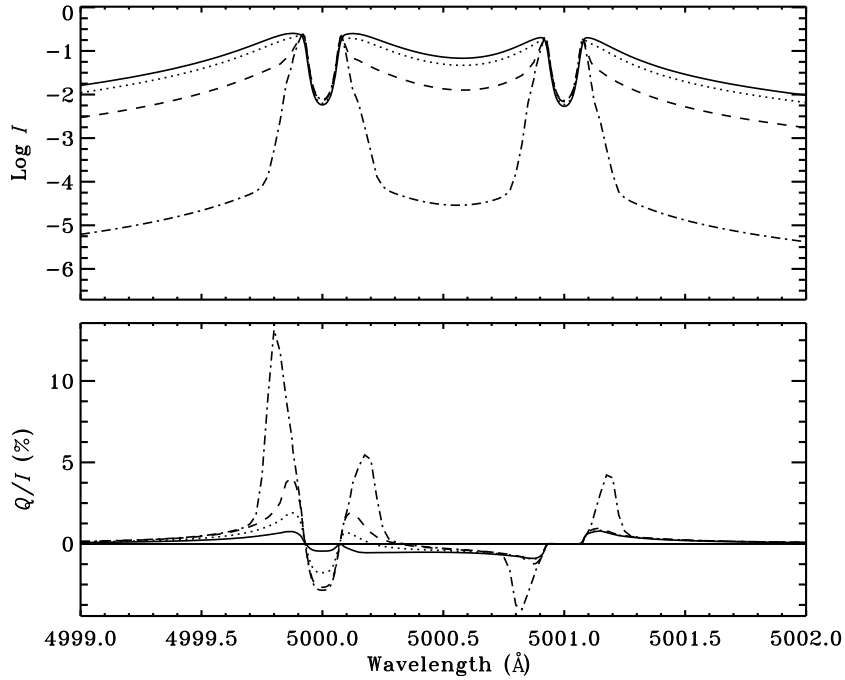


Figure 4.3: Emergent Stokes profiles at $\mu = 0.047$ computed for a slab of optical thickness $T = 2 \times 10^4$ in the absence of a background continuum. The other model parameters are $(a, \epsilon) = (10^{-3}, 10^{-4})$. The magnetic field strength is set to zero. The coherence fraction is $\gamma_{coh} = 0.1$ (solid line), $\gamma_{coh} = 0.5$ (dotted line), $\gamma_{coh} = 0.9$ (dashed line), and $\gamma_{coh} = 1$ (dot-dashed line).

In this section we present the emergent Stokes profiles computed by solving the polarized radiative transfer equation for a two-term atom including the effects of J -state interference and elastic collisions. For this we consider an isothermal constant property atmospheric slab with a given optical thickness T . The slabs are assumed to be self-emitting. The atmospheric model parameters used for the computations are represented by (T, a, ϵ) , where a is the damping parameter and ϵ is the thermalization parameter defined in Equation (4.39) and the paragraph that follows.

The Planck function B is taken as unity. The Doppler width for both the lines are assumed to be the same and equal to 0.025 \AA . For more details on the structure of the atmospheric slabs and the model parametrization we refer to Chapter 3.

The non-magnetic case

Figure 4.3 shows the emergent Stokes profiles which include the effects of J -state interference, elastic collisions and radiative transfer computed for a model atmosphere with parameters $T = 2 \times 10^4$, $a = 10^{-3}$ and $\epsilon = 10^{-4}$ in the absence of a background continuum. In these profiles the magnetic field is set to zero. Different line types represent different values of the coherence fraction γ_{coh} . A range of values of $\gamma_{coh} \in [1, 0]$ is considered. As seen from the Figure 4.3, a decrease in γ_{coh} results in a gradual decrease in Q/I in the line core as well as in the PRD peaks of the 5000 Å line. The intensity profiles are also quite sensitive to the effect of elastic collisions. As γ_{coh} goes from 1 (pure \mathbf{R}^{II} case) to 0.1 (\mathbf{R}^{III} dominated case), the self-reversed emission lines change over to nearly true absorption lines (thick solid lines). In Q/I the effects of collisions are confined only to the line core and the near wing PRD peaks. Specifically, it is shown by Nagendra (1994) that the elastic collisions $D^{(2)}$ depolarizes the line core, and Γ_E significantly depolarizes the line wing polarization (See Faurobert-Scholl (1992)). The same conclusions are valid in the two-term atom model also. The interference region between the two lines seems to be less sensitive to the effect of elastic collisions. However for

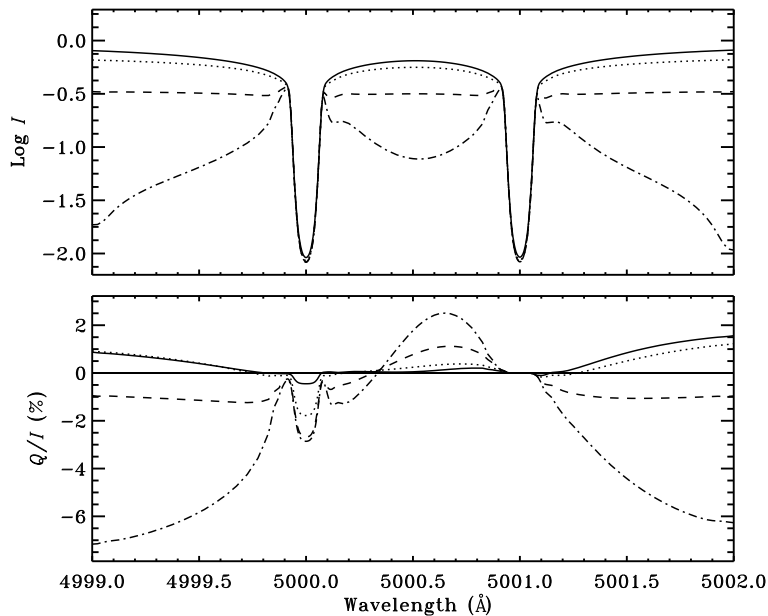


Figure 4.4: Same as Figure 4.3 but computed for an optical thickness $T = 2 \times 10^8$.

larger optical depths, significant dependence on γ_{coh} is exhibited in the wavelength region between the two lines. This can be seen in Figure 4.4 which shows the effect of elastic collisions in an optically thick atmospheric slab in the absence of a magnetic field. The model parameters are the same as in Figure 4.3 but with $T = 2 \times 10^8$. As γ_{coh} decreases, the collisions take over the line formation process. When $\gamma_{coh} = 0.1$ (thick solid line), deep absorption lines are formed in I with broad wings. The Q/I at the center of the 5000 Å line becomes very small like in Figure 4.3. The zero crossing

point at 5000.3 \AA remains the same for all the values of γ_{coh} . In general a depolarization in Q/I is seen throughout the line profile because the radiative transfer effect is significant at all the frequencies. As expected, the Q/I reaches zero very far in the wings of both the lines after exhibiting a wing maximum nearly 10 \AA away from their line centers. The difference in behavior in the line core as well as in the line wings of the Q/I profiles formed under \mathbf{R}^{II} dominated (dot-dashed line) and \mathbf{R}^{III} dominated (thick solid line) conditions are better seen for the $T = 2 \times 10^8$ case when compared to the $T = 2 \times 10^4$ case.

The magnetic case

Figure 4.5 shows a comparison between the emergent Stokes profiles computed with (dashed line) and without (solid line) the presence of a weak magnetic field including the effects of elastic collisions. The magnetic profiles are computed for a field strength of $v_H = 0.004$ with $\gamma_{coh} = 0.9$. The model parameters are $T = 2 \times 10^4$, $\epsilon = 10^{-4}$, $a = 10^{-3}$ in the absence of a background continuum. An external weak magnetic field (through the Hanle effect) affects the multiply scattered Stokes profiles in a way similar to the singly scattered Stokes profiles. The Hanle effect causes a depolarization in Q/I at the center of the 5000 \AA line and also generates a U/I signal at this line. We recall that these effects are not seen at the 5001 \AA line since its polarizability factor $W_2 = 0$. Like in the case of single scattered profiles, the magnetic field effects are confined only to the line core and the J -state interference signatures remain unaffected by the magnetic field. Also as discussed earlier, the wing Hanle effect in Q/I and U/I which were seen in the case of single scattered profiles in Figure 4.2 now disappear due to the radiative transfer effects.

4.6 Conclusions

In the present chapter, we have extended the theoretical framework for the J -state interference for type-II redistribution developed in Chapter 2 (see also Smitha et al., 2011b), to include the effects of collisions (type-III redistribution). The collisional PRD matrix is derived in the laboratory frame for a two-term atom with an unpolarized lower term and in the presence of magnetic fields of arbitrary strengths. However, the treatment is restricted to the linear Zeeman regime for which the Zeeman splitting is much smaller than the fine-structure splitting. The inelastic collisions coupling the upper term and the lower term and also the inelastic collisions coupling the fine structure states of the upper term are taken into account. However, the latter has been treated approximately. The approximation involves considering only the depolarizing effects of the inelastic collisions but neglecting the polarization transfer rates between the fine structure states.

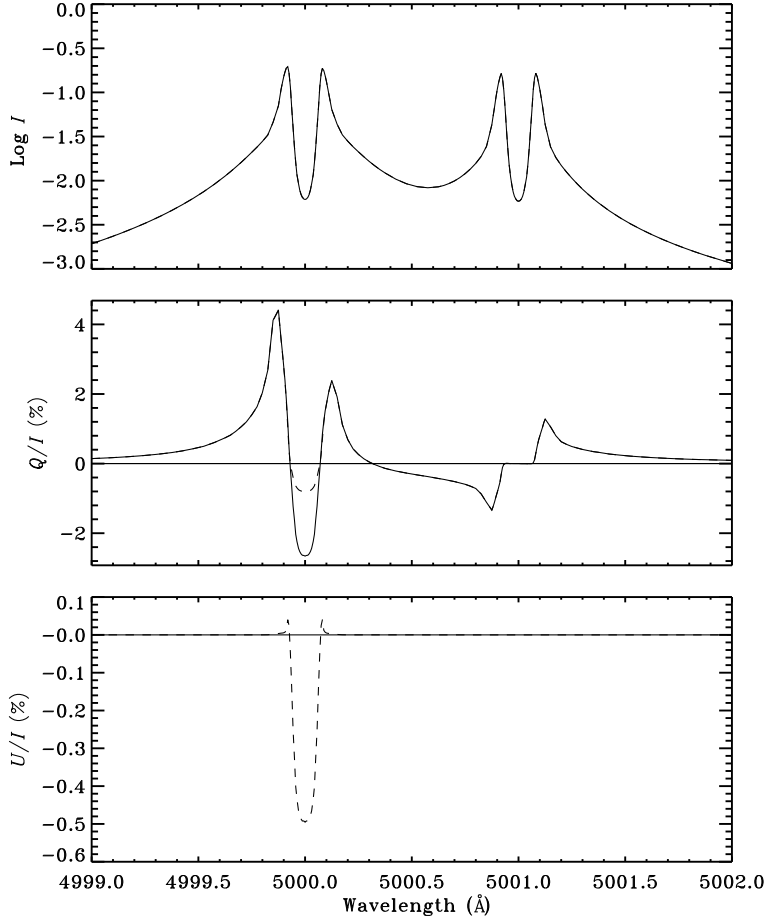


Figure 4.5: Emergent Stokes profiles at $\mu = 0.047$ computed for a magnetic field strength of $v_H = 0$ (solid line) and $v_H = 0.004$ (dashed line) with a coherence fraction $\gamma_{coh} = 0.9$ in the absence of a background continuum. The model parameters are $(T, a, \epsilon) = (2 \times 10^4, 10^{-3}, 10^{-4})$.

The depolarization caused by the inelastic collisions has the same type of consequences as the depolarization by elastic collisions. Therefore we can merge both these effects into a common damping rate for the state J_b and appropriately redefine the branching ratios and the thermalization parameter for a two-term atom. A proper treatment of the inelastic collisions which cause polarization transfer requires formulating and solving the polarized statistical equilibrium equations. This is outside the scope of the present thesis. The approximate treatment presented in this chapter leads to slightly larger values of polarization in the line core as the inelastic collisions are not handled exactly. A treatment involving the statistical equilibrium equation would yield correct values of linear polarization. However in the line wings the formulation presented here becomes accurate enough and would give the same result as a full treatment in terms of statistical equilibrium equation, including PRD mechanism.

The collisional frequency shift is inherently built into redistribution matrix through the type-III redistribution function and the branching ratios. We discuss in detail the procedure of assigning the correct multipolar index K to the collisional branching ratio

and depolarizing elastic collision rate $D^{(K)}$. This procedure requires a detailed understanding of the role played by the multipolar index K for both the atom and the radiation field. We show how it becomes necessary to introduce a quantum generalized profile function for the case of a two-term atom in order to assign appropriate index K to the branching ratios and to $D^{(K)}$. In general $D^{(K)}$ is defined for each of the fine structure components (by making it depend on the quantum number J_b). However in the present treatment we assume it to be independent of the J -quantum number.

Examples of the Stokes profiles resulting from single 90° scattering are illustrated for different values of the coherence fraction γ_{coh} . The profiles look similar to the ones presented in Chapter 2, which were computed using collisionless redistribution (the case of pure \mathbf{R}^{II}), except for the depolarization in the wings of the Q/I profiles, and non-zero polarization in the wings of the U/I profiles. This interesting feature, which we refer to as the wing Hanle effect, is discussed.

The effects of collisions are discussed by incorporating the newly derived collisional redistribution matrix in the polarized radiative transfer equation, in the simpler case of isothermal slab models. The technique of incorporating the Hanle redistribution matrix with the J -state interference and collisions, into the polarized radiative transfer equation for a two-term atom is presented. It is shown that the effects of elastic collisions in a two-term atom are similar to those of the two-level atom case. The redistribution matrices derived here have been used in the interpretation of the quantum interference signatures seen in the limb observations of the Cr I triplet in [Smitha et al. \(2012a\)](#), which will be discussed in Chapter 5). For simplicity the inelastic collisions between the fine structure states are neglected in that realistic modeling effort.

With the present work we have further extended the theoretical tools that are needed for modelling the various spectral structures arising due to the transitions between fine structure states of an atom that have been observed in the Second Solar Spectrum so that they can be used to diagnose magnetic fields in regimes not accessible to the Zeeman effect. This will be used in realistic modeling of the Cr I triplet in the next chapter.

Based on:

Smitha, H. N., Nagendra, K. N., Stenflo, J. O., Bianda, M., Samporna, M., Ramelli, R., & Anusha, L. S. 2012, *A&A*, 541, 24

5

Modeling the Cr I triplet at 5204-5208 Å in the Second Solar Spectrum

An Overview

The scattering polarization in the solar spectrum is traditionally modeled with each spectral line treated separately, but this is generally inadequate for multiplets where J -state interference plays a significant role. In this chapter, through simultaneous observations of all the 3 lines of the Cr I triplet around 5206 Å, combined with realistic radiative transfer modeling of the data, we show that it is necessary to include J -state interference consistently when modeling lines with partially interacting fine structure components. Polarized line formation theory developed in previous chapters is used to model the observations. We show that the resonance polarization in the Cr I triplet is strongly affected by the partial frequency redistribution (PRD) effects in the line core and near wing peaks. The Cr I triplet is quite sensitive to the temperature structure of the photospheric layers. Our complete frequency redistribution (CRD) calculations in semi-empirical models of the solar atmosphere cannot reproduce the observed near wing polarization or the cross-over of the Stokes Q/I line polarization about the continuum polarization level that is due to the J -state interference. When however PRD is included, a good fit to these features can be achieved. Further, to obtain a good fit to the far wings, a small temperature enhancement of the FALF model in the photospheric layers is necessary.

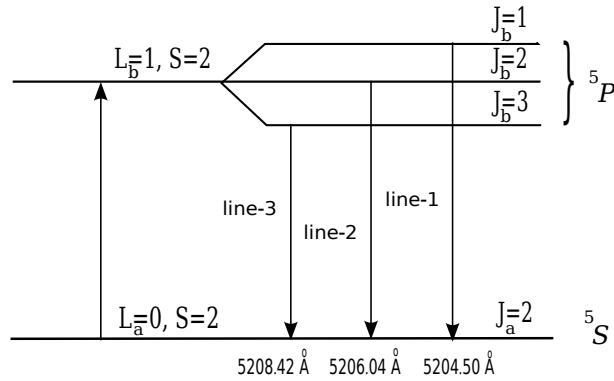


Figure 5.1: The term diagram showing transitions in the Cr I triplet. The diagram is not drawn to scale.

5.1 Introduction

Modeling the Second Solar Spectrum requires the solution of the polarized radiative transfer (RT) equation. It is well known that quantum interference between the fine structure (J) levels is responsible for the formation of line pairs such as the Na I D_1 and D_2 , Ca II H and K, etc. A theoretical framework which includes the quantum interference effects was developed in [Stenflo \(1980, 1997\)](#). This was used for RT modeling of J -state interference in the Na I D_1 and D_2 lines by [Fluri et al. \(2003a\)](#). The J -state interference theory used in the mentioned papers assumed frequency coherent scattering. In Chapter 2 (see also [Smitha et al., 2011b](#)), we have extended the theory of [Stenflo \(1997\)](#) to include PRD with J -state interference. It is restricted to the case of a two-term atom and uses the assumption that the lower term is unpolarized. In Chapter 3 (see also [Smitha et al., 2011a](#)), the redistribution matrix for the J -state interference derived in Chapter 2 was incorporated into the RT equation, which was solved for simple isothermal model atmospheres. Several theoretical aspects of RT in a hypothetical doublet line system were studied. The purpose of the present chapter is to perform one-dimensional RT modeling of the polarimetric observations of a multiplet where J -state interference is relevant. For this we have selected the Cr I triplet at 5204.50 \AA (line-1: $J_b = 1 \rightarrow J_a = 2$), 5206.04 \AA (line-2: $J_b = 2 \rightarrow J_a = 2$), and 5208.42 \AA (line-3: $J_b = 3 \rightarrow J_a = 2$). Hyperfine splitting can be neglected because the most abundant (90%) isotope of Cr I has zero nuclear spin.

[Kleint et al. \(2010a,b\)](#) have used the Cr I triplet for a synoptic program to explore solar cycle variations of the microturbulent field strength. Recently, [Belluzzi & Trujillo Bueno \(2011\)](#) applied the density matrix theory described in [Landi Degl'Innocenti & Landolfi \(2004\)](#) (which is based on the CRD approximation) in order to perform a basic investigation on the impact of J -state interference in several important multiplets in the solar spectrum including also the Cr I triplet. In this work they have neglected RT and PRD effects. However, they have included the effects of lower term polarization

and the dichroism. They identify and explain qualitatively the observational signatures produced by J -state interference in the Cr I triplet (i.e., the cross-over of Q/I about the continuum polarization level occurring between the lines, and the Q/I feature around the line-1 core).

In Section 5.2 we briefly present the basic equations required for realistic RT modeling of lines in the two-term atom picture. In Section 5.3 we present the polarimetric observations of the Cr I triplet. Section 5.4 is devoted to a description of realistic modeling of the observations. In Section 5.5 we present the main results. Concluding remarks are given in Section 5.6.

5.2 Polarized line transfer equation for a two-term atom

In a non-magnetic medium, polarization of the radiation field is represented by the Stokes vector $(I, Q)^T$, where positive Q is defined to represent linear polarization that is oriented parallel to the solar limb. In a medium that is axisymmetric around the vertical direction, it is advantageous to use a formulation in terms of the reduced Stokes vector \mathcal{I} instead of the traditional Stokes vector $(I, Q)^T$. The transformations between the two can be found in Appendix B of Frisch (2007). The relevant line transfer equation for the 2-component reduced Stokes vector is

$$\mu \frac{\partial \mathcal{I}(\lambda, \mu, z)}{\partial z} = -k_{\text{tot}}(\lambda, z) [\mathcal{I}(\lambda, \mu, z) - \mathcal{S}(\lambda, z)], \quad (5.1)$$

in standard notation (see Anusha et al., 2011b). z is the geometric height in the atmosphere. See Chapter 3 for details of Equation (5.1) and related quantities. The total opacity $k_{\text{tot}}(\lambda, z) = \eta_M(\lambda, z) + \sigma_c(\lambda, z) + k_c(\lambda, z)$, where σ_c and k_c are the continuum scattering and continuum absorption coefficients, respectively. The line absorption coefficient for the entire multiplet is

$$\eta_M(\lambda, z) = k_M(z) \phi_M(\lambda, z) = \sum_{J_a J_b} k_{l(J_b J_a)} \phi(\lambda_{J_b J_a}, z), \quad (5.2)$$

where $k_{l(J_b J_a)}$ is the wavelength averaged absorption coefficient for the $J_a \rightarrow J_b$ transition with the corresponding profile function denoted by $\phi(\lambda_{J_b J_a}, z)$. J_b and J_a are the total angular momentum quantum numbers of the fine-structure levels for the upper and lower terms (see Figure 5.1). $k_M(z)$ is the wavelength averaged absorption coefficient for the entire multiplet. For our case of a two-term atom, we need to define a combined profile function that determines the shape of the absorption coefficient across the whole multiplet. It can be shown that for the Cr I triplet line system $\phi_M(\lambda, z)$ is given by (see

Equations (3.7) and (3.8))

$$\phi_M(\lambda, z) = \frac{3\phi(\lambda_{12}, z) + 5\phi(\lambda_{22}, z) + 7\phi(\lambda_{32}, z)}{15}. \quad (5.3)$$

The reduced source vector is defined as

$$\mathcal{S}(\lambda, z) = \frac{k_M(z)\phi_M(\lambda, z)\mathcal{S}_l(\lambda, z) + \sigma_c(\lambda, z)\mathcal{S}_c(\lambda, z) + k_c(\lambda, z)\mathcal{S}_{\text{th}}(\lambda, z)}{k_{\text{tot}}(\lambda, z)}, \quad (5.4)$$

for a two-term atom with an unpolarized lower term. Here $\mathcal{S}_{\text{th}} = (B_\lambda, 0)^T$, where B_λ is the Planck function. The continuum scattering source vector is

$$\mathcal{S}_c(\lambda, z) = \frac{1}{2} \int_{-1}^{+1} \hat{\Psi}(\mu') \mathcal{I}(\lambda, \mu', z) d\mu'. \quad (5.5)$$

Since continuum polarization can be seen as representing scattering in the distant wings of spectral lines (in particular from the Lyman series lines, cf. Stenflo, 2005), we are justified to use the assumption of frequency coherent scattering for the continuum. The matrix $\hat{\Psi}$ is the Rayleigh scattering phase matrix in the reduced basis (see Frisch, 2007). The line source vector

$$\mathcal{S}_l(\lambda, z) = \epsilon \mathcal{S}_{\text{th}}(\lambda, z) + \int_0^{+\infty} \frac{d\lambda'}{2} \int_{-1}^{+1} \frac{\tilde{\mathcal{R}}(\lambda, \lambda', z)}{\phi_M(\lambda, z)} \hat{\Psi}(\mu') \mathcal{I}(\lambda', \mu', z) d\mu'. \quad (5.6)$$

The thermalization parameter $\epsilon = \Gamma_I / (\Gamma_R + \Gamma_I)$ where Γ_R and Γ_I are the radiative and inelastic collisional de-excitation rates, respectively. $\tilde{\mathcal{R}}(\lambda, \lambda', z)$ is a (2×2) diagonal matrix with elements $\tilde{\mathcal{R}} = \text{diag}(\mathcal{R}^0, \mathcal{R}^2)$, where \mathcal{R}^K are the redistribution functions which include the effects of J -state interference between different line components in a multiplet. \mathcal{R}^K represents a linear combination of redistribution functions of type-II and type-III. In the reduced Stokes vector basis, the angular phase matrix and the frequency redistribution functions are decoupled. The phase matrix part is built into the transfer equation through the $\hat{\Psi}$ matrix. The theory of redistribution matrices for the J -state interference in two-term atoms for the collisionless case is presented in chapter 2. This frequency redistribution part that includes J -state interference and the collisional redistribution is given by Equation (4.42), which is

$$\begin{aligned} \mathcal{R}^K(x, x') &= \frac{3(2L_b + 1)}{2S + 1} \sum_{J_a J_f J_b J_{b'}} (-1)^{J_f - J_a} \langle \tilde{r}_{J_b} \tilde{r}_{J_{b'}}^* \rangle_{J_a J_f} (2J_a + 1)(2J_f + 1) \\ &\times (2J_b + 1)(2J_{b'} + 1) \begin{Bmatrix} L_a & L_b & 1 \\ J_b & J_f & S \end{Bmatrix} \begin{Bmatrix} L_a & L_b & 1 \\ J_b & J_a & S \end{Bmatrix} \begin{Bmatrix} L_a & L_b & 1 \\ J_{b'} & J_f & S \end{Bmatrix} \\ &\times \begin{Bmatrix} L_a & L_b & 1 \\ J_{b'} & J_a & S \end{Bmatrix} \begin{Bmatrix} 1 & 1 & K \\ J_{b'} & J_b & J_a \end{Bmatrix} \begin{Bmatrix} 1 & 1 & K \\ J_{b'} & J_b & J_f \end{Bmatrix}. \end{aligned} \quad (5.7)$$

The ensemble averaged coherency matrix elements (see e.g. [Bommier & Stenflo, 1999](#)) in the above equation are given by

$$\begin{aligned} \langle \tilde{r}_{J_b} \tilde{r}_{J_{b'}}^* \rangle_{J_a J_f} &= A \cos \beta_{J_{b'} J_b} [\cos \beta_{J_{b'} J_b} (h_{J_b, J_{b'}}^{\text{II}})_{J_a J_f} - \sin \beta_{J_{b'} J_b} (f_{J_b, J_{b'}}^{\text{II}})_{J_a J_f}] \\ &+ B^{(K)} \cos \beta_{J_{b'} J_b} \cos \alpha_{J_{b'} J_b}^{(K)} \left\{ \cos (\beta_{J_{b'} J_b} + \alpha_{J_{b'} J_b}^{(K)}) \left[\Re \left(h_{J_b J_a, J_{b'} J_f}^{\text{III}} \right) - \Im \left(f_{J_b J_a, J_{b'} J_f}^{\text{III}} \right) \right] \right. \\ &\quad \left. - \sin (\beta_{J_{b'} J_b} + \alpha_{J_{b'} J_b}^{(K)}) \left[\Im \left(h_{J_b J_a, J_{b'} J_f}^{\text{III}} \right) + \Re \left(f_{J_b J_a, J_{b'} J_f}^{\text{III}} \right) \right] \right\}. \quad (5.8) \end{aligned}$$

The $(h_{J_b, J_{b'}}^{\text{II}})_{J_a J_f}$ and $(f_{J_b, J_{b'}}^{\text{II}})_{J_a J_f}$ are the auxiliary functions defined in Equations (2.14) and (2.15) but are used here for the non-magnetic case and with angle-averaged redistribution functions of type-II. The auxiliary functions of type-II derived in Chapter 2 represents generalizations of the corresponding quantities appearing in [Sampoorna \(2011a, see Equations \(22\) and \(23\)\)](#) using a semi-classical approach. The important difference between the two in the presence of the magnetic field is that in case of J -state interference these auxiliary functions depend on both J and m quantum numbers, unlike in case of m -state interference where they depend only on m . In the particular case of non-magnetic J -state interference theory, these quantities depend only on J quantum numbers, whereas the corresponding quantities in the m -state interference theory simply reduce to the well known type-II redistribution functions of [Hummer \(1962\)](#). Therefore for the notational brevity even in the J -state interference case we refer to these auxiliary functions as R_{II} hereafter (in the standard notation of [Hummer, 1962](#)). The auxiliary quantities for type-III redistribution are given in Chapter 4 (see also Appendix C). The assumptions made in deriving Equation 5.8 are listed in Section 4.1. Among these, the assumption of an unpolarized lower term is made for the sake of mathematical simplicity. The inelastic collisions that transfer polarization between the fine structure levels are neglected. This is justified because the colliding particles are isotropically distributed around the radiating atom. This situation is similar to the case of an atom immersed in an isotropic radiation field producing no atomic polarization (scattering polarization). Neglecting such inelastic collisions is particularly valid in the linear Zeeman regime in which we are interested. However these inelastic collisions do cause population transfer between the fine structure levels, and are properly accounted for in the calculations of line opacities (see Section 5.4).

The angle $\beta_{J_{b'} J_b}$ is defined in Equation (2.10). The angle $\alpha_{J_{b'} J_b}^{(K)}$ is defined as

$$\tan \alpha_{J_{b'} J_b}^{(K)} = \frac{\omega_{J_{b'} J_b}}{\Gamma_R + \Gamma_I + D^{(K)}}. \quad (5.9)$$

Here $\hbar\omega_{J_{b'} J_b}$ is the energy difference between the $J_{b'}$ and J_b states in the absence of a magnetic field. $D^{(K)}$ is the $2K$ multipole depolarizing elastic collisional destruction

rate. In general $D^{(K)}$ depend on the J quantum numbers of the fine structure states. As a simplifying assumption, we take these rates to be the same for all the fine structure states of the upper term, and use the classical value $D^{(K)} = \Gamma_E/2$ given by [Stenflo \(1994\)](#) where Γ_E is the elastic collision rate which is responsible for the broadening of the atomic states. A and $B^{(K)}$ are the branching ratios which are given by

$$A = \frac{\Gamma_R}{\Gamma_R + \Gamma_I + \Gamma_E}; \quad B^{(K)} = \frac{\Gamma_R}{\Gamma_R + \Gamma_I + D^{(K)}} \frac{\Gamma_E - D^{(K)}}{\Gamma_R + \Gamma_I + \Gamma_E}. \quad (5.10)$$

These branching ratios are the ones derived for a two-level atom model by [Bommier \(1997b\)](#). For simplicity, we continue to use the same branching ratios for the two-term atom case also.

The computation of angle-averaged type-III redistribution functions (that appear in Equation (5.8)) is very expensive, especially for the case of a realistic model atmosphere. Therefore we prefer to use the approximation of CRD in place of type-III redistribution functions (see [Mihalas, 1978](#)). We have verified by direct numerical computations that this replacement is valid and gives results which are almost identical to the explicit use of type-III redistribution functions. The necessary settings of the branching ratios in order to go to the limit of pure CRD are $A = 0$ and $B^{(K)} = (1 - \epsilon)$ (see also [Anusha et al., 2011b](#)).

5.3 Observational details

The Q/I spectra of CrI triplet were observed by [Gandorfer \(2000\)](#). In this chapter, we present new observations of this triplet obtained with the ZIMPOL-III polarimeter ([Ramelli et al., 2010](#)) at IRSOL in Switzerland. Figure 5.2 shows the observations recorded on September 6, 2011, at the heliographic north pole with the slit placed parallel to the limb at $\mu = 0.15$. The polarization modulation was done with a piezo-elastic modulator (PEM). The spectrograph slit was $60\mu\text{m}$ wide corresponding to a spatial extent of $0.5''$ on the solar image. The CCD covered $190''$ along the slit. The effective pixel resolution in the spatial direction is 4 actual pixels wide, due to the grouping of each four pixel rows covered by a cylindrical microlense, to allow simultaneous recording of all four Stokes parameters in the ZIMPOL demodulation scheme. The resulting CCD images have 140 such effective pixel resolution elements in the spatial direction, each element corresponding to $1.38''$, and 1240 pixels in the wavelength direction, with one pixel corresponding to $7.84 \text{ m}\text{\AA}$. In Figure 5.2 only the central part of the spectral window, corresponding to 1050 pixels spanning 8.23 \AA , is displayed. With the PEM it was possible to measure simultaneously one linear and the circular polarization component. Measurements of the linear polarization component Q/I were alternated with measurements of the U/I component through mechanical rotation of the analyzer by

45°. In total we accumulated for both the components 2000 exposures of 1 second each.

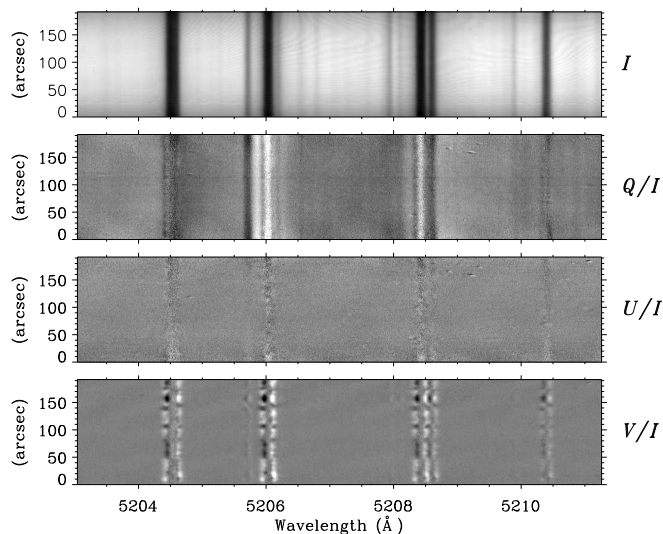


Figure 5.2: CCD image showing the (I , Q/I , U/I , V/I) of the Cr I triplet. The recording was made on September 6, 2011, near the heliographic north pole at a limb distance defined by $\mu = 0.15$. The grey scale cuts span a range (from black to white) of 0.1 % in Q/I and U/I , while for V/I the cuts are -0.2% (black) and $+0.2\%$ (white).

5.4 Modeling of Cr I triplet

To model the Cr I triplet the polarized spectrum is calculated by a two-stage process described in Holzreuter et al. (2005, see also Anusha et al. 2010, 2011b). In the first-stage a multi-level PRD-capable MALI (Multi-level Approximate Lambda Iteration) code of Uitenbroek (2001, referred to as the RH-code) solves the statistical equilibrium equation and the unpolarized RT equation self-consistently and iteratively. The RH-code is used to compute the unpolarized intensities, opacities and the collision rates. The angle-averaged redistribution functions of Hummer (1962) are used in the RH-code to represent PRD in line scattering. In the second stage the opacities and the collision rates are kept fixed, and the polarized intensity vector \mathcal{I} is computed perturbatively by solving the polarized RT equation with the redistribution matrices defined in Section 5.2, which are derived for a two-term atom with an unpolarized lower term.

5.4.1 Model atom and model atmosphere

The Cr I atom model is constructed for 14 levels (13 levels of Cr I and the ground state of Cr II), 11 line transitions, and 13 continuum transitions. The line transitions are shown in Figure 5.3.

5.4. Modeling of Cr I triplet

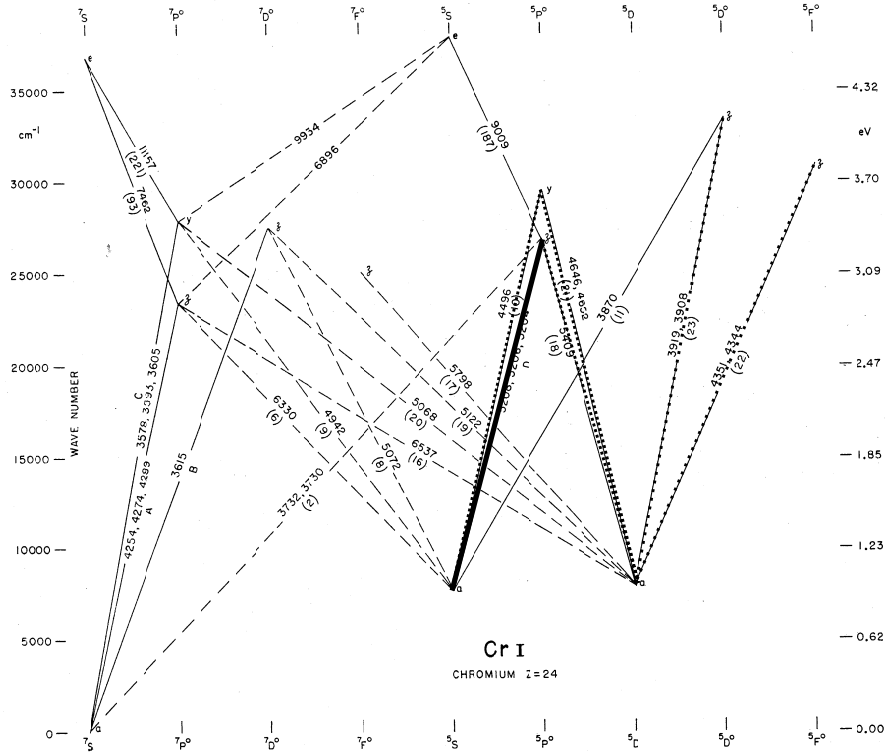


Figure 5.3: The grotrian diagram of Cr I atom. Thick solid line indicates the 5204 Å, 5206 Å, and 5208 Å transitions. Thick dotted lines are the other line transitions which are included in the construction of atom model.

The line components of the $^5S - ^5P$ triplet of Cr I are considered under PRD. The values of the various physical quantities required to build the atom model are taken from the NIST atomic data base¹ and the Kurucz data base². The data for the blend lines are also obtained from the Kurucz data base. The photo-ionization cross sections are taken from Bergemann & Cescutti (2010). The explicit dependence of these cross sections on wavelength is computed under the hydrogenic approximation.

Figure 5.4a shows the temperature structure in some of the standard model atmospheres of the Sun - namely FALA, FALC, FALF (Fontenla et al., 1993), and FALX (Avrett, 1995), which we have used in our attempts to fit the observed $(I, Q/I)$ spectra. Models A, C and F of Fontenla et al. (1993) represent respectively the supergranular cell center, the average quiet Sun, and the bright network region in the solar atmosphere. FALX represents the coolest model with a chromospheric temperature minimum located around 1000 km above the photosphere. Our attempts to fit the observed $(I, Q/I)$ spectra using these standard models will be discussed in Section 5.5.2.

We show that a reasonable fit could be obtained only with a small enhancement in the original temperature structure of the FALF model, in the height range of 100 km below the photosphere, extending up to 700 km above the photosphere (denoted

¹www.nist.gov/pml/data/asd.cfm

²kurucz.harvard.edu/linelists.html

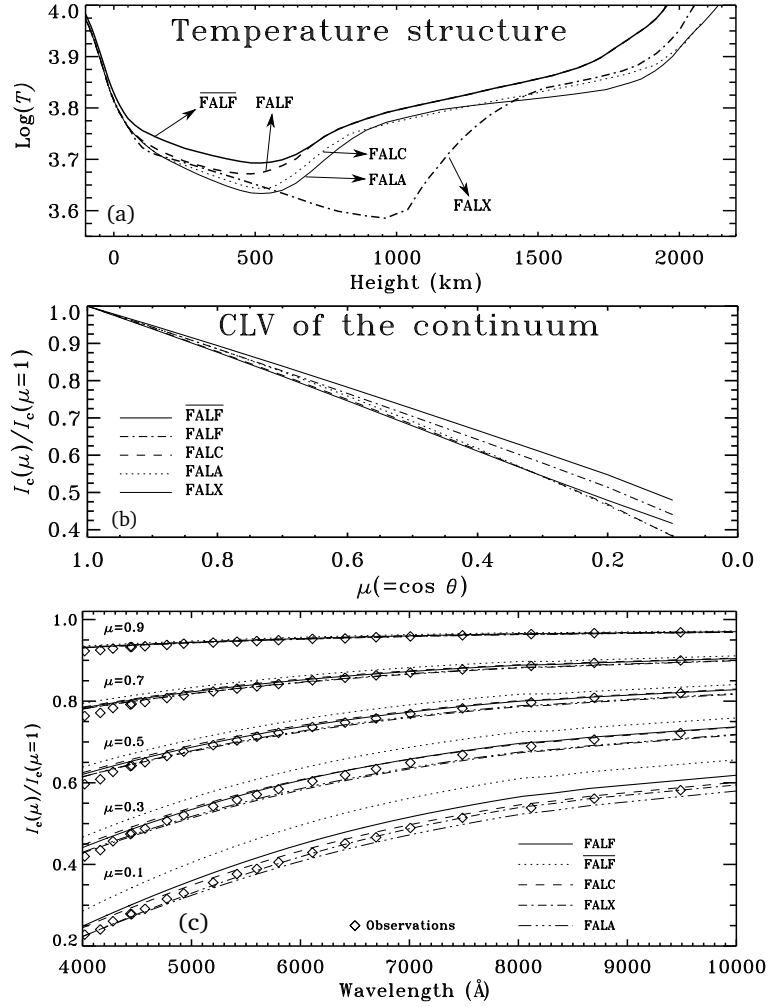


Figure 5.4: Panel (a) shows the temperature structure of several standard model atmospheres. $\overline{\text{FALF}}$ represents a model with an enhanced temperature structure of the original FALF model. In panel (b) we show the center to limb variation of the ‘limb darkening function’, $I_c(\mu)/I_c(\mu = 1)$, where $I_c(\mu)$ is the continuum intensity near the Cr I triplet. Panel (c) shows the CLV of the continuum intensity for all wavelengths covering the violet to the IR regions of the spectrum. The observed data are taken from Neckel & Labs (1994).

by $\overline{\text{FALF}}$). Such an enhancement does not affect the center to limb variation (CLV) of the continuum intensity as shown in Figure 5.4b. While such a modification of the temperature structure produces insignificant changes in the intensity spectra, Q/I turns out to be quite sensitive to these changes in the temperature gradient.

In order to explore the effect of temperature enhancement in a given model atmosphere used for computing line and continuous spectra, we have performed a simple test (similar to the Figure 3 of Asplund et al., 1999, see our Figure 5.4c). It is expected that 1D model atmospheres (like FALF in our case; or all the FAL class of models in general) fit the observed CLV data of continuum intensity to a good accuracy. To verify this, we have plotted the limb darkening function for the whole range of wavelengths,

for different μ values. The theoretical limb darkening function fits the corresponding observed data better for $\mu \rightarrow 1$. The fit is approximate in the limb positions (say $\mu = 0.1$). In Figure 5.4c we also show the theoretical curves computed for the $\overline{\text{FALF}}$ model (dotted lines). As can be seen, the limb darkening function of $\overline{\text{FALF}}$ does not greatly differ from that of the original FALF model atmosphere (a maximum relative difference of 15% in the extreme limb). Therefore it justifies a slight modification of temperature structure in a given model atmosphere to achieve a theoretical fit to the Q/I observations.

5.5 Results and discussion

5.5.1 Comparison between PRD and CRD

Figure 5.5 shows the comparison between the Q/I profiles computed using only CRD (to represent frequency non-coherent redistribution: solid line), only R_{II} (dotted line), and a combination of R_{II} and CRD (dashed line) (see Section 5.2 for the definition of CRD). As seen from the figure, the CRD profiles do not produce the wing peaks on either side of the line center, which are clearly seen in the PRD profiles. Also, the J -state interference signatures are more prominent in PRD than in CRD. A good fit to the observed Q/I can only be achieved through the use of PRD (see Section 5.5.2). We have verified that it is impossible to fit the observed near wing peaks with CRD alone. The pure R_{II} mechanism represents frequency coherent scattering in the line wings, the use of which alone also fails to achieve a good fit (since it produces too large values of Q/I throughout the wings). We find that a proper combination of R_{II} and CRD is essential to obtain a good fit to the observations. This can be seen more clearly in Figure 5.8, where we present a comparison with the observed Q/I profile. It is well known that only such a combination can correctly take into account the collisional frequency redistribution. Therefore the (R_{II} ,CRD) combination is adopted for the computations.

The effect of elastic collisions is to cause significant depolarization in the line wings. This can be seen from the dashed line in Figure 5.5a, which shows that due to elastic collisions the line wing amplitudes of Q/I are greatly suppressed with respect to the corresponding pure R_{II} case (dotted line). The issue of elastic collisions is discussed in some detail in Section 5.2.

Figure 5.5b shows the effect of spectral smearing that needs to be applied to the theoretical profiles in order to compare them with the observed profiles, which are broadened by the particular spectral resolution that was used in the observations. In the absence of smearing the Q/I in the line core computed with R_{II} and CRD differ significantly (see Figure 5.5a). These differences decrease drastically after application of spectral smearing. Although in isothermal atmospheric models Q/I computed with

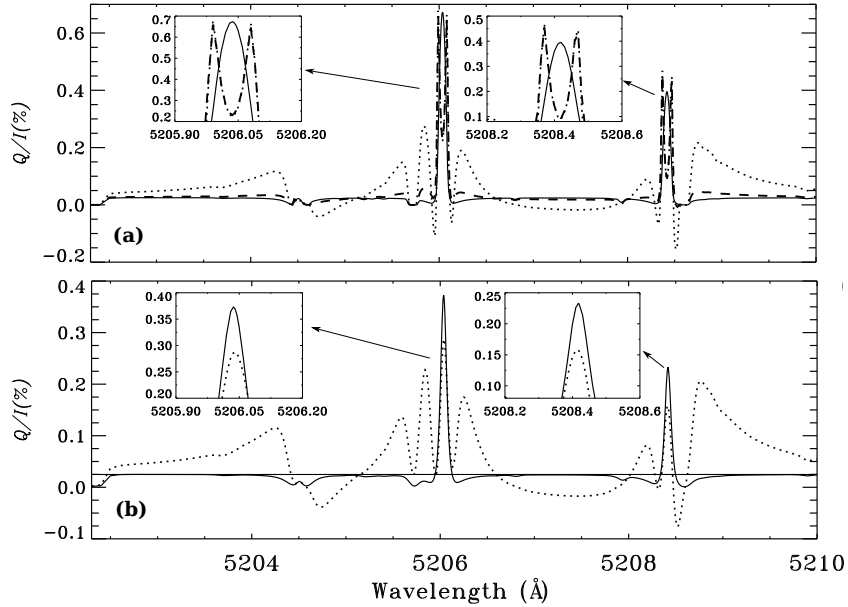


Figure 5.5: (Q/I) of the Cr I triplet computed with CRD (solid line), R_{II} (dotted line), and a combination of CRD and R_{II} (dashed line) for $\mu = 0.15$. The positive Q represents linear polarization parallel to the solar limb. The thin solid line in Q/I at the 0.025 % level represents the continuum polarization. The microturbulent magnetic field $B_{\text{turb}} = 0$. No spectral smearing is applied to the profiles in the panel (a). In the line core the Q/I profiles computed with pure R_{II} and with a combination of R_{II} and CRD nearly coincide (see the insets in the panel (a)). The panel (b) shows a comparison between the Q/I profiles computed with CRD and with R_{II} when we also apply a spectral smearing of 80 mÅ. The line types have the same meanings as in panel (a).

pure R_{II} and with CRD are very similar in the line center region, the same cannot be expected in computations with realistic atmospheres. Indeed Q/I computed with PRD shows a double peak structure in the line core region with a dip at line center (see [Holzreuter et al., 2005](#), for details). The smearing wipes out the double-peaked core structure that we see in Figure 5.5a.

5.5.2 Comparison with observations

In this section we compare the theoretical Stokes profiles computed using several standard atmospheric models of the Sun, with the observations. Figures 5.6 and 5.7 show the I/I_c and Q/I spectra. From Figure 5.6 we can see that the I/I_c is not sensitive to the choice of the model atmospheres, whereas Q/I is very sensitive. The reason for this sensitivity is the angular anisotropy of the radiation field, which is different for different atmospheres.

From Figure 5.4 it is clear that the temperature structure of these models are considerably different from each other in the line formation region. We find that a modification of the temperature structure at certain range in the atmosphere does not significantly affect the emergent I/I_c profile. However Q/I is quite sensitive to such ‘modifications’

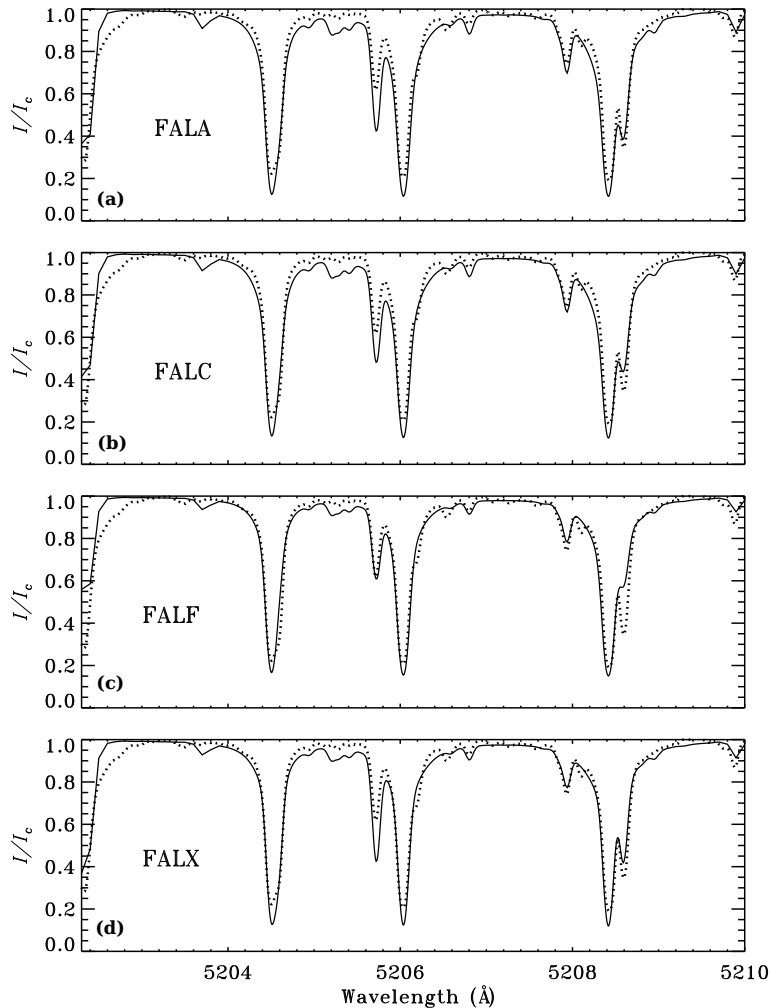


Figure 5.6: Intensity spectra for a choice of model atmospheres. The dotted line represents observations and the solid line represents the theoretical profiles. The line of sight is represented by $\mu = 0.15$.

in the temperature structure in the line formation region. The theoretical profiles (solid lines) in Figure 5.7 are computed taking into account the effects of microturbulent magnetic fields (B_{turb}) with an isotropic angular distribution (Stenflo, 1994). Further, the spectral smearing (see Anusha et al., 2010) is done using a Gaussian function with FWHM of 80 mÅ. The use of B_{turb} is essential to obtain correct line center amplitudes of Q/I . The values of B_{turb} for the three components of the Cr I triplet are different. They are chosen to fit the observed line center amplitudes of Q/I using the FALF model. In this way, the microturbulent magnetic field strength is only used as a free parameter to improve the fit with the observations. We have made no attempt to achieve a good fit to the line center amplitudes of the (Q/I) profile computed using FALA, FALC, and FALX models. FALF provides a better fit to the observed Q/I profiles at the cores of the three lines and in the interference regions in between them. However the far wings still remain poorly fitted even by the FALF model. To achieve a good fit to the far wing region of all the three lines, we found it necessary to enhance (see

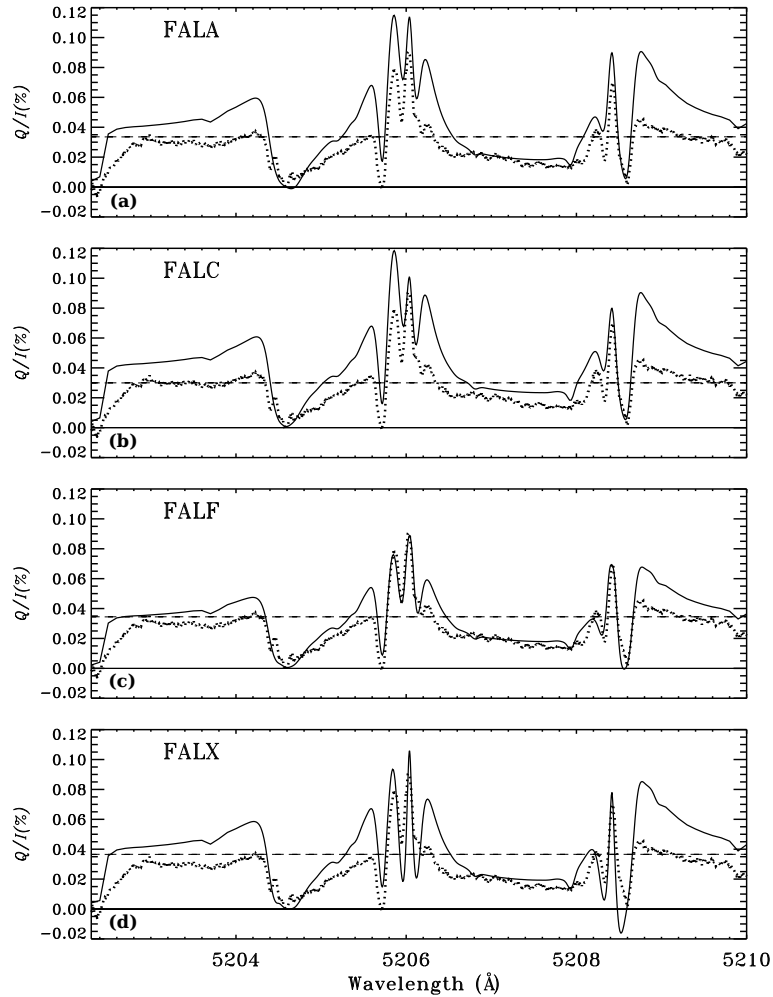


Figure 5.7: The polarized (Q/I) spectra computed at $\mu = 0.15$ and for a choice of model atmospheres. The line types are the same as in Figure 5.6. The dashed line represents the level of continuum polarization. The observations are taken at $\mu = 0.15$. The B_{turb} values used for the theoretical profiles are given in Table 5.1.

Figure 5.4) the temperature in the layers where the far wings are formed.

Figure 5.8 shows a comparison between the profiles of the Cr I triplet computed with the J -state interference theory (solid line) and the observed data (dotted line). This solid line is same as the dashed line in Figure 5.5a, except that it now also includes the contributions from B_{turb} and a spectral smearing of 80 mÅ to simulate the observations. The best fit values of B_{turb} for the 3 components of the Cr I triplet are given in Table 5.1. The approximate heights of formation given in Table 5.1 are the heights at which the condition $\tau(\lambda_0)/\mu \simeq 1$ is satisfied for $\mu = 0.15$. The quantity $\tau(\lambda_0)$ is the total optical depth at line center for the $\overline{\text{FALF}}$ model.

The observed Q/I spectra of the Cr I triplet have two main characteristics, namely (i) the presence of a triple peak structure in line-2 and line-3; (ii) the cross over in Q/I about the continuum polarization level, occurring between the line components. These two aspects are well reproduced in terms of the theoretical framework with the

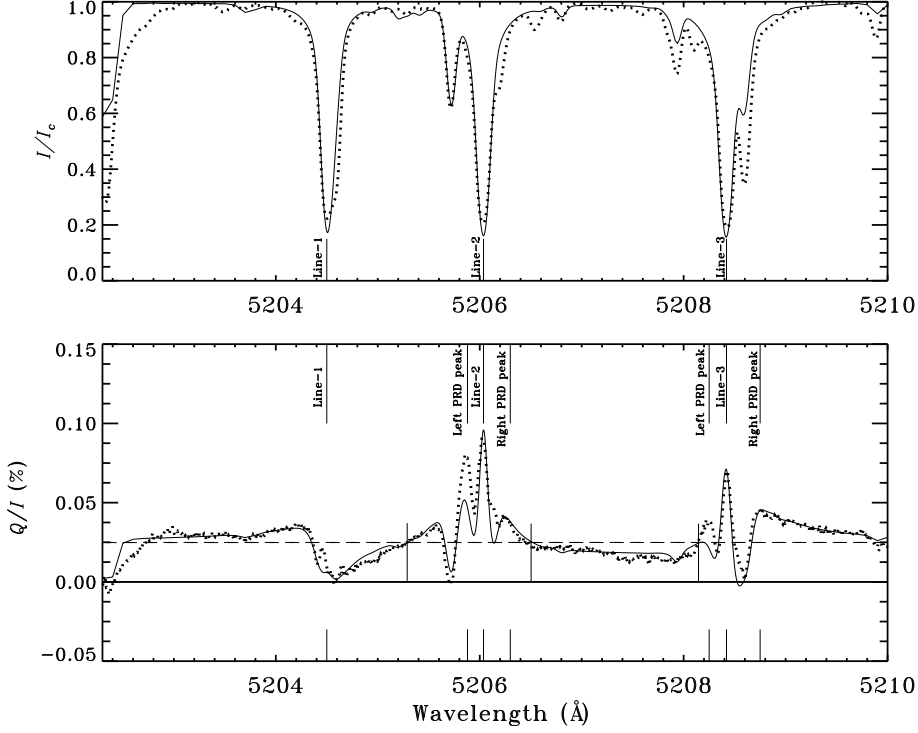


Figure 5.8: Comparison between the limb ($\mu = 0.15$) observations (dotted line, representing the Q/I spectrum of Figure 5.2 averaged along the slit) and the theoretical profile (solid line). The centers of the 3 lines, the PRD peak positions of line-2 and line-3, and the cross-over wavelength positions between the lines are marked with vertical lines. The dashed line in Q/I at 0.025% represents the continuum polarization level. The solid line is the same as the dashed line of Figure 5.5a, except that we have now introduced Hanle depolarization due to microturbulent magnetic fields (see Table 5.1), and added spectral smearing of $80 \text{ m}\text{\AA}$ to simulate the observations. The smearing wipes out the double-peaked core structure that we see in Figure 5.5a.

redistribution matrix theory for J -state interference developed in Chapters 2, 3 and 4. The small discrepancies between the observations and theoretical profiles in Q/I can be attributed to the presence of blend lines. The blend lines are assumed to be formed under LTE, and generally depolarize the wings of the main line as well as the continuum polarization. To fit the observed I spectra the oscillator strengths of the blend lines from the Kurucz data base are used unchanged, with the single exception of the Y II line at 5205.75 \AA , since the value from the data base for this line does not reproduce the Stokes I spectrum at all. Therefore the oscillator strength for this line is changed substantially to get a good Stokes I fit. As soon as the Stokes I fit becomes good, the Q/I fit automatically becomes good as well around 5205.75 \AA . Such enhancement of the Y II line oscillator strength is also used in computing the theoretical profiles shown in Figures 5.6 and 5.7. The discrepancy in the theoretically computed and observed intensity spectra of other blend lines is slightly model atmosphere dependent, particularly for the one at 5208.6 \AA (see Figure 5.6 for details). We have not made a detailed attempt to simultaneously fit the ($I, Q/I$) spectra of all the blend lines.

Table 5.1: Microturbulent magnetic field strengths necessary to obtain a best fit to the line center value of the observed Q/I using $\overline{\text{FALF}}$

Line	height at which $(\tau_\lambda/\mu) = 1$ for $\mu = 0.15$	B_{turb} (G)
5204.50 Å	845 km	4.0
5206.04 Å	884 km	6.0
5208.42 Å	953 km	4.5

The reasons for the lack of a good fit to the observed Q/I at the left-wing peaks of line-2 and line-3 remain unclear and need further investigation. The deviations of the model fit from the observations are possibly due to unidentified opacity sources. These deviations however do not affect the diagnostic potential of the Cr I triplet.

5.6 Conclusions

In this chapter we have studied the importance of J -state interference phenomena with realistic radiative transfer modeling of the Second Solar Spectrum. We have selected a Cr I triplet for this purpose and made use of the PRD theory with J -state interference developed in Chapters 2, 3, and 4 in the absence of lower term polarization. This theory is used in combination with realistic atmospheres and a model atom for Cr I. Our results demonstrate that it is indeed possible to obtain a good fit to the observed Q/I profiles without the use of lower term polarization, and also clearly show that accounting for the PRD mechanism is essential to model the observed scattering polarization in sufficient detail. The CRD approach alone cannot be used to model the observed spectra. We note that [Belluzzi & Trujillo Bueno \(2011\)](#) have carried out a basic investigation of the J -state interference phenomenon on different multiplets, neglecting RT and PRD effects (the theory they apply is based on the CRD assumption). Nevertheless, they were able to identify and explain qualitatively the observational signatures produced by J -state interference in the Cr I triplet (i.e., the cross over of Q/I about the continuum level occurring between the lines, and the Q/I feature around the line-1 core), neglecting and including the effects of lower-term polarization and dichroism.

Our observations were performed in quiet regions, but we find that microturbulent magnetic fields with an isotropic angular distribution are needed to fit the line center amplitudes of the Q/I spectra.

The near wing PRD peaks and the characteristic cross-overs in Q/I that are typical of J -state interference are well modeled only through a weighted combination of partially coherent (through R_{II}) and completely non-coherent (through CRD) scattering processes. The weighting factors (branching ratios) are the ones used to represent the collisional frequency redistribution in line scattering on a two-level atom, and they are

properly accounted for in our RT calculations. We find that elastic collisions indeed play a major role in modeling the wing polarization of the Cr I triplet. A hotter model atmosphere (FALF) with a slight additional temperature enhancement is found to be needed to obtain a good fit to the observed data, in particular for Q/I . This emphasizes that the Q/I spectrum (together with the I spectrum) provides a much stronger constraint on the model atmosphere than the intensity spectrum alone. The Second Solar Spectrum is thus not only useful for magnetic field diagnostics, but also for modeling the thermodynamic structure of the Sun's atmosphere.

Part II

Polarized line formation with F -state interference

Chapters 6-8

Based on:

Smitha, H. N., Sowmya, K., Nagendra, K. N., Sampoorna, M., & Stenflo, J. O. 2012, *ApJ*, 758, 112

6

Collisionless partial frequency redistribution in the non-magnetic regime

An Overview

In this chapter, we extend the redistribution matrix derived for the J -state interference to the case of F -state interference and in subsequent chapters apply it to the Second Solar Spectrum to model specific lines. Here, we incorporate the F -state interference redistribution matrix into the polarized radiative transfer equation and solve it for isothermal constant property slab atmospheres. The relevant transfer equation is solved using a polarized approximate lambda iteration (PALI) technique based on operator perturbation. An alternative method derived from the Neumann series expansion is also proposed and is found to be relatively more efficient than the PALI method. The effects of partial frequency redistribution (PRD) and the F -state interference on the shapes of the linearly polarized Stokes I and Q/I profiles are discussed. The emergent Stokes profiles are computed for hypothetical line transitions arising due to hyperfine structure splitting (HFS) of the upper $J = 3/2$ and lower $J = 1/2$ levels of a two-level atom model with nuclear spin $I_s = 3/2$. We confine our attention to the non-magnetic scattering in the collisionless regime. Like in the previous case, we compare our redistribution matrix approach with the $W_2(\lambda)$ approach.

6.1 Introduction

An atom undergoes hyperfine structure splitting due to the coupling of electronic angular momentum J and the nuclear spin I_s (see Figure 6.1). Second solar spectrum contains several lines which have signatures of F -state interference which arises due to the coherent superposition of these hyperfine structure states. Examples of these lines are Na I D₂ at 5890 Å, Ba II D₂ at 4554 Å, Mn I 8741 Å, Sc II 4247 Å etc. In this chapter (see also [Smitha et al., 2012b](#)) we are concerned with the line formation studies involving the F -state interference process and PRD. The F -state redistribution matrix derived in this chapter can be used for modeling the non-magnetic quiet region observations of HFS in the lines mentioned above.

The F -state interference theory applicable to the frequency coherent scattering was developed by [Stenflo \(1997\)](#). This theory, along with PRD, was applied by [Fluri et al. \(2003a\)](#) and [Holzreuter et al. \(2005\)](#) in the polarized line transfer computations. In [Landi Degl’Innocenti & Landolfi \(2004\)](#) the theory of F -state interference was developed under the approximation of complete frequency redistribution (CRD). The theory of F -state interference in a magnetic field for multi-term atoms in the collisionless regime and under the approximation of CRD is presented in [Casini & Manso Sainz \(2005\)](#).

In the present chapter, we extend the J -state interference theory presented in Chapter 2 to the case of F -state interference. The F -state redistribution matrix is derived here for the non-magnetic case and in the collisionless regime. The reason for considering the non-magnetic case, is that the formulation of Chapter 2 was confined to the linear Zeeman regime of field strengths (the spacing between the Zeeman m -states being smaller than the spacing between the fine structure states). In the present context, the hyperfine splitting becomes comparable to the Zeeman splitting even for weak magnetic fields, and we quickly enter the Paschen-Back regime of field strengths (level crossing of the m -states belonging to different F -states), in which the formulation presented in Chapter 2 is not valid. Since the Paschen-Back effect is outside the scope of our treatment, the results presented here is limited to the non-magnetic case. The extension to the Paschen-Back regime has been recently done by [Sowmya et al. \(2014b\)](#). We further assume that the lower level is unpolarized and infinitely sharp. While this assumption is made for the sake of mathematical simplicity, it is physically justified for the long-lived ground states, which are correspondingly more vulnerable to collisional depolarization.

Following Chapter 3, this PRD matrix is incorporated into the polarized line transfer equation, and solved using an operator perturbation method. We also propose a new method to solve the F -state interference problem. It is called the scattering expansion method (SEM) and is described in [Frisch et al. \(2009\)](#); [Sampoorna et al. \(2011\)](#). Re-

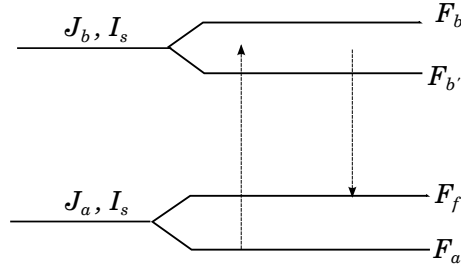


Figure 6.1: Level diagram representing the HFS in a two-level atom model.

cently, it has been applied to a variety of problems (see [Sowmya et al., 2012](#); [Supriya et al., 2012](#)). We compare the operator perturbation method and the SEM by applying them to the problem at hand.

In Section 6.2 we derive the PRD matrix for F -state interference and incorporate it into the line transfer equation. In Section 6.3 we describe the numerical methods used to solve the transfer equation. Results are presented in Section 6.4. Section 6.5 is devoted to the concluding remarks.

6.2 Basic equations

6.2.1 The redistribution matrix

In this section we present the redistribution matrix for the F -state interference, derived starting from the Kramers-Heisenberg formula. We restrict our attention to the case of a non-magnetic collisionless regime.

The redistribution matrix for the F -state interference can be derived through a straightforward replacement of quantum numbers, in the J -state interference redistribution matrix derived in Chapter 2. The replacements are as follows (see [Stenflo, 1997](#); [Landi Degl'Innocenti & Landolfi, 2004](#)):

$$L \rightarrow J; \quad J \rightarrow F; \quad S \rightarrow I_s, \quad (6.1)$$

where L , J and S represent the orbital, electronic, and spin quantum numbers of a given state. F is the total angular momentum and I_s is the nuclear spin of the atom under consideration. The expression for the F -state interference redistribution matrix expressed in terms of irreducible spherical tensors can be written as

$$\begin{aligned} \mathbf{R}_{ij}^{\Pi}(x, \mathbf{n}; x', \mathbf{n}') &= \frac{3(2J_b + 1)}{2I_s + 1} \sum_{K F_a F_f F_b F_{b'}} (-1)^{F_f - F_a} \cos \beta_{F_{b'}, F_b} e^{i\beta_{F_{b'}, F_b}} (2F_a + 1) \\ &\times (2F_f + 1)(2F_b + 1)(2F_{b'} + 1) \left[(h_{F_b, F_{b'}}^{\Pi})_{F_a F_f} + i(f_{F_b, F_{b'}}^{\Pi})_{F_a F_f} \right] \begin{Bmatrix} J_a & J_b & 1 \\ F_b & F_f & I_s \end{Bmatrix} \end{aligned}$$

$$\begin{aligned}
 & \times \begin{Bmatrix} J_a & J_b & 1 \\ F_b & F_a & I_s \end{Bmatrix} \begin{Bmatrix} J_a & J_b & 1 \\ F_{b'} & F_f & I_s \end{Bmatrix} \begin{Bmatrix} J_a & J_b & 1 \\ F_{b'} & F_a & I_s \end{Bmatrix} \begin{Bmatrix} 1 & 1 & K \\ F_{b'} & F_b & F_a \end{Bmatrix} \\
 & \times \begin{Bmatrix} 1 & 1 & K \\ F_{b'} & F_b & F_f \end{Bmatrix} \mathcal{T}_0^K(i, \mathbf{n}) \mathcal{T}_0^K(j, \mathbf{n}'). \quad (6.2)
 \end{aligned}$$

In the above expression the angle $\beta_{F_{b'}, F_b}$ is defined as

$$\tan \beta_{F_{b'}, F_b} = \frac{\omega_{F_{b'}, F_b}}{\gamma}, \quad (6.3)$$

where $\hbar\omega_{F_{b'}, F_b}$ represent the energy differences between the $F_{b'}$ and F_b states in the absence of a magnetic field. γ is the damping parameter of the upper state. The lower levels are assumed to be infinitely sharp and unpolarized. The h and f functions are the auxiliary quantities defined in the same way as Equations (2.14) and (2.15), but with the replacements given in Equation (6.1). \mathcal{T}_Q^K are the irreducible tensors for polarimetry introduced by Landi Degl'Innocenti (1984). For the non-magnetic case presented in this chapter, $Q = 0$. The indices i and j refer to the Stokes parameters ($i, j = 0, 1, 2, 3$) with $K = 0, 1, 2$ and $-K \leq Q \leq +K$. The directions of the incoming and scattered rays are given by \mathbf{n}' and \mathbf{n} respectively. $\mathbf{n} = (\theta, \varphi)$ where θ is the colatitude and φ is the azimuth of the outgoing ray. x' and x are the incoming and scattered frequencies in Doppler width units.

6.2.2 The polarized line transfer equation

The one dimensional radiative transfer equation for solving the line formation problems with PRD and F -state interference in scattering in the absence of a magnetic field is given by

$$\mu \frac{\partial \mathbf{I}(\tau, x, \mu)}{\partial \tau} = (\phi_{\text{HFS}}(x) + r)[\mathbf{I}(\tau, x, \mu) - \mathbf{S}(\tau, x, \mu)], \quad (6.4)$$

where $\mathbf{I} = (I, Q)^T$ is the Stokes vector and $\mathbf{S} = (S_I, S_Q)^T$ is the Stokes source vector. Equation (6.4) is valid for the case of a two-level atom with an infinitely sharp and unpolarized ground level. $\mu = \cos \theta$ represents the line of sight. r is the ratio of continuum to the frequency-integrated line absorption coefficient. The positive Stokes Q represents electric vector vibrations perpendicular to the solar limb. τ is the line optical depth defined by $d\tau = -k_L dz$, where k_L is the frequency-integrated line absorption coefficient defined for a two-level atom with HFS. If η_L is the line absorption coefficient then for the standard two-level atom without HFS, $\eta_L = k_L \phi(x)$ where $\phi(x)$ is the Voigt profile function. In the presence of HFS, η_L is given by (see Equation (3.7))

$$\eta_L(\nu) = \frac{k_L}{(2I_s + 1)} \sum_{F_a F_b} (2F_a + 1)(2F_b + 1) \begin{Bmatrix} J_b & J_a & 1 \\ F_a & F_b & I_s \end{Bmatrix}^2 \phi(\nu_{F_b F_a} - \nu), \quad (6.5)$$

where

$$k_L = \frac{h\nu_{J_b J_a}}{4\pi} N(J_a) B(J_a \rightarrow J_b), \quad (6.6)$$

is the frequency-integrated absorption coefficient for all the F -states. Thus $\phi_{\text{HFS}}(x)$ is the weighted sum of the individual Voigt profiles $\phi(\nu_{F_b F_a} - \nu)$ representing each $F_a \rightarrow F_b$ absorption.

For the particular case of the $J_a = 1/2 \rightarrow J_b = 3/2 \rightarrow J_f = 1/2$ transition with $I_s = 3/2$, $\phi_{\text{HFS}}(x)$ takes the form

$$\begin{aligned} \phi_{\text{HFS}}(x) = & \left[\frac{2}{32} \phi(\nu_{01} - \nu) + \frac{5}{32} \phi(\nu_{11} - \nu) + \frac{5}{32} \phi(\nu_{21} - \nu) \right. \\ & \left. + \frac{1}{32} \phi(\nu_{12} - \nu) + \frac{5}{32} \phi(\nu_{22} - \nu) + \frac{14}{32} \phi(\nu_{32} - \nu) \right]. \quad (6.7) \end{aligned}$$

We have verified that if the F -states are very closely spaced, then a single profile function $\phi(\nu_{J_b J_a} - \nu)$, corresponding to the $J_a \rightarrow J_b$ transition, can be used instead of $\phi_{\text{HFS}}(x)$ (see [Landi Degl'Innocenti & Landolfi, 2004](#)).

The total source vector \mathbf{S} in Equation (6.4) is given by

$$\mathbf{S}(\tau, x, \mu) = \frac{\phi_{\text{HFS}}(x) \mathbf{S}_l(\tau, x, \mu) + r \mathbf{S}_c}{\phi_{\text{HFS}}(x) + r}, \quad (6.8)$$

where the unpolarized continuum source vector $\mathbf{S}_c = B\mathbf{U}$, where B is the Planck function and $\mathbf{U} = (1, 0)^T$. The line source vector for a two-level atom with HFS is given by

$$\mathbf{S}_l(\tau, x, \mu) = \epsilon B\mathbf{U} + \frac{1}{\phi_{\text{HFS}}(x)} \int_{-\infty}^{+\infty} dx' \int_{-1}^{+1} \frac{d\mu'}{2} \mathbf{R}(x, \mu; x', \mu') \mathbf{I}(\tau, x', \mu'). \quad (6.9)$$

Here $\epsilon = \Gamma_I / (\Gamma_I + \Gamma_R)$ is the photon destruction probability per scattering also known as the thermalization parameter, with Γ_I and Γ_R being the inelastic and radiative de-excitation rates of the upper state F_b . To a first approximation these rates are assumed to be the same for all the F -states. $\mathbf{R}(x, \mu; x', \mu')$ is the redistribution matrix defined in Equation (6.2) but integrated over the azimuths φ' of the incoming radiation. Such a simplification is possible due to the azimuthal symmetry of the problem. This redistribution matrix can be rewritten as

$$\mathbf{R}_{ij}(x, \mu; x', \mu') = \sum_K \mathcal{R}^K(x, x') \mathcal{T}_0^K(i, \mu) \mathcal{T}_0^K(j, \mu'). \quad (6.10)$$

The redistribution function components $\mathcal{R}^K(x, x')$ are given by

$$\mathcal{R}^K(x, x') = \frac{3(2J_b + 1)}{2I_s + 1} \sum_{F_a F_f F_b F_b'} (-1)^{F_f - F_a} (2F_a + 1)(2F_f + 1)(2F_b + 1)$$

$$\begin{aligned}
 & \times (2F_{b'} + 1) \cos \beta_{F_{b'}, F_b} [\cos \beta_{F_{b'}, F_b} (h_{F_b, F_{b'}}^{\text{II}})_{F_a F_f} - \sin \beta_{F_{b'}, F_b} (f_{F_b, F_{b'}}^{\text{II}})_{F_a F_f}] \\
 & \times \begin{Bmatrix} J_a & J_b & 1 \\ F_b & F_f & I_s \end{Bmatrix} \begin{Bmatrix} J_a & J_b & 1 \\ F_b & F_a & I_s \end{Bmatrix} \begin{Bmatrix} J_a & J_b & 1 \\ F_{b'} & F_f & I_s \end{Bmatrix} \\
 & \times \begin{Bmatrix} J_a & J_b & 1 \\ F_{b'} & F_a & I_s \end{Bmatrix} \begin{Bmatrix} 1 & 1 & K \\ F_{b'} & F_b & F_a \end{Bmatrix} \begin{Bmatrix} 1 & 1 & K \\ F_{b'} & F_b & F_f \end{Bmatrix}. \tag{6.11}
 \end{aligned}$$

For simplicity, we use angle-averaged versions of the auxiliary functions $(h_{F_b, F_{b'}}^{\text{II}})_{F_a F_f}$ and $(f_{F_b, F_{b'}}^{\text{II}})_{F_a F_f}$.

6.2.3 Decomposition of the Stokes vectors into the reduced basis

Decomposition of the Stokes source vector \mathcal{S} in the reduced basis makes it independent of θ . The decomposition of \mathcal{S} defined in Equation (6.8) can be carried out in a way similar to the one presented in Section 3.2.1. Hence we do not repeat them here. The transfer equation for the reduced Stokes vector \mathcal{I} can be written as

$$\mu \frac{\partial \mathcal{I}(\tau, x, \mu)}{\partial \tau} = (\phi_{\text{HFS}}(x) + r) [\mathcal{I}(\tau, x, \mu) - \mathcal{S}(\tau, x)]. \tag{6.12}$$

The corresponding irreducible total and line source vectors are given by

$$\mathcal{S}(\tau, x) = \frac{\phi_{\text{HFS}}(x) \mathcal{S}_l(\tau, x) + r \mathcal{G}(\tau)}{\phi_{\text{HFS}}(x) + r}, \tag{6.13}$$

and

$$\mathcal{S}_l(\tau, x) = \epsilon \mathcal{G}(\tau) + \int_{-\infty}^{+\infty} \frac{\tilde{\mathcal{R}}(x, x')}{\phi_{\text{HFS}}(x)} \mathcal{J}(\tau, x') dx'. \tag{6.14}$$

Here $\tilde{\mathcal{R}}(x, x')$ is a (2×2) diagonal matrix with elements $\tilde{\mathcal{R}} = \text{diag}(\mathcal{R}^0, \mathcal{R}^2)$, where \mathcal{R}^K are defined in Equation (6.11). $\mathcal{G}(\tau) = (B, 0)^{\text{T}}$ is the primary source vector, and $\mathcal{J}(\tau, x)$ is the mean intensity defined in Equation (3.23).

6.3 Numerical methods

Here we describe two numerical techniques to solve the reduced form of the transfer equation. We compare their performance on some benchmark problems.

6.3.1 Operator perturbation method

The solution of the polarized line transfer equation defined in Equation (6.12) using the polarized approximate lambda iteration (PALI) method is described in Sections 3.3. The same equations also hold well for the present problem. Hence we do not repeat

those equations here. The only difference is that the redistribution matrix for J -state interference is now to be replaced by the corresponding redistribution matrix for the F -state interference presented in this chapter. Also, the profile function is to be replaced with $\phi_{\text{HFS}}(x)$.

6.3.2 Scattering expansion method

In recent years a new method based on Neumann series expansion of the polarized source vector has been developed (see Frisch et al., 2009). It is applied to a variety of astrophysical problems. Here we describe the application of this method to the problem at hand.

In this method, the reduced line source vector defined in Equation (6.14) is rewritten in the component form for the non-magnetic case as

$$S_0^K(\tau, x) = G(\tau)\delta_{K0}\delta_{00} + \int_{-1}^{+1} \frac{d\mu'}{2} \int_{-\infty}^{+\infty} dx' \frac{\mathcal{R}^K(x, x')}{\phi_{\text{HFS}}(x)} \sum_{K'} \Psi_0^{KK'}(\mu') I_0^{K'}(\tau, x', \mu'). \quad (6.15)$$

$\Psi_0^{KK'}$ are the components of the Rayleigh phase matrix in the reduced basis (see Appendix A of Frisch, 2007). We first consider the component S_0^0 . Expanding the summation over K' on the right-hand side of Equation (6.15) we obtain

$$S_0^0(\tau, x) = G(\tau) + \int_{-1}^{+1} \frac{d\mu'}{2} \int_{-\infty}^{+\infty} dx' \frac{\mathcal{R}^0(x, x')}{\phi_{\text{HFS}}(x)} \Psi_0^{00}(\mu') I_0^0(\tau, x', \mu') + \int_{-1}^{+1} \frac{d\mu'}{2} \int_{-\infty}^{+\infty} dx' \frac{\mathcal{R}^2(x, x')}{\phi_{\text{HFS}}(x)} \Psi_0^{02}(\mu') I_0^2(\tau, x', \mu'). \quad (6.16)$$

The degree of linear polarization arising due to Rayleigh scattering is small because of the small degree of anisotropy prevailing in the solar atmosphere. Hence the effect of linear polarization on Stokes I can be neglected to a good approximation. Neglecting the contribution from I_0^2 , in Equation (6.16) we get

$$\tilde{S}_0^0(\tau, x) \sim G(\tau) + \int_{-1}^{+1} \frac{d\mu'}{2} \int_{-\infty}^{+\infty} dx' \frac{\mathcal{R}^0(x, x')}{\phi_{\text{HFS}}(x)} \Psi_0^{00}(\mu') I_0^0(\tau, x', \mu'), \quad (6.17)$$

where \tilde{S}_0^0 denotes the approximate value of S_0^0 . It is the solution of a non-LTE unpolarized radiative transfer equation and is computed using the Frequency-by-Frequency (FBF) technique of Paletou & Auer (1995). The polarization is computed from the higher order terms in the series expansion. The S_0^2 component is given by

$$\begin{aligned} \tilde{S}_0^2(\tau, x) \sim & \int_{-1}^{+1} \frac{d\mu'}{2} \int_{-\infty}^{+\infty} dx' \frac{\mathcal{R}^2(x, x')}{\phi_{\text{HFS}}(x)} \Psi_0^{20}(\mu') \tilde{I}_0^0(\tau, x', \mu') \\ & + \int_{-1}^{+1} \frac{d\mu'}{2} \int_{-\infty}^{+\infty} dx' \frac{\mathcal{R}^2(x, x')}{\phi_{\text{HFS}}(x)} \times \Psi_0^{22}(\mu') \tilde{I}_0^2(\tau, x', \mu'). \end{aligned} \quad (6.18)$$

Retaining only the contribution from \tilde{I}_0^0 on the right-hand side of Equation (6.18), we obtain the single scattering approximation to the polarized component of the source vector as

$$[\tilde{S}_0^2(\tau, x)]^{(1)} \sim \int_{-1}^{+1} \frac{d\mu'}{2} \int_{-\infty}^{+\infty} dx' \frac{\mathcal{R}^2(x, x')}{\phi_{\text{HFS}}(x)} \Psi_0^{20}(\mu') \tilde{I}_0^0(\tau, x', \mu'). \quad (6.19)$$

The superscript (1) denotes single (first) scattering. This solution serves as a starting point for the computations of higher order scattering terms. Thus the iterative sequence of SEM can be represented by

$$\begin{aligned} [\tilde{S}_0^2(\tau, x)]^{(n)} \sim & [\tilde{S}_0^2(\tau, x)]^{(1)} + \int_{-1}^{+1} \frac{d\mu'}{2} \\ & \times \int_{-\infty}^{+\infty} dx' \frac{\mathcal{R}^2(x, x')}{\phi_{\text{HFS}}(x)} \times \Psi_0^{22}(\mu') [\tilde{I}_0^2(\tau, x', \mu')]^{(n-1)}, \end{aligned} \quad (6.20)$$

where the superscript (n) denotes the n th scattering. The iterative cycle is continued until the required convergence criteria are met.

In the following we compare the performance of these two numerical methods by plotting the maximum relative correction defined as

$$c^{(n)} = \max\{c_1^{(n)}, c_2^{(n)}\} < 10^{-8}, \quad (6.21)$$

where

$$c_1^{(n)} = \max_{\tau, x, \mu} \left\{ \frac{|\delta S_I^{(n)}(\tau, x, \mu)|}{|\bar{S}_I^{(n)}(\tau, x, \mu)|} \right\}, \quad (6.22)$$

and

$$c_2^{(n)} = \max_{x, \mu} \left\{ \frac{P^{(n)}(x, \mu) - P^{(n-1)}(x, \mu)}{P^{(n-1)}(x, \mu)} \right\}, \quad (6.23)$$

as a function of the iteration number as shown in Figure 6.2. In the above equations $P = [Q/I]$ is the degree of linear polarization and $\bar{S}_I^{(n)} = \frac{1}{2}[S_I^{(n)} + S_I^{(n-1)}]$.

Figure 6.2 is computed for an isothermal constant property atmospheric slab with the model parameters $(T, a, \epsilon, r, B) = (2 \times 10^{10}, 2 \times 10^{-3}, 10^{-4}, 0, 1)$ where T is the optical thickness of the self emitting slab and a is the damping parameter of the upper level J_b . From the figure one can clearly see that the convergence rate of the SEM is larger by several factors in comparison to the PALI method. The reason for the PALI method being slow is that the source function corrections are computed iteratively from

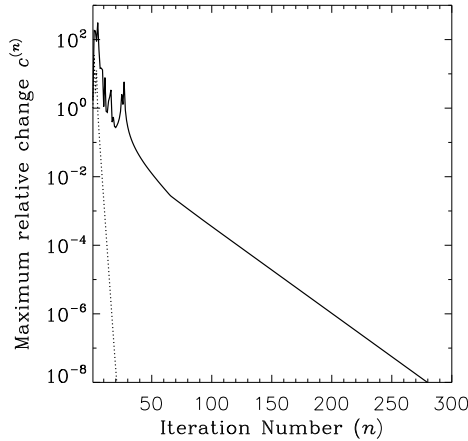


Figure 6.2: Comparison of PALI (solid line) and scattering expansion method (dotted line). The model parameters are given in the text. A convergence criteria of 10^{-8} is used.

an approximate initial guess and then the approximate lambda operator is perturbed until the source function corrections fall below a convergence criterion. On the other hand, the initial guess in the SEM for polarized line formation is the single scattered solution itself (which already contains the physical characteristics of the scattering mechanism under consideration). For this reason SEM takes just a few iterations to converge to the same level of accuracy as the PALI method. Furthermore, SEM is easy to implement for problems of any physical and/or numerical complexity. This makes the SEM the method of choice. For a detailed comparison of PALI and SEM we refer the reader to [Sampoorna et al. \(2011\)](#) and [Supriya et al. \(2012\)](#). The simple lambda iteration for polarization and the SEM is essentially similar. In the lambda iteration, a source vector correction is computed at each iteration, and the current source vector is updated until convergence is reached. In the SEM, each iteration can be seen as contributing a higher order scattering term to the series expansion of polarized component of the source vector. This component is updated by adding successively higher order terms in the scattering expansion of the source vector. These points are clearly explained respectively in [Trujillo Bueno & Manso Sainz \(1999, see the discussion following their Equation \(28\)\)](#), and [Frisch et al. \(2009, see the discussion following their Equation \(36\)\)](#).

6.4 Results and discussion

In this section we present the results computed for a standard two-level atom model with F -state interference using the PRD matrix presented in this chapter. Isothermal constant property media characterized by (T, a, ϵ, r, B) are used. The slabs are assumed to be self-emitting.

The results are presented for transitions centered at hypothetical wavelengths arising

Table 6.1: Wavelengths (\AA) of F -state transitions for a hypothetical atomic system

	$F_b = 0$	$F_b=1$	$F_b=2$	$F_b=3$
$F_a = 1$	5000.96093	5000.96075	5000.96036	N.A
$F_a = 2$	N.A	5000.98125	5000.98086	5000.98018

due to HFS of the $J_b = 3/2$ and $J_a = 1/2$ levels of a two-level atom with nuclear spin $I_s = 3/2$. Due to the hyperfine interactions the upper J -state splits into four F -states with $F_b = 0, 1, 2, 3$, and the lower J -state splits into $F_a = 1, 2$. Owing to the selection rule $\Delta F = 0, \pm 1$, these F -states are coupled by six radiative transitions (see Table 6.1). For simplicity the Doppler width of all the lines is taken to be constant at $\Delta\lambda_D = 25 \text{ m\AA}$. In the transfer computations, a grid resolution of $(N_d, N_x, N_\mu) = (5, 417, 5)$ is generally used, where N_d is the number of depth points per decade in the logarithmically spaced τ -grid. The first depth point is taken as $\tau_{\min} = 10^{-2}$. N_x is the total number of frequency points covering the full line profile. N_μ is the number of co-latitudes $\theta(\mu)$, taken as the 5 points of a Gauss-Legendre quadrature.

6.4.1 F -state interference effects in the case of single scattering

In this section we study the behavior of the F -state interference PRD matrix derived in Section 6.2.1 by computing the scattered profiles in a single scattering event. The results in Figure 6.3 are computed for a 90° single scattering event. This is done by giving an unpolarized beam of light incident on the scattering atom at $\mu' = -1$ as input, and observing the scattered ray at $\mu = 0$ in the scattering plane (see Chapter 2 for details on computing polarization profiles in a 90° single scattered event). The dashed line in Figure 6.3 is computed by ignoring the interference effects, whereas the solid line is computed by taking into account the interference effects between the F -states. A profile similar to the solid line can also be seen in Fluri et al. (2003a) and Holzreuter et al. (2005) where plots of the wavelength dependent polarizability factor $W_2(\lambda)$ are shown. In the single scattering case, the profiles of the $W_2(\lambda)$ and the $Q(\lambda)/I(\lambda)$ are similar in shape and differ only in magnitude (see below).

Principle of spectroscopic stability for F -state interference

It is well known that the principle of spectroscopic stability provides a useful tool to check any theory of quantum interference. This was first discussed in the context of scattering polarization and applied, in detail, in Stenflo (1994) (see also Stenflo, 1997; Landi Degl'Innocenti & Landolfi, 2004). In this chapter, we apply it to the case of F -state interference arising due to nuclear spin I_s . According to the principle of spectroscopic stability, in the limit of vanishing HFS in a two-level atom, the theory of

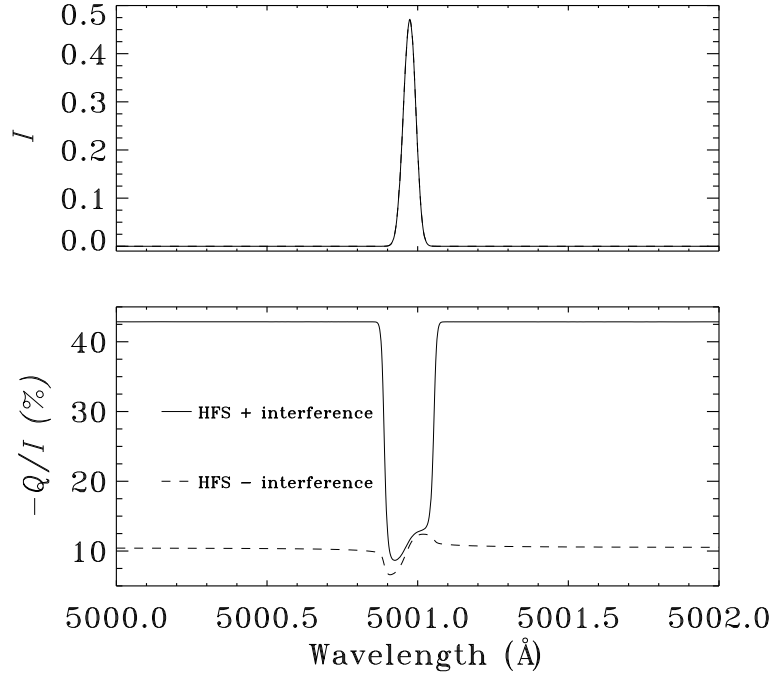


Figure 6.3: The profiles of the intensity I and the fractional polarization Q/I , plotted for a hypothetical line system with hyperfine structure splitting. Solid line represents the Q/I with F -state interference and dashed line represents Q/I without F -state interference. Single 90° scattering is assumed at the extreme limb ($\mu = 0$). The model parameters are $a = 0.002$, the Doppler width $\Delta\lambda_D = 0.025 \text{ \AA}$.

F -state interference should reduce to the standard two-level atom theory without HFS. This can be verified by computing the polarizability factor W_2 and in turn the fractional polarization Q/I in the limit of vanishing F -states. The value of W_2 in this asymptotic limit (which can be obtained by neglecting the I_s) can be computed as described in [Stenflo \(1997\)](#) with

$$(W_2)_{\text{asym}} = \frac{\begin{Bmatrix} 1 & 1 & 2 \\ J_b & J_b & J_a \end{Bmatrix} \begin{Bmatrix} 1 & 1 & 2 \\ J_b & J_b & J_f \end{Bmatrix}}{\begin{Bmatrix} 1 & 1 & 0 \\ J_b & J_b & J_a \end{Bmatrix} \begin{Bmatrix} 1 & 1 & 0 \\ J_b & J_b & J_f \end{Bmatrix}}. \quad (6.24)$$

For the particular case of $J_a = 1/2 \rightarrow J_b = 3/2 \rightarrow J_f = 1/2$ scattering transition, $(W_2)_{\text{asym}} = 0.5$. Hence $W_2(\lambda)$ is expected to approach 0.5 in the very far wings (see Figure 2 of [Stenflo, 1997](#)). In the 90° single scattering case, the Q/I and the $W_2(\lambda)$ are related through the formula (see [Landi Degl'Innocenti & Landolfi, 2004](#))

$$Q(\lambda)/I(\lambda) = \frac{3W_2(\lambda)}{4 - W_2(\lambda)}. \quad (6.25)$$

The above formula gives a value of $Q/I = 0.428$ for $(W_2)_{\text{asym}} = 0.5$ in the far wings.

From Figure 6.3, we can see that the solid curve reaches an asymptotic value of 42.8% as demanded by the principle of spectroscopic stability, whereas the dashed line reaches about 10% in the far wings, thereby violating the principle of spectroscopic stability. These arguments show that in the formulation of the redistribution matrix, the inclusion of interference effects between the F -states is essential.

6.4.2 Effects of F -state interference in multiply scattered Stokes profiles

In this section we present the results obtained by solving the transfer equation including the F -state interference. In the particular case of optically thin slabs, it can be shown, by choosing appropriate geometric arrangement, that the multiply scattered solution approaches single scattered solution and thus proving we have correctly incorporated the F -state redistribution matrix in the line transfer code. See Chapter 3 for more details regarding single scattering in a thin atmospheric slab.

When the optical thickness of the medium is large, multiple scattering effects come into play. Figure 6.4 shows one such example, where the emergent Stokes profiles are computed for different optical thicknesses. The dashed line in this figure is computed by neglecting HFS. This is the standard two-level atom case which results in a single radiative transition. The dotted line is computed with HFS but without interference between the F -states. In this case the six radiative transitions arising due to HFS are treated independently. The solid line is computed taking into account the F -state interference. This is comprised of six interfering radiative transitions between the F -states. The three line types in this figure are quite similar to each other in shape but differ prominently in amplitude.

For $T = 2$, the atmospheric slab is effectively thin and the Q/I profiles for both solid and dotted lines have a structuring within the line core that is different from that of the dashed line. This is due to the HFS of the given J -level. As the optical thickness increases, such a structuring gets smoothed out and the shape (not the amplitude) of the solid and dotted line profiles more closely resemble the dashed line profiles.

In the case of effectively thick atmospheric slabs ($T > 2$), two peaks are seen on either side of the line center arising due to PRD effects and are known as PRD wing peaks. In the line core, the solid and dotted lines nearly coincide whereas the dashed line differs from these two. This shows that the depolarization in the line core is purely due to HFS, irrespective of the interference effects between the F -states that are included. In the wings, the solid and dashed lines coincide whereas the dotted line differs significantly. Upon comparing the solid and dotted lines, it is evident that the interference effects show up in the line wing PRD peaks as in the case of J -state interference. However the J -state interference effects are seen even beyond the PRD wing peaks un-

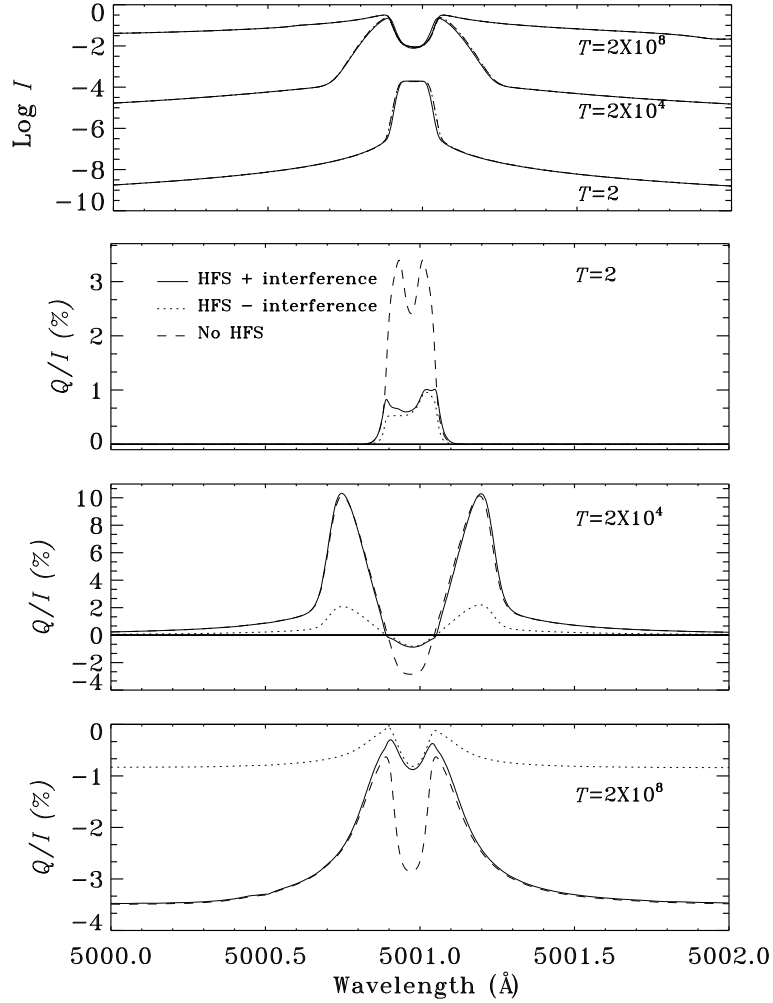


Figure 6.4: Comparison between the multiply scattered emergent Stokes profiles computed for different atomic systems as indicated in panel 2. The model parameters are $(a, \epsilon, r, B) = (2 \times 10^{-3}, 10^{-4}, 0, 1)$. The line of sight is given by $\mu = 0.047$. The wavelength positions of the six components are given in Table 1. The spacing between the hyperfine structure components is taken to be the same as those corresponding to the Na I D₂ line.

like the case of F -state interference. When F -state interference is taken into account the Q/I in the wings reaches the value of the single line case as expected from the principle of spectroscopic stability (see Section 6.4.1). But when interference is neglected, the dotted and dashed lines differ considerably in the wings which can be seen as a violation of the principle of spectroscopic stability. Thus the principle of spectroscopic stability serves as a powerful tool to check the correctness of our formulation not only in the case of single scattering but also in the radiative transfer computations.

Though such significant signatures of HFS and F -state interference are seen in Q/I , the intensity I remains unaffected by these effects.

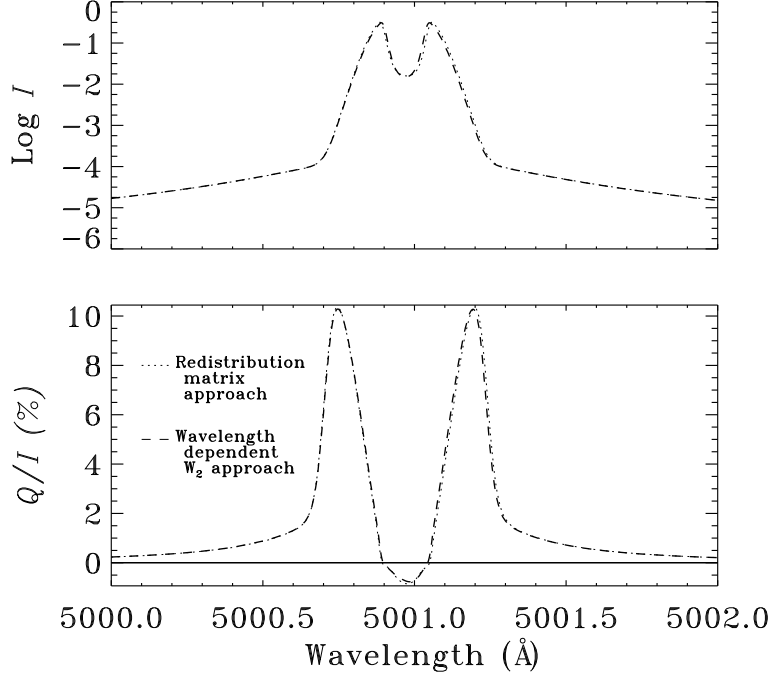


Figure 6.5: Comparison between the redistribution matrix theory (dotted line) and wavelength dependent polarizability factor $W_2(\lambda)$ theory of Stenflo (dashed line). The optical thickness of the atmospheric slab is $T = 2 \times 10^4$. The other model parameters are the same as in Figure 6.4.

6.4.3 Comparison with wavelength dependent polarizability theory of Stenflo

In this section we compare our redistribution matrix approach and the wavelength dependent polarizability $W_2(\lambda)$ theory for the case of F -state interference presented in Stenflo (1997) which used in Fluri et al. (2003a) and Holzreuter et al. (2005). The comparison is shown in Figure 6.5. The dotted lines show the profiles computed using the exact PRD F -state interference theory presented in Section 6.2. This is our redistribution matrix approach. The dashed lines show the profiles computed using the $W_2(\lambda)$ approach. The values of the $W_2(\lambda)$ are calculated from Equation (6.25) using the (Q/I) plotted in Figure 6.3 (solid line).

To use the $W_2(\lambda)$ in radiative transfer computations we replace the redistribution matrix $\mathcal{R}^K(x, x')$ in Equation (6.11) by $W_K(\lambda)[R^{\text{II-A}}(3/2 \rightarrow 1/2)]$. Here $R^{\text{II-A}}(J_b \rightarrow J_f)$ is the angle-averaged frequency redistribution function of Hummer (1962) for a line centered at λ_{J_b, J_f} corresponding to the $J_b \rightarrow J_f$ transition. For the hypothetical case under study, we have assumed the F -states to be very closely spaced. Under such an assumption, a single redistribution function computed for the $J = 3/2 \rightarrow 1/2$ transition can be used to represent all the F -state transitions. However if the F -states are far apart then the redistribution function needs to be computed for each of the $F_b \rightarrow F_f$ transition. In such a case, the redistribution matrix $\mathcal{R}^K(x, x')$

takes a form $W_K(\lambda) \sum_{F_b F_f} [R^{II-A}(F_b \rightarrow F_f)]$, in the $W_2(\lambda)$ approach.

The polarizability factor $W_0(\lambda) = 1$, and $W_2(\lambda)$ is the wavelength-dependent W_2 factor calculated from Equation (6.25). For the closely spaced F -states a common absorption profile function $\phi(x)$ corresponding to the $J_a = 1/2 \rightarrow J_b = 3/2$ transition is used. But in the case of widely spaced F -states, the $\phi(x)$ has to be taken as the sum of all the individual $F_a \rightarrow F_b$ absorption profile functions. As seen from Figure 6.5 both the redistribution matrix approach and the $W_2(\lambda)$ approach give nearly the same results.

6.5 Conclusions

In this chapter (Smitha et al., 2012b) we have extended the J -state interference formulation discussed in Chapters 2 and 3 to the case of F -state interference. The treatment is restricted to the collisionless and non-magnetic regime. The decomposition technique presented in Frisch (2007) is applied to the F -state interference problem. It helps to incorporate the F -state interference redistribution matrix into the reduced form of the line radiative transfer equation. The transfer equation is solved using the traditional PALI and the scattering expansion method by suitably adapting them to handle the F -state interference problem. The SEM is found to be more efficient and faster than the PALI method.

The Stokes profiles computed by taking into account HFS are similar to the profiles of a single line arising from a two-level atom model without HFS. The HFS causes a depolarization of Q/I in the line core irrespective of whether the F -state interference is taken into account or not. Like the J -state interference, the F -state interference affects mainly the line wing PRD peaks. We also show that when interference effects are neglected, the principle of spectroscopic stability is violated in both single scattered and multiple scattered profiles. Using the fractional polarization Q/I in the 90° single scattering case, we can numerically estimate the wavelength dependent polarizability factor $W_2(\lambda)$. The $W_2(\lambda)$ so computed can then be used in the transfer equation to compare with our exact redistribution matrix approach. The two approaches are found to give identical emergent Stokes profiles.

Based on:

Smitha, H. N., Nagendra, K. N., Stenflo, J. O., & Sampoorna, M. 2013, *ApJ*, 768, 163
Smitha, H. N., Nagendra, K. N., Stenflo, J. O., & Sampoorna, M. 2014, in *Solar Polarization Workshop 7*, in press

7

Modeling the Ba II D₂ 4554 Å line in the Second Solar Spectrum

An Overview

In previous chapters we have seen that quantum interference effects play a vital role in shaping the linear polarization profiles of solar spectral lines. The Ba II D₂ line at 4554 Å is a prominent example, where the F -state interference effects due to the odd isotopes produce polarization profiles, which are very different from those of the even isotopes that have no F -state interference. It is therefore necessary to account for the contributions from the different isotopes to understand the observed linear polarization profiles of this line. In this chapter (Smitha et al., 2013b) we do radiative transfer modeling with partial frequency redistribution (PRD) of such observations while accounting for the interference effects and isotope composition. The Ba II D₂ polarization profile is found to be strongly governed by the PRD mechanism. We show how a full PRD treatment succeeds in reproducing the observations, while complete frequency redistribution (CRD) alone fails to produce polarization profiles that have any resemblance with the observed ones. However, we also find that the line center polarization is sensitive to the temperature structure of the model atmosphere. To obtain a good fit to the line center peak of the observed Stokes Q/I profile, a small modification of the FALX model atmosphere is needed, by lowering the temperature in the line-forming layers. Because of the pronounced temperature sensitivity of the Ba II D₂ line it may not be a suitable tool for Hanle magnetic-field diagnostics of the solar chromosphere, because

there is currently no straightforward way to separate the temperature and magnetic-field effects from each other.

7.1 Introduction

When an atom possesses a non-zero nuclear spin (I_s) then the J states split into F states which is known as the hyperfine structure splitting. The quantum interference between the F states produces depolarization in the line core. Examples of lines governed by F -state interference are the Na I D_2 , Ba II D_2 , and Sc II line at 4247 Å. The Ba II D_2 line is due to the transition between the upper fine structure level $J = 3/2$ and the lower level $J = 1/2$ (see Figure 7.1(a)). In the odd isotopes of Ba, both the upper and lower levels undergo hyperfine structure splitting (HFS) due to the nuclear spin $I_s = 3/2$, resulting in four upper and two lower F -states (see Figure 7.1(b)). The quantum interference between the upper F -states needs to be taken into account in the modeling of the Ba II D_2 line. The odd isotopes contribute about 18% of the total Ba abundance in the Sun (c.f. Table 3 of [Asplund et al., 2009](#)). The remaining 82% comes from the even isotopes, which are not subject to HFS (because $I_s = 0$).

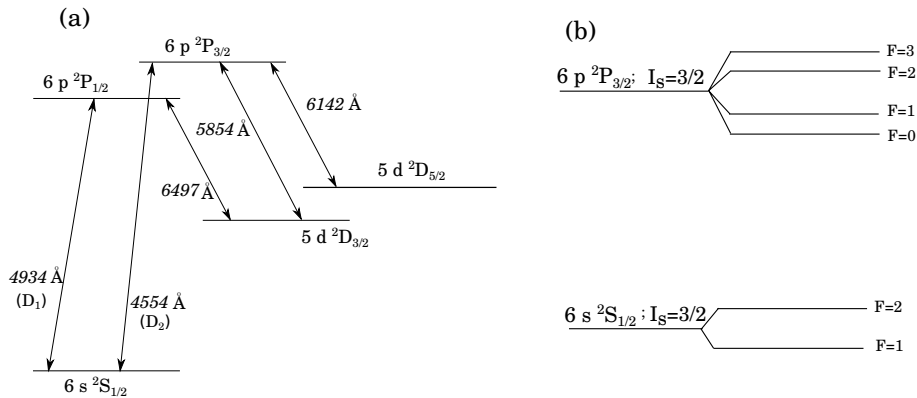


Figure 7.1: (a) represents the Ba II model atom for the even isotopes, while for the odd isotopes the atomic model is modified by replacing two of the levels, ${}^2P_{3/2}$ and ${}^2S_{1/2}$, with their hyperfine structure components, as shown in (b). In (b), I_s is the nuclear spin. The energy levels are not drawn to scale.

The intensity profile of the Ba II D_2 line has earlier been studied extensively, for example by [Holweger & Mueller \(1974\)](#) and [Rutten \(1978](#), and the references cited therein). Some of these studies aimed at determining the solar abundance of Ba. Observations with the high precision spectro-polarimeter ZIMPOL by [Stenflo & Keller \(1997\)](#) clearly revealed the existence of three distinct peaks in the linear polarization (Q/I) profiles of the Ba II D_2 line. The nature of these peaks could subsequently be theoretically clarified by [Stenflo \(1997\)](#), who used the last scattering approximation to model the Q/I profiles. It was demonstrated that the central Q/I peak is due to the

even isotopes of Ba, while the two side peaks are due to the odd isotopes.

Using a similar last scattering approximation, the magnetic sensitivity of the Ba line was explored by [Belluzzi et al. \(2007\)](#). Both these papers however did not account for radiative transfer or PRD effects. The potential of using the Ba II D₂ line as a diagnostic tool for chromospheric weak turbulent magnetic fields and the important role of PRD were discussed by [Faurobert et al. \(2009\)](#), but the treatment was limited to the even Ba isotopes, for which HFS is absent. In contrast, our radiative-transfer treatment with PRD in the present chapter includes both even and odd isotopes and the full effects of HFS with F -state interferences (see also [Smitha et al., 2013b](#)).

The theory of F -state interference in the non-magnetic collisionless regime including the effects of PRD was developed in Chapter 6 (see also [Smitha et al., 2012b](#)). In that chapter, the PRD matrix was also incorporated into the polarized radiative transfer equation. The transfer equation was then solved for the case of constant property isothermal atmospheric slabs. In this chapter we extend the work of Chapter 6 to solve the line formation problem in realistic 1-D model atmospheres in order to model the Ba II D₂ line profile observed in a quiet region close to the solar limb. Further we present center-to-limb variation (CLV) observations of this line and our initial attempts to model the same.

The outline of the chapter is as follows: In Section 7.2 we present the polarized radiative transfer equation which is suitably modified to handle several isotopes of Ba. In Section 7.3 we present the details of the observations. In Section 7.4 we discuss the model atom and the model atmosphere used. The results are presented in Section 7.5 with concluding remarks in Section 7.6.

7.2 Polarized line transfer equation with F -state interference

The polarization of the radiation field is in general represented by the full Stokes vector $(I, Q, U, V)^T$. However, in the absence of a magnetic field Stokes U and V are zero in an axisymmetric 1-D atmosphere. Hence in a non-magnetic medium the Stokes vector $(I, Q)^T$ is sufficient to express the polarization state of the radiation field. The transfer equation in the reduced Stokes vector basis (see [Smitha et al., 2012a](#)) is

$$\mu \frac{\partial \mathcal{I}(\lambda, \mu, z)}{\partial z} = -k_{\text{tot}}(\lambda, z) [\mathcal{I}(\lambda, \mu, z) - \mathcal{S}(\lambda, z)], \quad (7.1)$$

with positive Q defined to represent linear polarization oriented parallel to the solar limb. The quantities appearing in Equation (7.1) are defined in the reference mentioned above. However, we need to generalize the previous definitions of opacity and source

vector to handle even and odd isotope contributions together.

The total opacity $k_{\text{tot}}(\lambda, z) = k_l(z)\phi_g(\lambda, z) + \sigma_c(\lambda, z) + k_{\text{th}}(\lambda, z)$, where σ_c and k_{th} are the continuum scattering and continuum absorption coefficients, respectively. In the present treatment, k_{th} also includes the contribution from the blend lines, which are assumed to be depolarizing and hence are treated in LTE. k_l is the wavelength averaged absorption coefficient for the $J_a \rightarrow J_b$ transition. J_a and J_b are the electronic angular momentum quantum numbers of the lower and upper level, respectively. ϕ_g is the Voigt profile function written as

$$\phi_g(\lambda, z) = 0.822 \phi_e(\lambda, z) + 0.178 \phi_o(\lambda, z). \quad (7.2)$$

$\phi_e(\lambda, z)$ is the Voigt profile function for the even isotopes of Ba II corresponding to the $J_a = 1/2 \rightarrow J_b = 3/2$ transition in the absence of HFS. The profile function for the odd isotopes is $\phi_o(\lambda, z)$, which is the weighted sum of the individual Voigt profiles $\phi(\lambda_{F_b F_a}, z)$ representing each $F_a \rightarrow F_b$ absorption transitions. Here F_a and F_b are the total angular momentum quantum numbers of the initial and the intermediate hyperfine split levels, respectively. $\phi_o(\lambda, z)$ is the same as $\phi_{\text{HFS}}(\lambda, z)$ defined in Equation (6.7) and is given by

$$\phi_o(\lambda, z) = \left[\frac{2}{32} \phi(\lambda_{01}, z) + \frac{5}{32} \phi(\lambda_{11}, z) + \frac{5}{32} \phi(\lambda_{21}, z) + \frac{1}{32} \phi(\lambda_{12}, z) + \frac{5}{32} \phi(\lambda_{22}, z) + \frac{14}{32} \phi(\lambda_{32}, z) \right]. \quad (7.3)$$

The 17.8% of $\phi_o(\lambda, z)$ in Equation (7.2) contains contributions from both the ^{135}Ba (6.6%) and ^{137}Ba (11.2%) odd isotopes.

The reduced total source vector $\mathcal{S}(\lambda, z)$ appearing in Equation (7.1) is defined as

$$\mathcal{S}(\lambda, z) = \frac{k_l(z)\mathcal{S}_l(\lambda, z) + \sigma_c(\lambda, z)\mathcal{S}_c(\lambda, z)}{k_{\text{tot}}(\lambda, z)} + \frac{k_{\text{th}}(\lambda, z)\mathcal{S}_{\text{th}}(\lambda, z) + \epsilon k_l(z)\phi_g(\lambda, z)\mathcal{S}_{\text{th}}(\lambda, z)}{k_{\text{tot}}(\lambda, z)}, \quad (7.4)$$

for a two-level atom with an unpolarized lower level. For the case of Ba II D₂ it was shown by [Derouich \(2008\)](#) that any ground level polarization would be destroyed by elastic collisions with hydrogen atoms (see also [Faurobert et al., 2009](#)).

In Equation (7.4), $\mathcal{S}_{\text{th}} = (B_\lambda, 0)^T$, where B_λ is the Planck function. $\mathcal{S}_l(\lambda, z)$ is the line source vector defined as

$$\mathcal{S}_l(\lambda, z) = \int_0^{+\infty} \frac{1}{2} \int_{-1}^{+1} \tilde{\mathcal{R}}(\lambda, \lambda', z) \hat{\Psi}(\mu') \mathcal{I}(\lambda', \mu', z) d\mu' d\lambda', \quad (7.5)$$

with

$$\widetilde{\mathcal{R}}(\lambda, \lambda', z) = 0.822 \widetilde{\mathcal{R}}_e(\lambda, \lambda', z) + 0.178 \widetilde{\mathcal{R}}_o(\lambda, \lambda', z). \quad (7.6)$$

Here $\widetilde{\mathcal{R}}_o(\lambda, \lambda', z)$ is a (2×2) diagonal matrix, which includes the effects of HFS for the odd isotopes. Its elements are $\widetilde{\mathcal{R}}_o = \text{diag}(\mathcal{R}_o^0, \mathcal{R}_o^2)$, where \mathcal{R}_o^K are the redistribution function components for the multipolar index K , containing both type-II and type-III redistribution of Hummer (1962). The expression for \mathcal{R}^K is obtained by the quantum number replacement $L \rightarrow J$; $J \rightarrow F$; $S \rightarrow I_s$ in Equation (5.7) (see also Smitha et al., 2013a). In our present computations, we replace the type-III redistribution functions by CRD functions. We have verified that both of these give nearly identical results (see also Mihalas, 1978; Smitha et al., 2012a) and such a replacement drastically reduces the computation time. The redistribution matrix for the 17.8% of the odd isotopes includes the contributions from the individual redistribution matrices for the ^{135}Ba and ^{137}Ba isotopes.

$\widetilde{\mathcal{R}}_e(\lambda, \lambda', z)$ is also a (2×2) diagonal matrix for the even isotopes without HFS. Its elements \mathcal{R}_e^K are the redistribution functions corresponding to the $J_a = 1/2 \rightarrow J_b = 3/2 \rightarrow J_f = 1/2$ scattering transition. They are obtained by setting the nuclear spin $I_s = 0$ in $\widetilde{\mathcal{R}}_o(\lambda, \lambda', z)$. An expression for $\widetilde{\mathcal{R}}_e(\lambda, \lambda', z)$ can be found in Domke & Hubeny (1988) and in Bommier (1997a, see also Nagendra 1994, Sampoorna 2011a) in the Stokes vector basis. It is the angle averaged versions of these quantities that are used in our present computations. As has been demonstrated in Supriya et al. (2013b), the use of the angle-averaged redistribution matrix is sufficiently accurate for all practical purposes.

Like in Chapter 5 we use the two branching ratios defined by

$$A = \frac{\Gamma_R}{\Gamma_R + \Gamma_I + \Gamma_E}; \quad B^{(K)} = \frac{\Gamma_R}{\Gamma_R + \Gamma_I + D^{(K)}} \frac{\Gamma_E - D^{(K)}}{\Gamma_R + \Gamma_I + \Gamma_E}. \quad (7.7)$$

Γ_R and Γ_I are the radiative and inelastic collisional rates, respectively. Γ_E is the elastic collision rate computed from Barklem & O'Mara (1998). $D^{(K)}$ are the depolarizing elastic collision rates with $D^{(0)} = 0$. The $D^{(2)}$ is computed using (see Derouich, 2008; Faurobert et al., 2009)

$$D^{(2)} = 6.82 \times 10^{-9} n_{\text{H}} (T/5000)^{0.40} + 7.44 \times 10^{-9} (1/2)^{1.5} n_{\text{H}} (T/5000)^{0.38} \exp(\Delta E/kT), \quad (7.8)$$

where n_{H} is the neutral hydrogen number density, T the temperature, and ΔE the energy difference between the $^2P_{1/2}$ and $^2P_{3/2}$ fine structure levels. In the present treatment we neglect the collisional coupling between the $^2P_{3/2}$ level and the metastable $^2D_{5/2}$ level. The importance of such collisions for the line center polarization of Ba II

D_2 has been pointed out by [Derouich \(2008\)](#), who showed that the neglect of such collisions would lead to an overestimate of the line core polarization by $\sim 25\%$. This in turn would cause the microturbulent magnetic field (B_{turb}) to be overestimated by $\sim 35\%$, as shown by [Faurobert et al. \(2009\)](#). However, the aim of our work in this chapter is not to determine the value of B_{turb} but to explore the roles of PRD, HFS, quantum interferences, and the atmospheric temperature structure in the modeling of the triple peak structure of the Ba II D_2 linear polarization profile.

Frequency coherent scattering is assumed in the continuum (see Chapter 5) with its source vector given by

$$\mathcal{S}_c(\lambda, z) = \frac{1}{2} \int_{-1}^{+1} \hat{\Psi}(\mu') \mathcal{I}(\lambda, \mu', z) d\mu'. \quad (7.9)$$

The matrix $\hat{\Psi}$ is the Rayleigh scattering phase matrix in the reduced basis (see [Frisch, 2007](#)). The line thermalization parameter ϵ is defined by $\epsilon = \Gamma_I / (\Gamma_R + \Gamma_I)$. The Stokes vector $(I, Q)^T$ can be computed from the irreducible Stokes vector \mathcal{I} by simple transformations given by (see [Frisch, 2007](#))

$$\begin{aligned} I(\lambda, \theta, z) &= \mathcal{I}_0^0(\lambda, \mu, z) + \frac{1}{2\sqrt{2}}(3 \cos^2 \theta - 1) \mathcal{I}_0^2(\lambda, \mu, z), \\ Q(\lambda, \theta, z) &= \frac{3}{2\sqrt{2}}(1 - \cos^2 \theta) \mathcal{I}_0^2(\lambda, \mu, z), \end{aligned} \quad (7.10)$$

where θ is the colatitude of the scattered ray. The scattering geometry is shown in Figure 1 of [Anusha et al. \(2011b\)](#).

7.3 Observational details

The observed polarization profiles of the Ba II D_2 line that are used in this chapter for modeling purposes were acquired by the ETH team of Stenflo on June 3, 2008, using their ZIMPOL-II imaging polarimetry system ([Gandorfer et al., 2004](#)) at the THEMIS telescope on Tenerife. Figure 7.2 shows the CCD images of the intensity and linear polarization recorded at various distances from the heliographic north pole with the spectrograph slit placed parallel to the limb. The polarization modulation was done using Ferroelectric Liquid Crystal (FLC) modulators. The spectrograph slit was $1''$ wide and $70''$ long on the solar disk. The resulting CCD image has 140 pixels in the spatial direction and 770 pixels in the spectral direction. The effective pixel size was $0''.5$ spatially and 5.93 m\AA spectrally. The observed profiles used to compare with the theoretical ones have been obtained by averaging the I and Q/I images in Figures 7.2 over the suitable spatial intervals.

The recording presented in Figure 7.2 does not show much spatial variation along

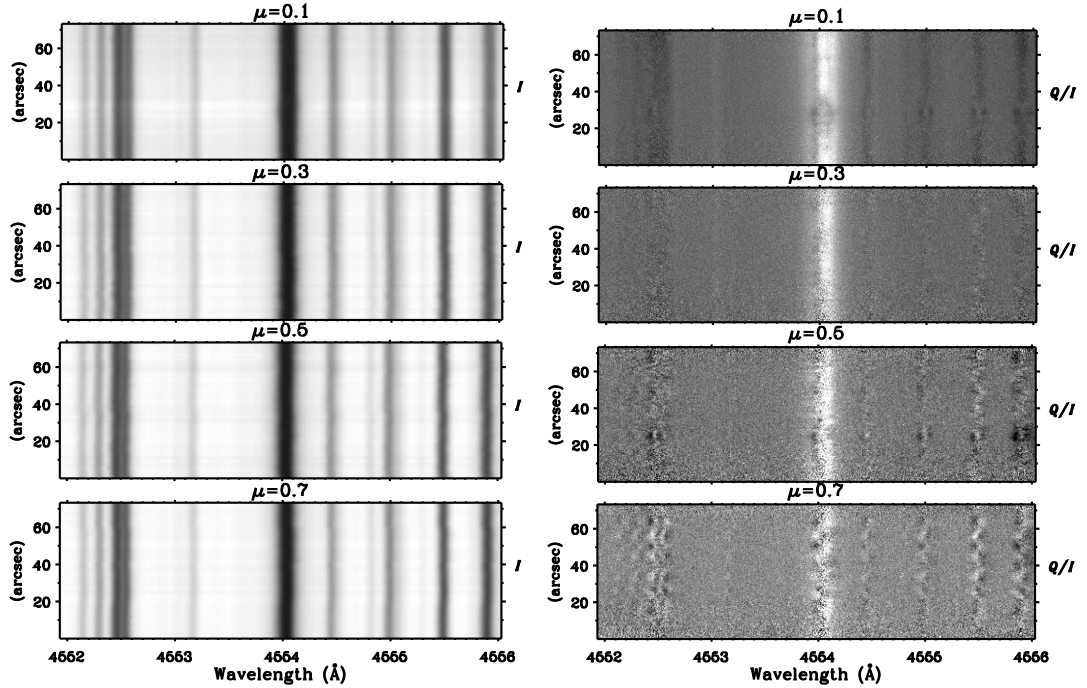


Figure 7.2: CCD image showing the I and Q/I spectra of the Ba II D₂ line at different limb distances on the solar disk. The observations were obtained on June 3, 2008, with ZIMPOL-II at the French THEMIS telescope on Tenerife.

the slit, since it represents a very quiet region. However, recordings near magnetic regions made during the same observing campaign with ZIMPOL on THEMIS exhibit large spatial variations. It has long been known that all strong chromospheric scattering lines (like the Ca I 4227 Å, Na I D₂, Sr II 4079 Å line, etc) have such spatial variations. Our observations confirm that the Ba II D₂ line is no exception, which means that it is sensitive to the Hanle effect like the other chromospheric lines. Observations of spatial variations of this line have also been carried out by López Ariste et al. (2009) and Ramelli et al. (2009).

7.4 Modeling procedure

To model the polarization profiles of the Ba II D₂ line we use a procedure similar to the one described in Holzreuter et al. (2005, see also Anusha et al. 2011b, Anusha et al. 2010, Smitha et al. 2012a). It involves the computation of the intensity, opacity and collisional rates from the PRD-capable MALI (Multi-level Approximate Lambda Iteration) code developed by Uitenbroek (2001, referred to as the RH-code). The code solves the statistical equilibrium equation and the unpolarized radiative transfer equation self-consistently. The opacities and the collision rates thus obtained are kept fixed, while the reduced Stokes vector \mathcal{I} is computed perturbatively by solving the polarized

radiative transfer equation with the angle-averaged redistribution matrices defined in Section 7.2.

Such a procedure requires a model atom and a model atmosphere as inputs to the RH-code. The details of the model atom and the atmosphere are discussed in the next subsections.

7.4.1 Model atom

Three different atom models are considered, two for the odd and one for the even isotope. The atom model for the even isotope (^{138}Ba) is given by the five levels of Figure 7.1(a), while for the odd isotopes (^{135}Ba and ^{137}Ba) the model is extended to include the hyperfine splitting as described by Figure 7.1(b). We neglect the contribution from other less abundant even isotopes. The wavelengths of the six hyperfine transitions for the odd isotopes are taken from Kurucz' database and are listed in Table 7.1. These transitions are weighted with their line strengths given in Equation (7.3) (see Table 7.1).

Table 7.1: Wavelengths (\AA) of the hyperfine transitions for the odd isotopes of Ba II

F_a	F_b	^{135}Ba	^{137}Ba	Line strength
1	0	4553.999	4553.995	0.15625
1	1	4554.001	4553.997	0.06250
1	2	4554.001	4553.998	0.15625
2	1	4554.046	4554.049	0.43750
2	2	4554.059	4554.051	0.15625
2	3	4554.050	4554.052	0.03125

7.4.2 Model atmosphere

We present the results computed for some of the standard realistic 1-D model atmospheres, like FALA, FALF, FALC (Fontenla et al., 1993) and FALX (Avrett, 1995). Among these four models FALF is the hottest and FALX the coolest. Their temperature structures are shown in the top panel of Figure 7.3. However, as will be discussed below, we find that a model atmosphere that is cooler than FALX is needed to fit the observed profiles. The new model, denoted $\overline{\text{FALX}}$, is obtained by reducing the temperature of the FALX model by about 300 K in the height range 500 – 1200 km above the photosphere.

We have verified that such a modification of the FALX model does not significantly affect the intensity spectra. In contrast, the Q/I spectra turn out to be very sensitive to such temperature changes. Like in Chapter 5, we test the $\overline{\text{FALX}}$ atmosphere by computing the limb darkening function for a range of wavelengths and μ values and

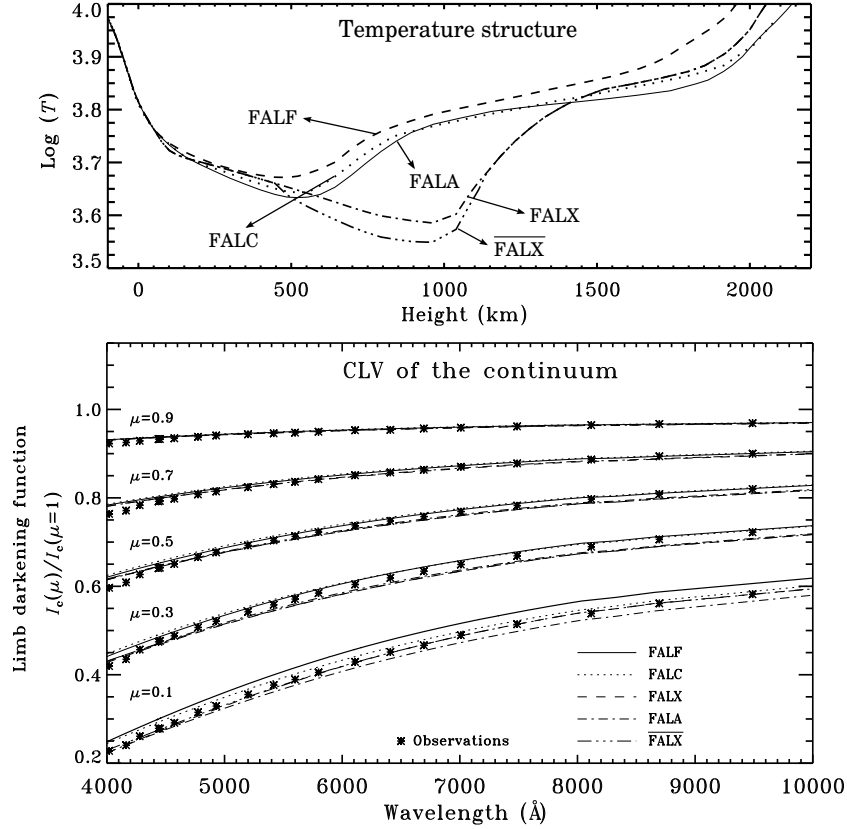


Figure 7.3: *Top panel:* The temperature structure of some of the standard model atmospheres. $\overline{\text{FALX}}$ represents the model for which the temperature is reduced by about 300 K over a 700 km range around the height of formation of the Ba II D₂ line. *Bottom panel:* Comparison between the observed center-to-limb variation (CLV) of the continuum intensity and the predictions from different model atmospheres including $\overline{\text{FALX}}$ for a wide range of wavelengths from the violet to the IR region of the spectrum. For all the μ values the dashed and the dash-triple dotted lines are practically indistinguishable as the models FALX and $\overline{\text{FALX}}$ produce nearly identical fits.

compare it with the observed data from [Neckel & Labs \(1994\)](#). This is shown in the bottom panel of Figure 7.3. One can see that $\overline{\text{FALX}}$ and the standard FALX fit the observed center-to-limb variation equally well. Therefore small modifications of the temperature structure to achieve a good fit to the observed Q/I profile can be made without affecting the model constraints imposed by the intensity spectrum.

7.5 Results

In the following we discuss the modeling details and the need for a model atmosphere that is cooler than FALX. This helps us to evaluate the temperature sensitivity of the Ba II D₂ line and its usefulness for magnetic-field diagnostics. In addition we demonstrate the profound role that PRD plays for the formation of the polarized line profile.

7.5.1 Modeling the Ba II D₂ line profile

Modeling details

From the three Ba II atom models described in Section 7.4.1 we obtain three sets of physical quantities (two for the odd isotopes and one for the even isotope) from the RH code. These quantities include line opacity, line emissivity, continuum absorption coefficient, continuum emissivity, continuum scattering coefficient, and the mean intensity. The mathematical expressions used to compute these various quantities for the even isotopes are given in Uitenbroek (2001). For the odd isotopes, the profile functions in these expressions are replaced by $\phi_o(\lambda, z)$ defined by Equation (7.3).

The three sets of quantities are then combined in the ratio of their respective isotope abundances and subsequently used as inputs to the polarization code.

Temperature sensitivity

The polarization profiles thus computed for the various model atmospheres are shown in Figure 7.4, displayed separately for the even, odd, and combined even-odd cases in three different panels. The Stokes Q/I profiles in Figure 7.4 are computed by setting the total abundance of Ba in the Sun equal to the abundance of even isotopes in the first panel; the abundance of odd isotopes in the second panel; and a fractional abundance of even (82%) and odd (18%) isotopes in the third panel. The profiles in the first panel can be compared to the results presented in Figure 6 of Faurobert et al. (2009). As seen from the first panel, the amplitude of the central peak for the even isotopes is very sensitive to the temperature structure of the model atmosphere in contradiction with the conclusions of Faurobert et al. (2009). Also in their paper, the amplitude of the central peak obtained from the FALC model is larger than the one obtained from FALX, which is opposite to our findings (although it could be that the version of the FALC model they used is not identical to the one that we have used). However, the profile computed with the FALX model in first panel of Figure 7.4 for the even isotopes is in good agreement with the one given in their paper.

The profiles in the second panel of Figure 7.4, which represent the odd isotopes, also exhibit a similar large sensitivity to the choice of model atmosphere. Therefore the combined even-odd isotopes profiles in the third panel are also very sensitive to the temperature structure.

For the sake of clarity, let us point out that the combined Q/I profiles in the bottom panel of Figure 7.4 differ profoundly from what one would obtain from a linear superposition of the corresponding profiles for the even and odd isotopes individually in the two other panels, in proportion to their isotope ratios. The reason is that the combination is highly non-linear, since the lines are formed in an optically thick medium

(namely the radiative transfer effects). While the opacities and redistribution matrices are combined in a linear way as described by Equations (7.2) and (7.6), the even and odd isotopes blend with each other in the radiative transfer process, which makes the combination as it appears in the emergent spectrum highly non-linear.

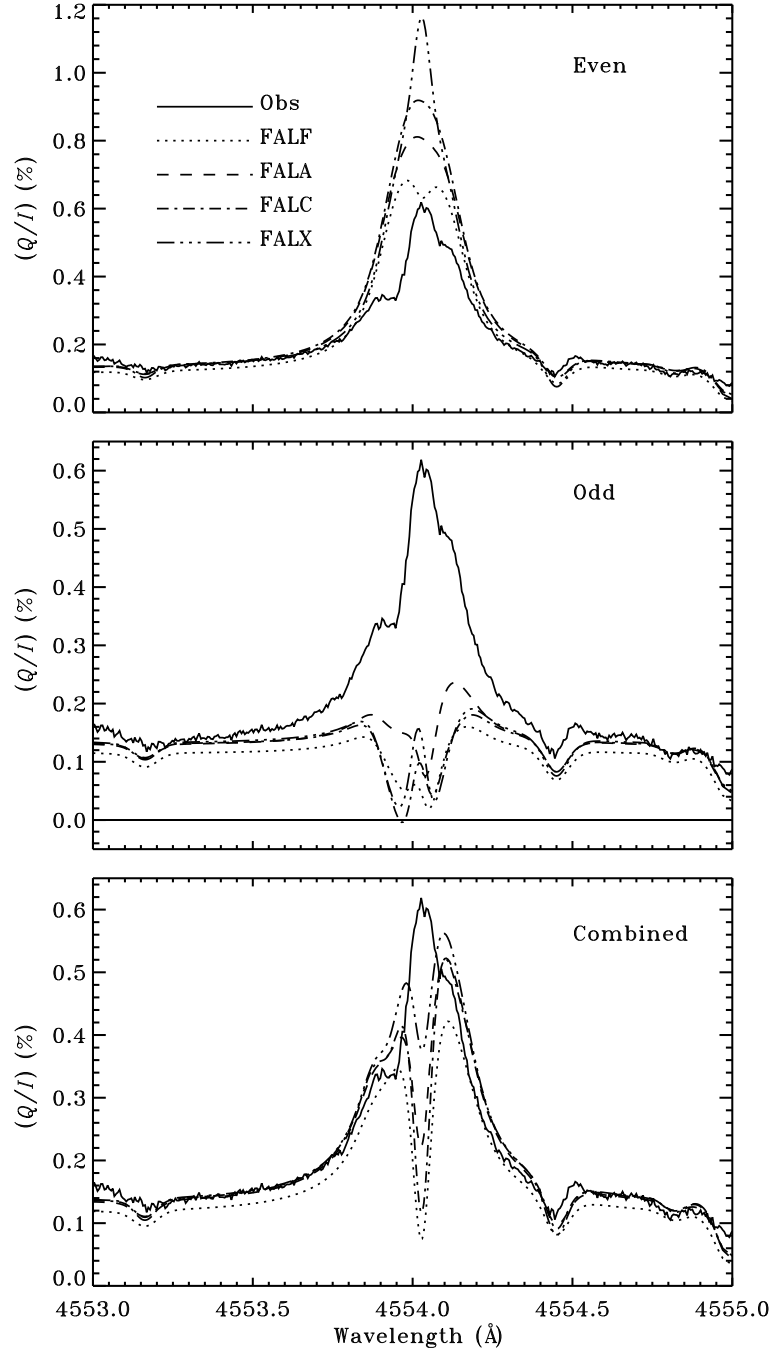


Figure 7.4: Comparison between the observed Q/I profile and the theoretical profiles for some of the standard model atmospheres, separately displayed for the even, odd, and combined even-odd cases. The theoretical profiles represent the non-magnetic case and have been smeared with a Gaussian having a full width at half maximum (FWHM) of 70 mÅ to account for instrumental and macro-turbulent broadening.

The drastic depolarization of Q/I in the line core has its origin in the polarizability

factor W_2 of the odd isotopes. It is well known that the trough like suppression of W_2 in the line core for Ba II is formed due to hyperfine structure for the odd isotopes (see [Stenflo, 1997](#)). In our radiative transfer calculations we have a superposition (in the proportion of the isotope ratios), of the trough-like scattering opacity of the odd isotopes, with the peak-like scattering opacity of the even isotopes. The shape of the Q/I profile depends on the details of radiative transfer and PRD (see Equations (7.2)-(7.6)) namely on how these two scattering opacities non-linearly blend to produce the net result for the emergent radiation in the optically thick cases.

Need for the $\overline{\text{FALX}}$ model

As seen from the last panel of Figure 7.4, the central peak is not well reproduced by any of the standard model atmospheres. All the models produce a dip at line center. Such a central dip is commonly due to the effects of PRD, caused by the properties of the type-II frequency redistribution. In the case of Ba II D₂, the contribution to this central dip comes mainly from the even isotopes, as shown in Figure 7.5. The three rows in this figure represent the even, odd and combined even-odd cases, respectively, for the FALX model atmosphere. The first column shows the profiles computed with only type-II redistribution, the second column those computed with CRD only. The CRD profiles are obtained by setting the branching ratios $A = 0$ and $B^{(K)} = (1 - \epsilon)$. None of the CRD profiles shows a central dip.

[Holzreuter et al. \(2005\)](#) have explored in detail, the occurrence and nature of this central dip. They show that its magnitude is strongly dependent on the choice of atmospheric parameters. This behavior is also evident from Figure 7.4. The cooler the atmosphere, the smaller is the central dip. The dip is often smoothed out by instrumental and macro-turbulent broadening. However, the profiles in Figure 7.4 have already been smeared with a Gaussian function having a full width at half maximum (FWHM) of 70 mÅ. The dip could be suppressed by additional smearing, but such large smearing would also suppress the observed side peaks of the odd isotopes and would make the intensity profile inconsistent with the observed one. The value 70 mÅ has been chosen to optimize the fit, but it is also consistent with what we expect based on the observing parameters and turbulence in the chromosphere.

The failure of all the tried standard model atmospheres therefore leads us to introduce a new model with a modified temperature structure, which is cooler than the standard FALX model. The details of the new cooler $\overline{\text{FALX}}$ model has been given in Section 7.4.2. This new model atmosphere succeeds in giving a good fit to both the intensity and the polarization profiles, as shown in Figure 7.6.

To simulate the effects of spectrograph stray light on the intensity and polarization profiles we have applied a spectrally flat unpolarized background of 4% of the contin-

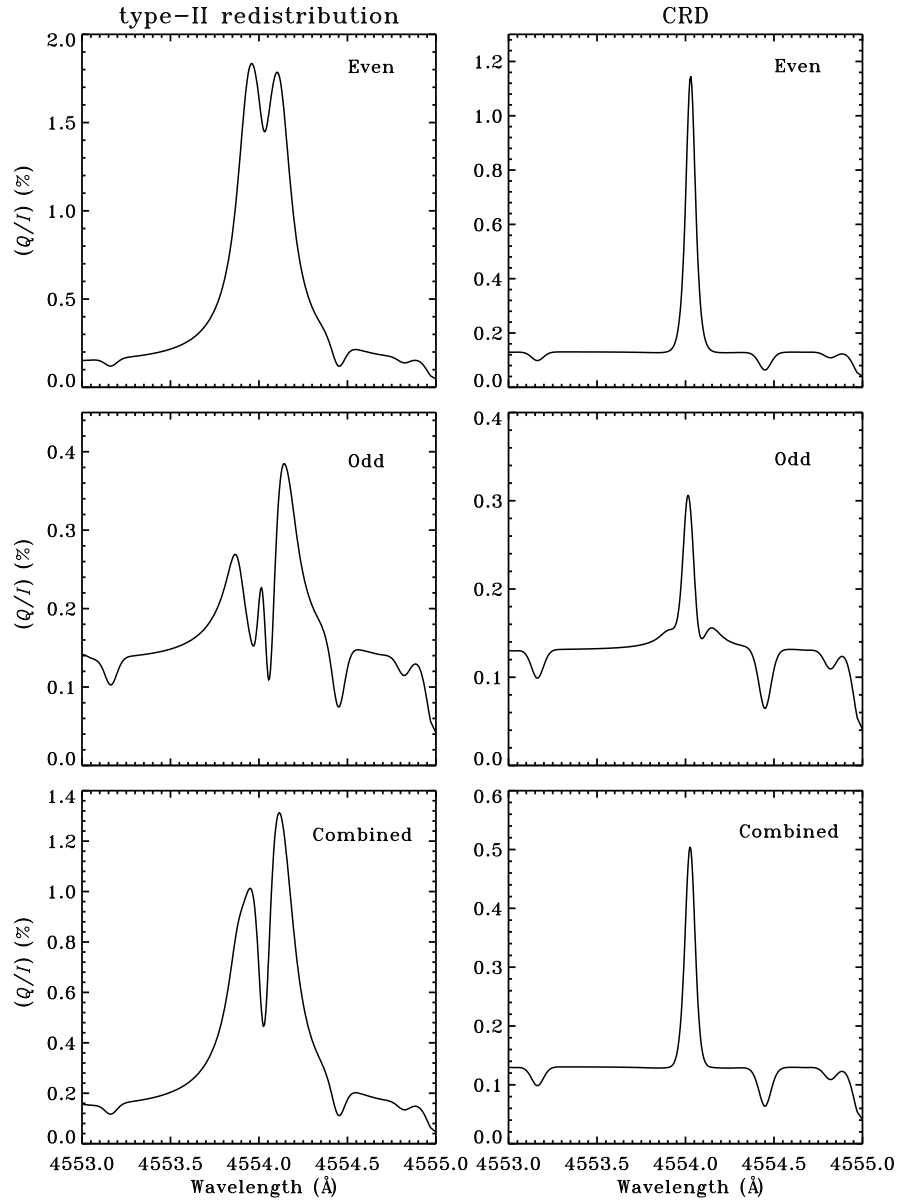


Figure 7.5: Theoretical Q/I profiles computed for the non-magnetic FALX model for the even (first row), odd (second row), and combined even-odd (third row) isotopes, with only type-II frequency redistribution (first column) and only complete frequency redistribution CRD (second column). A prominent central dip is present for the type-II redistribution profiles although they have been smeared with a Gaussian having FWHM = 70 mÅ.

uum intensity level to the theoretical $(I, Q/I)$ profiles. For a good Q/I line center fit, we find that it is necessary to include Hanle depolarization from a non-zero magnetic field. Our theoretical profiles are based on a micro-turbulent magnetic field of strength B_{turb} with an isotropic angular distribution. Our best fit to the Q/I profile corresponds to a field strength of $B_{\text{turb}} = 2$ G.

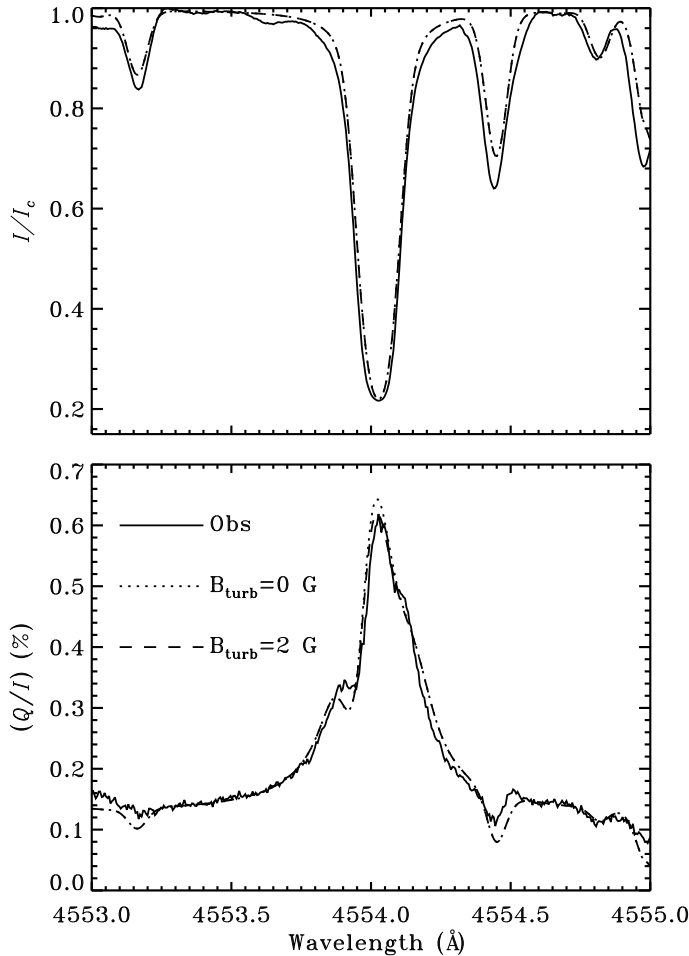


Figure 7.6: Fit to the observed profile using the $\overline{\text{FALX}}$ model with and without a micro-turbulent magnetic field B_{turb} . The theoretical profiles have been smeared using a Gaussian with $\text{FWHM} = 70 \text{ m}\text{\AA}$.

7.5.2 The importance of PRD

The importance of PRD in modeling the Ba II D₂ line has already been demonstrated in [Faurobert et al. \(2009\)](#), although by only considering the even isotopes. Figure 7.5 demonstrates the importance of PRD for both the odd and the even isotopes. As seen from the second column of this figure, the Q/I profiles for the odd isotopes when computed exclusively in CRD do not produce any side peaks, while the profiles computed with type-II redistribution exhibits such peaks. Also, by comparing the Q/I profiles for the even isotopes in the first row, we see that CRD fails to generate the needed line wing polarization. A comparison between the observed profiles and the theoretical profiles based on CRD alone (dotted line) and on full PRD (dashed line) for the $\overline{\text{FALX}}$ model is shown in Figure 7.7. While the intensity profile can be fitted well using either PRD or CRD, the polarization profile cannot be fitted at all with CRD alone. PRD is therefore essential to model the Q/I profiles of the Ba II D₂ line.

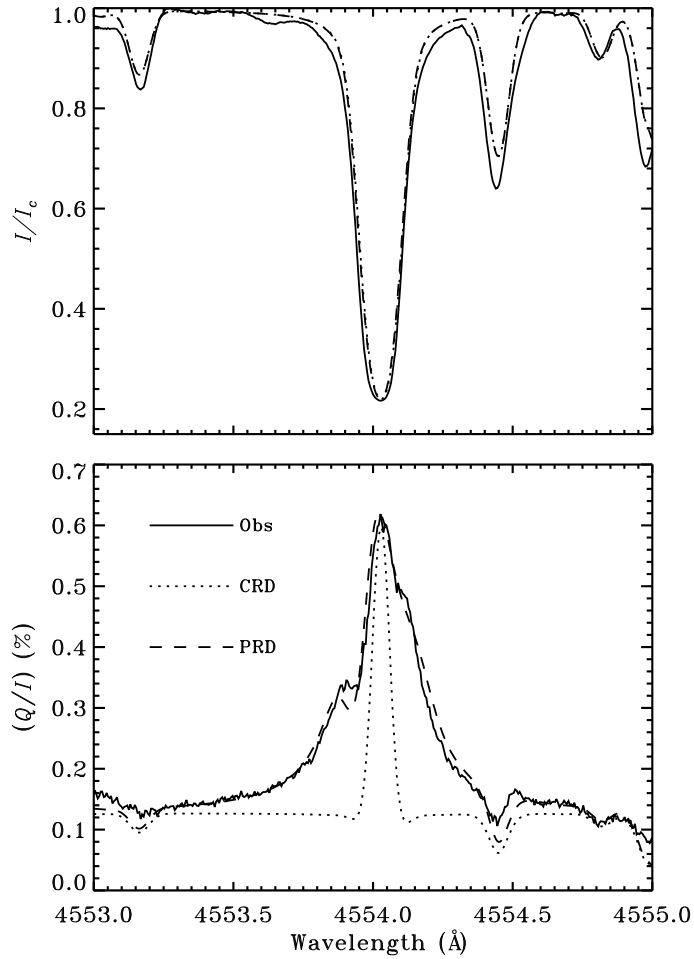


Figure 7.7: Comparison between the observed Stokes profiles and the profiles computed with CRD (dotted line) and PRD (dashed line) for the $\overline{\text{FALX}}$ model. The theoretical profiles have been smeared with a Gaussian having $\text{FWHM} = 70 \text{ m}\text{\AA}$. The strength of the micro-turbulent magnetic field B_{turb} has been chosen to be 2 G for the PRD and 5 G for the CRD profiles. The dashed line in this figure is same as the dashed line in Figure 7.6.

7.5.3 Modeling the CLV observations

The left panel of Figure 7.8 shows the CLV of the observed Q/I profiles. The right panel of this figure shows the CLV of the theoretical Q/I profiles computed using the $\overline{\text{FALX}}$ model atmosphere. As seen from the right panel, the newly constructed model atmosphere, though successfully fits the observed profiles for $\mu = 0.1$, fails to fit the observations for $\mu > 0.1$. In fact for $\mu > 0.1$, we again obtain a central dip instead of a peak in the Q/I profiles. The central dip becomes deeper as $\mu \rightarrow 1$. This behavior was noticed also for the case of Na I D_2 by Holzreuter et al. (2005). Thus the modification in the temperature structure of the $\overline{\text{FALX}}$ model atmosphere, presented in this chapter, helps only for $\mu = 0.1$. For other μ positions, the temperature structure has to be further modified. Thus we are unable to find a single 1D model atmosphere that fits the CLV

observations of the Ba II D₂ line.¹

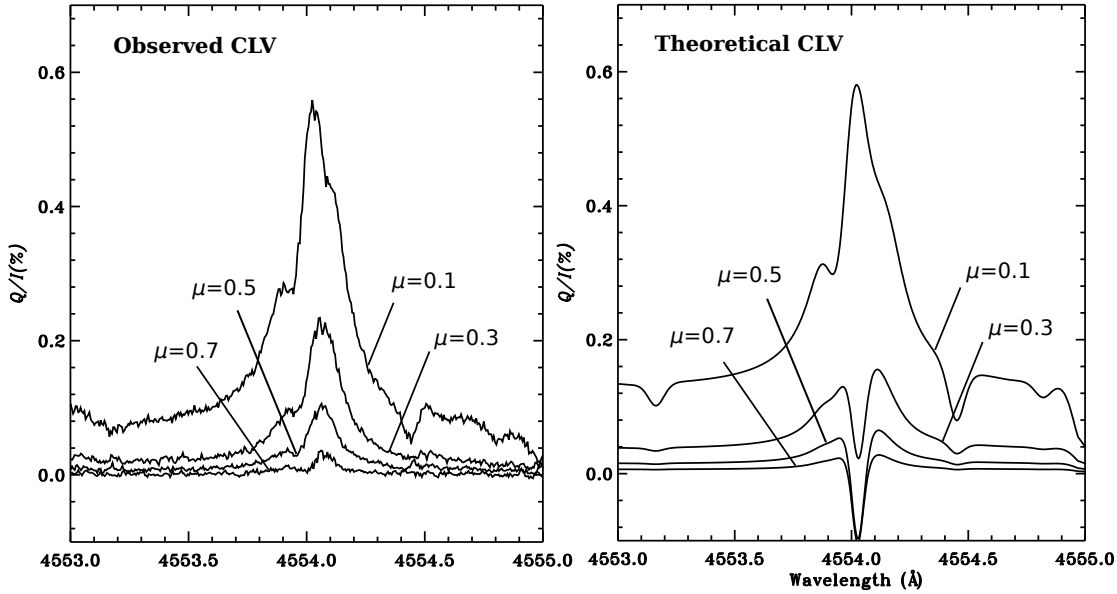


Figure 7.8: Comparison between the observed center to limb variation (CLV) of the Q/I profiles and the theoretically computed CLV. The theoretical profiles are computed using the FALX model atmosphere.

7.6 Conclusions

In the present chapter we have for the first time tried to model the polarization profiles of the Ba II D₂ line by taking full account of PRD, radiative transfer, and HFS effects. We use the theory of F -state interference developed in Chapters 4 and 6 in combination with different atom models representing different isotopes of Ba II and various choices of model atmospheres. Applications of the well known standard model atmospheres FALF, FALC, FALA, and FALX fail to reproduce the central peak, and instead produce a central dip mainly due to PRD effects. We have shown that in the case of Ba II D₂ the central dip is reduced by lowering the temperature of the atmospheric model. We can therefore achieve a good fit to the observed polarization profile by slightly reducing the temperature of the FALX model.

However the new model though successfully fits the observations for $\mu = 0.1$, it fails at other limb distances. Hence within the sample of the model atmospheres tested by us, no single one dimensional, single component model atmosphere succeeds in reproducing the observed Q/I profiles at all limb distances. This possibly indicates

¹In fact the complexity of the problem is such that no single 1D model atmosphere fits the observations of different lines, apart from observations of the same line at different μ positions. For example, when modeling the Cr I triplet in Chapter 5, we had to modify the temperature structure of the FALF model atmosphere in the deeper layers to obtain a fit to the $(I, Q/I)$ observations at $\mu = 0.15$.

that multi-dimensional transfer effects are required to model the CLV observations of this line.

In modeling the Ba II D₂ line we account for the depolarizing effects of elastic collisions with hydrogen atoms but neglect the alignment transfer between the $^2P_{3/2}$ level and the metastable $^2D_{5/2}$ level. It has been shown by [Derouich \(2008\)](#) that this alignment transfer affects the line center polarization and is needed for magnetic field diagnostics. The purpose of the present chapter is however not to determine magnetic fields but to clarify the physics of line formation.

We demonstrate that PRD is essential to reproduce the triple peak structure and the line wing polarization of the Ba II D₂ line, but find that the line center polarization is very sensitive to the temperature structure of the atmosphere, which contradicts the conclusions of [Faurobert et al. \(2009\)](#), who find that the barium line is temperature insensitive and therefore suitable for Hanle diagnostics. This contradiction illustrates that a full PRD treatment as done in the present chapter, including the contributions from both the even and odd isotopes, is necessary to bring out the correct temperature dependence of the line. The large temperature sensitivity of the Ba II D₂ line makes it rather unsuited for magnetic-field diagnostics, since there is no known straightforward way to separate the temperature and magnetic-field effects for this line.

Based on:

Smitha, H. N., Nagendra, K. N., Stenflo, J. O., Bianda, M., & Ramelli, R. 2014, under review

8

Quantum interference effects in the Sc II 4247 Å line of the Second Solar Spectrum

An Overview

The Sc II 4247 Å line formed in the chromosphere is one of the lines well known, like the Na I D₂ and Ba II D₂, for its prominent triple peak structure in Q/I and the underlying quantum interference effects governing it. In this chapter, we try to study the nature of this triple peak structure using the theory of F -state interference including the effects of partial frequency redistribution (PRD) and radiative transfer (RT), developed in Chapter 6 and 7. We compare our results with the observations taken in a quiet region near the solar limb. In spite of accounting for PRD and RT effects it has not been possible to reproduce the observed triple peak structure in Q/I . While the two wing PRD peaks (on either side of central peak) and the near wing continuum can be reproduced, the central peak is completely suppressed by the enhanced depolarization resulting from the hyperfine structure splitting. Also, the theoretical intensity profiles are much deeper than the observed ones. By conducting several tests we show that both the rest intensity and the Q/I core peak are not too sensitive to the variations in the model atmosphere. This leaves us with little hope even if we possibly go beyond the 1D standard model atmospheres. Hence this system has presented us with an enigma and

we suspect that there could be some fundamental aspect missing in our understanding of the Sc atomic system.

8.1 Introduction

With the advent of highly sensitive spectropolarimeters like the Zurich Imaging Polarimeter (ZIMPOL) we now have access to the linearly polarized spectrum of the Sun that is due to coherent scattering processes in the Sun's atmosphere (and which has nothing to do with the well-known transverse Zeeman effect), which is the "Second Solar Spectrum" (Stenflo & Keller, 1996, 1997). It is richly structured with signatures of different kinds of scattering processes taking place in atomic systems of varying complexity. Of particular interest are the many often enigmatic signatures of quantum interference effects between fine structure states, hyperfine structure states, and magnetic substates (Hanle effect).

Atoms with non-zero electron spin S undergo fine structure splitting and exhibit J -state interference whereas the atoms with non-zero nuclear spin I_s undergo hyperfine structure splitting (HFS) and show F -state interference. The Sc II 4247 Å line is governed by F -state interference.

Here we extend our previous work on the Ba II D₂ line (Chapter 7, see also Smitha et al., 2013b), to study the Sc II line at 4247 Å. This line arises due to the transition $J = 2 \rightarrow J = 2$. Due to coupling with the nuclear spin ($I_s = 7/2$) both the upper and the lower J levels are split into five F -states each with 13 radiative transitions between them.. The level diagram of this system is shown in Figure 8.1. We use the theory of F -state interference presented in Chapters 6 and 7, which takes account of PRD effects in the absence of magnetic fields. The results in this chapter do not include the contributions from magnetic fields. The theory of F -state interference in the presence of magnetic fields including the effects of PRD has been recently developed in Sowmya et al. (2014b).

The 4247 Å line of Sc II is a chromospheric line with an approximate height of formation between 900-1100 km above the photosphere. ⁴⁵Sc is the only stable isotope of scandium. It shows prominent triple peak structure in its Q/I spectra (see Gandorfer, 2002; Stenflo, 2003). Modeling of this triple peak structure using the last scattering approximation was attempted by Belluzzi (2009). The effects of PRD and radiative transfer were neglected in that work.

In the present chapter (see also Smitha et al., 2014b), by taking account of both PRD and radiative transfer effects, we study the sensitivity of the $(I, Q/I)$ profiles to different atomic and atmospheric parameters. From our efforts we find it difficult to reproduce the triple peak structure in Q/I and also the rest intensity. The central peak in Q/I is suppressed due to depolarization from HFS. However the PRD peaks and

the near wing continuum in the theoretical profiles match closely with the observed profiles. Our tests suggest that the observed Stokes profiles cannot be reproduced by modifications in the existing 1D standard model atmospheres. Hence we suspect the role of other physical effects in shaping the observed profiles, which may not have been accounted for in the present treatment. The lower level Hanle effect could qualify as being one such effect which can increase the polarization of the central peak, but its contribution is significant only for fields ≤ 1 G (Belluzzi, 2009).

The details of the various tests conducted by us are discussed in the sections below.

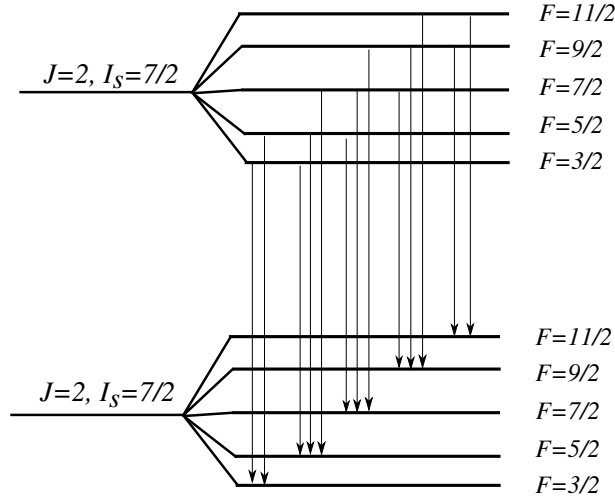


Figure 8.1: Level diagram showing the hyperfine structure splitting of the $3d4s$ and $3d4p$ atomic levels of the Sc II atom.

8.2 Computing the theoretical profiles

The details of computing the Stokes profiles with F -state interference including the effects of PRD and radiative transfer using realistic 1D model atmospheres are presented in Smitha et al. (2013b). We use the same here too and hence do not repeat them. However certain physical quantities need to be redefined to represent the Sc II 4247 Å line system, and they are presented below.

The Voigt profile function: For the case of Sc II 4247 Å line, the Voigt profile function defined in Equation (7.3) is to be replaced by

$$\begin{aligned} \phi(\lambda, z) = & \left[\frac{1}{25}\phi(\lambda_{33}, z) + \frac{3}{50}\phi(\lambda_{35}, z) + \frac{3}{50}\phi(\lambda_{53}, z) + \frac{1}{1400}\phi(\lambda_{55}, z) + \frac{5}{56}\phi(\lambda_{57}, z) \right. \\ & + \frac{5}{56}\phi(\lambda_{75}, z) + \frac{2}{105}\phi(\lambda_{77}, z) + \frac{11}{120}\phi(\lambda_{79}, z) + \frac{11}{120}\phi(\lambda_{97}, z) \\ & \left. + \frac{25}{264}\phi(\lambda_{99}, z) + \frac{7}{110}\phi(\lambda_{911}, z) + \frac{7}{110}\phi(\lambda_{119}, z) + \frac{13}{55}\phi(\lambda_{1111}, z) \right], \quad (8.1) \end{aligned}$$

where $\phi(\lambda_{F_a F_b}, z)$ is the Voigt profile function for the $F_a \rightarrow F_b$ transition with F_a and F_b being the initial and excited F -states respectively. For notational brevity, the subscripts F_a and F_b in the ϕ terms are multiplied by 2 in the above equation.

The depolarizing elastic collision rate $D^{(2)}$: The branching ratios which describe the contribution from type-II and collisional redistribution (type-III) are defined in Equation (7.7). The depolarizing elastic collision rate $D^{(2)}$ which enter through the branching ratio $B^{(2)}$ can be computed using Equation (7.102) of Landi Degl'Innocenti & Landolfi (2004)

$$D^{(K)}(J) = C_E^{(0)}(J) - C_E^{(K)}(J), \quad (8.2)$$

where $C_E^{(K)}(J)$ is given by

$$C_E^{(K)}(J) = (-1)^K \frac{\begin{Bmatrix} J & J & K \\ J & J & \tilde{K} \end{Bmatrix}}{\begin{Bmatrix} J & J & 0 \\ J & J & \tilde{K} \end{Bmatrix}} C_E^{(0)}(J), \quad (8.3)$$

with $C_E^{(0)}(J) = \Gamma_E / (2J + 1)$.

If the interaction between the atom and the colliding particle is assumed to be of dipolar type then $\tilde{K} = 1$. In this case $D^{(2)}(J) = 0.1 \Gamma_E$. If the interaction is assumed to be dipole-dipole in nature, then $\tilde{K} = 2$. In this case $D^{(2)}(J) = 0.243 \Gamma_E$. We have tested that both these values of $D^{(2)}$ give nearly identical emergent Q/I profiles. This is because the Sc II 4247 Å line is formed at a height of 900-1100 km above the photosphere. This can be seen from Figure 8.2 where the contribution functions are plotted as a function of height for different model atmospheres. At these heights, the branching ratio $B^{(2)}$ is nearly zero as seen from Figure 8.3. We choose $D^{(2)}(J) = 0.243 \Gamma_E$ for further computations.

8.3 Observations

The observations of the Sc II 4247 Å line analyzed in this chapter were recorded on September 15, 2012 at IRSOL, Switzerland using the ZIMPOL-III imaging polarimeter (Ramelli et al., 2010). The photoelastic modulator (PEM) followed by a linear polarizer (beam splitter) was used as the polarization analyzer.

Though the telescope is almost free from instrumental polarization and cross talk effects around the equinox, to minimize residual instrumental signatures, a glass compensation plate was inserted in the optical path between the calibration optics and the analyzer. This also reduces the residual linear polarization offset. The optics was adjusted such that the positive Q represents the linear polarization parallel to the spec-

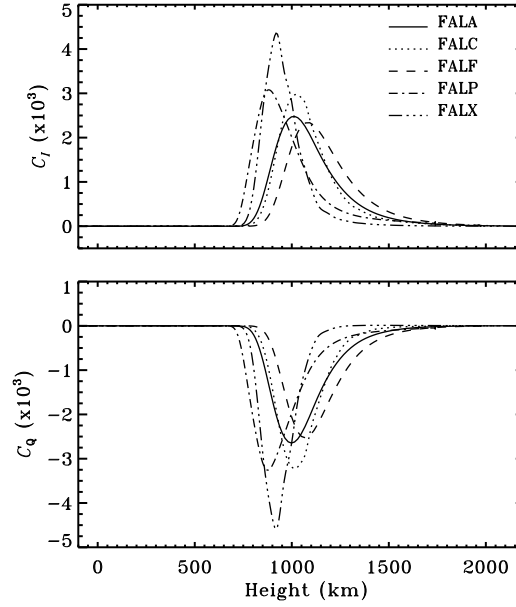


Figure 8.2: Contribution functions C_I and C_Q computed from different model atmospheres for $\mu = 0.1$.

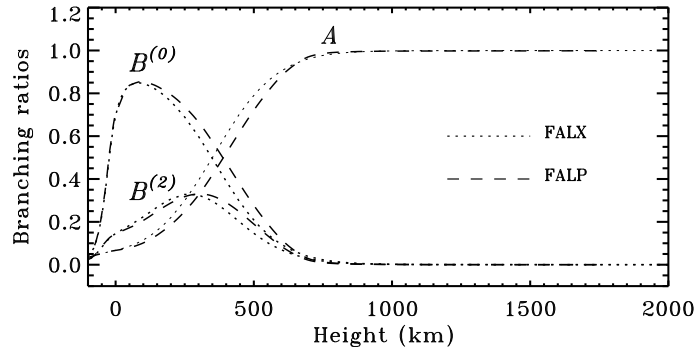


Figure 8.3: The branching ratios A and $B^{(K)}$, with $K = 0$ and 2 , as a function of height computed using the FALX and FALP model atmospheres.

trograph slit. An image derotator (Dove prism) placed between the analyzer and the slit-jaw allowed to rotate the solar image, and compensate for the solar rotation. The analyzer and the calibration optics were also rotated correspondingly. The observations were performed at a quiet region with the spectrograph slit placed parallel to the solar East limb. The spectrograph grating angle and a prefilter were selected to work with the 13th spectral order. On the CCD we got a resolution of $1.44''$ per pixel along the spatial direction and 5.25 mÅ per pixel along the spectral direction. Three measurements were obtained by placing the slit at $5''$, $15''$, and $25''$ from the solar limb. The observations at each μ -position consisted of a sum of 1000 frames obtained with an exposure of 1 sec, making the total exposure time as 16 minutes. The image motion perpendicular to the limb was compensated with a glass tilt-plate. The tilt of the plate was determined automatically with a limb recognition software using the information in the slit jaw image. The Stokes ($I, Q/I$) images shown in Figure 8.4 were obtained after the data

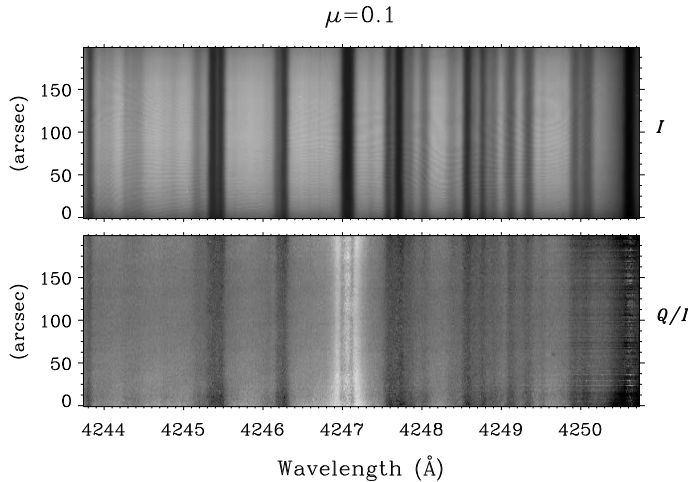


Figure 8.4: CCD image showing ($I, Q/I$) for the Sc II 4247 Å line recorded on September 15, 2012 using the ZIMPOL spectropolarimeter at IRSOL, Switzerland.

reduction. We also did a flat-field recording by moving the telescope around the disk center while recording 20 frames. The flat-field observations were used to correct the intensity images.

The observed ($I, Q/I$) profiles used in this chapter were obtained after performing a spatial averaging from 60'' to 140'' along the slit.

8.3.1 Determining the absolute zero level of polarization

The absolute zero level of polarization is determined using the blend lines as described in Stenflo (2005, see also Stenflo et al. 1998). According to this method, the relative line depths of the blend lines in Stokes I and Q/I are related with the following one-parameter model as

$$\left(\frac{p_c - p}{p_c}\right) = \left(\frac{I_c - I}{I_c}\right)^\alpha, \quad (8.4)$$

where I_c, p_c are the intensity and polarization of the continuum, and I, p are the respective quantities for the blend lines. α is a free model parameter that determines the shape of the depolarizing lines. We choose $\alpha = 0.6$ for further analysis. Figure 8.5 shows the comparison between the observed profile (solid line) and the profile computed using Equation (8.4, second panel: dotted line). This dotted line represents $p_c[1 - (1 - \frac{I}{I_c})^{0.6}] - p_0$. Here p_0 is a free model parameter that represents the apparent level of the true zero point of the polarization scale. The blend line depth is sensitive to the value of p_c . To get the observed line depths we need $p_c = 0.15\%$ ($p_{c,obs}$). Also to match the solid and the dotted profiles a shift of $p_0 = 0.07\%$ has to be applied. As seen from this figure, we obtain a good match between the solid and the dotted profiles for this set of parameters.

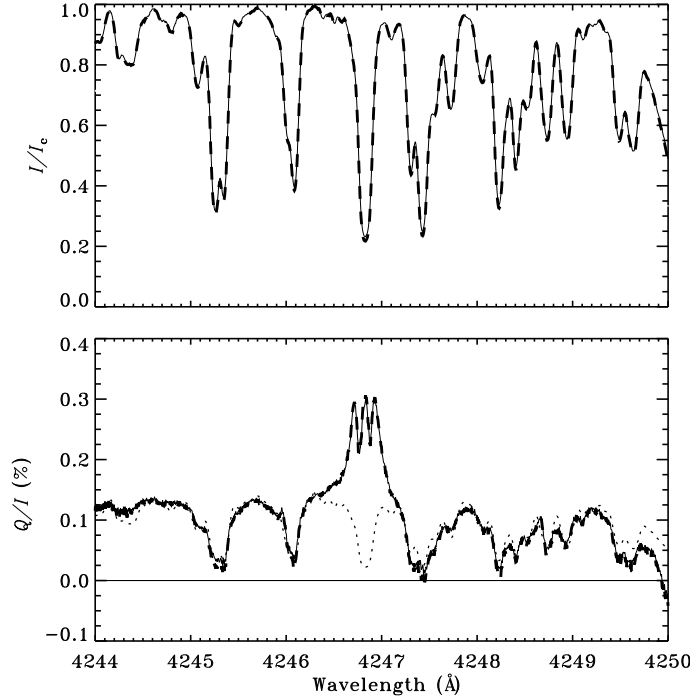


Figure 8.5: Fit to the blend lines around the Sc II 4247 Å line profile using Equation (8.4). The solid lines represent the observations, and dotted line in the second panel represents $p_c[1 - (1 - \frac{I}{I_c})^{0.6}] - p_0$. To obtain a fit we choose $p_c = 0.15\%$ and $p_0 = 0.07\%$. The dashed lines show the observed profiles corrected for 2% stray light. The dashed and solid lines nearly overlap.

8.3.2 Stray light correction

Next, we applied a stray light correction of 2% of the continuum to both I and Q/I . For correcting the Q/I profile we have used the value of p_c determined above. The details of the steps followed are given in [Supriya et al. \(2014\)](#). The comparison between the observed profiles with stray light correction (dashed line) and without (solid line) is shown in Figure 8.5. The stray light corrected observed profiles nearly overlap with the profiles without this correction.

8.4 Comparing the theoretical and the observed Stokes profiles

We compute the theoretical Stokes profiles using a procedure similar to the one described in [Holzreuter et al. \(2005\)](#), see also [Anusha et al. 2011b](#); [Smitha et al. 2012a, 2013b](#), Chapters 5 and 7). The Sc II atom model is constructed with eight J -levels which are coupled by six line transitions and ten continuum transitions.

To represent the solar atmosphere, we use the realistic 1D model atmospheres of [Fontenla et al. \(1993\)](#) and [Avrett \(1995\)](#). While computing the Stokes profiles, we find

that the theoretical continuum polarization ($p_{c,th}$) from the standard model atmospheres like the FALA, FALC, FALF, and FALX is greater than the value determined using the blend lines (as in Section 8.3.1). This discrepancy between $p_{c,th}$ and $p_{c,obs}$ has been studied in detail by Stenflo (2005). In that paper, the author points out that for $\lambda > 4000 \text{ \AA}$, the $p_{c,th} > p_{c,obs}$ (see Figure 6 of Stenflo, 2005). We also note that a similar problem with $p_{c,th}$ and $p_{c,obs}$ was encountered while modeling the Cr I triplet around 5206 \AA in Chapter 5 (Smitha et al., 2012a), and the model atmosphere FALF had to be modified in the deeper layers of the atmosphere, where the continuum is formed, to fit the $p_{c,obs}$. Here too we face a similar problem. Hotter the model atmosphere, smaller is the value of $p_{c,th}$. The FALX (cool) model gives $p_{c,th} = 0.22\%$ and the FALF (hot) model gives $p_{c,th} = 0.19\%$. The FALP model which is hotter than the FALF gives $p_{c,th} = 0.16\%$. The temperature structure of this model in comparison with the other FAL models is shown in Figure 8.6. In the next section, we compute the Stokes ($I, Q/I$) profiles from all these five model atmospheres and compare them with the observed profiles.

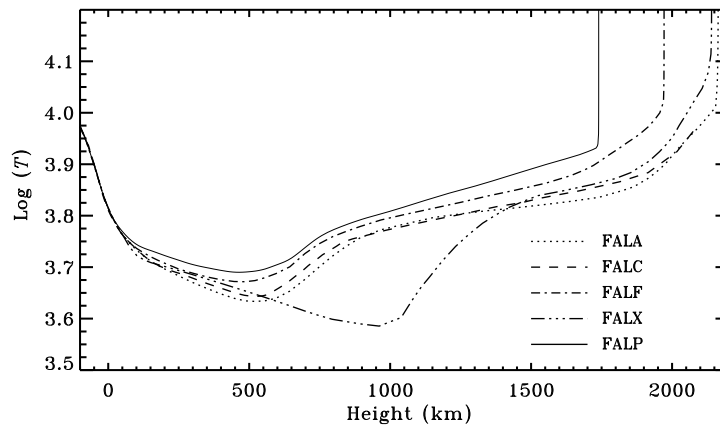


Figure 8.6: Temperature structures of some of the standard FAL model atmospheres.

Table 8.1: HFS constants in MHz

Level	Experiment		Theory	
	A	B	A	B
Lower	128.2(8)	-39(11)	146.8	-25.5
Upper	215.7(8)	18(7)	202.5	-10.8

8.4.1 The ($I, Q/I$) profiles from different model atmospheres

The theoretical ($I, Q/I$) profiles computed using the standard FAL model atmospheres are shown in Figure 8.7. We have used the experimentally determined HFS constants given in Table 8.4 to calculate the energies of the F -states. The profiles in this figure are smeared using a Gaussian with FWHM=80 mÅ. This smearing contains contributions

from both instrument and macroturbulent velocity fields. Instrumental broadening is about 40 mÅ. The rest corresponds to a macroturbulent velocity of 2.9 km/s.

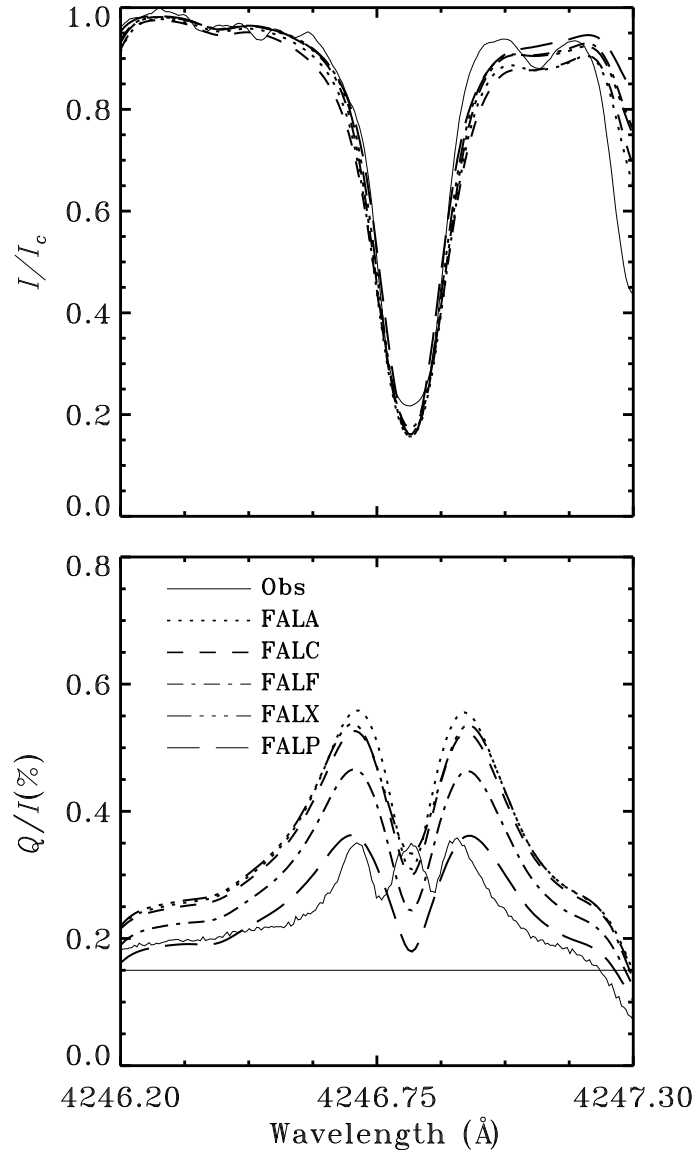


Figure 8.7: Theoretical ($I, Q/I$) profiles from the five standard model atmospheres. The profiles are smeared using a Gaussian with FWHM=80 mÅ.

The observed Q/I profiles show prominent triple peak structure with the central peak mostly governed by the F -state interference effects, and the peaks on either side formed due to PRD. The theoretical profiles in Figure 8.7 do not show the triple peak structure for any of the five model atmospheres. In addition, none of them provide a match to the observed rest intensity. It is clear from this figure that the rest intensity and the line core polarization are not very sensitive to the variations in the model atmospheres. This indicates that it is not possible to improve the fit by modifying any of these standard 1D model atmospheres. Hence the solution to this problem might not be from solar physics but from atomic physics.

In the sections below, we conduct a few tests by varying other parameters. We use the FALP model as it gives the closest match to the PRD wing peaks, and the continuum compared to other models. Note that in all the figures, the horizontal thin solid line in Q/I represents the value of $p_{c,obs}$.

8.4.2 Studying the sensitivity of the $(I, Q/I)$ profiles

Effects of F -state interference

It is well known that the decoherence caused by the hyperfine structure splitting of the J states leads to depolarization in the core of the Q/I line profile. In the case of Sc II 4247 Å line, the splitting between them is quite large and hence the decoherence. This results in an enhanced depolarization at the line core with a fully suppressed central peak. When the nuclear spin $I_s = 0$, we recover the triple peak structure in Q/I as demanded by the principle of spectroscopic stability (Stenflo, 1994). Figure 8.8 shows the comparison between the profiles with and without HFS. Note that in all other remaining figures, we show only the Q/I profiles. The intensity profiles do not show much variation to the tests conducted below.

To better understand the large depolarization, we try to compare the F -state splitting with the radiative widths of the upper levels. We recall that, in our treatment, the lower levels are assumed to be infinitely sharp and hence do not interfere. The interfering upper F -states, the splitting between them and the ratio (Ω) between the splitting and the radiative width are given in Table 8.2, where the Einstein A co-efficient is taken as $1.29 \times 10^8/s$. We know that when Ω is close to unity, the splitting sensitivity is

Table 8.2: Comparison between the F -state splitting and their radiative widths

F_{u1}	F_{u2}	ΔE (Hz)	$s = (\Delta\lambda)_F$ (mÅ)	Ω
3/2	5/2	5.3121×10^8	2.605	25.874
3/2	7/2	1.27941×10^9	6.274	62.296
3/2	9/2	2.24910×10^9	11.029	109.542
3/2	11/2	3.44605×10^9	16.89	167.844
5/2	7/2	7.48200×10^8	3.669	36.442
5/2	9/2	1.71788×10^9	8.424	83.672
5/2	11/2	2.91484×10^9	14.293	141.972
7/2	9/2	9.69685×10^8	4.755	47.230
7/2	11/2	2.16664×10^9	10.624	105.518
9/2	11/2	1.19695×10^9	5.869	58.297

maximum. But in case of the Sc II 4247 Å line system, we see from Table 8.2 that Ω is much greater than one. This partly explains the large depolarization in Q/I at the line center. When the HFS constants are rescaled by a factor of 50 or 100, such that Ω approaches unity, the central peak rises up. This again is a proof of the principle of

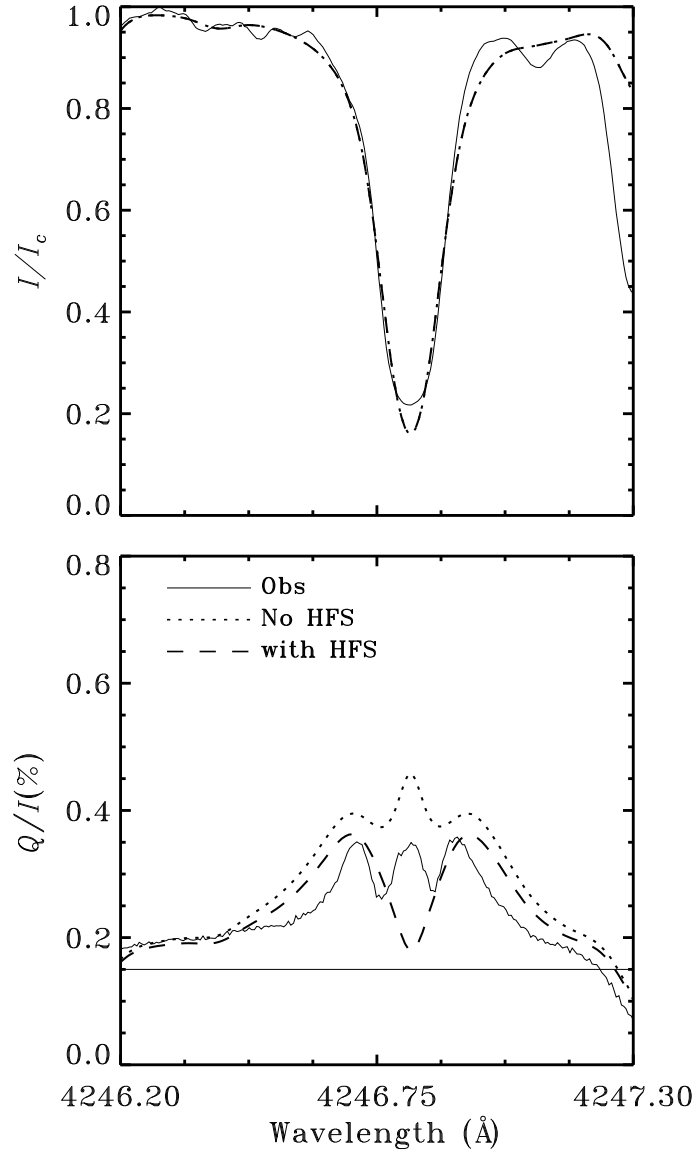


Figure 8.8: The $(I, Q/I)$ profiles computed for the cases with and without hyperfine structure splitting.

spectroscopic stability being satisfied. These profiles are shown in Figure 8.9. Rescaling the HFS constants reduces the splitting between F -states and hence the decoherence.

Also, as seen from Equation (8.1) the $F_b = 11/2 \rightarrow F_a = 11/2$ is the strongest transition and it has maximum coupling with the $F_b = 9/2 \rightarrow F_a = 11/2$ transition. In other words, the shape of the emergent Q/I profile is controlled mainly by these transitions and the interference between their upper levels. When the HFS wavelengths of these two transitions are set equal to each other, we recover the central peak in Q/I as shown in Figure 8.10. Such a modification, once again, reduces the decoherence and hence the depolarization.

One can notice from Figure 8.10 that the width of theoretical Q/I profile and the amplitude of the PRD peaks are larger than in the observed profile. Both of these are

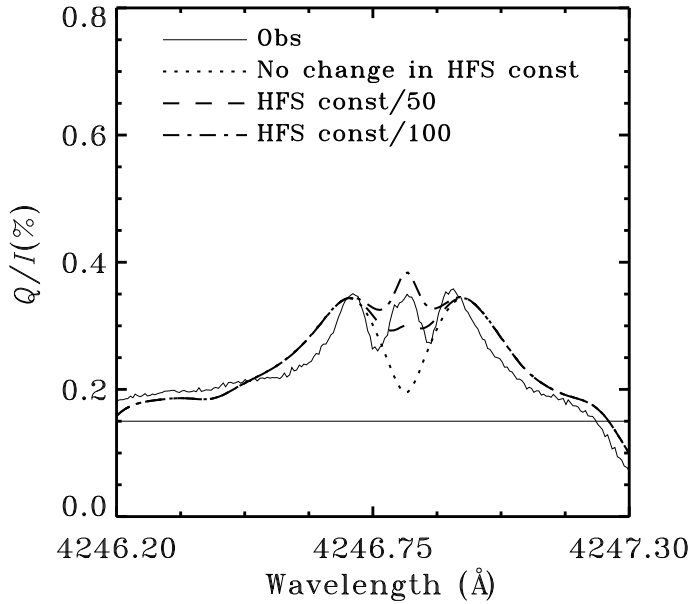


Figure 8.9: The Q/I profiles computed by reducing the HFS constants of the upper level by factors of 50 and 100.

sensitive to the solar abundance of Sc. Zhang et al. (2008) discuss the uncertainty in the abundance value of Sc in the Sun. Their study is based on modeling the observed intensity profiles of different Sc lines. They find that different abundances are needed to fit different lines and conclude that the abundance value is 3.07 ± 0.04 . The long dashed line in Figure 8.10 is the profile computed with an abundance of 2.90. With this reduced abundance, the fit to the PRD peaks and the near wing continuum in the Q/I profile improves.

Collisions

In addition to the HFS, collisions can significantly modify the line core polarization of the observed profiles. The contribution from collisional redistribution depends on the branching ratio B . In case of the Sc II 4247 Å line, this contribution is insignificant. Figure 8.11 shows the individual contributions from type-II frequency redistribution and complete frequency redistribution (CRD), with their corresponding branching ratios being multiplied. We note that in our computations the type-III redistribution has been replaced with CRD like in Chapters 5 and 7 (Smitha et al., 2012a, 2013b) to reduce the computing time. This replacement does not affect the Stokes profiles.

The variation of the branching ratios A and $B^{(K)}$ as a function of height in the atmosphere for the FALP model is shown in Figure 8.3. $B^{(K)}$ takes a value close to zero at higher layers in the atmosphere. Since the Sc II 4247 Å line is formed in the upper chromosphere, the contribution to the line center is primarily from type-II redistribution. The Q/I profile $B^{(K)} \times \text{CRD}$ goes nearly to zero at the line center (dotted line

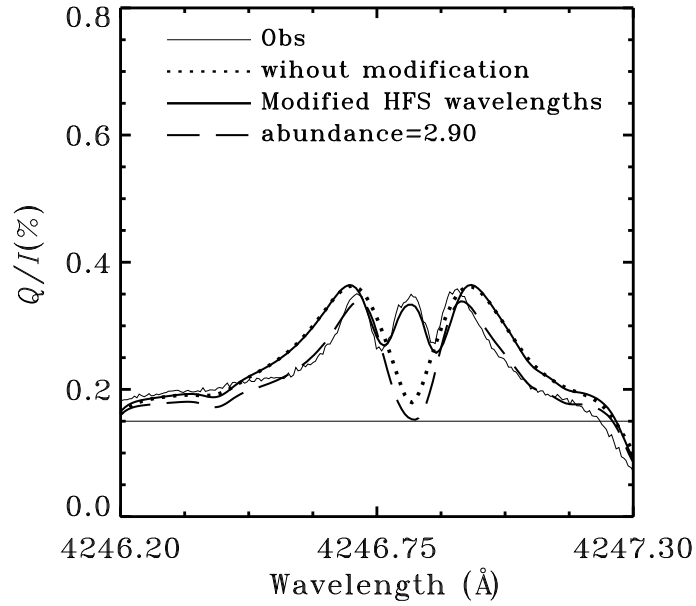


Figure 8.10: The Q/I profiles computed by modifying one of the HFS wavelengths and by modifying the abundance of Sc.

in Figure 8.11). Thus we can exclude the possibility that an approximate treatment of collisions might be contributing to the difficulties in reproducing the Q/I central peak.

Figure 8.11 also shows the Q/I profiles computed with type-II redistribution and CRD alone (without A and $B^{(K)}$ multiplied). The two side peaks on either side of the central peak are formed due to PRD and can be reproduced only by type-II redistribution. CRD alone cannot reproduce them. Thus a proper account of PRD is essential to model this line.

Variation in μ

The observed profiles studied till now were recorded at a limb distance $\mu = 0.1$. When the line profiles were observed at nearby μ positions, they showed a large variation in the polarization of the central peak. These profiles are shown in Figure 8.12. At $\mu = 0.145, 0.175$, the central peak is depolarized and only the two PRD side peaks stand out. The larger CLV of the central peak as compared with the side peaks is to be expected from spatially varying magnetic fields, since the Hanle effect can only operate in the Doppler line core but not in the wings. This behavior is supported by the observed spatial fluctuations along the spectrograph slit: we find the line core amplitude of Q/I to vary much more than the side peaks. In contrast, the theoretical profiles computed for different μ values in the absence of magnetic fields (cf. Figure 8.13) do not show a variation of this kind.

There is therefore strong reasons to believe that the line core is greatly influenced by magnetic fields via the Hanle effect. This influence is normally in the form of depolar-

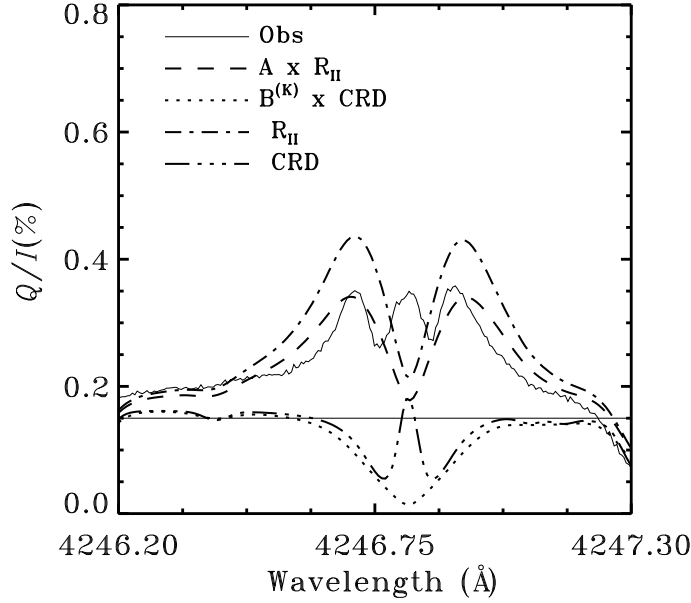


Figure 8.11: The contributions to the Q/I profile from type-II frequency redistribution and CRD. The profiles before and after multiplying the branching ratios are shown.

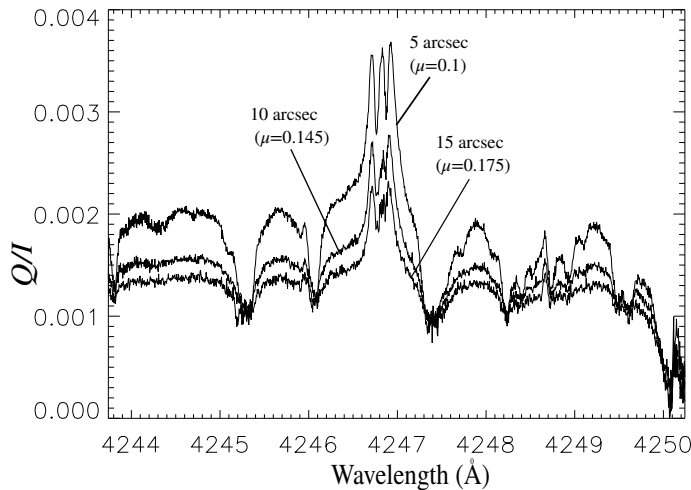


Figure 8.12: The Q/I profiles of Sc II 4247 Å line observed at different limb distances.

ization, reduction of the polarization in the core. However, the Hanle effect may also go in the opposite direction when the atomic polarization in the lower level is considered, as found by Belluzzi (2009) for fields of order 1 G. It therefore remains a possibility that the observed Q/I central peak that we are unable to reproduce with our non-magnetic modeling could be due to the Hanle effect in the lower atomic level.

8.5 Conclusions

In this chapter, we have tried to study the Sc II 4247 Å line, the polarization profiles of which are governed by the F -state interference effects. The observations, used by

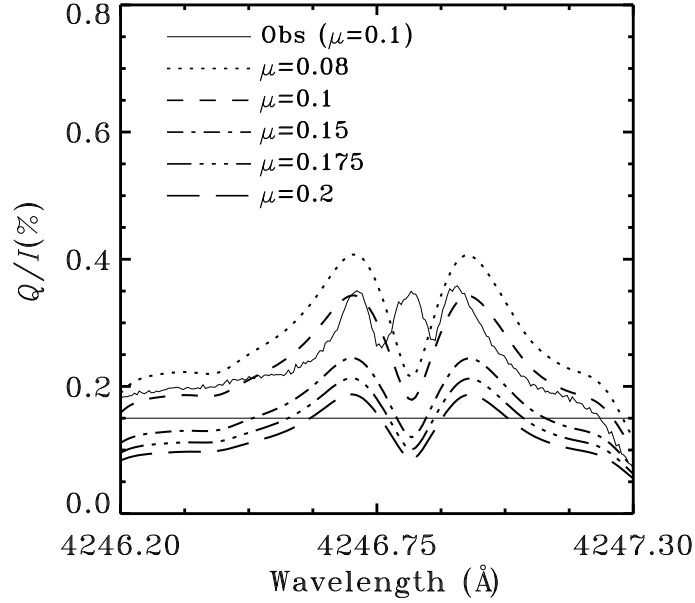


Figure 8.13: The theoretical Q/I profiles computed at various limb distances.

us, were taken at IRSOL using ZIMPOL-III polarimeter in September, 2012 in a quiet region near the solar limb.

Due to its large nuclear spin, the upper and lower J -levels split into five F -states each giving rise to thirteen radiative transitions between them. The decoherence between the F -states is quite large and the emergent polarization profiles are sensitive to the energy difference between the F -states. We have investigated the sensitivity of the theoretical Stokes profiles, in the absence of magnetic fields, to different atmospheric and atomic parameters. All the five standard model atmospheres tried by us, fail to reproduce the triple peak structure in Q/I and also the rest intensity. The PRD peaks and the near wing continuum in the theoretical profiles match closely with the observed ones. To model this line, a proper treatment of PRD is essential and CRD alone cannot reproduce the PRD peaks.

The rest intensity and the Q/I core peak do not show much sensitivity to the variations in model atmosphere. Hence, we believe that multi dimensional radiative transfer might not be the solution to the problem at hand. However the central peak in Q/I is quite sensitive to the Hanle effect. There might be positive contributions from the magnetic field to the central peak polarization through the lower level Hanle effect for field strengths of order 1 G.

Thus, in spite of a detailed account of PRD, radiative transfer and HFS effects we are unable to reproduce the central peak. All these results lead us to believe that there might be other physical effects, unaccounted for in our treatment, playing a role in shaping the Q/I profiles. One such effect is the mentioned lower-state Hanle effect, a possibility that needs to be explored in the future.

Part III

Polarized line formation with J and F -state combined interferences

Chapter 9

Based on:

Smitha, H. N., Nagendra, K. N., & Stenflo, J. O., under review

9

Collisionless partial frequency redistribution in the absence of magnetic fields

An Overview

In the previous chapters, we have derived the theory for the J -state interference, and F -state interference phenomena. There are atomic systems which exhibit both these effects simultaneously and it becomes necessary to account for both J and F -state interferences together. Such is the case with most of the multiplets seen in the Second Solar Spectrum. After having derived the redistribution matrix with partial frequency redistribution (PRD) for the cases of J -state interference and F -state interference, we now combine the two into a single theory which can handle both these effects simultaneously. We derive the PRD matrix for the non-magnetic case in the absence of collisions. This matrix is studied by computing the $(I, Q/I)$ Stokes profiles emerging from a 90° single scattering event. For this, we consider a hypothetical atomic system with two fine structure components separated by 1\AA . As expected, the emergent Stokes profiles show signatures of J -state interference between the two lines, in the form of a cross over in Q/I about the zero level, and F -state interference in the line cores through a depolarization in Q/I . We also study the effects of an unpolarized background continuum on the $(I, Q/I)$ profiles.

9.1 Introduction

An atom with a non-zero electron spin (S) undergoes fine structure splitting due to (L, S) coupling. The atomic level with an orbital angular momentum L splits into fine structure states with electronic angular momentum J . These J -states undergo quantum interference referred to as the J -state interference. The signatures of these interferences get imprinted in the polarization profiles of the radiation scattered off from such an atomic system. In order to study the polarization profiles, the redistribution matrix which relates the Stokes vector of the scattered radiation to that of the incident radiation needs to be derived. The redistribution matrix for polarized scattering at such an atomic system including the effects of PRD and magnetic fields in the linear Zeeman regime was developed in Chapters 2, 4 (Smitha et al., 2011b, 2013a, see also Landi Degl’Innocenti et al. 1997). This was incorporated in the radiative transfer equation and solved for the case of isothermal atmospheres in Chapter 3 (Smitha et al., 2011a). Later this theory was tested by modeling the Cr I triplet profile at 5206 Å observed at a quiet region near the solar limb in Chapter 5 (Smitha et al., 2012a). An extension of this theory to include the non-linear effects like the Paschen-Back effect in the absence of collisions is recently done in Sowmya et al. (2014a).

Further, if the atom has a non-zero nuclear spin I_s then its coupling with the J -states will split them into hyperfine structure states with total angular momentum F . The PRD theory of J -state interference was extended to the case of F -state interference and used in the radiative transfer equation with isothermal model atmospheres in Chapter 6 (Smitha et al., 2012b). Later this theory was used to model the observed Stokes profiles of the Ba II D₂ line in Chapter 7 (Smitha et al., 2013b). However this treatment was restricted to the non-magnetic case. The PRD theory of F -state interference in the presence of magnetic fields is developed in Sowmya et al. (2014b).

Multiplets like the Na I D₁ & D₂, Ba II D₁ & D₂, Li I D₁ & D₂, Cr I triplet at 5206 Å etc., show signatures of both J and F -state interferences. In order to study the polarized line formation in such multiplets, it is important to use a combined theory which can handle both these effects. In this chapter (see also Smitha et al., 2014a), we derive the necessary redistribution matrix for the combined case by taking account of PRD in the absence of collisions. Our treatment is restricted to the non-magnetic case. Though the current theory can easily be extended to include Hanle effect, it will be valid only in the linear Zeeman regime of magnetic fields. However the atomic systems with hyperfine structure splitting enter the non-linear Paschen-Back effect regime for fields of the order of a few tens of gauss. This is because the F -states are separated by only a few mÅ and even for small magnetic fields, the spectral lines arising from these states start to show signatures of Paschen-Back effect. Deriving the theory of Paschen-Back effect for the combined J and F -state interferences case is beyond the scope of this thesis.

However, a combined theory for J and F -state interferences including the effects of magnetic fields but using complete frequency redistribution in the absence of collisions is developed in [Casini & Manso Sainz \(2005\)](#).

In this chapter, starting from the Kramers-Heisenberg formula we derive the redistribution matrix in Section 9.2. This is re-written in terms of the irreducible spherical tensors in Section 9.2.1. The Stokes profiles formed in a 90° single scattering event are discussed in Section 9.3. Section 9.4 is devoted to concluding remarks.

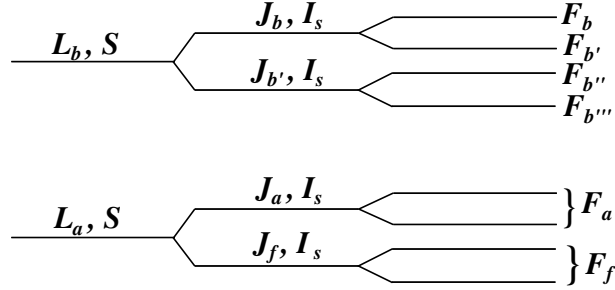


Figure 9.1: Level diagram representing an atomic system with fine structure and hyper-fine structure splitting.

9.2 Redistribution matrix for J and F -state interferences

To derive the redistribution matrix for the combined case of J and F -state interferences, we start from the Kramers-Heisenberg formula which gives complex probability amplitude for scattering from a given initial magnetic substate $\beta_a \mu_a$ to a final substate $\beta_f \mu_f$ via all possible intermediate substates $\beta_b \mu_b$. This can be written as

$$w_{\alpha\beta} \sim \sum_{J_b F_b \mu_b} \frac{\langle \beta_f \mu_f | \mathbf{r} \cdot \mathbf{e}_\alpha | \beta_b \mu_b \rangle \langle \beta_b \mu_b | \mathbf{r} \cdot \mathbf{e}_\beta | \beta_a \mu_a \rangle}{\omega_{bf} - \omega - i\gamma/2}, \quad (9.1)$$

where $\beta_f = J_f I_s F_f$, $\beta_a = J_a I_s F_a$, $\beta_b = J_b I_s F_b$. The subscripts a, b, f denote the initial, excited and final atomic states respectively. I_s is the nuclear spin. The summation over $J_b F_b \mu_b$ accounts for the coherent superposition of all μ_b which are substates of F_b belonging to J_b . The frequency of the scattered radiation in the atomic frame is given by $\omega = 2\pi\xi$ and $\hbar\omega_{bf}$ is the energy difference between the excited (F_b) and final (F_f) states. The damping constant of the upper states is given by γ while the initial and the final states are assumed to be infinitely sharp. $\mu_{a,b,f}$ represent the magnetic substates of the $F_{a,b,f}$ states respectively. These magnetic substates are degenerate since the magnetic field is zero.

The matrix elements appearing in Equation (9.1) can be expanded using the Wigner-

Eckart theorem (see [Stenflo, 1994](#), pp. 145 and 199). This gives us

$$\begin{aligned}
 w_{\alpha\beta}(J_f F_f \mu_f J_a F_a \mu_a) &\sim \sum_{J_b F_b \mu_b} (-1)^{J_a + J_f + q - q'} \sqrt{(2F_a + 1)(2F_f + 1)(2J_a + 1)} \\
 &\times \sqrt{(2J_f + 1)(2J_b + 1)(2F_b + 1)(2L_a + 1)} \begin{Bmatrix} L_a & L_b & 1 \\ J_b & J_f & S \end{Bmatrix} \begin{Bmatrix} L_a & L_b & 1 \\ J_b & J_a & S \end{Bmatrix} \\
 &\times \begin{Bmatrix} J_a & J_b & 1 \\ F_b & F_a & I_s \end{Bmatrix} \begin{Bmatrix} J_f & J_b & 1 \\ F_b & F_f & I_s \end{Bmatrix} \begin{pmatrix} F_b & F_a & 1 \\ -\mu_b & \mu_a & -q' \end{pmatrix} \begin{pmatrix} F_b & F_f & 1 \\ -\mu_b & \mu_f & -q \end{pmatrix} \\
 &\times \Phi_\gamma(\nu_{F_b F_f} - \xi) \varepsilon_q^{\alpha*} \varepsilon_{q'}^\beta. \tag{9.2}
 \end{aligned}$$

$\varepsilon_q^{\alpha*}, \varepsilon_{q'}^\beta$ are the geometrical factors defined in Equation (2) of [Stenflo \(1998\)](#) with q, q' given by Equation (2.3).

In Equation (9.2), $\Phi_\gamma(\nu_{F_b F_f} - \xi)$ is the area-normalized profile function given by

$$\Phi_\gamma(\nu_{F_b F_f} - \xi) = \frac{1/(\pi i)}{\nu_{F_b F_f} - \xi - i\gamma/4\pi}, \tag{9.3}$$

with $h\nu_{F_b F_f}$ being the energy difference between F_b and F_f in the absence of magnetic fields.

To transform the incident Stokes vector to the scattered Stokes vector, we need the Mueller matrix \mathbf{M} defined as (see Equation (7) of [Stenflo, 1998](#))

$$\mathbf{M} = \mathbf{T}\mathbf{W}\mathbf{T}^{-1}. \tag{9.4}$$

\mathbf{T} and \mathbf{T}^{-1} are purely mathematical transformation matrices defined in Equation (9) of [Stenflo \(1998\)](#). \mathbf{W} is the coherency matrix with

$$\mathbf{W} = \sum_{J_a F_a \mu_a} \sum_{J_f F_f \mu_f} \mathbf{w}(J_f F_f \mu_f J_a F_a \mu_a) \otimes \mathbf{w}^*(J_f F_f \mu_f J_a F_a \mu_a). \tag{9.5}$$

$w_{\alpha\beta}(J_f F_f \mu_f J_a F_a \mu_a) w_{\alpha'\beta'}^*(J_f F_f \mu_f J_a F_a \mu_a)$ are the bilinear products which form the elements of the tensor product in the above equation. They are needed for the computation of the redistribution matrix and can be derived in the atomic frame using the steps described in Chapter 2 as

$$\begin{aligned}
 w_{\alpha\beta}(J_f F_f \mu_f J_a F_a \mu_a) w_{\alpha'\beta'}^*(J_f F_f \mu_f J_a F_a \mu_a) &\sim \sum_{J_b F_b \mu_b J_{b'} F_{b'} \mu_{b'}} (-1)^{q-q'} (-1)^{q''-q'''} \\
 &\times \varepsilon_q^{\alpha*} \varepsilon_{q'}^{\alpha'} \varepsilon_{q''}^\beta \varepsilon_{q'''}^{\beta'*} \cos \beta_{F_{b'} F_b} e^{i\beta_{F_{b'} F_b}} \Phi_{F_b F_{b'} F_a}^\gamma(\xi') \delta(\xi - \xi' - \nu_{F_a F_f}) \\
 &\times (2J_a + 1)(2J_f + 1)(2J_b + 1)(2J_{b'} + 1)(2F_a + 1)(2F_f + 1) \\
 &\times (2F_b + 1)(2F_{b'} + 1)(2L_a + 1)^2 \begin{Bmatrix} L_a & L_b & 1 \\ J_b & J_f & S \end{Bmatrix} \begin{Bmatrix} L_a & L_b & 1 \\ J_b & J_a & S \end{Bmatrix} \begin{Bmatrix} L_a & L_b & 1 \\ J_{b'} & J_f & S \end{Bmatrix}
 \end{aligned}$$

$$\begin{aligned}
 & \times \begin{Bmatrix} L_a & L_b & 1 \\ J_{b'} & J_a & S \end{Bmatrix} \begin{Bmatrix} J_a & J_b & 1 \\ F_b & F_a & I_s \end{Bmatrix} \begin{Bmatrix} J_f & J_b & 1 \\ F_b & F_f & I_s \end{Bmatrix} \begin{Bmatrix} J_a & J_{b'} & 1 \\ F_{b'} & F_a & I_s \end{Bmatrix} \begin{Bmatrix} J_f & J_{b'} & 1 \\ F_{b'} & F_f & I_s \end{Bmatrix} \\
 & \times \begin{pmatrix} F_b & F_a & 1 \\ -\mu_b & \mu_a & -q' \end{pmatrix} \begin{pmatrix} F_{b'} & F_a & 1 \\ -\mu_{b'} & \mu_a & -q''' \end{pmatrix} \begin{pmatrix} F_b & F_f & 1 \\ -\mu_b & \mu_f & -q \end{pmatrix} \begin{pmatrix} F_{b'} & F_f & 1 \\ -\mu_{b'} & \mu_f & -q'' \end{pmatrix}, \quad (9.6)
 \end{aligned}$$

$\delta(\xi - \xi' - \nu_{F_a F_f})$ is the energy conservation term (see Equations (9.7) and (9.10) of [Stenflo, 1994](#)) with $h\nu_{F_a F_f}$ being the energy difference between the states F_a and F_f in the absence of a magnetic field. The angle $\beta_{F_{b'}, F_b}$ is defined by

$$\tan \beta_{F_{b'}, F_b} = \frac{E_{F_{b'}, F_b}}{\gamma \hbar}. \quad (9.7)$$

Following [Bommier & Stenflo \(1999\)](#) we define the generalized profile function as

$$\Phi_{F_b F_{b'} F_f}^\gamma(\xi) = \frac{1}{2} [\Phi_\gamma(\nu_{F_b F_f} - \xi) + \Phi_\gamma^*(\nu_{F_{b'} F_f} - \xi)]. \quad (9.8)$$

To transform Equation (9.6) into the laboratory frame, we use the method described in Section 2.2 of [Sampoorna et al. \(2007a\)](#), see also Section 3.3 of [Bommier 1997b](#); [Smitha et al. 2011b](#), Chapter 2). This is done with the following replacement

$$\Phi_{F_b F_{b'} F_a}^\gamma(\xi') \delta(\xi - \xi' - \nu_{F_a F_f}) \left[(h_{F_b, F_{b'}}^{\text{II}})_{F_a F_f} + i(f_{F_b, F_{b'}}^{\text{II}})_{F_a F_f} \right], \quad (9.9)$$

where

$$(h_{F_b, F_{b'}}^{\text{II}})_{F_a F_f} = \frac{1}{2} [R_{F_b F_a F_f}^{\text{II}, \text{H}} + R_{F_{b'} F_a F_f}^{\text{II}, \text{H}}], \quad (9.10)$$

$$(f_{F_b, F_{b'}}^{\text{II}})_{F_a F_f} = \frac{1}{2} [R_{F_{b'} F_a F_f}^{\text{II}, \text{F}} - R_{F_b F_a F_f}^{\text{II}, \text{F}}], \quad (9.11)$$

and the redistribution functions of type II are given by

$$\begin{aligned}
 R_{F_b F_a F_f}^{\text{II}, \text{H}}(x_{ba}, x'_{ba}, \Theta) &= \frac{1}{\pi \sin \Theta} \exp \left\{ - \left[\frac{x_{ba} - x'_{ba} + x_{af}}{2 \sin(\Theta/2)} \right]^2 \right\} \\
 &\times H \left(\frac{a}{\cos(\Theta/2)}, \frac{x_{ba} + x'_{ba} + x_{af}}{2 \cos(\Theta/2)} \right), \quad (9.12)
 \end{aligned}$$

and

$$\begin{aligned}
 R_{F_b F_a F_f}^{\text{II}, \text{F}}(x_{ba}, x'_{ba}, \Theta) &= \frac{1}{\pi \sin \Theta} \exp \left\{ - \left[\frac{x_{ba} - x'_{ba} + x_{af}}{2 \sin(\Theta/2)} \right]^2 \right\} \\
 &\times 2F \left(\frac{a}{\cos(\Theta/2)}, \frac{x_{ba} + x'_{ba} + x_{af}}{2 \cos(\Theta/2)} \right). \quad (9.13)
 \end{aligned}$$

In the above equations $H(a, x)$ and $F(a, x)$ are the Voigt and Faraday-Voigt functions defined in Equation (2.18). The scattering angle between the incident and scattered rays is denoted by Θ (see Figure 2.2). The dimensionless quantities appearing in Equations (9.12) and (9.13) are given by

$$x_{ba} = x_{F_b F_a} = \frac{\nu_{0F_b F_a} - \nu}{\Delta\nu_D}; \quad a = \frac{\gamma}{4\pi\Delta\nu_D}; \quad x_{af} = x_{F_a F_f} = \frac{\nu_{F_a F_f}}{\Delta\nu_D}, \quad (9.14)$$

where x_{ba} , a and $\Delta\nu_D$ are the emission frequency, damping parameter, and Doppler width, respectively.

Substituting Equation (9.6) in Equations (9.4) and (9.5), we obtain the redistribution matrix for the combined case of J and F -state interferences.

9.2.1 Redistribution matrix in terms of irreducible spherical tensors

Writing the redistribution matrix in terms of the irreducible tensors $\mathcal{T}_Q^K(i, \mathbf{n})$ has several advantages as already discussed in Frisch (2007, see also Smitha et al. 2011b, and Chapter 2). For the non-magnetic case, the index i in $\mathcal{T}_Q^K(i, \mathbf{n})$ takes values 0,1 representing the Stokes parameters, while $K = 0, 2$ with $Q = 0$. We follow the steps described in Appendix C of Sampoorna et al. (2007b). Using Equation (3.84) of Stenflo (1994) and Equations (C1) and (C2) of Sampoorna et al. (2007b), we can express the electric field E_μ of the scattered ray in terms of the electric field of the incident ray (E'_ρ) as

$$\begin{aligned} E_\mu &\sim \sum_{\rho J_b F_b \mu_b} (-1)^{J_a + J_f + q - q'} (2J_b + 1)(2F_b + 1)(2L_a + 1) \\ &\times \sqrt{(2J_a + 1)(2J_f + 1)(2F_a + 1)(2F_f + 1)} \begin{Bmatrix} L_a & L_b & 1 \\ J_b & J_f & S \end{Bmatrix} \begin{Bmatrix} L_a & L_b & 1 \\ J_b & J_a & S \end{Bmatrix} \\ &\times \begin{Bmatrix} J_f & J_b & 1 \\ F_b & F_f & I_s \end{Bmatrix} \begin{Bmatrix} J_a & J_b & 1 \\ F_b & F_a & I_s \end{Bmatrix} \begin{pmatrix} F_b & F_a & 1 \\ -\mu_b & \mu_a & -q' \end{pmatrix} \begin{pmatrix} F_b & F_f & 1 \\ -\mu_b & \mu_f & -q \end{pmatrix} \\ &\times \Phi_\gamma(\nu_{F_b F_f} - \xi) [e_\mu(\mathbf{n})]_q^* [e_\rho(\mathbf{n}')]_{q'} E'_\rho, \end{aligned} \quad (9.15)$$

with indices μ and ρ taking values 1 and 2. $[e_\mu(\mathbf{n})]$, $[e_\rho(\mathbf{n}')]$ are the polarization unit vectors defined in Equation (C3) of Sampoorna et al. (2007b). The elements of the coherency matrix may be written as

$$I_{\mu\nu}^S \sim \sum_{J_a F_a \mu_a J_f F_f \mu_f} E_\mu E_\nu^*. \quad (9.16)$$

Substituting for E_μ we obtain

$$I_{\mu\nu}^S \sim \sum_{\rho\sigma} T_{\mu\nu,\rho\sigma}^S(\xi, \mathbf{n}; \xi', \mathbf{n}') I_{\rho\sigma}^{S'} \quad (9.17)$$

where

$$\begin{aligned} T_{\mu\nu,\rho\sigma}^S(\xi, \mathbf{n}; \xi', \mathbf{n}') = & \sum_{J_a F_a \mu_a J_f F_f \mu_f J_b F_b \mu_b J_{b'} F_{b'} \mu_{b'}} (-1)^{q-q'} (-1)^{q''-q'''} \mathcal{E}_{qq''}^S(\mu, \nu, \mathbf{n}) \\ & \times \mathcal{E}_{q''q'''}^S(\sigma, \rho, \mathbf{n}') \cos\beta_{F_{b'}, F_b} e^{i\beta_{F_{b'}, F_b}} \Phi_{F_b F_{b'} F_a}^\gamma(\xi') \delta(\xi - \xi' - \nu_{F_a F_f}) (2J_a + 1) \\ & \times (2J_f + 1)(2J_b + 1)(2J_{b'} + 1)(2L_a + 1)^2 (2F_a + 1)(2F_f + 1)(2F_b + 1) \\ & \times (2F_{b'} + 1) \begin{Bmatrix} L_a & L_b & 1 \\ J_b & J_f & S \end{Bmatrix} \begin{Bmatrix} L_a & L_b & 1 \\ J_b & J_a & S \end{Bmatrix} \begin{Bmatrix} L_a & L_b & 1 \\ J_{b'} & J_f & S \end{Bmatrix} \begin{Bmatrix} L_a & L_b & 1 \\ J_{b'} & J_a & S \end{Bmatrix} \\ & \times \begin{Bmatrix} J_f & J_b & 1 \\ F_b & F_f & I_s \end{Bmatrix} \begin{Bmatrix} J_a & J_b & 1 \\ F_b & F_a & I_s \end{Bmatrix} \begin{Bmatrix} J_f & J_{b'} & 1 \\ F_{b'} & F_f & I_s \end{Bmatrix} \begin{Bmatrix} J_a & J_{b'} & 1 \\ F_{b'} & F_a & I_s \end{Bmatrix} \begin{pmatrix} F_b & F_a & 1 \\ -\mu_b & \mu_a & -q' \end{pmatrix} \\ & \times \begin{pmatrix} F_b & F_f & 1 \\ -\mu_b & \mu_f & -q \end{pmatrix} \begin{pmatrix} F_{b'} & F_a & 1 \\ -\mu_{b'} & \mu_a & -q''' \end{pmatrix} \begin{pmatrix} F_{b'} & F_f & 1 \\ -\mu_{b'} & \mu_f & -q'' \end{pmatrix}. \end{aligned} \quad (9.18)$$

Here $\mathcal{E}_{qq''}^S(\mu, \nu, \mathbf{n})$ is a reducible spherical tensor (see Equation (C6) of [Sampoorna et al., 2007b](#)). The transformation to the Stokes vector formalism from the coherency matrix formalism is described in Appendix C of [Sampoorna et al. \(2007b\)](#). The scattered Stokes vector in the laboratory frame is given by

$$S_i = \sum_{j=0}^1 \mathbf{R}_{ij}^{\text{II}}(x, \mathbf{n}; x', \mathbf{n}') S'_j, \quad (9.19)$$

where the normalized type-II redistribution matrix in the laboratory frame in the absence of magnetic fields is given by

$$\begin{aligned} \mathbf{R}_{ij}^{\text{II}}(x, \mathbf{n}; x', \mathbf{n}') = & \frac{3(2L_b + 1)}{(2S + 1)(2I_s + 1)} \sum_{K J_a F_a J_f F_f J_b F_b J_{b'} F_{b'}} (-1)^{F_f - F_a} \\ & \times \cos\beta_{F_{b'}, F_b} e^{i\beta_{F_{b'}, F_b}} (2J_{b'} + 1)(2F_{b'} + 1)(2J_a + 1)(2J_f + 1)(2J_b + 1) \\ & \times (2F_a + 1)(2F_f + 1)(2F_b + 1) \left[(h_{F_b, F_{b'}}^{\text{II}})_{F_a F_f} + i(f_{F_b, F_{b'}}^{\text{II}})_{F_a F_f} \right] \\ & \times \begin{Bmatrix} L_a & L_b & 1 \\ J_b & J_f & S \end{Bmatrix} \begin{Bmatrix} L_a & L_b & 1 \\ J_b & J_a & S \end{Bmatrix} \begin{Bmatrix} L_a & L_b & 1 \\ J_{b'} & J_f & S \end{Bmatrix} \begin{Bmatrix} L_a & L_b & 1 \\ J_{b'} & J_a & S \end{Bmatrix} \\ & \times \begin{Bmatrix} J_f & J_b & 1 \\ F_b & F_f & I_s \end{Bmatrix} \begin{Bmatrix} J_a & J_b & 1 \\ F_b & F_a & I_s \end{Bmatrix} \begin{Bmatrix} J_f & J_b & 1 \\ F_{b'} & F_f & I_s \end{Bmatrix} \begin{Bmatrix} J_a & J_b & 1 \\ F_{b'} & F_a & I_s \end{Bmatrix} \\ & \times \begin{Bmatrix} 1 & 1 & K \\ F_{b'} & F_b & F_a \end{Bmatrix} \begin{Bmatrix} 1 & 1 & K \\ F_{b'} & F_b & F_f \end{Bmatrix} \mathcal{T}_0^K(i, \mathbf{n}) \mathcal{T}_0^K(j, \mathbf{n}'). \end{aligned} \quad (9.20)$$

9.3 Stokes profiles from a 90° single scattering event

To study the Stokes profiles of the radiation scattered off from an atom with fine and hyperfine structure splitting, we consider a hypothetical 90° single scattering event. The scattered radiation arises due to an $L = 0 \rightarrow 1 \rightarrow 0$ transition with $S = 1/2$ and $I_s = 3/2$. The lower $L = 0$ and upper $L = 1$ states split into fine structure states with quantum numbers $J_a = J_f = 1/2$ and $J_b = 1/2, 3/2$ respectively. Due to coupling with the nuclear spin, the lower J state splits into two F -states with $F = 1, 2$. The upper $J = 1/2$ state splits into two ($F = 1, 2$) states and the upper $J = 3/2$ state splits into four ($F = 0, 1, 2, 3$) states. We assume that the transition $J_b = 3/2 \rightarrow J_f = 1/2$ is centered at 5000 Å (Line-1) and $J_b = 1/2 \rightarrow J_f = 1/2$ transition is centered at 5001 Å (Line-2). The energy differences between the F -states are assumed to be same as those in the Na I D₁, D₂ atomic system. An unpolarized spectrally flat radiation ($[I_{\text{in}} = 1, 0, 0, 0]^T$) is assumed to be incident on the atom in the vertical direction (parallel to the polar z -axis). In all the figures, the damping constant $a = 0.002$ and the Doppler width $\Delta\lambda_D = 33 \text{ mÅ}$.

The single scattered ($I, Q/I$) profiles for the combined case of J and F -state interferences are shown in Figure 9.2. The J -state interference acts in the wings in between the two lines and the F -state interference acts in the cores of the two lines. The atomic polarizability factor (W_2) of Line-1 is 0.5 whereas that of Line-2 is zero. Thus Q/I is zero at Line-2. The dotted and dashed curves respectively show the profiles with J -state and F -state interferences which are the limiting cases. As expected, the J -state interference results in a cross-over in Q/I about the zero level between the two spectral lines (see Chapter 2, Smitha et al., 2011b). The F -state interference results in a depolarization at the core of Line-1 (Chapter 6, Smitha et al., 2012b). The combined profile coincides with the J -state interference profile in the wings of the two lines. In the core of Line-1, the combined profile coincides with the F -state interference profile. In Q/I , the dashed curve affects only the core of Line-1 and at other frequencies it remains constant at a level corresponding to the Rayleigh scattering.

The third panel of Figure 9.2 shows a plot of W_2 as a function of wavelength. The $W_2(\lambda)$ is computed using Equation (6.25) which is

$$W_2(\lambda) = \frac{4(Q/I)}{3 + (Q/I)}. \quad (9.21)$$

The $W_2(\lambda)$ profiles in this panel can be compared with those in the left panel of Figure 3 in Fluri et al. (2003a). They are found to be identical.

In Figure 9.3 we show the Q/I profiles for three different separations between the fine structure states. The separation is 0.1 Å (4999.9 Å - 5000 Å) in the first panel, 1 Å (5000 Å - 5001 Å) in the second panel and 4 Å (4997 Å - 5001 Å) in the third panel re-

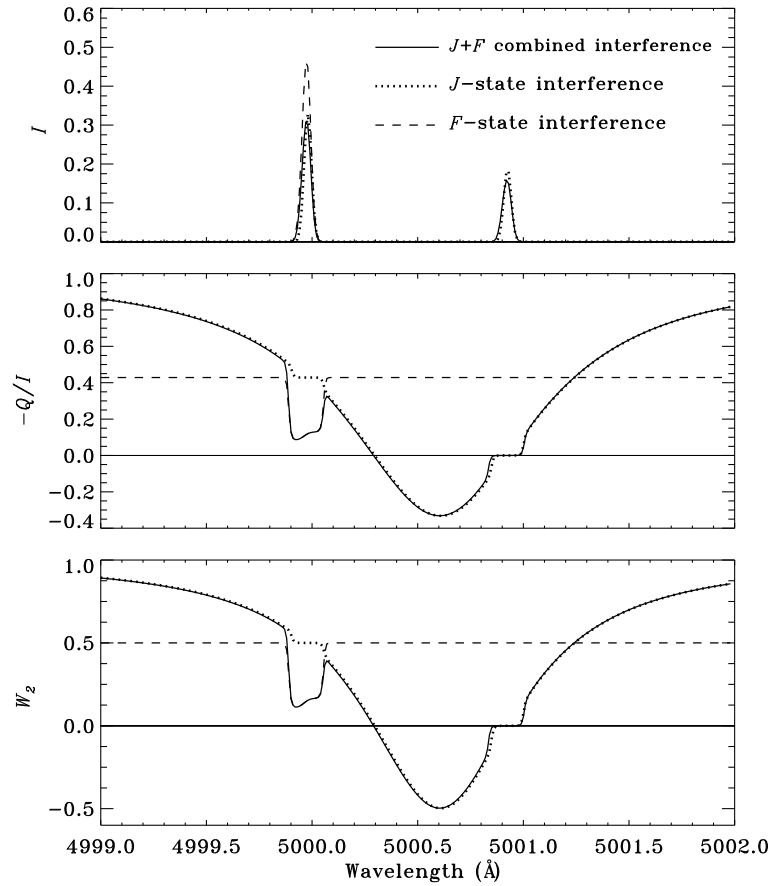


Figure 9.2: The $(I, Q/I)$ and $W_2(\lambda)$ profiles computed for the case of 90° single scattering. The profiles in the two limiting cases, J -state interference and F -state interference are also shown.

spectively. As the two fine structure components get closer, the J -state interference effects increases and the F -state interference effects remain unaffected since they act only in the line core.

Figure 9.4 shows the effects of an unpolarized background continuum on the single scattered $(I, Q/I)$ profiles. The continuum is added following the procedure described in [Stenflo \(1998\)](#), see also Chapter 2 and [Smitha et al. 2011b](#)). In this figure, I'_c represents the intensity of the background continuum radiation and I' is the total intensity. P'_Q is the linear polarization which includes the contribution from unpolarized background continuum. For all the three cases shown in this figure, the limb darkening function $\beta_c = 0.5$, the continuum polarization $b = 0$, the constant c which represents the background continuum is set to 1×10^{-8} (dashed line), 1×10^{-6} (solid line), and 1×10^{-4} (dotted line). These quantities are used in Equations (2.38) and (2.39) to compute I'/I'_c and P'_Q . The Stokes profiles show a behaviour similar to the ones in Figure 2.7. In the presence of a continuum, the intensity takes the shape of an absorption line. In Q/I , the background continuum affects only the line wings and the line core remains unaffected. As c increases, the continuum dominates over J -state interference in the wings. For

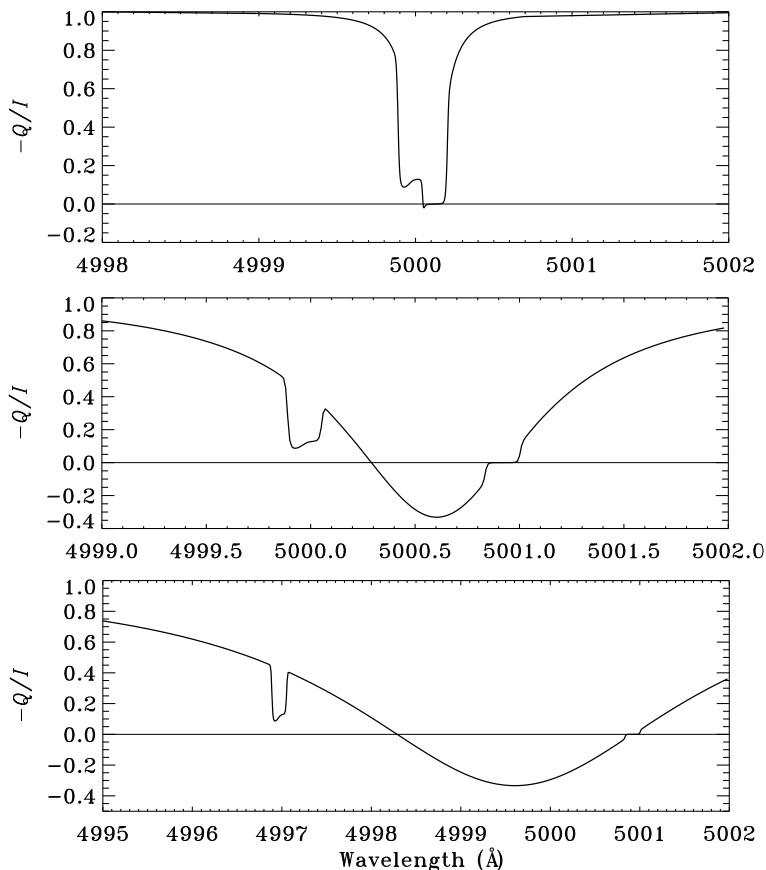


Figure 9.3: The Q/I profiles with J and F -state interferences computed by varying the separation between Line-1 and Line-2. The separations are: 0.1 Å, 1 Å and 4 Å in the first, second, and third panels respectively.

$c > 1 \times 10^{-4}$, the J -state interference signatures nearly vanish.

9.4 Conclusions

In this chapter, we have derived a partial frequency redistribution matrix that includes both J -state and F -state interferences. There are several multiplets in the Second Solar Spectrum which require a combined theory of J and F state interferences for their interpretation. The present work is limited to the collisionless regime in the absence of magnetic fields. We present the redistribution matrix in both atomic and laboratory frames.

We have studied the nature of this redistribution matrix by computing 90° single scattered Stokes profiles. We do this by considering a hypothetical atomic system with two fine structure states separated by 1 Å. The emergent Stokes profiles show signatures of J -state interference in the line wings and F -state interference in the line core. In the hypothetical atomic system considered by us, one of the lines has $W_2 = 0$. This does not show any Q/I at its line core and hence no F -state interference. We present the

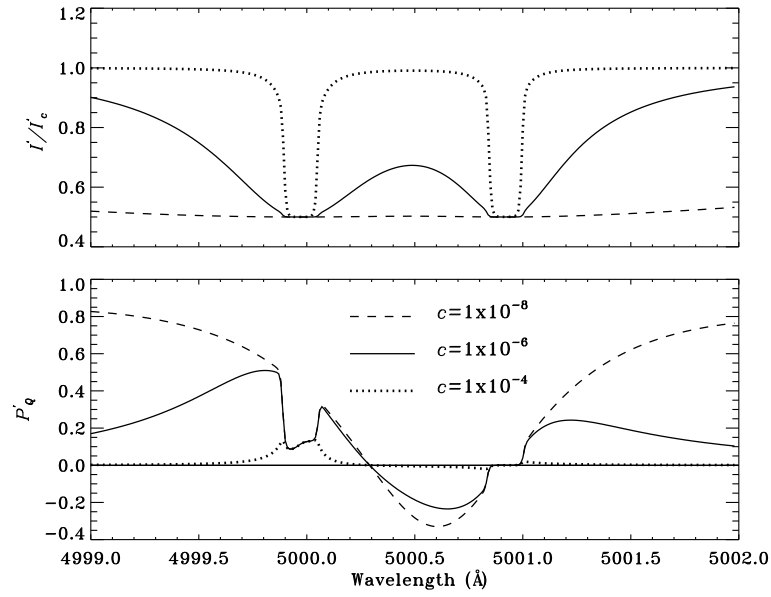


Figure 9.4: The 90° single scattered Stokes profiles with J and F -state interferences in the presence of an unpolarized background continuum. The limb-darkening parameter $\beta_c = 0.5$ is kept constant and strength of the background continuum is varied.

Q/I profiles for three different separations between the fine structure states and show that the J -state interference effects increases with the decrease in separation. Also, we study the effects of an unpolarized background continuum of different strengths on the Stokes I and Q/I profiles. The continuum acts only in the line wings and the line core remains unaffected. We also find that stronger the background continuum, smaller is the J -state interference signatures seen between the two lines.

10

Summary and future work

10.1 Summary

In this thesis we have developed several theoretical tools which can be used in analyzing the linear polarization profiles resulting from coherent scattering processes in the solar atmosphere, which constitute the Second Solar Spectrum. In the absence of a magnetic field, the observed Stokes ($I, Q/I$) profiles in the Sun not only depend on the prevailing atmospheric conditions but also on the structure of the scattering atom. The solar atmosphere consists of different elements from hydrogen to thorium ([Asplund et al., 2009](#)), and several of their isotopes and ionized states. Atoms from each species have their own unique atomic structures. This thesis is devoted to studying the scattering occurring on atoms whose states undergo fine and/or hyperfine structure splitting. These split states exhibit quantum mechanical interferences, and their signatures are imprinted in the linear polarization profiles. In this thesis, we investigate the importance of taking these interferences into account while studying the Second Solar Spectrum.

The thesis is divided into three parts. The first part deals with the atoms which undergo fine structure splitting and exhibit J -state interference. In the second part this is extended to the case of F -state interference occurring between the hyperfine structure states. In the third part we combine both the cases to derive a general theory which can handle both these effects simultaneously.

The primary theoretical tool needed to carry out the analysis is the redistribution matrix. It relates the Stokes vector of the incident radiation to that of the scattered radi-

ation. We derive this matrix using a semi-classical approach starting from the Kramers-Heisenberg formula. The redistribution matrices for the case of J -state interference, F -state interference and the combined case of J and F -states interferences are derived in Chapters 2, 6, and 9 respectively. While the first one includes the effects of magnetic fields, the latter two are derived in the absence of magnetic fields.

The radiation from the Sun gets multiply scattered before leaving the solar atmosphere, and its effects are to be accounted for while analyzing the spectrum. This is done by solving the polarized radiative transfer equation for the specific problem at hand. This forms the second important tool. The redistribution matrices derived in Chapters 2, 6, and 9 enter the radiative transfer equation through the line source vector. The transfer equation is then solved using suitable numerical methods and the emergent Stokes profiles are computed. This is done for the case of J -state interference in Chapters 3, 4 and for the case of F -state interference in Chapter 6. In these chapters, for the sake of simplicity and to understand the effects of multiple scattering, we consider the atmosphere to be an isothermal constant property plane parallel slab.

In case of the Sun, the atmosphere is far from being isothermal. The gradients in its temperature, densities, pressure etc have to be accounted for while modeling the actual observed line profiles. This is taken up in Chapters 5, 7 and 8 where we consider the examples of the Cr I triplet, Ba II D₂ and the Sc II 4247 Å lines respectively. The Cr I triplet around 5206 Å is governed by J -state interference, while the latter two by F -state interference. In these chapters we solve the polarized radiative transfer equation for a realistic 1D model atmosphere. In case of the Cr I triplet and the Ba II D₂, we get a good match with the observed ($I, Q/I$) profiles only after slight modifications in the standard 1D model atmospheres. This shows that the actual solar atmosphere cannot be represented by 1D model atmospheres, and that multi-dimensional radiative transfer effects need to be considered. However in this thesis we confine our attention to 1D model atmospheres. The Sc II line at 4247 Å poses an interesting challenge. Its prominent triple peak structure in Q/I cannot be reproduced from our theory. While the two side peaks on either side of the central peak which are formed due to the PRD effects can be reproduced, the central peak gets completely suppressed due to the effects of F -state interference. We suspect the role of some other physical effect, not accounted for in our treatment to be playing a role in increasing the magnitude of polarization in the core peak. The lower level Hanle effect could be one possibility. However further studies are required to confirm this speculation.

Thus, in this thesis we have developed some important theoretical tools that will help us in modeling certain class of spectral line profiles in the Second Solar Spectrum. Forward modeling using these tools is the key to understand the role of different physical effects contributing to the dynamics of the solar atmosphere. A mismatch between the theoretically computed and the observed profiles indicates either an incomplete quan-

tum mechanical treatment of the atomic system or an inappropriate representation of the solar atmosphere, and sometimes both. Simultaneous forward modeling of different Stokes profiles will not only provide us with better constraints on the selection of the model atmosphere, but also hints us on some of the fundamental aspects missing in our understanding of the physics of line scattering, if any!

10.2 Future prospects

The next logical step would be apply the formalism presented in this thesis for the measurement of solar magnetic fields. Each part of this thesis can be taken up independently, or together, and exploited to understand the solar magnetism. Below we present some of the interesting research problems that can be taken up as a continuation of the results already established in this thesis.

The J -state interference theory including the effects of magnetic fields has already been derived by us in Chapter 2 and 4. The theory holds good in the linear Zeeman regime of magnetic fields where the magnetic substates of different J -states do not interfere. In case of most of the multiplets observed in the Second Solar Spectrum, this is valid upto a few kilogauss. Thus we can apply this theory to measure magnetic fields with strengths ranging from a few G upto a few KG. If we choose a multiplet where the lines arising from different fine structure states are formed at slightly different heights in the solar atmosphere, then a simultaneous modeling of all the lines will help us understand the depth dependence of the magnetic fields, and in turn, the evolution of the magnetic fields over different atmospheric layers.

The polarized radiative transfer equation solved in the presence of a magnetic field in Chapter 4 holds good in the weak field regime of field strengths, where the Stokes V decouples from Stokes (I, Q, U) . But when the fields are strong, this is no more valid and the transfer equation needs to be solved for arbitrary strength magnetic fields. The tools necessary for handling this problem are yet to be developed for the case of J -state interference, and is a challenging problem to work on.

In Chapter 2, we saw that even when the magnetic fields are large (\sim KG), the signatures of J -state interference remain unaffected since it acts only in the wings and the magnetic fields control the line core polarization. It will be interesting to see if this holds true even after the radiative transfer effects are taken into account. These results can then be compared with the Stokes profiles observed close to an active region.

The collisions in case of both the J -state interference and F -state interference are included in our treatment heuristically. For a better understanding of how collisions affect the interferences, it is important to develop a detailed theory of collisional redistribution. It will be interesting to study the importance of different kinds of collisions at various heights in the atmosphere and identifying the spectral lines which need a

detailed account of collisions and those which can be analyzed with an approximate treatment like the one presented in this thesis.

Also, in case of the combined theory, the redistribution matrix derived in Chapter 9 can be included in the polarized radiative transfer equation and solved for a simple case like an isothermal constant property atmospheric slab, and then extended to the case of realistic model atmospheres. In addition, every sophistication to the individual cases of J and F -state interferences can also be extended to the case of combined interference.

Most of the satellites observing the Sun and measuring its magnetic field, do so using the photospheric lines. The magnetic maps developed from these are that of the photosphere. In the chromosphere and corona, the magnetic field structures are not completely understood. With the various tools developed in this thesis one can step towards magnetic mapping of the chromosphere by forward modeling of the chromospheric lines like the Cr I triplet. However before doing so, it is important to pick out the right lines with magnetic field diagnostic potentials. It will be interesting to conduct a survey of the chromospheric and coronal lines suitable for such purposes.

The above listed research problems will help us better understand the scattering in solar atmosphere and also the solar magnetism.

Appendices



Rayleigh scattering phase matrix including fine-structure splitting

A QED-theory for a multi-term atom in the presence of magnetic fields of arbitrary strength is developed by [Landi Degl’Innocenti & Landolfi \(2004\)](#), hereafter LL04, see their Chapter 7). Their theory covers a wide range of field strengths, including the Paschen-Back effect regime, but it is restricted to the case of CRD. In their Section 10.16, they derive the Rayleigh (non-magnetic) phase matrix for a two-term atom without lower-level polarization, but including J -state interference. They refer to such a phase matrix as the “fine-structure scattering phase matrix”. The aim of this appendix is to show that we can recover the fine-structure scattering phase matrix presented in Equation (10.132) of LL04, starting from the semi-classical approach of [Stenflo \(1998\)](#). We start by converting the expressions of [Stenflo \(1998\)](#) into the irreducible spherical tensors for polarimetry, following the procedure given in Appendix C of [Sampoorna et al. \(2007b\)](#). $\mathcal{T}_Q^K(i, \mathbf{n})$ introduced by [Landi Degl’Innocenti \(1984\)](#), where i refers to the Stokes parameters ($i = 0, 1, 2, 3$), and $K = 0, 1, 2$ with $-K \leq Q \leq +K$.

In the non-magnetic case the profile function $\Phi_\gamma(\nu_{J_b\mu_b J_f\mu_f} - \xi)$, though independent of the magnetic sub-states μ_b and μ_f , still depends on the J -states J_b and $J_{b'}$ (see Equations (2.4) and (2.5)). Therefore, in the scattering amplitude $w_{\alpha\beta}(J_f\mu_f J_a\mu_a)$ given in Equation (2.2), we can replace $\Phi_\gamma(\nu_{J_b\mu_b J_f\mu_f} - \xi)$ by the profile function $\Phi_\gamma(\nu_{J_b J_f} - \xi)$ that is independent of the magnetic sub-states.

Using Equation (3.84) of [Stenflo \(1994\)](#) and Equations (C1) and (C2) of [Sampoorna](#)

et al. (2007b), we can express the electric field E_μ of the scattered ray as

$$\begin{aligned}
E_\mu &\sim \sum_{\rho J_b \mu_b} (-1)^{q-q'} \sqrt{(2J_a+1)(2J_f+1)(2J_b+1)(2L_a+1)} \\
&\times \begin{Bmatrix} L_a & L_b & 1 \\ J_b & J_f & S \end{Bmatrix} \begin{Bmatrix} L_a & L_b & 1 \\ J_b & J_a & S \end{Bmatrix} \begin{pmatrix} J_b & J_a & 1 \\ -\mu_b & \mu_a & -q' \end{pmatrix} \\
&\times \begin{pmatrix} J_b & J_f & 1 \\ -\mu_b & \mu_f & -q \end{pmatrix} \Phi_\gamma(\nu_{J_b J_f} - \xi) [e_\mu(\mathbf{n})]_q^* [e_\rho(\mathbf{n}')]_{q'} E'_\rho, \quad (\text{A.1})
\end{aligned}$$

where E'_ρ is the electric field of the incident radiation, and indices μ and ρ take the values 1 and 2. The above equation is written in the basis defined in Equation (C3) of Sampoorna et al. (2007b). The elements of the coherency matrix may be written as

$$I_{\mu\nu}^S \sim \sum_{J_a \mu_a J_f \mu_f} E_\mu E_\nu^*. \quad (\text{A.2})$$

Inserting Equation (A.1) we obtain

$$I_{\mu\nu}^S \sim \sum_{\rho\sigma} T_{\mu\nu,\rho\sigma}^S(\mathbf{n}, \mathbf{n}', \xi) I_{\rho\sigma}^S, \quad (\text{A.3})$$

where

$$\begin{aligned}
T_{\mu\nu,\rho\sigma}^S &= \sum_{J_a \mu_a J_f \mu_f J_b \mu_b J_{b'} \mu_{b'}} (-1)^{q-q'} (-1)^{q''-q'''} [e_\mu(\mathbf{n})]_q^* [e_\nu(\mathbf{n}')]_{q'} \\
&\times [e_\rho(\mathbf{n}')]_{q'} [e_\sigma(\mathbf{n}')]_{q'''}^* (2J_a+1)(2J_f+1)(2J_b+1)(2J_{b'}+1) \\
&\times (2L_a+1)^2 \Phi_\gamma(\nu_{J_b J_f} - \xi) \Phi_\gamma^*(\nu_{J_{b'} J_f} - \xi) \begin{Bmatrix} L_a & L_b & 1 \\ J_b & J_f & S \end{Bmatrix} \\
&\times \begin{Bmatrix} L_a & L_b & 1 \\ J_b & J_a & S \end{Bmatrix} \begin{Bmatrix} L_a & L_b & 1 \\ J_{b'} & J_f & S \end{Bmatrix} \begin{Bmatrix} L_a & L_b & 1 \\ J_{b'} & J_a & S \end{Bmatrix} \begin{pmatrix} J_b & J_a & 1 \\ -\mu_b & \mu_a & -q' \end{pmatrix} \\
&\times \begin{pmatrix} J_b & J_f & 1 \\ -\mu_b & \mu_f & -q \end{pmatrix} \begin{pmatrix} J_{b'} & J_a & 1 \\ -\mu_{b'} & \mu_a & -q''' \end{pmatrix} \begin{pmatrix} J_{b'} & J_f & 1 \\ -\mu_{b'} & \mu_f & -q'' \end{pmatrix}. \quad (\text{A.4})
\end{aligned}$$

Using Equation (C6) of Sampoorna et al. (2007b), the above equation can for the case of frequency coherent scattering be rewritten as

$$\begin{aligned}
T_{\mu\nu,\rho\sigma}^S(\mathbf{n}, \mathbf{n}', \xi) &= \sum_{J_a \mu_a J_f \mu_f J_b \mu_b J_{b'} \mu_{b'}} (-1)^{q-q'} (-1)^{q''-q'''} \mathcal{E}_{qq''}^S(\mu, \nu, \mathbf{n}) \mathcal{E}_{q'''q'}^S(\sigma, \rho, \mathbf{n}') \\
&\times (2J_a+1)(2J_f+1)(2J_b+1)(2J_{b'}+1)(2L_a+1)^2 \cos\beta_{J_{b'} J_b} e^{i\beta_{J_{b'} J_b}} \Phi_{J_b J_{b'} J_f}^\gamma \\
&\times \begin{Bmatrix} L_a & L_b & 1 \\ J_b & J_f & S \end{Bmatrix} \begin{Bmatrix} L_a & L_b & 1 \\ J_b & J_a & S \end{Bmatrix} \begin{Bmatrix} L_a & L_b & 1 \\ J_{b'} & J_f & S \end{Bmatrix} \begin{Bmatrix} L_a & L_b & 1 \\ J_{b'} & J_a & S \end{Bmatrix} \begin{pmatrix} J_b & J_a & 1 \\ -\mu_b & \mu_a & -q' \end{pmatrix}
\end{aligned}$$

$$\times \begin{pmatrix} J_b & J_f & 1 \\ -\mu_b & \mu_f & -q \end{pmatrix} \begin{pmatrix} J_{b'} & J_a & 1 \\ -\mu_{b'} & \mu_a & -q''' \end{pmatrix} \begin{pmatrix} J_{b'} & J_f & 1 \\ -\mu_{b'} & \mu_f & -q'' \end{pmatrix}. \quad (\text{A.5})$$

Here $\beta_{J_{b'}J_b}$ and $\Phi_{J_bJ_{b'}J_f}^\gamma$ are given respectively by Equations (2.10) and (2.11) but with $\omega_L = 0$, and $\mathcal{E}_{qq''}^S(\mu, \nu, \mathbf{n})$ is a reducible spherical tensor (see Equation (C6) of Samporna et al., 2007b). The transformation to the Stokes vector formalism from the coherency matrix formalism is described in Appendix C of Samporna et al. (2007b). The scattered Stokes vector is given by

$$S_i = \sum_{j=0}^3 \mathbf{P}_{ij}(\mathbf{n}, \mathbf{n}', \xi) S'_j, \quad (\text{A.6})$$

where

$$\mathbf{P}_{ij}(\mathbf{n}, \mathbf{n}', \xi) = \frac{1}{2} \sum_{\mu\nu\rho\sigma} (\boldsymbol{\sigma}_i)_{\nu\mu} (\boldsymbol{\sigma}_j)_{\rho\sigma} T_{\mu\nu,\rho\sigma}^S(\mathbf{n}, \mathbf{n}', \xi). \quad (\text{A.7})$$

Inserting Equation (A.5) and then using Equations (C15) and (C18) of Samporna et al. (2007b), we obtain

$$\begin{aligned} \mathbf{P}_{ij}(\mathbf{n}, \mathbf{n}', \xi) &= \frac{2}{3} \sum_{KK'QJ_a\mu_aJ_f\mu_fJ_b\mu_bJ_{b'}\mu_{b'}} (-1)^{q''+q'+Q} \sqrt{(2K+1)(2K'+1)} \\ &\times (2J_a+1)(2J_f+1)(2J_b+1)(2J_{b'}+1)(2L_a+1)^2 \cos\beta_{J_{b'}J_b} e^{i\beta_{J_{b'}J_b}} \Phi_{J_bJ_{b'}J_f}^\gamma \\ &\times \begin{Bmatrix} L_a & L_b & 1 \\ J_b & J_f & S \end{Bmatrix} \begin{Bmatrix} L_a & L_b & 1 \\ J_b & J_a & S \end{Bmatrix} \begin{Bmatrix} L_a & L_b & 1 \\ J_{b'} & J_f & S \end{Bmatrix} \begin{Bmatrix} L_a & L_b & 1 \\ J_{b'} & J_a & S \end{Bmatrix} \\ &\times \begin{pmatrix} J_b & J_a & 1 \\ -\mu_b & \mu_a & -q' \end{pmatrix} \begin{pmatrix} J_b & J_f & 1 \\ -\mu_b & \mu_f & -q \end{pmatrix} \begin{pmatrix} J_{b'} & J_a & 1 \\ -\mu_{b'} & \mu_a & -q''' \end{pmatrix} \begin{pmatrix} J_{b'} & J_f & 1 \\ -\mu_{b'} & \mu_f & -q'' \end{pmatrix} \\ &\times \begin{pmatrix} 1 & 1 & K \\ q & -q'' & -Q \end{pmatrix} \begin{pmatrix} 1 & 1 & K' \\ q''' & -q' & Q \end{pmatrix} (-1)^Q \mathcal{T}_{-Q}^K(i, \mathbf{n}) \mathcal{T}_Q^{K'}(j, \mathbf{n}'). \end{aligned} \quad (\text{A.8})$$

The six 3- j symbols appearing in the above equation can be contracted into two 6- j symbols by first applying Equation (2.42) and then Equation (2.34) of LL04. After some algebra we obtain

$$\begin{aligned} \mathbf{P}_{ij}(\mathbf{n}, \mathbf{n}', \xi) &= \frac{2}{3} \sum_{KQJ_bJ_{b'}J_aJ_f} (-1)^{J_f-J_a} (-1)^Q \cos\beta_{J_{b'}J_b} e^{i\beta_{J_{b'}J_b}} \Phi_{J_bJ_{b'}J_f}^\gamma \\ &\times (2J_a+1)(2J_f+1)(2J_b+1)(2J_{b'}+1)(2L_a+1)^2 \\ &\times \begin{Bmatrix} L_a & L_b & 1 \\ J_b & J_f & S \end{Bmatrix} \begin{Bmatrix} L_a & L_b & 1 \\ J_b & J_a & S \end{Bmatrix} \begin{Bmatrix} L_a & L_b & 1 \\ J_{b'} & J_f & S \end{Bmatrix} \begin{Bmatrix} L_a & L_b & 1 \\ J_{b'} & J_a & S \end{Bmatrix} \\ &\times \begin{Bmatrix} 1 & 1 & K \\ J_{b'} & J_b & J_a \end{Bmatrix} \begin{Bmatrix} 1 & 1 & K \\ J_{b'} & J_b & J_f \end{Bmatrix} \mathcal{T}_Q^K(i, \mathbf{n}) \mathcal{T}_{-Q}^K(j, \mathbf{n}'). \end{aligned} \quad (\text{A.9})$$

As our aim is to recover Equation (10.132) of LL04, there is a need to relate our profile function defined in Equation (2.4) to the one introduced by LL04 in their Equation (6.59). For notational brevity we denote their profile function as $\Phi^L(\nu_{J_b J_f} - \xi)$. Comparing our Equation (2.4) with Equation (6.59) of LL04, it is easy to verify that $\Phi_\gamma(\nu_{J_b J_f} - \xi) = \Phi^{L*}(\nu_{J_b J_f} - \xi)$. Interchanging J_b and $J_{b'}$ (necessary to obtain the LL04 equation), and using the fact that $\beta_{J_b J_{b'}} = -\beta_{J_{b'} J_b}$, we can rewrite Equation (A.8) as

$$\begin{aligned} \mathbf{P}_{ij}(\mathbf{n}, \mathbf{n}', \xi) &= \frac{2}{3} \sum_{KQJ_b J_{b'} J_a J_f} (-1)^{J_f - J_a} \cos \beta_{J_{b'} J_b} e^{-i\beta_{J_{b'} J_b}} \frac{1}{2} \left[\Phi^L(\nu_{J_b J_f} - \xi) \right. \\ &\quad \left. + \Phi^{L*}(\nu_{J_{b'} J_f} - \xi) \right] (2J_a + 1)(2J_f + 1)(2J_b + 1)(2J_{b'} + 1)(2L_a + 1)^2 \\ &\quad \times \begin{Bmatrix} L_a & L_b & 1 \\ J_b & J_f & S \end{Bmatrix} \begin{Bmatrix} L_a & L_b & 1 \\ J_b & J_a & S \end{Bmatrix} \begin{Bmatrix} L_a & L_b & 1 \\ J_{b'} & J_f & S \end{Bmatrix} \begin{Bmatrix} L_a & L_b & 1 \\ J_{b'} & J_a & S \end{Bmatrix} \\ &\quad \times \begin{Bmatrix} 1 & 1 & K \\ J_{b'} & J_b & J_a \end{Bmatrix} \begin{Bmatrix} 1 & 1 & K \\ J_{b'} & J_b & J_f \end{Bmatrix} (-1)^Q \mathcal{T}_Q^K(i, \mathbf{n}) \mathcal{T}_{-Q}^K(j, \mathbf{n}'). \end{aligned} \quad (\text{A.10})$$

In order to obtain the scattering phase matrix, which is independent of frequency, we follow LL04 and integrate Equation (A.10) over frequency ξ . As the profile function is normalized to unity, the frequency ξ dependent terms in Equation (A.10) become unity after frequency integration. It then becomes possible to perform the summation over J_a and J_f using Equation (2.41) of LL04. Thus we get

$$\begin{aligned} \mathbf{P}_{ij}(\mathbf{n}, \mathbf{n}') &= \frac{2}{3} \sum_{KQJ_b J_{b'}} (2J_b + 1)(2J_{b'} + 1)(2L_a + 1)^2 \cos \beta_{J_{b'} J_b} e^{-i\beta_{J_{b'} J_b}} \\ &\quad \times \begin{Bmatrix} 1 & 1 & K \\ L_b & L_b & L_a \end{Bmatrix}^2 \begin{Bmatrix} L_b & L_b & K \\ J_b & J_{b'} & S \end{Bmatrix}^2 (-1)^Q \mathcal{T}_Q^K(i, \mathbf{n}) \mathcal{T}_{-Q}^K(j, \mathbf{n}'). \end{aligned} \quad (\text{A.11})$$

We can write

$$\cos \beta_{J_{b'} J_b} e^{-i\beta_{J_{b'} J_b}} = \frac{1}{1 + 2\pi i \nu_{J_{b'} J_b} / A_{L_b L_a}}, \quad (\text{A.12})$$

where $A_{L_b L_a}$ is the Einstein coefficient for the transition $L_b \rightarrow L_a$ and is equal to γ . Hence Equation (A.11) can be rewritten as

$$\mathbf{P}_{ij}(\mathbf{n}, \mathbf{n}') = \sum_{KQ} W_K(L_a L_b) (-1)^Q \mathcal{T}_Q^K(i, \mathbf{n}) \mathcal{T}_{-Q}^K(j, \mathbf{n}'), \quad (\text{A.13})$$

with

$$W_K(L_a L_b) = \frac{3(2L_b + 1)}{2S + 1} \sum_{J_b J_{b'}} (2J_b + 1)(2J_{b'} + 1)$$

$$\times \begin{Bmatrix} 1 & 1 & K \\ L_b & L_b & L_a \end{Bmatrix}^2 \begin{Bmatrix} L_b & L_b & K \\ J_b & J_{b'} & S \end{Bmatrix}^2 \frac{1}{1 + 2\pi i \nu_{J_{b'} J_b} / A_{L_b L_a}}. \quad (\text{A.14})$$

We have absorbed the factor $2(2S + 1)(2L_a + 1)^2/[9(2L_b + 1)]$ into the normalization constant. It is easy to verify that Equations (A.13) and (A.14) are identical to Equations (10.132) and (10.133) of LL04.

B

Expression for the type II redistribution matrix

After elaborate algebra, Equation (2.33) can be rewritten as

$$\begin{aligned} \mathbf{R}^{\text{II}}(x, \mathbf{n}; x', \mathbf{n}', \mathbf{B}) = & \mathbf{R}^{\text{II}}_{\lambda_1 \lambda_1}(x, \mathbf{n}; x', \mathbf{n}', \mathbf{B}) + \mathbf{R}^{\text{II}}_{\lambda_2 \lambda_2}(x, \mathbf{n}; x', \mathbf{n}', \mathbf{B}) \\ & + \mathbf{R}^{\text{II}}_{\lambda_1 \lambda_2}(x, \mathbf{n}; x', \mathbf{n}', \mathbf{B}), \end{aligned} \quad (\text{B.1})$$

where $\mathbf{R}^{\text{II}}_{\lambda_1 \lambda_1}$, $\mathbf{R}^{\text{II}}_{\lambda_2 \lambda_2}$ are the redistribution matrices for the $J = 1/2 \rightarrow 1/2 \rightarrow 1/2$ and $J = 1/2 \rightarrow 3/2 \rightarrow 1/2$ transition, respectively, and $\mathbf{R}^{\text{II}}_{\lambda_1 \lambda_2}$ represents the interference term. The redistribution matrix for $J = 1/2 \rightarrow 1/2 \rightarrow 1/2$ transition is given by

$$\begin{aligned} \mathbf{R}^{\text{II}}_{\lambda_1 \lambda_1} = & \frac{f_{\frac{1}{2}\frac{1}{2}}^2}{2f_{\frac{1}{2}\frac{1}{2}}^2 + f_{\frac{1}{2}\frac{3}{2}}^2} \frac{1}{4} \left\{ [(c_{1,-1,1,-1}^{\text{II}})_{1,1} \pm (c_{1,1,1,1}^{\text{II}})_{-1,-1}] \mathbf{C}_{\pm}^0 \right. \\ & + [(c_{1,1,1,1}^{\text{II}})_{1,1} + (c_{1,-1,1,-1}^{\text{II}})_{-1,-1}] \mathbf{C}_0^0 + [(c_{1,-1,1,-1}^{\text{II}})_{-1,1} \pm (c_{1,1,1,1}^{\text{II}})_{1,-1}] \mathbf{D}_{01}^{\pm} \\ & + [(c_{1,-1,1,-1}^{\text{II}})_{1,-1} \pm (c_{1,1,1,1}^{\text{II}})_{-1,1}] \mathbf{D}_{10}^{\pm} + 2 \sin \theta \sin \theta' \left\{ [(c_{1,-1,1,1}^{\text{II}})_{1,1} \right. \\ & \mp (c_{1,-1,1,1}^{\text{II}})_{1,-1}] (\mathbf{F}_1^{(1)} + \mathbf{F}_{\pm 3}^{(1)}) + [(c_{1,-1,1,1}^{\text{II}})_{-1,-1} \mp (c_{1,-1,1,1}^{\text{II}})_{-1,1}] (\mathbf{F}_1^{(1)} - \mathbf{F}_{\pm 3}^{(1)}) \\ & + [(c_{1,-1,1,1}^{\text{II}})_{1,1} + (c_{1,-1,1,1}^{\text{II}})_{1,-1} + (c_{1,-1,1,1}^{\text{II}})_{-1,1} + (c_{1,-1,1,1}^{\text{II}})_{-1,-1}] \mathbf{F}_2^{(1)} \\ & + [\pm (s_{1,-1,1,1}^{\text{II}})_{1,1} - (s_{1,-1,1,1}^{\text{II}})_{-1,1}] \mathbf{S}_{\pm}^1 + [(s_{1,-1,1,1}^{\text{II}})_{-1,-1} \mp (s_{1,-1,1,1}^{\text{II}})_{1,-1}] \mathbf{S}_{\pm}^1 \\ & \left. + [(s_{1,-1,1,1}^{\text{II}})_{1,1} - (s_{1,-1,1,1}^{\text{II}})_{-1,-1} + (s_{1,-1,1,1}^{\text{II}})_{1,-1} - (s_{1,-1,1,1}^{\text{II}})_{-1,1}] \mathbf{S}_3^{(1)} \right\} \left. \right\}, \end{aligned} \quad (\text{B.2})$$

while the redistribution matrix for $J = 1/2 \rightarrow 3/2 \rightarrow 1/2$ transition is given by

$$\begin{aligned}
\mathbf{R}^{\text{II}}_{\lambda_2\lambda_2} = & \frac{f_{\frac{1}{2}\frac{3}{2}}^2}{2f_{\frac{1}{2}\frac{1}{2}}^2 + f_{\frac{1}{2}\frac{3}{2}}^2} \left\{ \left[\left((c_{3,-1,3,-1}^{\text{II}})_{1,1} + (c_{3,1,3,1}^{\text{II}})_{-1,-1} \right) + 9 \left((c_{3,3,3,3}^{\text{II}})_{1,1} \right. \right. \right. \\
& \left. \left. \left. + (c_{3,-3,3,-3}^{\text{II}})_{-1,-1} \right) \right] \frac{\mathbf{C}_+^0}{64} + \left[(c_{3,1,3,1}^{\text{II}})_{1,1} + (c_{3,-1,3,-1}^{\text{II}})_{-1,-1} \right] \frac{\mathbf{C}_0^0}{4} + \left[(c_{3,-1,3,-1}^{\text{II}})_{1,-1} \right. \right. \\
& \left. \left. \pm (c_{3,1,3,1}^{\text{II}})_{-1,1} \right] \frac{\mathbf{D}_{10}^\pm}{16} + \left[(c_{3,-1,3,-1}^{\text{II}})_{-1,1} \pm (c_{3,1,3,1}^{\text{II}})_{1,-1} \right] \frac{\mathbf{D}_{01}^\pm}{16} + \left[\left((c_{3,-1,3,-1}^{\text{II}})_{1,1} \right. \right. \right. \\
& \left. \left. \left. - (c_{3,1,3,1}^{\text{II}})_{-1,-1} \right) + 9 \left((c_{3,-3,3,-3}^{\text{II}})_{-1,-1} - (c_{3,3,3,3}^{\text{II}})_{1,1} \right) \right] \frac{\mathbf{C}_-^0}{64} + \left[(c_{3,-1,3,3}^{\text{II}})_{1,1} \right. \right. \\
& \left. \left. + (c_{3,-3,3,1}^{\text{II}})_{-1,-1} \right] \frac{3\mathbf{C}_+^2}{32} + \left[(s_{3,-1,3,3}^{\text{II}})_{1,1} + (s_{3,-3,3,1}^{\text{II}})_{-1,-1} \right] \frac{3\mathbf{S}_+^2}{16} \right. \\
& \left. + \sin\theta \sin\theta' \left\{ \left[\pm (c_{3,1,3,3}^{\text{II}})_{1,1} + (c_{3,-3,3,-1}^{\text{II}})_{-1,-1} \right] \frac{3\mathbf{C}_\pm^1}{8} + \left[(c_{3,-1,3,1}^{\text{II}})_{1,1} \right. \right. \right. \\
& \left. \left. \left. - (c_{3,-1,3,1}^{\text{II}})_{1,-1} \right] \left(\frac{\mathbf{F}_1^{(1)} + \mathbf{F}_{+3}^{(1)}}{8} \right) + \left[(c_{3,-1,3,1}^{\text{II}})_{-1,-1} - (c_{3,-1,3,1}^{\text{II}})_{-1,1} \right] \left(\frac{\mathbf{F}_1^{(1)} - \mathbf{F}_{+3}^{(1)}}{8} \right) \right. \right. \\
& \left. \left. + \left[(c_{3,-1,3,1}^{\text{II}})_{1,1} + (c_{3,-1,3,1}^{\text{II}})_{1,-1} \right] \left(\frac{\mathbf{F}_2^{(1)} + \mathbf{F}_{-3}^{(1)}}{8} \right) + \left[(c_{3,-1,3,1}^{\text{II}})_{-1,1} + (c_{3,-1,3,1}^{\text{II}})_{-1,-1} \right] \right. \right. \\
& \left. \left. \times \left(\frac{\mathbf{F}_2^{(1)} - \mathbf{F}_{-3}^{(1)}}{8} \right) + \left[(s_{3,1,3,3}^{\text{II}})_{1,1} + (s_{3,-3,3,-1}^{\text{II}})_{-1,-1} \right] \frac{3\mathbf{S}_+^1}{8} + \left[(s_{3,-1,3,1}^{\text{II}})_{-1,1} \right. \right. \right. \\
& \left. \left. \left. - (s_{3,-1,3,1}^{\text{II}})_{1,1} \right] \left(\frac{\mathbf{S}_1^{(1)} - \mathbf{S}_3^{(1)}}{8} \right) + \left[(s_{3,-1,3,1}^{\text{II}})_{1,-1} - (s_{3,-1,3,1}^{\text{II}})_{-1,-1} \right] \left(\frac{\mathbf{S}_1^{(1)} + \mathbf{S}_3^{(1)}}{8} \right) \right. \right. \\
& \left. \left. + \left[(s_{3,-1,3,1}^{\text{II}})_{-1,-1} + (s_{3,-1,3,1}^{\text{II}})_{1,-1} - (s_{3,-1,3,1}^{\text{II}})_{1,1} - (s_{3,-1,3,1}^{\text{II}})_{-1,1} \right] \frac{\mathbf{S}_-^1}{8} \right. \right. \\
& \left. \left. + \left[- (s_{3,1,3,3}^{\text{II}})_{1,1} + (s_{3,-3,3,-1}^{\text{II}})_{-1,-1} \right] \frac{3\mathbf{S}_4^{(1)}}{8} \right\} \right\}. \tag{B.3}
\end{aligned}$$

The interference term is given by

$$\begin{aligned}
\mathbf{R}^{\text{II}}_{\lambda_1\lambda_2} = & \frac{f_{\frac{1}{2}\frac{1}{2}} f_{\frac{1}{2}\frac{3}{2}}}{2f_{\frac{1}{2}\frac{1}{2}}^2 + f_{\frac{1}{2}\frac{3}{2}}^2} \left\{ \left[(c_{1,1,3,1}^{\text{II}})_{1,1} + (c_{1,-1,3,-1}^{\text{II}})_{-1,-1} \right] \frac{\mathbf{C}_0^0}{2} + \left[(c_{1,-1,3,-1}^{\text{II}})_{1,1} \right. \right. \\
& \left. \left. \pm (c_{1,1,3,1}^{\text{II}})_{-1,-1} \right] \frac{\mathbf{C}_\pm^0}{8} + \left[\mp (c_{1,1,3,1}^{\text{II}})_{1,-1} - (c_{1,-1,3,-1}^{\text{II}})_{-1,1} \right] \frac{\mathbf{D}_{01}^\pm}{4} \right. \\
& \left. + \left[\mp (c_{1,-1,3,-1}^{\text{II}})_{1,-1} - (c_{1,1,3,1}^{\text{II}})_{-1,1} \right] \frac{\mathbf{D}_{10}^\pm}{4} + \left[(c_{1,-1,3,3}^{\text{II}})_{1,1} + (c_{3,-3,1,1}^{\text{II}})_{-1,-1} \right] \frac{3\mathbf{C}_+^2}{8} \right. \\
& \left. + \left[(s_{1,-1,3,3}^{\text{II}})_{1,1} + (s_{3,-3,1,1}^{\text{II}})_{-1,-1} \right] \frac{3\mathbf{S}_+^2}{4} + \sin\theta \sin\theta' \left\{ \left[(c_{3,-1,1,1}^{\text{II}})_{1,1} \right. \right. \right. \\
& \left. \left. \pm (c_{1,-1,3,1}^{\text{II}})_{-1,-1} \right] \frac{\mathbf{C}_\pm^1}{8} + \left[(c_{3,-3,1,-1}^{\text{II}})_{-1,-1} \pm (c_{1,1,3,3}^{\text{II}})_{1,1} \right] \frac{3\mathbf{C}_\pm^1}{8} \right. \\
& \left. + \left[(c_{1,-1,3,1}^{\text{II}})_{1,1} \pm (c_{3,-1,1,1}^{\text{II}})_{-1,-1} \right] \frac{\mathbf{C}_\pm^1}{2} + \left[(c_{1,-1,3,1}^{\text{II}})_{-1,1} + (c_{3,-1,1,1}^{\text{II}})_{-1,1} \right] \right. \\
& \left. \times \left(\frac{\mathbf{C}_1^{(1)} + \mathbf{C}_2^{(1)}}{4} \right) + \left[(c_{3,-1,1,1}^{\text{II}})_{1,-1} + (c_{1,-1,3,1}^{\text{II}})_{1,-1} \right] \left(\frac{\mathbf{C}_1^{(1)} - \mathbf{C}_2^{(1)}}{4} \right) \right\}.
\end{aligned}$$

$$\begin{aligned}
 & + [(s_{3,-3,1,-1}^{\text{II}})_{-1,-1} \pm (s_{1,1,3,3}^{\text{II}})_{1,1}] \frac{3\mathbf{S}_{\pm 1}^{(1)}}{8} + [(s_{3,-1,1,1}^{\text{II}})_{1,1} \pm (s_{1,-1,3,1}^{\text{II}})_{-1,-1}] \frac{\mathbf{S}_{\pm 1}^{(1)}}{8} \\
 & + [(s_{1,-1,3,1}^{\text{II}})_{1,1} \pm (s_{3,-1,1,1}^{\text{II}})_{-1,-1}] \frac{\mathbf{S}_{\pm 1}^{(1)}}{2} + [(s_{3,-1,1,1}^{\text{II}})_{-1,1} + (s_{1,-1,3,1}^{\text{II}})_{-1,1}] \\
 & \times \left(\frac{\mathbf{S}_+^1 + \mathbf{S}_2^{(1)}}{4} \right) + [(s_{1,-1,3,1}^{\text{II}})_{1,-1} + (s_{3,-1,1,1}^{\text{II}})_{1,-1}] \left(\frac{\mathbf{S}_+^1 - \mathbf{S}_2^{(1)}}{4} \right) \Big\}. \quad (\text{B.4})
 \end{aligned}$$

The various 4×4 angular matrices appearing in Equations (B.2) to (B.4) are listed below:

$$\mathbf{C}_0^0 = (1 - \mu^2)(1 - \mu'^2) \begin{bmatrix} 1 & 1 & 0 & 0 \\ 1 & 1 & 0 & 0 \\ 0 & 0 & 0 & 0 \\ 0 & 0 & 0 & 0 \end{bmatrix}, \quad (\text{B.5})$$

$$\mathbf{C}_+^0 = \begin{bmatrix} (1 + \mu^2)(1 + \mu'^2) & -(1 + \mu^2)(1 - \mu'^2) & 0 & 0 \\ -(1 - \mu^2)(1 + \mu'^2) & (1 - \mu^2)(1 - \mu'^2) & 0 & 0 \\ 0 & 0 & 0 & 0 \\ 0 & 0 & 0 & 4\mu\mu' \end{bmatrix}, \quad (\text{B.6})$$

$$\mathbf{D}_{10}^+ = \begin{bmatrix} (1 - \mu^2)(1 + \mu'^2) & -(1 - \mu^2)(1 - \mu'^2) & 0 & 0 \\ (1 - \mu^2)(1 + \mu'^2) & -(1 - \mu^2)(1 - \mu'^2) & 0 & 0 \\ 0 & 0 & 0 & 0 \\ 0 & 0 & 0 & 0 \end{bmatrix}, \quad (\text{B.7})$$

$$\mathbf{D}_{01}^+ = \begin{bmatrix} (1 + \mu^2)(1 - \mu'^2) & (1 + \mu^2)(1 - \mu'^2) & 0 & 0 \\ -(1 - \mu^2)(1 - \mu'^2) & -(1 - \mu^2)(1 - \mu'^2) & 0 & 0 \\ 0 & 0 & 0 & 0 \\ 0 & 0 & 0 & 0 \end{bmatrix}, \quad (\text{B.8})$$

$$\mathbf{C}_+^2 = \begin{bmatrix} (1 - \mu^2)(1 - \mu'^2) & -(1 - \mu^2)(1 + \mu'^2) & 0 & 0 \\ -(1 + \mu^2)(1 - \mu'^2) & (1 + \mu^2)(1 + \mu'^2) & 0 & 0 \\ 0 & 0 & 4\mu\mu' & 0 \\ 0 & 0 & 0 & 0 \end{bmatrix}, \quad (\text{B.9})$$

$$\mathbf{D}_{01}^- = 2\mu(1 - \mu'^2) \begin{bmatrix} 0 & 0 & 0 & 0 \\ 0 & 0 & 0 & 0 \\ 0 & 0 & 0 & 0 \\ 1 & 1 & 0 & 0 \end{bmatrix}; \quad \mathbf{D}_{10}^- = 2\mu'(1 - \mu^2) \begin{bmatrix} 0 & 0 & 0 & 1 \\ 0 & 0 & 0 & 1 \\ 0 & 0 & 0 & 0 \\ 0 & 0 & 0 & 0 \end{bmatrix}, \quad (\text{B.10})$$

$$\mathbf{C}_-^0 = 2 \begin{bmatrix} 0 & 0 & 0 & (1 + \mu^2)\mu' \\ 0 & 0 & 0 & -(1 - \mu^2)\mu' \\ 0 & 0 & 0 & 0 \\ \mu(1 + \mu'^2) & -\mu(1 - \mu'^2) & 0 & 0 \end{bmatrix}, \quad (\text{B.11})$$

$$\mathbf{S}_+^2 = \begin{bmatrix} 0 & 0 & -(1 - \mu^2)\mu' & 0 \\ 0 & 0 & (1 + \mu^2)\mu' & 0 \\ \mu(1 - \mu'^2) & -\mu(1 + \mu'^2) & 0 & 0 \\ 0 & 0 & 0 & 0 \end{bmatrix}, \quad (\text{B.12})$$

$$\mathbf{C}_+^1 = \mu\mu' \begin{bmatrix} 1 & 1 & 0 & 0 \\ 1 & 1 & 0 & 0 \\ 0 & 0 & 0 & 0 \\ 0 & 0 & 0 & 0 \end{bmatrix} + \mathbf{E}_{33} + \mathbf{E}_{44}; \quad \mathbf{C}_-^1 = \begin{bmatrix} 0 & 0 & 0 & \mu \\ 0 & 0 & 0 & \mu \\ 0 & 0 & 0 & 0 \\ \mu' & \mu' & 0 & 0 \end{bmatrix}, \quad (\text{B.13})$$

$$\mathbf{C}_1^{(1)} = \mu\mu' \begin{bmatrix} 1 & 1 & 0 & 0 \\ 1 & 1 & 0 & 0 \\ 0 & 0 & 0 & 0 \\ 0 & 0 & 0 & 0 \end{bmatrix} + \mathbf{E}_{33} - \mathbf{E}_{44}; \quad \mathbf{C}_2^{(1)} = \mathbf{C}_-^1 \quad (\text{B.14})$$

$$\mathbf{F}_1^{(1)} = \mu\mu' \begin{bmatrix} 1 & 1 & 0 & 0 \\ 1 & 1 & 0 & 0 \\ 0 & 0 & 0 & 0 \\ 0 & 0 & 0 & 0 \end{bmatrix} + \mathbf{E}_{33}; \quad \mathbf{F}_2^{(1)} = \mathbf{E}_{44}, \quad (\text{B.15})$$

$$\mathbf{F}_{+3}^{(1)} = \mu \begin{bmatrix} 0 & 0 & 0 & 1 \\ 0 & 0 & 0 & 1 \\ 0 & 0 & 0 & 0 \\ 0 & 0 & 0 & 0 \end{bmatrix}; \quad \mathbf{F}_{-3}^{(1)} = \mu' \begin{bmatrix} 0 & 0 & 0 & 0 \\ 0 & 0 & 0 & 0 \\ 0 & 0 & 0 & 0 \\ 1 & 1 & 0 & 0 \end{bmatrix}, \quad (\text{B.16})$$

$$\mathbf{S}_1^{(1)} = \begin{bmatrix} 0 & 0 & -\mu & 0 \\ 0 & 0 & -\mu & 0 \\ \mu' & \mu' & 0 & 0 \\ 0 & 0 & 0 & 0 \end{bmatrix}; \quad \mathbf{S}_2^{(1)} = \mathbf{E}_{43} + \mathbf{E}_{34}, \quad (\text{B.17})$$

$$\mathbf{S}_+^1 = \begin{bmatrix} 0 & 0 & \mu & 0 \\ 0 & 0 & \mu & 0 \\ -\mu' & -\mu' & 0 & 0 \\ 0 & 0 & 0 & 0 \end{bmatrix}; \quad \mathbf{S}_-^1 = \mathbf{E}_{34}; \quad \mathbf{S}_{+1}^{(1)} = \mathbf{S}_+^1; \quad \mathbf{S}_{-1}^{(1)} = \mathbf{S}_4^{(1)}, \quad (\text{B.18})$$

$$\mathbf{S}_{+1}^{(1)} = \mathbf{S}_+^1, \quad \mathbf{S}_{-1}^{(1)} = \mathbf{S}_4^{(1)}; \quad \mathbf{S}_3^{(1)} = \mathbf{E}_{43}; \quad \mathbf{S}_4^{(1)} = \mathbf{E}_{43} - \mathbf{E}_{34}. \quad (\text{B.19})$$

Here \mathbf{E}_{ij} denotes a matrix that has a single element $E_{ij} = 1$, while all the remaining elements are zero.

C

Magnetic redistribution functions for type-III redistribution

In this appendix we present the expressions for the magnetic redistribution functions of the type HH, HF, FH and FF appearing in Equations (4.16) and (4.17). They are defined as follows

$$R_{b_m a_m, b'_m f_m}^{\text{III, HH}}(x_{b'f}, x'_{ba}, \Theta) = \frac{1}{\pi^2 \sin \Theta} \int_{-\infty}^{+\infty} du e^{-u^2} \left[\frac{a_b}{a_b^2 + (v'_{b_m a_m} - u)^2} \right] \times H \left(\frac{a_{b'}}{\sin \Theta}, \frac{v'_{b'_m f_m}}{\sin \Theta} - u \cot \Theta \right), \quad (\text{C.1})$$

$$R_{b_m a_m, b'_m f_m}^{\text{III, HF}}(x_{b'f}, x'_{ba}, \Theta) = \frac{1}{\pi^2 \sin \Theta} \int_{-\infty}^{+\infty} du e^{-u^2} \left[\frac{a_b}{a_b^2 + (v'_{b_m a_m} - u)^2} \right] \times {}_2F \left(\frac{a_{b'}}{\sin \Theta}, \frac{v'_{b'_m f_m}}{\sin \Theta} - u \cot \Theta \right), \quad (\text{C.2})$$

$$R_{b_m a_m, b'_m f_m}^{\text{III, FH}}(x_{b'f}, x'_{ba}, \Theta) = \frac{1}{\pi^2 \sin \Theta} \int_{-\infty}^{+\infty} du e^{-u^2} \left[\frac{(v'_{b_m a_m} - u)}{a_b^2 + (v'_{b_m a_m} - u)^2} \right] \times H \left(\frac{a_{b'}}{\sin \Theta}, \frac{v'_{b'_m f_m}}{\sin \Theta} - u \cot \Theta \right), \quad (\text{C.3})$$

and

$$R_{b_m a_m, b'_m f_m}^{\text{III, FF}}(x_{b'f}, x'_{ba}, \Theta) = \frac{1}{\pi^2 \sin \Theta} \int_{-\infty}^{+\infty} du e^{-u^2} \left[\frac{(v'_{b_m a_m} - u)}{a_b^2 + (v'_{b_m a_m} - u)^2} \right] \times 2F \left(\frac{a_{b'}}{\sin \Theta}, \frac{v'_{b'_m f_m}}{\sin \Theta} - u \cot \Theta \right). \quad (\text{C.4})$$

In the above equations $H(a, x)$ and $F(a, x)$ are the Voigt and Faraday-Voigt functions (see Equation (2.18) for their definition). Θ is the scattering angle (the angle between the incident and scattered rays; see Figure 2.2. The dimensionless quantities appearing in Equations (C.1) to (C.4) are given by

$$x_{ba} = \frac{\nu_{0ba} - \nu}{\Delta\nu_D}; \quad a_b = \frac{\gamma_b + \gamma_c}{4\pi\Delta\nu_D}; \quad v_{b_m a_m} = x_{ba} + (g_b \mu_b - g_a \mu_a) \frac{\nu_L}{\Delta\nu_D}, \quad (\text{C.5})$$

where ν_{0ba} is the line center frequency corresponding to a $J_a \rightarrow J_b$ transition in the absence of magnetic fields, a_b is the damping parameter of the excited state b , and $\Delta\nu_D$ is the Doppler width. In the limit of a two-level atom (obtained by setting $J_b = J'_b$ and $J_a = J_f$) and in the absence of a magnetic field the $R^{\text{III, HH}}$ and $R^{\text{II, H}}$ (defined in Chapter 2) reduce to the Hummer's R^{III} and R^{II} functions respectively (see also Sampoorna et al., 2007a).

The angle-averaged analogues of Equations (C.1)-(C.4) are obtained through

$$R_{b_m a_m, b'_m f_m}^{\text{III, XY}}(x_{b'f}, x'_{ba}) = \frac{1}{2} \int_0^\pi R_{b_m a_m, b'_m f_m}^{\text{III, XY}}(x_{b'f}, x'_{ba}, \Theta) \sin \Theta d\Theta, \quad (\text{C.6})$$

(see Equations (103) and (104) of Bomnier (1997b) and Equations (30) and (31) of Sampoorna et al. (2008b)), where X and Y stand for H and/or F.

A similar expression can be used for computing angle-averaged analogues of the type-II functions.

Bibliography

- Anusha, L. S., & Nagendra, K. N. 2011a, *ApJ*, 726, 6
- . 2011b, *ApJ*, 738, 116
- . 2011c, *ApJ*, 739, 40
- . 2012, *ApJ*, 746, 84
- Anusha, L. S., Nagendra, K. N., & Paletou, F. 2011a, *ApJ*, 726, 96
- Anusha, L. S., Nagendra, K. N., Stenflo, J. O., Bianda, M., Sampoorna, M., Frisch, H., Holzreuter, R., & Ramelli, R. 2010, *ApJ*, 718, 988
- Anusha, L. S., et al. 2011b, *ApJ*, 737, 95
- Asplund, M., Grevesse, N., Sauval, A. J., & Scott, P. 2009, *Ann. Rev. Astron. Astrophys.*, 47, 481
- Asplund, M., Nordlund, Å., & Trampedach, R. 1999, in *Astronomical Society of the Pacific Conference Series*, Vol. 173, *Stellar Structure: Theory and Test of Connective Energy Transport*, ed. A. Gimenez, E. F. Guinan, & B. Montesinos, 221
- Auer, L., Bendicho, P. F., & Trujillo Bueno, J. 1994, *A&A*, 292, 599
- Auer, L. H., Rees, D. E., & Stenflo, J. O. 1980, *A&A*, 88, 302
- Avrett, E. H. 1995, in *Infrared tools for solar astrophysics: What's next?*, ed. J. R. Kuhn & M. J. Penn, 303–311
- Avrett, E. H., Kurucz, R. L., & Loeser, R. 1984, in *Bulletin of the American Astronomical Society*, Vol. 16, *Bulletin of the American Astronomical Society*, 450
- Avrett, E. H., & Loeser, R. 2008, *APJS*, 175, 229
- Barklem, P. S., & O'Mara, B. J. 1998, *MNRAS*, 300, 863
- Belluzzi, L. 2009, *A&A*, 508, 933

- Belluzzi, L., Landi Degl'Innocenti, E., & Trujillo Bueno, J. 2009, *ApJ*, 705, 218
- Belluzzi, L., & Trujillo Bueno, J. 2011, *ApJ*, 743, 3
- . 2012, *Astrophys. J., Lett.*, 750, L11
- Belluzzi, L., Trujillo Bueno, J., & Landi Degl'Innocenti, E. 2007, *ApJ*, 666, 588
- Bergemann, M., & Cescutti, G. 2010, *A&A*, 522, A9
- Berman, P. R., & Lamb, W. E. 1969, *Physical Review*, 187, 221
- Bianda, M., Solanki, S. K., & Stenflo, J. O. 1998, *A&A*, 331, 760
- Bianda, M., Stenflo, J. O., Gandorfer, A., & Gisler, D. 2003, in *Astronomical Society of the Pacific Conference Series*, Vol. 286, *Current Theoretical Models and Future High Resolution Solar Observations: Preparing for ATST*, ed. A. A. Pevtsov & H. Uitenbroek, 61
- Bianda, M., et al. 2011, *A&A*, 530, L13
- Bommier, V. 1997a, *A&A*, 328, 706
- . 1997b, *A&A*, 328, 726
- Bommier, V. 2003, in *Astronomical Society of the Pacific Conference Series*, Vol. 307, *Solar Polarization*, ed. J. Trujillo-Bueno & J. Sanchez Almeida, 213
- Bommier, V., & Sahal-Brechot, S. 1978, *A&A*, 69, 57
- Bommier, V., & Stenflo, J. O. 1999, *A&A*, 350, 327
- Brückner, G. 1963, *Z. Astrophys.*, 58, 73
- Casini, R., & Manso Sainz, R. 2005, *ApJ*, 624, 1025
- Chandrasekhar, S. 1950, *Radiative transfer*.
- Derouich, M. 2008, *A&A*, 481, 845
- Dirac, P. A. M. 1927a, *Royal Society of London Proceedings Series A*, 114, 710
- . 1927b, *Royal Society of London Proceedings Series A*, 114, 243
- Domke, H., & Hubeny, I. 1988, *ApJ*, 334, 527
- Dumont, S., Pecker, J.-C., & Omont, A. 1973, *Sol. Phys.*, 28, 271
- Fabiani Bendicho, P., Trujillo Bueno, J., & Auer, L. 1997, *A&A*, 324, 161

- Fano, U. 1957, *Reviews of Modern Physics*, 29, 74
- Faurobert, M. 1987, *A&A*, 178, 269
- . 1988, *A&A*, 194, 268
- Faurobert, M. 2000, in *Astronomical Society of the Pacific Conference Series*, Vol. 205, *Last Total Solar Eclipse of the Millennium*, ed. W. Livingston & A. Özgüç, 156
- Faurobert, M. 2003, in *EAS Publications Series*, Vol. 9, *EAS Publications Series*, ed. J. Arnaud & N. Meunier, 77
- . 2012, *IAU Special Session*, 6
- Faurobert, M., Derouich, M., Bommier, V., & Arnaud, J. 2009, *A&A*, 493, 201
- Faurobert-Scholl, M. 1991, *A&A*, 246, 469
- . 1992, *A&A*, 258, 521
- . 1994, *A&A*, 285, 655
- . 1996, *Sol. Phys.*, 164, 79
- Faurobert-Scholl, M., Feautrier, N., Machefer, F., Petrovay, K., & Spielfiedel, A. 1995, *A&A*, 298, 289
- Faurobert-Scholl, M., Frisch, H., & Nagendra, K. N. 1997, *A&A*, 322, 896
- Fluri, D. M., Holzreuter, R., Klement, J., & Stenflo, J. O. 2003a, in *Astronomical Society of the Pacific Conference Series*, Vol. 307, *Solar Polarization*, ed. J. Trujillo-Bueno & J. Sanchez Almeida, 263
- Fluri, D. M., Nagendra, K. N., & Frisch, H. 2003b, *A&A*, 400, 303
- Fontenla, J. M., Avrett, E., Thuillier, G., & Harder, J. 2006, *ApJ*, 639, 441
- Fontenla, J. M., Avrett, E. H., & Loeser, R. 1990, *ApJ*, 355, 700
- . 1991, *ApJ*, 377, 712
- . 1993, *ApJ*, 406, 319
- . 2002, *ApJ*, 572, 636
- Fontenla, J. M., Balasubramaniam, K. S., & Harder, J. 2007, *ApJ*, 667, 1243
- Fontenla, J. M., Curdt, W., Haberreiter, M., Harder, J., & Tian, H. 2009, *ApJ*, 707, 482

- Frisch, H. 2007, *A&A*, 476, 665
- . 2010, *A&A*, 522, A41
- Frisch, H., Anusha, L. S., Sampoorna, M., & Nagendra, K. N. 2009, *A&A*, 501, 335
- Gandorfer, A. 2000, *The Second Solar Spectrum: A high spectral resolution polarimetric survey of scattering polarization at the solar limb in graphical representation. Volume I: 4625 Å to 6995 Å*
- . 2002, *The Second Solar Spectrum: A high spectral resolution polarimetric survey of scattering polarization at the solar limb in graphical representation. Volume II: 3910 Å to 4630 Å*
- . 2005, *The Second Solar Spectrum: A high spectral resolution polarimetric survey of scattering polarization at the solar limb in graphical representation. Volume III: 3160 Å to 3915 Å*
- Gandorfer, A. M., Steiner, H. P. P. P., Aebersold, F., Egger, U., Feller, A., Gisler, D., Hagenbuch, S., & Stenflo, J. O. 2004, *A&A*, 422, 703
- Gu, Y., Jefferies, J. T., Lindsey, C., & Avrett, E. H. 1997, *ApJ*, 484, 960
- Hale, G. E. 1908a, *ApJ*, 28, 315
- . 1908b, *Publ. Astron. Soc. Pac.*, 20, 220
- Hamilton, D. R. 1947, *ApJ*, 106, 457
- Hanle, W. 1924, *Zeitschrift fur Physik*, 30, 93
- Heinzl, P., & Hubený, I. 1982, *JQSRT*, 27, 1
- Holweger, H., & Mueller, E. A. 1974, *Sol. Phys*, 39, 19
- Holzreuter, R., Fluri, D. M., & Stenflo, J. O. 2005, *A&A*, 434, 713
- . 2006, *A&A*, 449, L41
- Howard, R., & Stenflo, J. O. 1972, *Sol. Phys*, 22, 402
- Hummer, D. G. 1962, *MNRAS*, 125, 21
- Ivanov, V. V. 1991, in *NATO ASIC Proc. 341: Stellar Atmospheres - Beyond Classical Models*, ed. L. Crivellari, I. Hubeny, & D. G. Hummer, 81
- Kerkeni, B. 2002, *A&A*, 390, 783

- Kerkeni, B., & Bommier, V. 2002, *A&A*, 394, 707
- Kleint, L., Berdyugina, S. V., Gisler, D., Shapiro, A. I., & Bianda, M. 2010a, *Astronomische Nachrichten*, 331, 644
- Kleint, L., Berdyugina, S. V., Shapiro, A. I., & Bianda, M. 2010b, *A&A*, 524, A37
- Kramers, H. A., & Heisenberg, W. 1925, *Zeitschrift fur Physik*, 31, 681
- Kurucz, R. 1969, in *Theory and Observation of Normal Stellar Atmospheres*, ed. O. Gingerich, 375
- Kurucz, R. L. 1973, PhD thesis, HARVARD UNIVERSITY.
- . 1979, *ApJS*, 40, 1
- Kurucz, R. L. 1990, in *3rd International Collogium of the Royal Netherlands Academy of Arts and Sciences*, ed. J. E. Hansen, 20
- Landi Degl’Innocenti, E. 1983, *Sol. Phys*, 85, 3
- . 1984, *Sol. Phys*, 91, 1
- . 1985, *Sol. Phys*, 102, 1
- Landi Degl’Innocenti, E., Bommier, V., & Sahal-Brechot, S. 1991, *A&A*, 244, 401
- Landi Degl’Innocenti, E., Landi Degl’Innocenti, M., & Landolfi, M. 1997, in *Proc. Forum THÉMIS, Science with THÉMIS*, ed. N. Mein & S. Sahal-Bréchet, *Proc. Forum THÉMIS, Science with THÉMIS*, 56
- Landi Degl’Innocenti, E., & Landolfi, M., eds. 2004, *Astrophysics and Space Science Library*, Vol. 307, *Polarization in Spectral Lines*
- Leroy, J. L. 1985, in *Measurements of Solar Vector Magnetic Fields*, ed. M. J. Hagyard, 121–140
- López Ariste, A., Asensio Ramos, A., Manso Sainz, R., Derouich, M., & Gelly, B. 2009, *A&A*, 501, 729
- Machado, M. E., Avrett, E. H., Vernazza, J. E., & Noyes, R. W. 1980, *ApJ*, 242, 336
- Maltby, P., Avrett, E. H., Carlsson, M., Kjeldseth-Moe, O., Kurucz, R. L., & Loeser, R. 1986, *ApJ*, 306, 284
- Manso Sainz, R., & Trujillo-Bueno, J. 1999, in *Astrophysics and Space Science Library*, Vol. 243, *Polarization*, ed. K. N. Nagendra & J. O. Stenflo, 143–156

- Manso Sainz, R., & Trujillo Bueno, J. 2003, in *Astronomical Society of the Pacific Conference Series*, Vol. 307, *Solar Polarization*, ed. J. Trujillo-Bueno & J. Sanchez Almeida, 251
- Manso Sainz, R., & Trujillo Bueno, J. 2010, *ApJ*, 722, 1416
- Michelson, A. A. 1891, *Philosophical Magazine Series 5*, 31, 338
- Michelson, A. A., & Morley, E. W. 1887, *Philosophical Magazine Series 5*, 24, 463
- Mihalas, D. 1978, *Stellar atmospheres /2nd edition/*
- Moruzzi, G., & Strumia, F., eds. 1991, *The Hanle Effect and Level-Crossing Spectroscopy*
- Nagendra, K. N. 1994, *ApJ*, 432, 274
- Nagendra, K. N. 2003a, in *Astronomical Society of the Pacific Conference Series*, Vol. 288, *Stellar Atmosphere Modeling*, ed. I. Hubeny, D. Mihalas, & K. Werner, 583
- Nagendra, K. N. 2003b, in *Astronomical Society of the Pacific Conference Series*, Vol. 288, *Stellar Atmosphere Modeling*, ed. I. Hubeny, D. Mihalas, & K. Werner, 611
- Nagendra, K. N., Anusha, L. S., & Sampoorna, M. 2009, *Mem. Soc. Astron. Ital.*, 80, 678
- Nagendra, K. N., Frisch, H., & Faurobert, M. 2002, *A&A*, 395, 305
- Nagendra, K. N., Frisch, H., & Faurobert-Scholl, M. 1998, *A&A*, 332, 610
- Nagendra, K. N., Frisch, H., & Fluri, D. M. 2003, in *Astronomical Society of the Pacific Conference Series*, Vol. 307, *Solar Polarization*, ed. J. Trujillo-Bueno & J. Sanchez Almeida, 227
- Nagendra, K. N., Paletou, F., Frisch, H., & Faurobert-Scholl, M. 1999, in *Astrophysics and Space Science Library*, Vol. 243, *Polarization*, ed. K. N. Nagendra & J. O. Stenflo, 127–142
- Nagendra, K. N., & Sampoorna, M. 2009, in *Astronomical Society of the Pacific Conference Series*, Vol. 405, *Solar Polarization 5: In Honor of Jan Stenflo*, ed. S. V. Berdyugina, K. N. Nagendra, & R. Ramelli, 261
- Nagendra, K. N., & Sampoorna, M. 2011, *A&A*, 535, A88
- Neckel, H., & Labs, D. 1994, *Sol. Phys*, 153, 91
- Olson, G. L., Auer, L. H., & Buchler, J. R. 1986, *JQSRT*, 35, 431

- Omont, A., Smith, E. W., & Cooper, J. 1972, *ApJ*, 175, 185
- . 1973, *ApJ*, 182, 283
- Paletou, F., & Auer, L. H. 1995, *A&A*, 297, 771
- Paletou, F., & Faurobert-Scholl, M. 1997, *A&A*, 328, 343
- Pauli, W. 1924, *Naturwissenschaften*, 12, 741
- Penny, C. M. 1969, *J. Opt. Soc. Am.*, 59, 34
- Pereira, T. M. D., Asplund, M., Collet, R., Thaler, I., Trampedach, R., & Leenaarts, J. 2013, *A&A*, 554, A118
- Podgoretskii, M. I., & Khrustalev, O. A. 1964, *Soviet Physics Uspekhi*, 6, 682
- Povel, H., Aebersold, H., & Stenflo, J. O. 1990, *Appl. Opt.*, 29, 1186
- Povel, H.-P. 1995, *Optical Engineering*, 34, 1870
- Povel, H. P. 2001, in *Astronomical Society of the Pacific Conference Series*, Vol. 248, *Magnetic Fields Across the Hertzsprung-Russell Diagram*, ed. G. Mathys, S. K. Solanki, & D. T. Wickramasinghe, 543
- Ramelli, R., Bianda, M., Trujillo Bueno, J., Belluzzi, L., & Landi Degl’Innocenti, E. 2009, in *Astronomical Society of the Pacific Conference Series*, Vol. 405, *Solar Polarization 5: In Honor of Jan Stenflo*, ed. S. V. Berdyugina, K. N. Nagendra, & R. Ramelli, 41
- Ramelli, R., et al. 2010, in *Society of Photo-Optical Instrumentation Engineers (SPIE) Conference Series*, Vol. 7735, *Society of Photo-Optical Instrumentation Engineers (SPIE) Conference Series*
- Rees, D. E. 1978, *Publ. Aston. Soc. Jpn.*, 30, 455
- Rees, D. E., & Saliba, G. J. 1982, *A&A*, 115, 1
- Rutten, R. J. 1978, *Sol. Phys*, 56, 237
- Sahal-Brechot, S., Bommier, V., & Leroy, J. L. 1977, *A&A*, 59, 223
- Sampoorna, M. 2008, PhD thesis, Indian Institute of Science
- . 2011a, *ApJ*, 731, 114
- . 2011b, *A&A*, 532, A52

- Sampoorna, M., Nagendra, K. N., & Frisch, H. 2008a, *JQSRT*, 109, 2349
- . 2011, *A&A*, 527, A89
- Sampoorna, M., Nagendra, K. N., & Stenflo, J. O. 2007a, *ApJ*, 663, 625
- . 2007b, *ApJ*, 670, 1485
- . 2008b, *ApJ*, 679, 889
- . 2013, *ApJ*, 770, 92
- Sampoorna, M., Stenflo, J. O., Nagendra, K. N., Bianda, M., Ramelli, R., & Anusha, L. S. 2009, *ApJ*, 699, 1650
- Shchukina, N. G., & Trujillo Bueno, J. T. 2009, in *Astronomical Society of the Pacific Conference Series*, Vol. 405, *Solar Polarization 5: In Honor of Jan Stenflo*, ed. S. V. Berdyugina, K. N. Nagendra, & R. Ramelli, 275
- Smitha, H. N., Nagendra, K. N., Sampoorna, M., & Stenflo, J. O. 2011a, *A&A*, 535, A35
- . 2013a, *JQSRT*, 115, 46
- Smitha, H. N., Nagendra, K. N., & Stenflo, J. O. 2014a, *MNRAS*, under review
- Smitha, H. N., Nagendra, K. N., Stenflo, J. O., Bianda, M., & Ramelli, R. 2014b, *ApJ*, under review
- Smitha, H. N., Nagendra, K. N., Stenflo, J. O., Bianda, M., Sampoorna, M., Ramelli, R., & Anusha, L. S. 2012a, *A&A*, 541, A24
- Smitha, H. N., Nagendra, K. N., Stenflo, J. O., & Sampoorna, M. 2013b, *ApJ*, 768, 163
- Smitha, H. N., Sampoorna, M., Nagendra, K. N., & Stenflo, J. O. 2011b, *ApJ*, 733, 4
- Smitha, H. N., Sowmya, K., Nagendra, K. N., Sampoorna, M., & Stenflo, J. O. 2012b, *ApJ*, 758, 112
- Sommerfeld, A. 1915, *Annalen der Physik*, 351, 721
- . 1916a, *Naturwissenschaften*, 4, 1
- . 1916b, *Annalen der Physik*, 356, 125
- Sowmya, K., Nagendra, K. N., & Sampoorna, M. 2012, *MNRAS*, 423, 2949

- Sowmya, K., Nagendra, K. N., Sampoorna, M., & Stenflo, J. O. 2014a, under review
- Sowmya, K., Nagendra, K. N., Stenflo, J. O., & Sampoorna, M. 2014b, *ApJ*, in press
- Stenflo, J., ed. 1994, *Astrophysics and Space Science Library*, Vol. 189, *Solar Magnetic Fields: Polarized Radiation Diagnostics*
- Stenflo, J. O. 1973, *Sol. Phys.*, 32, 41
- . 1974, *Sol. Phys.*, 37, 31
- Stenflo, J. O. 1976, in *IAU Symposium*, Vol. 71, *Basic Mechanisms of Solar Activity*, ed. V. Bumba & J. Kleczek, 69
- . 1978, *A&A*, 66, 241
- . 1980, *A&A*, 84, 68
- . 1982, *Sol. Phys.*, 80, 209
- . 1984, *Appl. Opt.*, 23, 1267
- Stenflo, J. O. 1985, in *Solar Physics and Interplanetary Travelling Phenomena*, ed. C. de Jager & B. Chen, 1275
- . 1997, *A&A*, 324, 344
- . 1998, *A&A*, 338, 301
- Stenflo, J. O. 2002, in *Astrophysical Spectropolarimetry*, ed. J. Trujillo-Bueno, F. Moreno-Insertis, & F. Sánchez, 55–100
- Stenflo, J. O. 2003, in *Astronomical Society of the Pacific Conference Series*, Vol. 307, *Solar Polarization*, ed. J. Trujillo-Bueno & J. Sanchez Almeida, 385
- . 2005, *A&A*, 429, 713
- . 2007, *Mem. Soc. Astron. Ital.*, 78, 181
- . 2009a, *Central European Astrophysical Bulletin*, 33, 1
- Stenflo, J. O. 2009b, in *Astronomical Society of the Pacific Conference Series*, Vol. 405, *Solar Polarization 5: In Honor of Jan Stenflo*, ed. S. V. Berdyugina, K. N. Nagendra, & R. Ramelli, 3
- Stenflo, J. O., Baur, T. G., & Elmore, D. F. 1980, *A&A*, 84, 60
- Stenflo, J. O., & Keller, C. U. 1996, *Nature*, 382, 588

—. 1997, *A&A*, 321, 927

Stenflo, J. O., Keller, C. U., & Gandorfer, A. 1998, *A&A*, 329, 319

Stenflo, J. O., & Povel, H. 1985, *Appl. Opt.*, 24, 3893

Supriya, H. D., Nagendra, K. N., Sampoorna, M., & Ravindra, B. 2012, *MNRAS*, 425, 527

Supriya, H. D., Sampoorna, M., Nagendra, K. N., Ravindra, B., & Anusha, L. S. 2013a, *JQSRT*, 119, 67

Supriya, H. D., Smitha, H. N., Nagendra, K. N., Ravindra, B., & Sampoorna, M. 2013b, *MNRAS*, 429, 275

Supriya, H. D., Smitha, H. N., Nagendra, K. N., Stenflo, J. O., Bianda, M., Ramelli, R., Ravindra, B., & Anusha, L. S. 2014, *ApJ*, under review

Trujillo Bueno, J. 1999, in *Astrophysics and Space Science Library*, Vol. 243, *Polarization*, ed. K. N. Nagendra & J. O. Stenflo, 73–96

Trujillo Bueno, J. 2001, in *Astronomical Society of the Pacific Conference Series*, Vol. 236, *Advanced Solar Polarimetry – Theory, Observation, and Instrumentation*, ed. M. Sigwarth, 161

Trujillo Bueno, J. 2003, in *Astronomical Society of the Pacific Conference Series*, Vol. 288, *Stellar Atmosphere Modeling*, ed. I. Hubeny, D. Mihalas, & K. Werner, 551

Trujillo Bueno, J. 2011, in *Astronomical Society of the Pacific Conference Series*, Vol. 437, *Solar Polarization 6*, ed. J. R. Kuhn, D. M. Harrington, H. Lin, S. V. Berdyugina, J. Trujillo-Bueno, S. L. Keil, & T. Rimmele, 83

Trujillo Bueno, J., Casini, R., Landolfi, M., & Landi Degl’Innocenti, E. 2002, *Astrophys. J., Lett.*, 566, L53

Trujillo Bueno, J., & Landi Degl’Innocenti, E. 1997, *Astrophys. J., Lett.*, 482, L183

Trujillo Bueno, J., & Manso Sainz, R. 1999, *ApJ*, 516, 436

Trujillo Bueno, J., & Shchukina, N. 2009, *ApJ*, 694, 1364

Uitenbroek, H. 2001, *ApJ*, 557, 389

Štěpán, J., & Trujillo Bueno, J. 2013, *A&A*, 557, A143

Vernazza, J. E., Avrett, E. H., & Loeser, R. 1973, *ApJ*, 184, 605

—. 1976, *ApJS*, 30, 1

—. 1981, *ApJS*, 45, 635

Wiehr, E. 1975, *A&A*, 38, 303

Wood, R. W., & Ellett, A. 1923a, *Nature*, 111, 255

—. 1923b, *Royal Society of London Proceedings Series A*, 103, 396

Zhang, H. W., Gehren, T., & Zhao, G. 2008, *A&A*, 481, 489